Investigation of Transition Metal-Based Catalysts for Electrochemical Energy Storage and Conversion

by

Shuwen Wu

A thesis submitted in partial fulfillment of the requirements for the degree of

Doctor of Philosophy

in

Materials Engineering

Department of Chemical and Materials Engineering

University of Alberta

Abstract

Electrochemical energy conversion and storage, such as electrocatalytic hydrogen generation, metal-air batteries, and fuel cells, are one of the most efficient and reliable systems for renewable energy storage, which address the intermittency of renewable energy systems. However, the energy conversion efficiency is severely restricted by the oxygen redox catalysis, including the oxygen evolution reaction (OER) and oxygen reduction reaction (ORR), because of the sluggish kinetics. To date, state-of-the-art oxygen electrocatalysts are noble-metal-based materials (such as Pt-, Ru- and Ir-), but the limited resources and high cost impede their practical applications. Thus, the development of efficient, durable, and low-cost noble-metal-free oxygen electrocatalysts is significantly important to realize the widespread applications and advance those electrochemical technologies. In this thesis, I aim to develop earth-abundant transition-metal-based catalysts with high electrocatalytic activity and durability and reveal the reaction mechanisms that lead to the enhancement effects of the developed catalysts.

For transition-metal-based layered double hydroxides (LDHs) to become more competitive OER catalysts, substantial progress is required to advance the catalytic activity and durability. I developed a robust electrode composed of Ni_3S_2-embedded NiFe LDH heterostructured nanosheets with a porous structure supported on nickel foam (NF) *via* a one-pot solution approach at room temperature in 15 min. The as-prepared Ni_3S_2-NiFe LDH/NF catalyst delivers 50, 500, and 1000 mA cm^{-2} with an overpotential of only 230, 285 and 303 mV for oxygen evolution reaction, respectively. *In situ* and *ex-situ* analysis reveal that the Ni_3S_2 was *in situ* partially transformed under an electrooxidation environment into NiOOH over an equally important electrically conductive Ni_3S_2 to drive proficient catalysis. This strategy can be extended to fabricate Ru-Ni_3S_2-NiFe LDHs/NF electrocatalyst for high active hydrogen evolution reaction.

The coupled Ni_3S_2-NiFe LDHs/NF-2 ‖ Ru-Ni_3S_2-NiFe LDHs/NF electrodes showed a significantly boosted overall water splitting activity with low voltages of 1.47, 1.71 and 1.85 V to deliver high j_s of 10, 100 and 500 mA cm^{-2}, respectively, far surpassing current commercial requirements (1.8-2.40 V for 200-400 mA cm^{-2}).

Apart from boosting the water electrolysis by improving the anodic OER catalytic activity, replacing OER with a more efficient reaction is compelling because the anodic product O_2 is not of high value. I developed the nanowires composed of CoF_2/CoP heterostructure grown on nickel foam as a robust bifunctional electrocatalyst for 5-hydroxymethylfurfural oxidation reaction (HMFOR) and hydrogen evolution reaction (HER). The developed CoF_2/CoP-2 exhibits excellent HMFOR activity with a working potential of 1.33 V to deliver 100 mA cm^{-2} and a Tafel slope of 21.1 mV dec^{-1}. Meanwhile, the FDCA yield achieved 98.8 % and the faradic efficiency is 98 %. In addition, CoF_2/CoP-2 delivers a current density of 10 mA cm^{-2} at an overpotential of 59 mV with a Tafel slope of 59.8 mV dec^{-1} toward HER. Furthermore, bifunctional CoF_2/CoP-2 exhibits excellent full-cell electrocatalytic activity when employing CoF_2/CoP-2 for cathodic H_2 and anodic FDCA production, which only requires the cell voltage of 1.33 V at 10 mA cm^{-2}, superior to the voltage of 1.54 V at 10 mA cm^{-2} for pure water splitting.

The energy conversion efficiency of metal-air batteries and fuel cells is also severely restricted by the kinetically sluggish oxygen catalysis. Highly efficient and low-cost electrocatalysts for cathodic ORR are highly desirable. I demonstrated an effective strategy of Cu–N_4 sites functionalizing atomic Fe clusters on hierarchical porous carbon nanofibers (Fe_x/Cu–N@CNF) for high-performance ORR. Fe_x/Cu–N@CNF exhibits superior catalytic performances with an onset potential (E_{onset}) of 1.03 V, an ultrahigh half-wave potential ($E_{1/2}$) of 0.944 V, and remarkable durability in alkaline medium, outperforming commercial Pt/C and most recently reported

transition-metal-based catalysts. The theoretical calculations indicate that the single Cu–N$_4$ sites assist the activation of O$_2$ to reduce the energy barrier of O$_2$* protonation and facilitate O–O bond cleavage, boosting the ORR activity. I used Fe$_x$/Cu–N@CNF as a cathode for zinc-battery application, it achieves an impressive specific capacity (1110.4 mA h g^{-1} at 100 mA cm^{-2}) and long-cycling over 400 h, exceeding those Pt/C-based devices.

Preface

This thesis is an original work conducted by Shuwen Wu and under the supervision of Dr. Zhi Li and Dr. Ken Cadien.

Chapter 1 is the introduction that contains the background knowledge and principles of electrochemical oxygen evolution/ reduction.

Chapter 2 covers the literature survey of electrocatalysts for electrochemical oxygen evolution/ reduction.

Chapter 3 briefly introduces the employed methodologies and characterizations.

Chapter 4 has been published as S. W. Wu, S. Q. Liu, X. H. Tan, W. Y. Zhang, K. Cadien, Z. Li. Ni_3S_2-embedded NiFe LDH porous nanosheets with abundant heterointerfaces for high-current water electrolysis. *Chemical Engineering Journal*, 2022, 442, 136105. Dr. S.-Q. Liu provided valuable discussion about conceptualization and helped with VHX-700F digital microscopic images. Dr. X.-H. Tan and W.-Y Zhang helped with TEM test and *in situ* Raman. Dr. Z. Li and Dr. K. Cadien provided valuable comments, suggestions, and feedback for manuscript writing and revision.

Chapter 5 has been submitted to Journal as S. W. Wu, S.-Q. Liu, R. F. Feng, K. Cadien, Z. Li. Bifunctional CoF_2/CoP Heterostructured Nanowires for Enhanced Electrooxidation of 5-Hydroxymethylfurfural and Hydrogen Production. Dr. S.-Q. Liu and Dr. R.-F. Feng worked on the synchrotron measurements. Dr. Z. Li and Dr. K. Cadien provided valuable comments, suggestions, and feedback for manuscript writing and revision.

Chapter 7 includes the summary and prospects.

Acknowledgments

I would like to express my gratitude for the help from individuals and organizations throughout my academic journey at U of A. I extend my heartfelt appreciation to my supervisors Dr. Ken Cadien and Dr. Zhi Li for not only their expertise and guidance but also for offering me a great chance of conducting research on one of my most interested topics.

I thank the committee members of my defense examination: Dr. Hyo-Jick Choi, Dr. Shiva Mohajernia, Dr. Jinguang Hu, and Dr. Anthony Yeung, for their valuable time and help. I send my sincere appreciation to Dr. Anastasia Elias for her valuable suggestions and guidance on my candidacy exam.

I am grateful to my peers and colleagues for all their help and collaboration during my research in the lab. My thanks go to Dr. Shaoqing Liu for many great discussions and constructive advice on my research, Dr. Xuehai Tan for taking the time to methodically answer my questions about the electrochemical test, particularly at the beginning of this research. Besides, many thanks go to Dr. Shihong Xu, Dr. Nancy Zhang, Dr. Xuehai Tan, and Dr. Peng Li, for their assistance in the materials characterizations.

I am greatly thankful to my parents for their unconditional love, support, and care in my life. Finally, I would like to thank my gentleman Shaoqing Liu again for the love, encouragement, and support that he gave me during this amazing chapter of my life.

Table of Contents

List of Tables

List of Figures

List of Symbols

j	Current density
η	Overpotential
C_{dl}	Double layer capacitace
R_{ct}	Charge transfer resistance
E_{onset}	Onset potential
$E_{1/2}$	Half-wave potential
j_L	Measured limited current density
j_k	kinetic current density

List of Abbreviations

HER   Hydrogen evolution reaction

OER   Oxygen evolution reaction

ORR   Oxygen reduction reaction

HOR   Hydrogen oxidation reaction

RHE   Reversible hydrogen electrode

SHE   Standard hydrogen potential

ZABs   Zinc-air batteries

PEMFCs   Proton-exchange membrane fuel cells

DFT   Density functional theory

LSV   Linear sweep voltammetry

CV   Cyclic voltammetry

GDL   Gas diffusion layer

RDE   Rotation disk electrode

RRDE   Rotation ring-disk electrode

SACs   Single-atom catalysts

ECSA   Electrochemical surface area

EIS   Electrochemical Impedance Spectroscopy

XRD   X-ray Diffraction

FESEM   Field Emission Scanning Electron Microscopy

EDX   Energy dispersive X-ray spectroscopy

TEM   Transmission electron microscopy

STEM   Scanning transmission electron microscopy

XPS   X-ray photoelectron spectroscopy

UPS   Ultraviolet photoelectron spectroscopy

FTIR   Fourier transform infrared spectroscopy

XANES   X-ray absorption near-edge structure

EXAFS   Extended X-ray adsorption fine structure

BET   Brunauer–Emmett–Teller

HRTEM   High resolution electron transmission electron microscopy

HAADF   High angle annular dark field

FFT   Fast Fourier transformation

DMF   N-dimethylformamide

PAN   Polyacrylonitrile

ICP-OES   Inductively coupled plasma optical emission spectroscopy

GC   Glassy carbon

Chapter 1. Introduction

The current global capacity for generating electricity is estimated to be around 20 terawatt hours (TW, $\times$ 1012 watts).[1] Approximately 68% of electrical energy is produced from fossil fuels such as coal (42%), natural gas (21%), and oil (5%).[2] However, the combustion of fossil fuels results in air pollution and contributes to the issue of global warming. The environmental concerns over the use of fossil fuels and their resource limitations have aroused great interest in producing electricity from renewable energy sources. Solar and wind energy are among the most abundant and easily accessible sources of energy on earth. The fluctuating nature of these renewable sources poses significant challenges for electric grid operation, as other power facilities (such as power plants) must compensate for the variability. So, there will be a growing need for low-cost electrical energy storage and conversion systems to smooth out the intermittency of renewable energy production.

Electrochemical energy storage and conversion refer to the process of converting electrical energy into chemical energy and then storing it in the electrodes where it can be retrieved and converted back into electrical energy when needed.[3, 4] This process is essential for many applications, including batteries, fuel cells, and capacitors. Electrochemical energy storage and conversion typically involve the use of a redox reaction, which is a chemical reaction in which one substance is reduced (gains electrons) while another is oxidized (loses electrons). In a battery, for example, the positive and negative electrodes are made of materials that can undergo redox reactions, and the electrolyte facilitates the transfer of ions between the electrodes.[5, 6] The development of new and improved electrochemical energy storage and conversion systems is particularly important for the transition to a sustainable energy future, as they can enable the integration of renewable energy sources into the electrical grid and help reduce our dependence on fossil fuels.

Electrochemical energy conversion and storage devices have been extensively explored, including rechargeable batteries, electrolyzers, metal-air batteries and fuel cells.[7, 8] The electrode materials, such as anodes and cathodes, are the key components of these devices, which have a critical impact in determining performance. Clean electrochemical energy conversion, particularly processes involving water, hydrogen, and oxygen, heavily relies on electrocatalysis, enabling a variety of sustainable processes for future technologies. For example, water electrolyzers have gained significant interest, which utilize the hydrogen evolution reaction (HER) and oxygen evolution reaction (OER) to produce H_2 and O_2. Moreover, H_2 is an appealing energy carrier that can be used to generate clean electricity in fuel cells through the hydrogen oxidation reaction (HOR) and oxygen reduction reaction (ORR) to convert chemical energy into electricity. And ORR/OER also play a significant role in metal-air batteries.

1.1 Research Motivation

Energy conversion from renewable sources has been considered as a solution to reduce reliance on fossil fuels that cause the excessive emission of carbon dioxide, the primary contributor to global warming. However, renewable power generated from natural sources, such as solar and wind, is not constant and reliable because of variable weather conditions, which require energy storage devices to counterbalance the intermittency. Electrochemical energy conversion and storage are one of the most efficient and reliable systems, converting electricity into chemical energy or vice versa by reversible electrochemical oxidation-reduction reactions, including electrocatalytic hydrogen generation, metal-air batteries, and fuel cells. However, the energy conversion efficiency is severely restricted by the oxygen redox catalysis (OER/ORR), because of the sluggish kinetics. Thus, it is imperative and necessary to develop highly efficient electrochemical energy storage systems to mitigate the environmental issue.

1.2 The need for intermittent energy storage

Over the past few decades, extensive research has been conducted to explore alternative fuels to fossil fuels, including energy sources such as hydroelectric, geothermal, wind, and solar power. [9] Among these, solar energy and wind power are widely recognized as the most abundant and geographically widespread. However, their intermittent nature poses a challenge due to fluctuations in wind strength and sunlight intensity throughout the day. The electrical energy storage system is an ideal solution for fulfilling this role as it can absorb excess electric energy during periods of high generation and store it for later use during times when generation falls short. Conversely, it can also discharge electric energy into the power grid when there is insufficient generation to meet the demand. (Figure 1.1) Conventional gas or steam turbine technologies have typically been utilized for this role. However, instead of adjusting the torque of large rotary turbomachinery at a rapid pace, fast-responding electrochemical electrical energy storage is better equipped to promptly meet the needs.[10] A promising remedy involves exploiting renewable and earth-abundant biomass, such as lignocellulose, lipids, and starch crops, as substitutes for fossil resources to establish sustainable supply chains.
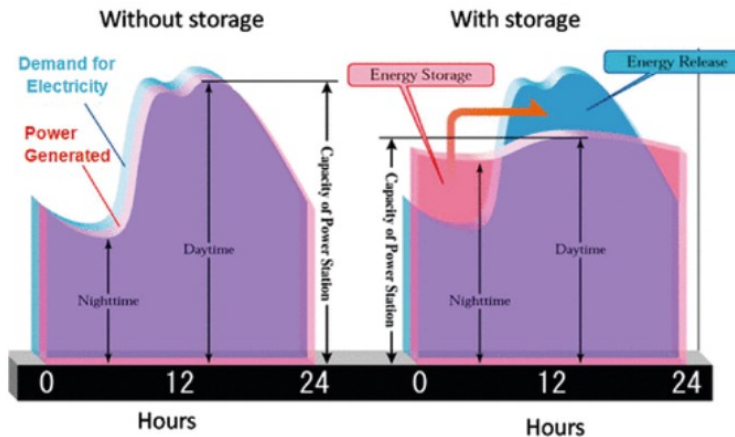
Figure 1. 1 Schematic of balancing generation and demand via load leveling, a typical case of load shifting (Courtesy of NGK, Inc.).[2]

1.3 Electrocatalytic oxygen reactions

Oxygen electrocatalysis involves oxygen evolution and reduction reactions (OER/ORR), which serve as the half-reaction of water electrolyzers, fuel cells and metal-air batteries. Electrochemical water splitting is a promising sustainable technology to produce high-purity H_2 in the conversion of renewable electricity, which can be divided into two half-reactions, named the oxygen evolution reaction (OER) at the anode and the hydrogen evolution reaction (HER) at the cathode (Figure 1.2).[11] The cathodic HER can readily occur on some metals at low overpotentials because of the relatively facile two-electron process. (Eq. 1.1-1.2) In contrast, the anodic OER is a four-electron transfer process with sluggish kinetics (Eq. 1.3-1.5), leading to large overpotentials (ca. 0.3–0.6 V) to drive the reaction, which thus severely impedes the overall efficiency of H_2 production for practical application of water electrolysis.[12] The four steps involved in the OER process are thermodynamically uphill and the rate-limiting step has the highest energy barrier. During the process, the intermediates of *OH, *O, and *OOH are sequentially produced due to simultaneous electron and proton transfer. The bonding interactions within these intermediates play a significant

4

role in determining the catalytic activity. As a result, the adsorption energies of these intermediates are often employed as descriptors for electrocatalytic ability.
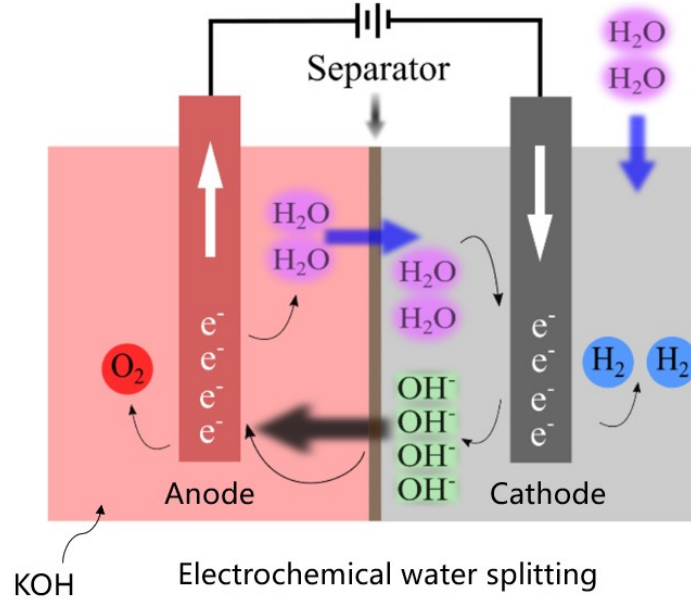
Figure 1. 2 Schematic illustration of electrocatalytic water splitting.

Cathode: $H_2O + e^- \rightarrow *H + OH^-$ (Eq. 1.1)

$*H + H_2O \rightarrow OH^- + H_2$ (Eq. 1.2)

Anode: $OH^- \rightarrow *OH + e^-$ (Eq. 1.3)

$*OH + e^- \rightarrow *O + H_2O + e^-$ (Eq. 1.4)

$*O + OH^- \rightarrow *OOH + e^-$ (Eq. 1.5)

$*OOH + OH^- \rightarrow O_2 + H_2O + e^-$ (Eq. 1.6)

Overall: $2H_2O \rightarrow O_2 + 2H_2;\quad E_0 = 1.23\,V$ (Eq. 1.7)

Electrolysis of water is pH dependent, the correlated pH-dependent potential can be as the following equation,

$$E(RHE) = E_{applied} + 0.059\,pH + E_{reference} \qquad \text{(Eq. 1.8)}$$

The equilibrium potential of water splitting is 1.23 V at 25 $^{\circ}$C and 1 atm.

Since the electrolysis efficiency is significantly limited by the kinetically sluggish OER, it is urgent and necessary to develop effective anodic electrocatalysts, boosting water oxidation performance. Despite the exceptional OER activity demonstrated by noble-metal-based catalytic materials such as IrO_2 and RuO_2, their high costs, limited availability and unsatisfactory stability limit their large-scale application.[13] Therefore, great efforts have been devoted to the development of noble-metal-free electrocatalysts with low cost, improved activity, and excellent stability for OER.

One strategy to boost water electrolysis is by enhancing the catalytic activity for OER. Besides, replacing OER with a more efficient reaction is also compelling with the generation of value-added products during the reaction, because O_2 generated from OER is not particularly valuable. Biomass is various organisms generated via photosynthesis, including plants, animals, and microorganisms.[14] The favorable kinetics of biomass electrooxidation reactions (BEORs) replacing OER have recently gained much attention, because the oxidation products have important applications in various fields, such as agrochemicals and pharmaceuticals.[15-17] Thus, pairing HER with BEOR could be able to realize the highly efficient generation of hydrogen and value-added products.

ORR is a reverse process of OER, which involves multistep electron transfer and multiple adsorbed intermediates. ORR occurs mainly by two reaction mechanisms: the full reduction of O_2 to H_2O in acidic electrolytes or to OH^- in alkaline electrolytes with four-electron transfer, and the 2-electron, partial reduction pathway resulting in H_2O_2 in acidic electrolytes or HO_2^- in alkaline electrolytes. The electrochemical reactions are written as follows:[18]

Four-electron process in basic solution:
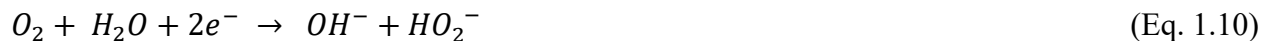
$$O_2 + 2H_2O + 4e^- \rightarrow 4OH^-$$ (Eq. 1.9)

Two-electron process in basic solution:

$$O_2 + H_2O + 2e^- \rightarrow OH^- + HO_2^-$$ (Eq. 1.10)

Four-electron process in acidic solution:

$$O_2 + 4H^+ + 4e^- \rightarrow 2H_2O$$ (Eq. 1.11)

Two-electron process in acidic solution:

$$O_2 + 2H^+ + 2e^- \rightarrow H_2O_2$$ (Eq. 1.12)

The standard Nernstian potential for the oxygen half-cell reaction is 1.23 V related to reversible hydrogen electrode (RHE), which is established based on the hydrogen standard electrode potential at a given pH value.[19] At pH = 0, this potential is known as the standard hydrogen electrode (SHE) scale.[20] The RHE can be corrected by SHE at 300 K via:

$$E_{RHE} = E_{SHE} + 0.059 \times pH \quad [21]$$

The ORR selectivity plays a crucial role in determining the number of electrons transferred during the reaction.[22] The final products and reaction pathways of ORR are strongly affected by the surface properties of the electrocatalyst materials.[23] If the electrocatalyst surface has a strong bond with the O_2 molecule or OOH* intermediate, it can selectively dissociate the O–O bond to produce H_2O via 4e-transfer process. Conversely, electrocatalysts that maintain the O–O bond in the key OOH* species will result in a higher 2e-ORR product.

The electrocatalytic performance of ORR catalysts can be primarily evaluated by the metrics onset potential, half-wave potential, and diffusion-limited current properties.[24, 25] The different dynamic processes, such as kinetic, mixed kinetic-diffusion, or diffusion, determine these parameters. The best catalysts should have an optimal binding strength with intermediates, which is neither too strong nor too weak, resulting in a volcano-type relationship in Figure 1.3.[26] The binding energy should be optimized to boost the sluggish kinetics obtaining high current density at low overpotentials. Typically, two strategies have been adopted to improve the electrocatalysis activity, increasing the number of active sites (e.g., the effective electrochemical active areas (ECSAs)) and enhancing the intrinsic activity of active sites. Along with the progressive nanotechnologies, certain Pt-based catalysts have achieved current densities that surpass the U.S. Department of Energy's specifications for Pt catalysts in PEMFCs ($0.44 \ A \ mgPt^{-1}$ at 0.9 vs RHE). [27]
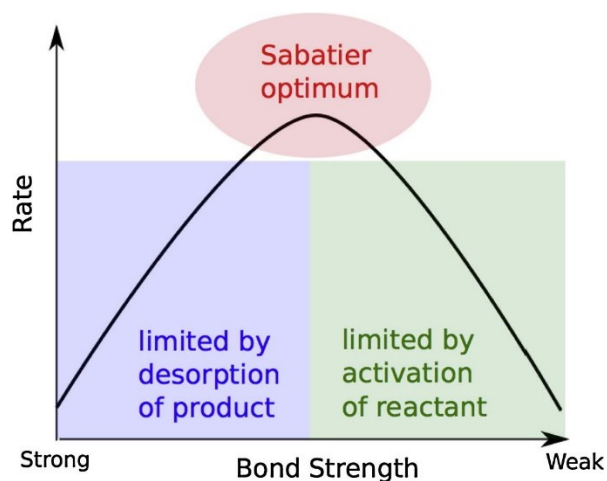
Figure 1. 3 Schematic representation of the qualitative Sabatier principle.

1.4 References

1. Cozzi, L.; Gould, T.; Bouckart, S.; Crow, D.; Kim, T.; Mcglade, C.; Olejarnik, P.; Wanner, B.; Wetzel, D., World energy outlook 2020. *International Energy Agency: Paris,*

France, 2020, 1-461.

2. Yang, Z.; Zhang, J.; Kintner-Meyer, M. C.; Lu, X.; Choi, D.; Lemmon, J. P.; Liu, J., Electrochemical energy storage for green grid. *Chem. Rev.* 2011, *111* (5), 3577-613.

3. Chen, H.; Cong, T. N.; Yang, W.; Tan, C.; Li, Y.; Ding, Y., Progress in electrical energy storage system: A critical review. *Prog. Nat. Sci.* 2009, *19* (3), 291-312.

4. Zhang, F.; Liu, J.; Yang, W.; Logan, B. E., A thermally regenerative ammonia-based battery for efficient harvesting of low-grade thermal energy as electrical power. *Energy Environ. Sci.* 2015, *8* (1), 343-349.

5. Peng, L.; Zhu, Y.; Chen, D.; Ruoff, R. S.; Yu, G., Two-Dimensional Materials for Beyond-Lithium-Ion Batteries. *Adv. Energy Mater.* 2016, *6* (11), 1600025.

6. Thakur, V. K.; Ding, G.; Ma, J.; Lee, P. S.; Lu, X., Hybrid materials and polymer electrolytes for electrochromic device applications. *Adv. Mater.* 2012, *24* (30), 4071-96.

7. Lu, X. F.; Fang, Y.; Luan, D.; Lou, X. W. D., Metal-Organic Frameworks Derived Functional Materials for Electrochemical Energy Storage and Conversion: A Mini Review. *Nano Lett.* 2021, *21* (4), 1555-1565.

8. Chen, J.; Wei, L.; Mahmood, A.; Pei, Z.; Zhou, Z.; Chen, X.; Chen, Y., Prussian blue, its analogues and their derived materials for electrochemical energy storage and conversion. *Energy Stor. Mater.* 2020, *25*, 585-612.

9. Yang, Z.; Liu, J.; Baskaran, S.; Imhoff, C. H.; Holladay, J. D., Enabling renewable energy—and the future grid—with advanced electricity storage. Jom. 2010, *62*, 14-23.

10. Subinas Seco de Herrera, J. M., Development of a microgrid with renewable energy sources and electrochemical storage system integration. 2015.

11. Song, J.; Wei, C.; Huang, Z. F.; Liu, C.; Zeng, L.; Wang, X.; Xu, Z. J., A review on

fundamentals for designing oxygen evolution electrocatalysts. *Chem. Soc. Rev.* 2020, *49* (7), 2196-2214.

12. Li, Y.; Wei, X.; Chen, L.; Shi, J., Electrocatalytic Hydrogen Production Trilogy. *Angew. Chem. Int. Ed.* 2021, *60* (36), 19550-19571.

13. Gopalakrishnan, M.; Mohamad, A. A.; Nguyen, M. T.; Yonezawa, T.; Qin, J.; Thamyongkit, P.; Somwangthanaroj, A.; Kheawhom, S., Recent advances in oxygen electrocatalysts based on tunable structural polymers. *Mater. Today Chem.* 2022, *23*, 100632.

14. Rodionova, M. V.; Poudyal, R. S.; Tiwari, I.; Voloshin, R. A.; Zharmukhamedov, S. K.; Nam, H. G.; Zayadan, B. K.; Bruce, B. D.; Hou, H. J. M.; Allakhverdiev, S. I., Biofuel production: Challenges and opportunities. *Int. J. of Hydrog. Energy* 2017, *42* (12), 8450-8461.

15. Yang, G.; Jiao, Y.; Yan, H.; Xie, Y.; Wu, A.; Dong, X.; Guo, D.; Tian, C.; Fu, H., Interfacial Engineering of MoO(2) -FeP Heterojunction for Highly Efficient Hydrogen Evolution Coupled with Biomass Electrooxidation. *Adv. Mater.* 2020, *32* (17), e2000455.

16. Yang, G.; Jiao, Y.; Yan, H.; Tian, C.; Fu, H., Electronic Structure Modulation of Non-Noble-Metal-Based Catalysts for Biomass Electrooxidation Reactions. *Small Structures* 2021, *2* (10), 2100095.

17. Yang, C.; Wang, C.; Zhou, L.; Duan, W.; Song, Y.; Zhang, F.; Zhen, Y.; Zhang, J.; Bao, W.; Lu, Y.; Wang, D.; Fu, F., Refining d-band center in Ni0.85Se by Mo doping: A strategy for boosting hydrogen generation via coupling electrocatalytic oxidation 5-hydroxymethylfurfural. *Chem. Eng. J.* 2021, *422*, 130125.

18. Singh, S. K.; Takeyasu, K.; Nakamura, J., Active Sites and Mechanism of Oxygen

Reduction Reaction Electrocatalysis on Nitrogen-Doped Carbon Materials. *Adv. Mater.* 2019, *31* (13), e1804297.

19. Vanysek, P., Electrochemical series. *CRC handbook of chemistry and physics* 2000, *8*, 8-33.

20. McNaught, A. D.; Wilkinson, A., Compendium of chemical terminology. *Blackwell Science Oxford*: 1997; Vol. 1669.

21. Sawyer, D. T.; Roberts, J. L., Experimental electrochemistry for chemists. Wiley: 1974.

22. Woo, J.; Lim, J. S.; Kim, J. H.; Joo, S. H., Heteroatom-doped carbon-based oxygen reduction electrocatalysts with tailored four-electron and two-electron selectivity. *Chem. Commun.* 2021, *57* (60), 7350-7361.

23. Jiao, Y.; Zheng, Y.; Jaroniec, M.; Qiao, S. Z., Design of electrocatalysts for oxygen- and hydrogen-involving energy conversion reactions. *Chem. Soc. Rev.* 2015, *44* (8), 2060-86.

24. Xia, W.; Mahmood, A.; Liang, Z.; Zou, R.; Guo, S., Earth-Abundant Nanomaterials for Oxygen Reduction. *Angew. Chem. Int. Ed.* 2016, *55* (8), 2650-76.

25. Zhang, L.; Jiang, S.; Ma, W.; Zhou, Z., Oxygen reduction reaction on Pt-based electrocatalysts: Four-electron vs. two-electron pathway. *Chin. J. Catal.* 2022, *43* (6), 1433-1443.

26. Che, M., Nobel Prize in chemistry 1912 to Sabatier: Organic chemistry or catalysis? *Catal. Today* 2013, *218-219*, 162-171.

27. Strasser, P.; Kühl, S., Dealloyed Pt-based core-shell oxygen reduction electrocatalysts. *Nano Energy* 2016, *29*, 166-177.

Chapter 2. Literature review

To date, state-of-the-art oxygen electrocatalysts are Pt-, Ru- and Ir-based materials, but the limited resources and high cost impede the widespread applications in electrochemical storage and conversion systems.[1, 2] Noble-metal-free materials have gained huge attention for the development of oxygen electrocatalysts, including transition-metal materials, such as hydroxides, oxides, phosphides, sulfides, selenides, carbides, alloys, single-atom catalysts, etc.[3, 4] Different strategies have been explored to develop the high activity of oxygen electrocatalysts.

2.1 Main design principles of nanostructured energy materials

Nanostructures have a common feature of large surface-to-volume ratio comparison to the bulk counterparts with relatively low ratio of surface atoms. The surfaces play an important role in the chemical and physical properties of materials. Thus, surface engineering is an effective way to explore the new properties of materials in different applications. Particularly, inorganic nanostructures are a fascinating type of catalyst that have great potential for various applications such as energy conversion, energy storage, and environmental remediation. The chemical and physical processes can be tuned via the surface engineering techniques (such as morphology control, defect incorporation and interface manipulation), leading to a high impact on catalytic activity (Figure 2.1). The exposed active surface area and facets can be managed by morphology engineering.[5, 6] In addition, the enhancement of orbital hybridization can be achieved by the means of introduction of surface defects, which can change the electron density near the Fermi level and produce unsaturated coordination with more dangling bonds for catalytic reactions. Furthermore, the construction of interfaces and heterojunctions can be easily formed by incorporation other nanostructures. Then the electronic properties can be adjusted, including the energy gap and conductivity, which affects the catalytic performance. For example, the combination of metallic

nanomaterials and semiconductive nanomaterials can impact the distribution of electrons and holes, which substantially alters the activation energy of catalytic reactions.[7, 8]
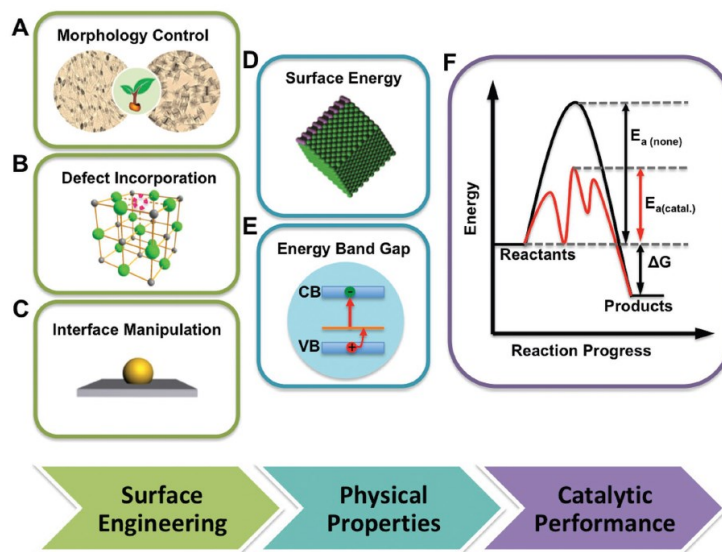
Figure 2. 1 Surface engineering techniques offer opportunities for regulating physical and chemical properties towards enhanced catalytic performance.[5, 6, 9, 10]

2.1.1 Morphology control

The morphologies of nanomaterials have a significant influence on their properties, in addition to their chemical composition. For instance, the nanostructured materials of same chemical composition have different morphologies, such as nanospheres vs nanowires, solid vs hollow, which can display distinctive optical and catalytic properties.[7, 8, 11] As a result, controlling the morphology of nanomaterials has become increasingly crucial in modifying and refining their physical and chemical attributes, which can enhance their performance in various applications. The conventional approach tailoring the morphology of nanostructures involves regulating the nuclei's structure and selectively adhering capping ligands on specific facets during their growth.

In addition, seeded growth and templated synthesis have also widely reported to be an effective way for manipulating the morphologies of nanostructured catalysts.

The ligand-capping effect occurs mainly during the evolution of crystalline seeds in an organic solvent or a mixture of solvents containing well-dispersed metal precursors and reductants. The surfactants in the solution coordinate with metal ions/atoms via covalent bonding, physical adsorption, electrostatic interaction, or van der Waals force. The confine of facets is realized by controlling precursors, solvents, reductants and temperature to modulate the metallic nanocrystal growth. Thus, the well-defined nanostructures can be achieved by controlling selective adhesion of the capping agent to a specific crystal surface. For example, Popczun et al. reported facet-controlled metal phosphide in a cosolvent of trioctylphosphine (TOP) and oleylamine (OAm), where the presence of trioctylphosphine oxide (TOPO) in the TOP enables the branches of CoP nanorods predominantly enclosed by (111) facets.[12] In another instance, Ni_2P nanorods were prepared by using TOP as the capping ligand, because the decomposition of Ni–TOP complexes produces octyl groups that causes the transformation of Ni_2P nanospheres into nanorods.[13] It was demonstrated that the octyl groups selectively attached to the (210) facets and inhibited the growth on these facets while the growth along the [001] direction continued, leading to the formation of Ni_2P nanorods.

Preformed-seed-mediated growth is a versatile colloid chemical method for the preparation of a wide variety of nanostructures with tightly controlled size and diverse morphologies, such as nanorods, nanosheets, and other complex hierarchical structures.[14-16] The seeded growth methods generally involve the preparation of seeds and subsequent epitaxial growth in the reaction solution. The initial production of fine seed particles is finished in the seeding growth process through the reduction of metal ions using an appropriate reducing agent. In a subsequent step, the seed particles

can be introduced to growth solutions containing the same or different metal ions along with other additives (e.g., dopants, ligands, etc.). During the growth process, the metal ions in the growth solutions undergo the reduction at the surface of the seed particles via heterogeneous nucleation. Therefore, the nanoparticles can be controllable prepared with different size and shape by varying the concentration and composition of the seeds in the growth solution, which provides excellent opportunities for boosting the performance of nanostructured catalysts in many energy-related applications.[17, 18] For example, Zou's group reported bimetallic metal–organic framework hybrid structures (core/shell CoZn-ZIFs) synthesized using a low Co/Zn ratio, where the core containing Co^{2+} was first formed quickly, a Zn^{2+} contained layer was following formed on the core.[19] Besides, tunable core/shell thickness ratio of the nanostructures were achieved by changing time intervals, while only agglomerates of irregular shape formed due to the weak nucleation ability of Zn^{2+} with first addition of Zn^{2+}.

2.1.2 Defect incorporation

The introduction of defects can create abundant dangling bonds and unsaturated coordination sites on the nanostructure surface, which have a significant impact on their electronic, magnetic and catalytic properties.[20] The defects can be divided into three types: vacancy defects, heteroatom (N, S, P and B) and metal-defect coordination structures.[21] Particularly, the defect incorporation in the nanostructure can tailor the physical properties such as conductivity, energy band gap, adsorption and desorption energy and interaction with surroundings, which further affects the catalytic performance. Defect electrocatalysis has gained significant interest due to the experimental and theoretical evidence suggesting that solid electrocatalysts (such as metal oxides, transition-metal dichalcogenides, zeolites, carbides, and carbons) that possess defects can enhance the reactivity and selectivity in processes like OER and ORR.[22-24] Remarkably, defects can not only modify the

surrounding electronic but also serve as a "docking" location for trapping atomic metal species, leading to the creation of new synergistic coordination structures that act as active sites.

Pit digging is an effective way to enhance the degree of surface defects through creating more dangling bonds and unsaturated coordination sites to surface of nanostructures. Xie's group fabricated a three-atomic-layer thin CeO_2 sheet with approximately 20% pits occupancy via a ultrafast open space transformation strategy, which possesses abundant pit-surrounding Ce sites.[25] As a result, the existence of coordination-unsaturated cerium sites in CeO_2 sheet not only enhances hole density, facilitating rapid diffusion, but also lowers activation barriers and reduced the possibility of catalyst poisoning. In addition, the presence of oxygen vacancies near the surfaces of nanostructures also has a significant impact on catalytic processes because of the increased number of active sites surrounding these defects. It is reported that the existence of vacancies on nanostructured metal oxide surfaces leads to a weaker bond between metal and oxygen, thereby facilitating more rapid exchange of intermediates and more efficient transfer of electrons.[26, 27] For example, the oxygen-vacancy-enriched cobalt oxides were developed via a plasma engraving strategy, which exhibit a higher current density and a lower onset potential in comparison to pristine Co_3O_4, due to the improved electronic conductivity and more active sites for OER.[26]

The electronic structures of functional nanomaterials can also be regulated by the controlled introduction of heteroatoms with a certain degree of disorder. It is reported that stabilizing non-metallic and metallic heteroatoms to generate heteroatom-defect-based patterns with varying coordination environments and robust stability can result in efficient and durable ORR performance.[21] For example, Jia et al. fabricated various topological defects (pentagons, heptagons, and octagons) on the edge of the graphene by removing intentionally doped heteroatoms (Figure 2.2).[28] The DG exhibited more boosted ORR activity in contrast to NG, which

can be attributed to alterations in the charge and spin distributions within the DG as well as variations in the adsorption energies of intermediates on the active sites. Moreover, Various configurations of topological carbon defects exhibit unique appeal to different electrochemical reactions (ORR, OER, and HER) due to their specific, modulated electronic structures.
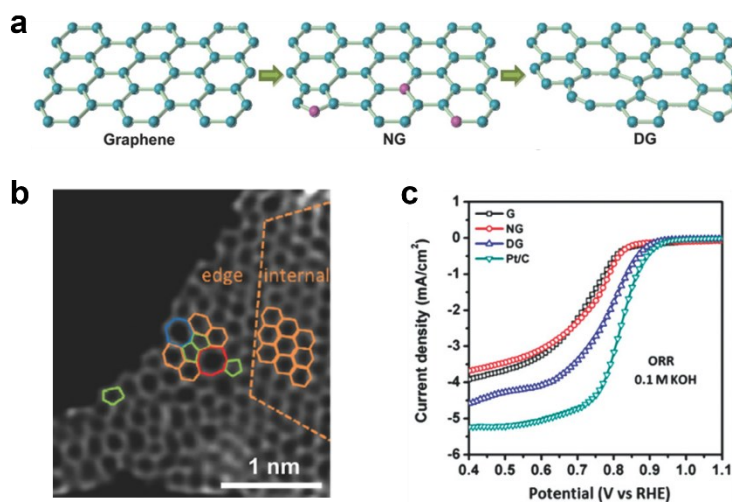
Figure 2. 2 (a) The schematic of the formation of DG. (b) HAADF image of DG. (c) The polarization curves of oxygen reduction reaction.

2.1.3 Interface manipulation

Hybridizing the catalytically active components with a host nanostructure can not only combine the properties of the two materials but also afford new functionalities due to the formation of abundant interfaces facilitating mass and charge transfer during catalytic reactions. Interface engineering can be realized through various routes such as chemical doping and post-treatment. The coupling effects between two phases generally is related to covalent bonding, hydrogen bonding, electrostatic attraction and van der Waals interaction.[29] This coupling effect can lead to the modification of local coordination environment and electronic states, while also enabling distinct reaction processes to occur in proximity at different active sites. The interfaces can serve

as active sites for electrocatalytic reactions in certain cases, especially for exposed interfaces. These concepts offer alternative approaches for the design of efficient electrocatalysts and present new prospects for enhancing their catalytic efficiencies.

Extensive research has been conducted on oxygen electrocatalytic reactions on the surfaces of heterostructures based on transition metals. Layered double hydroxide (LDH) is a typical example of two-dimensional (2D) materials that exhibits exceptional OER activity, due to its remarkable features such as a large surface area, open structure, and chemical versatility. Zhu et al. developed a NiFe LDH/NiTe heterostructure as an OER electrocatalyst, which exhibits a robust electronic interaction between NiFe LDH and NiTe, leading to a decrease of the d-band center of Ni in the prepared sample.[30] As a result, the catalyst surface has an optimal binding energy for OER intermediate species. Pankaj and the co-workers developed a Cu-CuFe$_2$O$_4$ nanocrystal heterostructure supported by carbon for ORR electrocatalysis.[31] They observed that the interface formed between metallic Cu and semi-conductive CuFe$_2$O$_4$ led to enhanced electron mobilization, resulting in a high limiting current density.

Meeting the bifunctional performance requirements can be challenging for single component electrocatalysts. Constructing heterostructures can combine the unique properties of different components, resulting in exceptional functionality. Consequently, the development of appropriate heterointerface structures is crucial in optimizing bifunctional electrocatalytic performance. For example, CoO/CoxP hybrids were prepared by a facile phosphorylation process, where the strong electronic interaction between the phases promotes the adsorption of intermediates during ORR and OER (Figure 2.3a-c). For ORR, the high adsorption of O$_2$ leads to a substantial energy barrier for the OOH* decomposition process. CoO mainly contributes to the ORR activity due to the moderate adsorption energy of O$_2$. Conversely, the high binding energy of OH and low binding

energy O_2 are advantageous for OER, indicating that CoP and Co2P are more critical in catalyzing OER than CoO (Figure 2.3 d).[32] In another case, the $NiFe_2O_4/FeNi_2S_4$ was reported for enhanced electrocatalytic performance of both OER and ORR due to an abundance of oxide/sulfide interfaces.[33] The oxygen adsorption energy on the interfaces between $NiFe_2O_4$ and $FeNi_2S_4$ significantly was reduced in comparison to the individual $NiFe_2O_4$ and $FeNi_2S_4$.
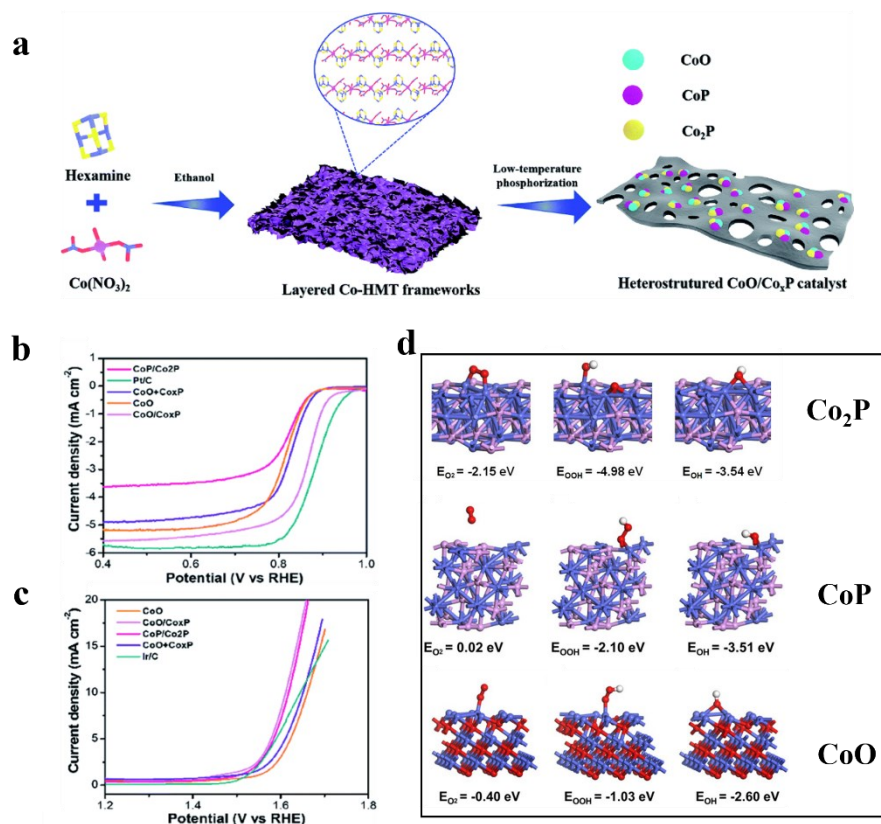
Figure 2. 3 (a) Schematic illustration for the synthesis process of CoO/Co_xP. (b) ORR polarization curves of investigated catalysts in O_2-saturated 0.1 M KOH solution at 1600 rpm. (c) OER polarization curves for different catalysts in N_2-saturated 0.1 M KOH at 1600 rpm. (d) The optimized configurations and adsorption energy of oxygen intermediates on Co_2P, CoP and CoO.[32]

2.1.4 Coupling with substrates

The self-supported electrode poses catalytically active phases grown on a conductive substrate without post coating process and using polymeric binders and conducting agents. It can be used in electrochemical storage and conversion systems directly, which simplifies the electrode preparation process and lowers the costs.[34] And the integration of active phases and the conductive substrate enhances the kinetics and stability in terms of the high loading of active components and rapid charge transfer.[35, 36]

The fabrication strategies of self-supported electrode, where the catalytically active phases are in situ grown on the substrate, have been widely explored, including hydro/solvothermal, electrodeposition, vapor deposition, freeze drying, and the combination of different methods. Common substrates used for the preparation of electrode mainly focused on metal, carbon, and other conductive materials in different forms, including metal foam (e.g., Ni/Cu foam),[37, 38] metal plate/foil (e.g., Ti plate and W/Mo/Cu foil),[39, 40] carbon fiber papers (CFP),[41, 42] carbon cloth (CC),[43] fluorine-doped tin oxide (FTO),[44] and so on.

The hydro/solvothermal method is an effective way to prepare the metal-based catalytic compounds such as metal oxides and hydroxides by controlling reaction temperature and time in a pressure-tight reactor.[45, 46] During the synthetic process, the defects and oxyl groups on the substrate can serve as the nucleation sites for the later growth of active materials to form the uniform distribution of nanostructure on the substrate.[47] For example, Chen et al. synthesized NiCo Layered Double Hydroxides (LDH) (e.g. α-NiCo LDH and β-NiCo LDH) on nickel foam by controlling the volume ratio of deionized water and N-methyl pyrrolidone through hydrothermal process.[48] The prepared metal oxyl compounds can be directly used as catalysts or as a precursor for synthesis of other materials, such as sulfides, phosphides and alloys through post treatment.

Electrodeposition can also be used for the fabrication of self-supported electrode. A three-electrode electrochemical cell is needed for the electrodeposition process, where the target materials uniformly deposit on the selected substrate as working electrode under the applied electric field. Most transition metal-based compounds can be electrodeposited on the conducting substrate, including metal oxides, hydroxides, sulfides, phosphides, and alloys.[49, 50] Wang et al. fabricated Ni–Mo electrocatalysts using electrodeposition technique on Cu foam at current densities between 10 to 200 mA cm^{-2} with 3600 s of deposition time(Figure 2.4).[51] Electrodeposition offers a rapid synthetic process and controllable catalyst loading on the substrate through simply changing deposition time and applied current density.
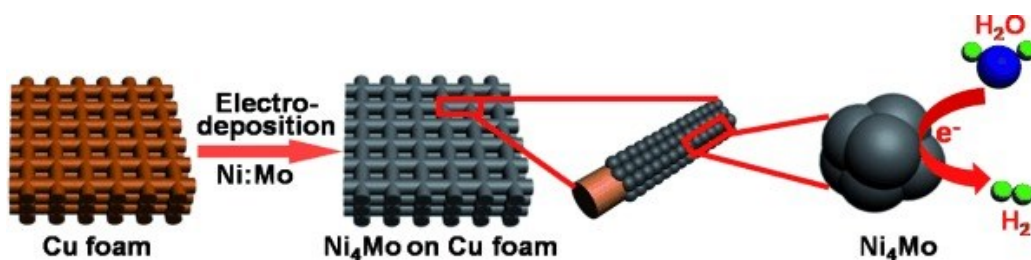
Figure 2. 4 3D nanoporous Ni–Mo electrocatalysts fabricated on Cu foam.

Chemical vapor deposition (CVD) has been extensively explored for the synthesis of inorganic catalysts. During the sintering process, the metallic compounds grown on the substrate can react with the nonmetal precursors gas such as phosphorus (PH_3 or P), fluorine, nitrogen (NH_3 or N_2) and sulfur to form the corresponding phosphides, fluorides, nitrides and sulfides.[52] Specifically, $WS_{2(1-x)}Se_{2x}$ nanotubes supported on carbon fibers were prepared by in situ transforming from WO_3, where WO_3 nanotubes react with sulfur and selenium vapor.[53] The element component can be controlled by altering the proportion of S and Se precursors (Figure 2.5).
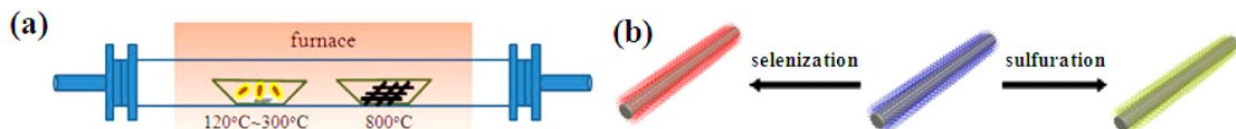
Figure 2. 5 The fabrication of $WS_{2(1-x)}Se_{2x}$ nanotubes.

2.2 Transition Metal Hydroxides/Oxyhydroxides

Layered double hydroxides (LDHs) consist of positively charged metal hydroxide layers that interleaved with negatively charged interlayer anions, which has been widely explored for electrocatalysts, particularly for OER. The compositions are tunable by changing the positively charged metals or negatively charged interlayer anions, allowing for the modification of their catalytic properties. However, LDHs have a poor electrical conductivity resulting in an unsatisfied catalytic activity. LDHs in situ grown on a conductive substrate to fabricate a self-supported electrode is a effective way to improve the activity and long-term stability. For example, Liu et al. use a homogeneous precipitation method to vertically grow highly oriented flakes arrays of NiFe LDH on the Ni foam (NF) substrate based on urea and assisted with NH_4F as directing agent.[54]

To further enhance the catalytic activity of LDHs, the nanocomposites construction and cation doping have adopted. Zou et al. developed a ultrafast synthesis of amorphous Ni-Fe-OH on Ni_3S_2 nanosheet arrays with NF supported (Figure 2.6).[55] Such fabricated nanocomposite not only provides high intrinsic activity of amorphous Ni–Fe hydroxide but endows the high conductivity of the Ni_3S_2 array. Besides, their strongly coupled interface also benefits the stability of the self-supported Ni–Fe–OH@Ni_3S_2/NF electrode presenting superior and stable OER activity. Sun's group synthesized vanadium doped NiFe LDHs nanosheet arrays in situ grown on nickel foam via a one-step hydrothermal method.[56] The Electronic Structure of NiFe LDHs were tuned by V-doping forming ternary NiFeV LDHs to reduce the onset potential, enhancing the water oxidation performance.

22
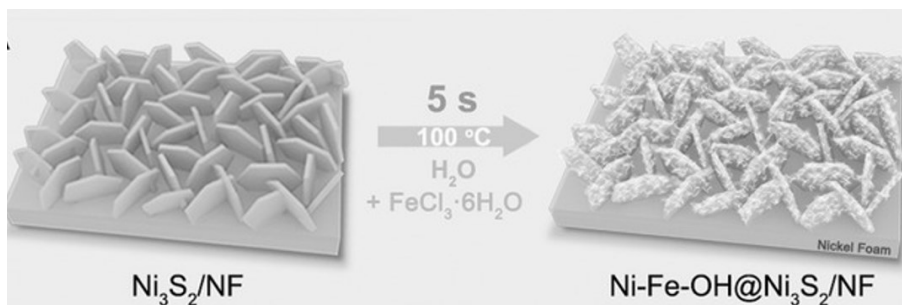
Figure 2. 6 Schematic illustration of the synthesis of Ni-Fe-OH@Ni$_3$S$_2$/NF

2.3 Transition Metal Oxides

The most widely used oxide catalysts for OER and ORR are till precious metal-based, for example, IrO$_2$ and RuO$_2$ for OER, Pt-based oxides for ORR.[4, 57, 58] However, the high price and scarcity of noble metals hinder the practical application of electrochemical energy devices. Transition metal oxides are attractive for electrocatalyst application, because of the low cost, earth-rich and anti-corrosion properties in alkaline environment. The transition metal oxides have been extensively investigated for oxygen redox electrocatalysis, such as rock-salt-type oxides, spinel-type oxides, rutile oxides, and perovskite-based oxides.

Spinel-type oxides as a family of composite oxides have attracted particular interest. The general formula can be expressed as A$_3$O$_4$ (A = Co, Mn, etc.) and AB$_2$O$_4$ (A and B = transition metals, such as Ni, Co, Mn, Zn, Fe, Cu, etc.). The representative electrocatalysts applied for the oxygen reaction include Co$_3$O$_4$, Mn$_3$O$_4$, CoFe$_2$O$_4$, NiCo$_2$O$_4$ and MnCo$_2$O$_4$. Among them, Co$_3$O$_4$ and Ni-containing cobalt oxides have gained intensive investigation for OER and ORR, due to the high catalytic activity. Taking a self-supported oxide electrode as an example (Figure 2.7), the hybrid porous nanowire arrays composed of Co$_3$O$_4$ and carbon grown on Cu foil were prepared by carbonization of the Co-based metal organic framework (Co-MOF).[59] The uniform distribution and synergy between Co$_3$O$_4$ and carbon result in large active surface area, enhanced charge/mass

23

transport and high structural stability, which affords high OER activity with a low onset potential of 1.47 V vs RHE, a long electrocatalytic stability for 30 h under current density of 10.0 mA cm^{-2} and a high Faradaic efficiency of 99.3%.
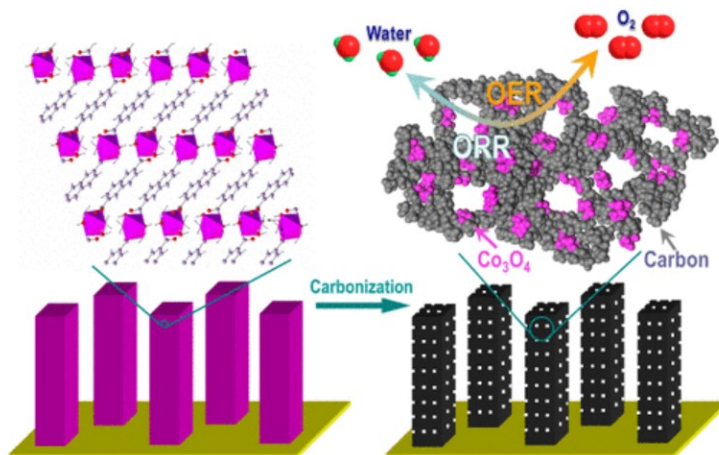
Figure 2. 7 Fabrication process of Hybrid Co_3O_4-Carbon Porous Nanowire Arrays on Cu foil.

Other types of metal oxides were also developed as self-supported oxygen rection catalysts. The mostly investigated rutile oxides are MoO_2 and MnO_2 working as oxygen reaction catalysts. The fabrication of nanostructured rutile oxides on 3D substrates (e.g., Nickel foam and carbon paper) have been widely investigated. For example, the porous MoO_2 nanosheets grown on the nickel foam directly work as working electrode to deliver current density of 10 mA cm^{-2} with a low potential of only 260 mV, owning to the higher surface area and more active sites contributed by porous nanostructure.[60] Manganese dioxide materials also show a potential for OER electrocatalysis, in which the engineering of Mn/O vacancies and cation doping can obviously improve the conductivity boosting the electrocatalytic activity.[61-64] The self-supported ultrathin δ-MnO_2 nanosheet arrays on nickel foam exhibit enhanced charge transfer, which was further demonstrated by calculation of the density of states (DOS) revealing half-metallicity property of oxygen-deficient MnO_2 nanosheet. As a result, it afforded a high OER performance with an

overpotential of 320 mV at 10 mA cm^{-2}.[61] Besides, metal-doping is also a effective way to improve the conductivity of MnO$_2$. Transition metal-ion (Fe, V, Co, and Ni) doped γ-MnO2 ultrathin nanosheet electrodeposited on Carbon fiber paper exhibits an improved electrocatalytic activity comparison to pure MnO2 composite electrode.[63]

2.4 Transition Metal Nonoxide Catalysts

The catalytic activity of metal oxides is impeded by the relatively low electronic preventing them from practical applications. Thus, metallic or half-metallic properties of transition metal chalcogenides (sulfide[65], selenides[66], and telluride[67]) and pnictides (nitride[68] and phosphide[69]) have been employed for electrocatalyst investigation. The catalytic performance can be boosted owing to the intrinsic conductivity. However, the metallic nonoxides do not directly impact the catalytic activity since they typically experience oxidation during OER. The newly transformed phase (e.g., oxyhydroxides) serves as actual active sites for OER. Even so, the metallic nonoxides based catalysts take advantage of their metallic nature favoring the electron transport, which accelerates the transformation of active phase improving the catalytic performance. For example, Stern et al. reported the core–shell Ni$_2$P/NiO$_x$ for OER, where the metallic Ni$_2$P plays an important role in bridging the catalytic active species NiO$_x$ and the external potential (Figure 2.8).[70] The in situ formation of NiO$_x$ on the pristine Ni$_2$P surface under catalytic potential is the actual active phase. As a result, the core–shell Ni$_2$P/NiO$_x$ delivers the current density of 10 mA cm^{-2} at the overpotential of 290 mV. A robust electrode composed of Fe (PO$_3$)$_2$ grown on the surface of a conductive Ni$_2$P/NF scaffold was fabricated.[71] The Fe (PO$_3$)$_2$ phase was in situ converted into amorphous FeOOH as the real catalytic sites during the OER electrocatalysis. Benefiting from the highly catalytically active FeOOH and the 3D conductive structure, the electrode exported current

density of 500 mA cm^{-2} at overpotentials of 265 mV. And a TOF value achieved around 0.12 s^{-1} per 3d Fe atom at an overpotential of 300 mV, along with excellent durability in 1 M KOH.
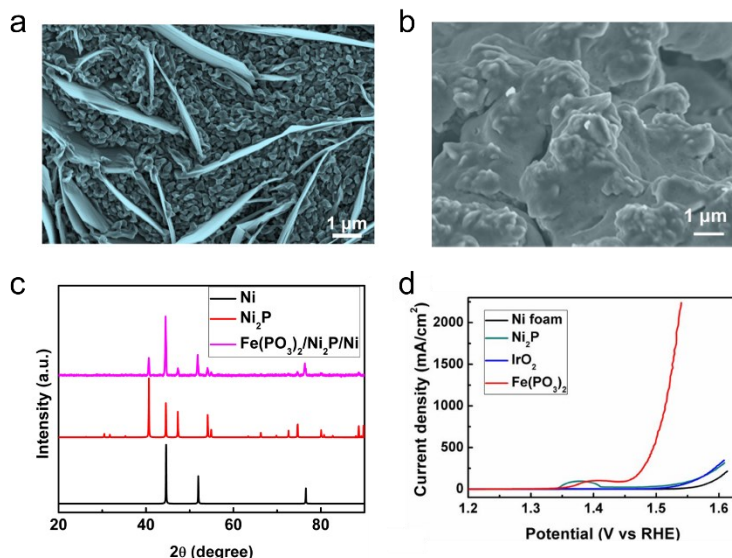
Figure 2. 8 (a) SEM image of Ni$_2$P/NF. (b) SEM image of Fe (PO$_3$)$_2$/ Ni$_2$P/NF. (c) XRD patterns of Ni$_2$P/NF, Fe (PO$_3$)$_2$/ Ni$_2$P/NF and Ni. (d) Polarization curves recorded on different electrodes in 1 M KOH electrolyte.[71]

2.5 Single-atom electrocatalysts

Single-atom catalysis represents a compelling and potent approach that offers remarkable performance, significant cost savings, and impressive catalytic efficacy and specificity. In single-atom catalysis, supported single-atom catalysts consist of isolated atoms that are distributed across or bonded with the surface atoms of suitable substrates. This not only optimizes the utilization of metallic elements at the atomic level but also presents an alternative strategy to fine-tune the activity and selectivity of catalytic processes. The essential condition for creating Single-Atom Catalysts (SACs) involves dispersing individual metal atoms onto suitable support surfaces. Nevertheless, crafting SACs proves to be a complex task due to the natural tendency of metal atoms to preferentially aggregate during the synthesis or subsequent treatment phases.

26

Consequently, the wider adoption of materials consisting of single metal atoms require the advancement of sophisticated synthetic techniques, such as Atomic Layer Deposition (ALD), wet impregnation, and co-precipitation.

The composition of carbon nanomaterials can be tuned through chemical methods by introducing different heteroatoms like N into the carbon backbone. These doping sites can then serve as anchorage centers that facilitate the incorporation of metal moieties through strong coupling effects, leading to the formation of stable and electrocatalytically active metal-nitrogen-carbon (M–N–C) species.[72] Organometallic materials M-N comprising transition metal elements (e.g., Fe, Co, Ni, Cu) coordinated by macrocycles (such as phthalocyanine and phenanthroline) can guarantee a quick electron transport process in electrochemical reactions, which could attribute to the existence of delocalized π-electrons in the macrocyclic structures.[73] However, the metal dissolution and material decomposition in strong acid or alkaline environments lead to the inferior stability of these organometallic complex, which limits its application. M–N$_x$–C materials were generally fabricated through pyrolysis and carbonization of the transition-metal macrocycles under the inert gases at temperatures over 700 °C (Figure 2.9).[74] As a result, the M–N$_x$–C materials show a significantly improved activity and stability in contrast to pristine organic macrocycles. N-ligands can be converted into various nitrogen species such as graphitic, pyridinic, and pyrrolic nitrogen during the process of heat treatment, which are chemically bonded to both the metal centers and carbon atoms in the carbon framework. At the same time, the elementary metals generated from the reduction of pyrolysis gas can catalyze the production of graphitic carbon shells, leading to an improvement in the conductivity of the resulting material. Consequently, this technique not only ensures an even distribution of catalytically active sites but also enhances the electronic connectivity throughout the entire system.
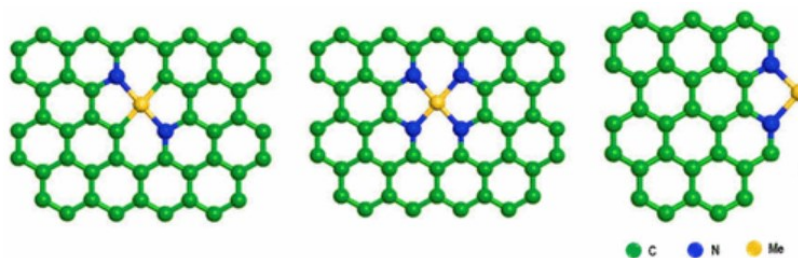
Figure 2. 9 General structures of the M–N$_x$–C material.

Although the natural catalytic activity of M–N$_x$–C systems has been demonstrated, the catalytic performance is significantly impacted by the porosity and micro- or nanostructures, because the accessibility of the active site is also vital to the overall catalytic efficiency. [75, 76] Thus, to fabricate the porous structures, some rigid templates (e.g., silica nanoparticles, anodic alumina) are generally utilized during carbonization.[77] The rigid-templating route normally involves preparation and dispersion of templates and the post synthesis removal of templates. Such tedious and time-consuming procedures hinder the large-scale production. Polymeric templates (e.g., polystyrene (PS), F127) were also reported for the manufacturing porous nanostructure. Because polymers have the ability to homogeneously penetrate precursor matrices, which can be removed subsequently under high-temperature calcination to create porous M-N$_x$-C.[78] The combination of hierarchical porosity and good conductivity provides the composite electrocatalysts with outstanding ORR activity, which is closely comparable or even superior to commercial Pt/C.

Bimetal-based M-N$_x$-C catalysts have shown significant potential in ORR compared to single metal counterparts, owing to their tunable electronic structure of the active sites by introducing another metallic center. For example, the cooperation between two metal atoms in diatomic metal catalysts enables more effective adjustment of the center position of the D-band.[79] This leads to the optimization of the interaction between reactants or intermediates and the active sites. Zeolitic

imidazolate frameworks (ZIFs)-based materials have shown a significant potential in bimetal-based catalyst synthesis. To date, several strategies for synthesizing atomically dispersed $M-N_x/C$ catalysts based on ZIF-derived precursors have been widely reported, such as ion exchange, spatial confinement, defects trapping, and others. As a representative study, a novel electrocatalyst with Fe−Co dual sites was fabricated by transforming the initial bimetallic MOF into N-doped carbon nanotubes through the pyrolysis process, which displayed excellent activity towards the ORR with a superior $E_{1/2}$ of 0.954 V in 0.1M KOH solution.[80]

2.6 Current status and remaining challenges

Over the past few decades, significant research efforts have been dedicated to enhancing the electrocatalytic activities of oxygen reactions for energy conversion and storage applications, including hydrogen production, metal-air batteries, and full cells. The development of oxygen reaction catalysts has progressed from traditional noble metal-based materials (such as Ru, Ir, and Pt) to virous transition metallic and carbonaceous materials. The electronic structure of catalysts directly determines the functionalities and performances of materials. Thus, extensive strategies (e.g., morphology control, interface manipulation, heteroatom doping) have been explored to design advanced electrocatalysts. However, the catalytic activity of transition metal-based materials is still inferior to the state-of-art noble metal-based catalysts, let alone putting them in practical applications.

Heterostructure engineering is an effective strategy to boost catalytic activity benefitting from the improved electron transfer capability and tuned electronic structure. The interfaces within the heterostructure are believed to be the real catalytic active sites. Various strategies have been developed to promote the catalytic activity in terms of exposure of the more active sites and enhancing electrical conductivity. For example, tailoring transition-metal-based layered double

hydroxides (LDHs) into single or few-layer nanosheets exposes more surface sites and reduces the diffusion length for ions and/or electrons. Although some encouraging developments have been made on boosting the catalytic activity in OER, the electrocatalytic performance still falls behind commercial requirements (current density, $j \geq 500$ mA cm^{-2} at overpotential, $\eta \leq 300$ mV), because of the limited exposure of active sites and low electrical conductivity.

Apart from large overpotential required for OER in anode to obtain appreciable current densities because of the sluggish kinetics, which could drag down the whole efficiency of hydrogen production. The anodic product (O_2) is of low value and does not contribute to economic feasibility. Thus, replacing OER with biomass electrooxidation reactions (BEORs) is an attractive strategy to lower the full-cell potential and simultaneously produce valuable products at the anode. Interfacial engineering has been demonstrated as an effective approach for designing efficient BEORs electrocatalysts by integrating two components, where the instructed heterointerfaces can promote electron transfer, influence the adsorption/desorption energies of active species during electrocatalytic process, regulating catalytic ability. Nevertheless, most reported electrocatalysts could only deliver satisfying activity for a single HER or BEOR. Developing low-cost transition metal-based electrocatalysts with bifunctionality for both HER and BEOR is imperative but remains a grand challenge.

In addition, the energy conversion efficiency of metal-air batteries is also severely restricted by the kinetically sluggish of oxygen catalysis. For cathodic ORR, the high energy needs of O=O bond breaking and sluggish kinetics of the $4e^-/4H^+$ transfer process result in most electrocatalysts suffering from unsatisfactory catalytic performance. Single atom catalysts present the unique appeal for energy conversion application due to the high atomic availability and specific activity. Wherein, Fe–N–C single-atom catalysts (SACs) with Fe–N_4 moieties dispersed on carbon matrix

have been considered as promising alternatives to platinum-group-metal (PGM)-based catalysts for ORR due to the maximized atomic utilization and low cost. However, substituting PGM catalysts with Fe–N$_4$ catalysts while achieving superior activity and durability for practical applications is still challenging, due to the high energy barrier of O–O bond cleavage.

Therefore, motivated by the above discussion, I came up with a hypothesis about whether increasing the contact area of two domains could regulate the electronic structure more efficiently for catalytic performance in terms of activity and stability. The excellent catalysts should possess good intrinsic activity and charge transferability. For engineering two different components, the morphology, and the arrangement of two components should be taken into consideration. Well-defined morphology such as nanosheets and nanowires can provide high surface area and expose more active sites. Thus, to confirm the feasibility of above hypothesis. The objectives of this research are to develop effective heterointerfaces from nanoscale to atomic scale regulating the electronic structure for efficient electrocatalyst, which are as follows:

1. Maximize the exposure of heterostructured interfaces via constructing interconnected heterointerfaces in nanosheets.
2. Develop the nanostructured catalyst by interface engineering with bifunctionality for both HER and HMFOR for energy-saving H$_2$ production and value-added product generation.
3. Develop hetero-single-atom catalysts with optimized electronic structure for efficient ORR that is comparable to PGM in metal-air battery application.

2.7 References

1. Shi, Y.; Zhang, B., Recent advances in transition metal phosphide nanomaterials: synthesis and applications in hydrogen evolution reaction. *Chem. Soc. Rev*. 2016, *45* (6), 1529-1541.
2. Zheng, Y.; Jiao, Y.; Vasileff, A.; Qiao, S. Z., The Hydrogen Evolution Reaction in Alkaline

Solution: From Theory, Single Crystal Models, to Practical Electrocatalysts. *Angew. Chem. Int. Ed.* 2018, *57* (26), 7568-7579.

3. Zou, X.; Zhang, Y., Noble metal-free hydrogen evolution catalysts for water splitting. *Chem. Soc. Rev.* 2015, *44* (15), 5148-80.

4. Suen, N. T.; Hung, S. F.; Quan, Q.; Zhang, N.; Xu, Y. J.; Chen, H. M., Electrocatalysis for the oxygen evolution reaction: recent development and future perspectives. *Chem. Soc. Rev.* 2017, *46* (2), 337-365.

5. Liu, Y.; Tang, A.; Zhang, Q.; Yin, Y., Seed-mediated growth of anatase TiO2 nanocrystals with core–antenna structures for enhanced photocatalytic activity. *J. Am. Chem. Soc.* 2015, *137* (35), 11327-11339.

6. Wang, Z.; Yang, G.; Zhang, Z.; Jin, M.; Yin, Y., Selectivity on Etching: Creation of High-Energy Facets on Copper Nanocrystals for CO2 Electrochemical Reduction. *ACS Nano* 2016, *10* (4), 4559-64.

7. Zhang, S.; Ma, Y.; Zhang, H.; Zhou, X.; Chen, X.; Qu, Y., Additive-Free, Robust H2 Production from H2O and DMF by Dehydrogenation Catalyzed by Cu/Cu2O Formed In Situ. *Angew. Chem. Int. Ed.* 2017, *56* (28), 8245-8249.

8. Shi, R.; Cao, Y.; Bao, Y.; Zhao, Y.; Waterhouse, G. I. N.; Fang, Z.; Wu, L. Z.; Tung, C. H.; Yin, Y.; Zhang, T., Self-Assembled Au/CdSe Nanocrystal Clusters for Plasmon-Mediated Photocatalytic Hydrogen Evolution. *Adv. Mater.* 2017, *29* (27), 1700803.

9. Xu, W.; Lyu, F.; Bai, Y.; Gao, A.; Feng, J.; Cai, Z.; Yin, Y., Porous cobalt oxide nanoplates enriched with oxygen vacancies for oxygen evolution reaction. *Nano Energy* 2018, *43*, 110-116.

10. Ding, D.; Liu, K.; He, S.; Gao, C.; Yin, Y., Ligand-exchange assisted formation of

Au/TiO2 Schottky contact for visible-light photocatalysis. *Nano Lett.* 2014, *14* (11), 6731-6.

11. Zhang, Q.; Lima, D. Q.; Lee, I.; Zaera, F.; Chi, M.; Yin, Y., A highly active titanium dioxide based visible-light photocatalyst with nonmetal doping and plasmonic metal decoration. *Angew. Chem. Int. Ed.* 2011, *50* (31), 7088-92.

12. Popczun, E. J.; Roske, C. W.; Read, C. G.; Crompton, J. C.; McEnaney, J. M.; Callejas, J. F.; Lewis, N. S.; Schaak, R. E. J. J. o. M. C. A., Highly branched cobalt phosphide nanostructures for hydrogen-evolution electrocatalysis. *J. Mater. Chem. A* 2015, *3* (10), 5420-5425.

13. Seo, B.; San Baek, D.; Sa, Y. J.; Joo, S. H., Shape effects of nickel phosphide nanocrystals on hydrogen evolution reaction. *Cryst. Eng. Comm.* 2016, *18* (32), 6083-6089.

14. Tan, C.; Chen, J.; Wu, X.-J.; Zhang, H., Epitaxial growth of hybrid nanostructures. *Nat. Rev. Mater.* 2018, *3* (2), 1-13.

15. Xia, Y.; Xiong, Y.; Lim, B.; Skrabalak, S. E., Cover Picture: Shape-Controlled Synthesis of Metal Nanocrystals: Simple Chemistry Meets Complex Physics? *Angew. Chem. Int. Ed.* 2009, *48* (1), 1-1.

16. Wu, X. J.; Chen, J.; Tan, C.; Zhu, Y.; Han, Y.; Zhang, H., Controlled growth of high-density CdS and CdSe nanorod arrays on selective facets of two-dimensional semiconductor nanoplates. *Nat. Chem.* 2016, *8* (5), 470-5.

17. Gao, C.; Goebl, J.; Yin, Y., Seeded growth route to noble metal nanostructures. *J. Mater. Chem. C* 2013, *1* (25), 3898-3909.

18. Chen, J.; Wu, X. J.; Gong, Y.; Zhu, Y.; Yang, Z.; Li, B.; Lu, Q.; Yu, Y.; Han, S.; Zhang, Z.; Zong, Y.; Han, Y.; Gu, L.; Zhang, H., Edge Epitaxy of Two-Dimensional MoSe(2)

and MoS(2) Nanosheets on One-Dimensional Nanowires. *J. Am. Chem. Soc.* 2017, *139* (25), 8653-8660.

19. Guo, W.; Xia, W.; Cai, K.; Wu, Y.; Qiu, B.; Liang, Z.; Qu, C.; Zou, R., Kinetic-Controlled Formation of Bimetallic Metal–Organic Framework Hybrid Structures. *Small* 2017, *13* (41), 1702049.

20. Araki, T.; Serra, F.; Tanaka, H. J., Defect science and engineering of liquid crystals under geometrical frustration. *Soft Matter* 2013, *9* (34), 8107-8120.

21. Jia, Y.; Jiang, K.; Wang, H.; Yao, X., The role of defect sites in nanomaterials for electrocatalytic energy conversion. *Chem* 2019, *5* (6), 1371-1397.

22. Yan, X.; Jia, Y.; Yao, X., Defects on carbons for electrocatalytic oxygen reduction. *Chem. Soc. Rev.* 2018, *47* (20), 7628-7658.

23. Yan, D.; Li, Y.; Huo, J.; Chen, R.; Dai, L.; Wang, S., Defect Chemistry of Nonprecious-Metal Electrocatalysts for Oxygen Reactions. *Adv. Mater.* 2017, *29* (48), 1606459.

24. Jia, Y.; Chen, J.; Yao, X., Defect electrocatalytic mechanism: concept, topological structure and perspective. *Mater. Chem. Front.* 2018, *2* (7), 1250-1268.

25. Sun, Y.; Liu, Q.; Gao, S.; Cheng, H.; Lei, F.; Sun, Z.; Jiang, Y.; Su, H.; Wei, S.; Xie, Y., Pits confined in ultrathin cerium(IV) oxide for studying catalytic centers in carbon monoxide oxidation. *Nat. Commun.* 2013, *4* (1), 2899.

26. Xu, L.; Jiang, Q.; Xiao, Z.; Li, X.; Huo, J.; Wang, S.; Dai, L., Plasma-engraved Co3O4 nanosheets with oxygen vacancies and high surface area for the oxygen evolution reaction. *Angew. Chem. Int. Ed.* 2016, *128* (17), 5363-5367.

27. Kim, J.; Yin, X.; Tsao, K.-C.; Fang, S.; Yang, H., Ca2Mn2O5 as oxygen-deficient perovskite electrocatalyst for oxygen evolution reaction. *J. Am. Chem. Soc.* 2014, *136* (42),

14646-14649.

28. Jia, Y.; Zhang, L.; Du, A.; Gao, G.; Chen, J.; Yan, X.; Brown, C. L.; Yao, X., Defect graphene as a trifunctional catalyst for electrochemical reactions. *Adv. mater.* 2016, *28* (43), 9532-9538.

29. Liu, T.; Bai, L.; Tian, N.; Liu, J.; Zhang, Y.; Huang, H. J. I., Interfacial engineering in two-dimensional heterojunction photocatalysts. *Int. J. Hydrog. Energy* 2023.

30. Hu, L.; Zeng, X.; Wei, X.; Wang, H.; Wu, Y.; Gu, W.; Shi, L.; Zhu, C., Interface engineering for enhancing electrocatalytic oxygen evolution of NiFe LDH/NiTe heterostructures. *Appl. Catal. B* 2020, *273*, 119014.

31. Borah, B. J.; Yamada, Y.; Bharali, P., Unravelling the role of metallic Cu in Cu-CuFe2O4/C nanohybrid for enhanced oxygen reduction electrocatalysis. *ACS Appl. Energy Mater.* 2020, *3* (4), 3488-3496.

32. Niu, Y.; Xiao, M.; Zhu, J.; Zeng, T.; Li, J.; Zhang, W.; Su, D.; Yu, A.; Chen, Z., A" trimurti" heterostructured hybrid with an intimate CoO/CoxP interface as a robust bifunctional air electrode for rechargeable Zn–air batteries. *J. Mater. Chem. A* 2020, *8* (18), 9177-9184.

33. An, L.; Zhang, Z.; Feng, J.; Lv, F.; Li, Y.; Wang, R.; Lu, M.; Gupta, R. B.; Xi, P.; Zhang, S., Heterostructure-promoted oxygen electrocatalysis enables rechargeable zinc–air battery with neutral aqueous electrolyte. *J. Am. Chem. Soc.* 2018, *140* (50), 17624-17631.

34. Chen, G. F.; Ma, T. Y.; Liu, Z. Q.; Li, N.; Su, Y. Z.; Davey, K.; Qiao, S. Z., Efficient and stable bifunctional electrocatalysts Ni/NixMy (M= P, S) for overall water splitting. *Adv. Funct. Mater.* 2016, *26* (19), 3314-3323.

35. Yan, Z.; Sun, H.; Chen, X.; Liu, H.; Zhao, Y.; Li, H.; Xie, W.; Cheng, F.; Chen, J., Anion insertion enhanced electrodeposition of robust metal hydroxide/oxide electrodes for oxygen evolution. *Nat. Commun.* 2018, *9* (1), 2373.

36. Jin, T.; Han, Q.; Jiao, L., Binder-Free Electrodes for Advanced Sodium-Ion Batteries. *Adv. Mater.* 2020, *32* (3), e1806304.

37. Wu, S.-W.; Liu, S.-Q.; Tan, X.-H.; Zhang, W.-Y.; Cadien, K.; Li, Z, Ni3S2-embedded NiFe LDH porous nanosheets with abundant heterointerfaces for high-current water electrolysis. *Chem. Eng. J.* 2022, *442*, 136105.

38. Liu, S.-Q.; Gao, M.-R.; Liu, S.; Luo, J.-L., Hierarchically assembling cobalt/nickel carbonate hydroxide on copper nitride nanowires for highly efficient water splitting. *Appl. Catal. B* 2021, *292*, 120148.

39. Quan, X.; Yang, S.; Ruan, X.; Zhao, H., Preparation of titania nanotubes and their environmental applications as electrode. *Environ. Sci. Technol.* 2005, *39* (10), 3770-3775.

40. Lee, C.; Min, K., Effects of heat treatment on the microstructure and properties of HVOF-sprayed Ni–Cr–W–Mo–B alloy coatings. *Surf. Coat. Technol.* 2000, *132* (1), 49-57.

41. Kong, D.; Wang, H.; Lu, Z.; Cui, Y., CoSe2 nanoparticles grown on carbon fiber paper: an efficient and stable electrocatalyst for hydrogen evolution reaction. *J. Am. Chem. Soc.* 2014, *136* (13), 4897-900.

42. Liu, S. Q.; Shahini, E.; Gao, M. R.; Gong, L.; Sui, P. F.; Tang, T.; Zeng, H.; Luo, J. L., Bi(2)O(3) Nanosheets Grown on Carbon Nanofiber with Inherent Hydrophobicity for High-Performance CO2 Electroreduction in a Wide Potential Window. *ACS Nano* 2021, *15* (11), 17757-17768.

43. Fan, X.-Z.; Pang, Q.-Q.; Yi, S.-S.; Du, X.; Zhang, S.; Liu, Z.-Y.; Yue, X.-Z., Intrinsic-

structural-modulated carbon cloth as efficient electrocatalyst for water oxidation. *Appl. Catal. B* 2021, *292*, 120152.

44. Kunimoto, T.; Naya, S.-i.; Tada, H., Hydrogen Peroxide Production from Oxygen and Water by Two-electrode Electrolytic Cell Using a Gold Nanoparticle-loaded Fluorine-doped Tin Oxide Cathode. *Chem. Lett.* 2021, *50* (8), 1589-1591.

45. Liu, B.; Zhao, Y. F.; Peng, H. Q.; Zhang, Z. Y.; Sit, C. K.; Yuen, M. F.; Zhang, T. R.; Lee, C. S.; Zhang, W. J., Nickel-Cobalt Diselenide 3D Mesoporous Nanosheet Networks Supported on Ni Foam: An All-pH Highly Efficient Integrated Electrocatalyst for Hydrogen Evolution. *Adv. Mater.* 2017, *29* (19), 1606521.

46. Pi, Y.; Shao, Q.; Wang, P.; Lv, F.; Guo, S.; Guo, J.; Huang, X., Trimetallic Oxyhydroxide Coralloids for Efficient Oxygen Evolution Electrocatalysis. *Angew. Chem. Int. Ed.* 2017, *56* (16), 4502-4506.

47. Gopalakrishnan, A.; Durai, L.; Ma, J.; Kong, C. Y.; Badhulika, S., Vertically aligned few-layer crumpled MoS2 hybrid nanostructure on porous Ni foam toward promising binder-free methanol electro-oxidation application. Energy Fuels 2021, *35* (12), 10169-10180.

48. Chen, H.; Jiang, J.; Zhang, L.; Zhao, Y.; Guo, D.; Ruan, Y.; Xia, D., One-Pot Fabrication of Layered α-Phase Nickel–Cobalt Hydroxides as Advanced Electrode Materials for Pseudocapacitors. *ChemPlusChem* 2015, *80* (1), 181-187.

49. Li, H.; Han, X.; Zhao, W.; Azhar, A.; Jeong, S.; Jeong, D.; Na, J.; Wang, S.; Yu, J.; Yamauchi, Y., Electrochemical preparation of nano/micron structure transition metal-based catalysts for the oxygen evolution reaction. *Mater, Horiz,* 2022, *9* (7), 1788-1824.

50. Li, R.; Li, Y.; Yang, P.; Wang, D.; Xu, H.; Wang, B.; Meng, F.; Zhang, J.; An, M.,

Electrodeposition: synthesis of advanced transition metal-based catalyst for hydrogen production via electrolysis of water. *J. Energy Chem.* 2021, *57*, 547-566.

51. Wang, Y.; Zhang, G.; Xu, W.; Wan, P.; Lu, Z.; Li, Y.; Sun, X., A 3D nanoporous Ni–Mo electrocatalyst with negligible overpotential for alkaline hydrogen evolution. *ChemElectroChem* 2014, *1* (7), 1138-1144.

52. Pierson, H. O., *Handbook of chemical vapor deposition: principles, technology and applications*. William Andrew: 1999.

53. Xu, K.; Wang, F.; Wang, Z.; Zhan, X.; Wang, Q.; Cheng, Z.; Safdar, M.; He, J., Component-controllable WS2(1–x) Se2x nanotubes for efficient hydrogen evolution reaction. *ACS nano* 2014, *8* (8), 8468-8476.

54. Liu, X.; Wang, X.; Yuan, X.; Dong, W.; Huang, F., Rational composition and structural design of in situ grown nickel-based electrocatalysts for efficient water electrolysis. *J. Mater. Chem. A* 2016, *4* (1), 167-172.

55. Zou, X.; Liu, Y.; Li, G. D.; Wu, Y.; Liu, D. P.; Li, W.; Li, H. W.; Wang, D.; Zhang, Y.; Zou, X., Ultrafast Formation of Amorphous Bimetallic Hydroxide Films on 3D Conductive Sulfide Nanoarrays for Large-Current-Density Oxygen Evolution Electrocatalysis. *Adv. Mater.* 2017, *29* (22), 1700404.

56. Li, P.; Duan, X.; Kuang, Y.; Li, Y.; Zhang, G.; Liu, W.; Sun, X., Tuning electronic structure of NiFe layered double hydroxides with vanadium doping toward high efficient electrocatalytic water oxidation. *Adv. Energy Mater.* 2018, *8* (15), 1703341.

57. Nie, Y.; Li, L.; Wei, Z., Recent advancements in Pt and Pt-free catalysts for oxygen reduction reaction. *Chem. Soc. Rev.* 2015, *44* (8), 2168-201.

58. Doyle, R. L.; Godwin, I. J.; Brandon, M. P.; Lyons, M. E., Redox and electrochemical

water splitting catalytic properties of hydrated metal oxide modified electrodes. *Phys. Chem. Chem. Phys.* 2013, *15* (33), 13737-83.

59. Ma, T. Y.; Dai, S.; Jaroniec, M.; Qiao, S. Z., Metal–organic framework derived hybrid Co3O4-carbon porous nanowire arrays as reversible oxygen evolution electrodes. *J. Am. Chem. Soc.* 2014, *136* (39), 13925-13931.

60. Jin, Y.; Wang, H.; Li, J.; Yue, X.; Han, Y.; Shen, P. K.; Cui, Y., Porous MoO2 nanosheets as non-noble bifunctional electrocatalysts for overall water splitting. *Adv. Mater.* 2016, *28* (19), 3785-3790.

61. Zhao, Y.; Chang, C.; Teng, F.; Zhao, Y.; Chen, G.; Shi, R.; Waterhouse, G. I.; Huang, W.; Zhang, T., Defect-engineered ultrathin δ-MnO2 nanosheet arrays as bifunctional electrodes for efficient overall water splitting. *Adv. Energy Mater.* 2017, *7* (18), 1700005.

62. Kölbach, M.; Fiechter, S.; van de Krol, R.; Bogdanoff, P., Evaluation of electrodeposited α-Mn2O3 as a catalyst for the oxygen evolution reaction. Catal. Today 2017, *290*, 2-9.

63. Ye, Z.; Li, T.; Ma, G.; Dong, Y.; Zhou, X., Metal-Ion (Fe, V, Co, and Ni)-doped MnO2 ultrathin nanosheets supported on Carbon fiber paper for the oxygen evolution reaction. *Adv. Funct. Mater.* 2017, *27* (44), 1704083.

64. Zhang, T.; Cheng, F.; Du, J.; Hu, Y.; Chen, J., Efficiently enhancing oxygen reduction electrocatalytic activity of MnO2 using facile hydrogenation. *Adv. Energy Mater.* 2015, *5* (1), 1400654.

65. Zhou, M.; Weng, Q.; Zhang, X.; Wang, X.; Xue, Y.; Zeng, X.; Bando, Y.; Golberg, D., In situ electrochemical formation of core–shell nickel–iron disulfide and oxyhydroxide heterostructured catalysts for a stable oxygen evolution reaction and the associated mechanisms. *J. Mater. Chem. A* 2017, *5* (9), 4335-4342.

66. Xu, X.; Song, F.; Hu, X., A nickel iron diselenide-derived efficient oxygen-evolution catalyst. *Nat. Commun.* 2016, *7* (1), 12324.

67. Gao, Q.; Huang, C. Q.; Ju, Y. M.; Gao, M. R.; Liu, J. W.; An, D.; Cui, C. H.; Zheng, Y. R.; Li, W. X.; Yu, S. H., Phase-Selective Syntheses of Cobalt Telluride Nanofleeces for Efficient Oxygen Evolution Catalysts. *Angew. Chem. Int. Ed.* 2017, *56* (27), 7769-7773.

68. Ullah, N.; Ullah, R.; Khan, S.; Xu, Y., Boron nitride-based electrocatalysts for HER, OER, and ORR: A mini-review. *Front. Mater.* 2021, 1-10.

69. Parra-Puerto, A.; Ng, K. L.; Fahy, K.; Goode, A. E.; Ryan, M. P.; Kucernak, A., Supported transition metal phosphides: activity survey for HER, ORR, OER, and corrosion resistance in acid and alkaline electrolytes. *ACS Catal.* 2019, *9* (12), 11515-11529.

70. Stern, L.-A.; Feng, L.; Song, F.; Hu, X., Ni2P as a Janus catalyst for water splitting: the oxygen evolution activity of Ni2P nanoparticles. *Energy Environ. Sci.* 2015, *8* (8), 2347-2351.

71. Zhou, H.; Yu, F.; Sun, J.; He, R.; Chen, S.; Chu, C.-W.; Ren, Z., Highly active catalyst derived from a 3D foam of Fe (PO3) 2/Ni2P for extremely efficient water oxidation. *PNAS.* 2017, *114* (22), 5607-5611.

72. Shao, M.; Chang, Q.; Dodelet, J. P.; Chenitz, R., Recent Advances in Electrocatalysts for Oxygen Reduction Reaction. *Chem. Rev.* 2016, *116* (6), 3594-657.

73. Tang, J.; Su, C.; Shao, Z., Covalent Organic Framework (COF)-Based Hybrids for Electrocatalysis: Recent Advances and Perspectives. *Small Methods* 2021, *5* (12), e2100945.

74. Chen, M. X.; Tong, L.; Liang, H. W., Understanding the catalytic sites of metal–nitrogen–carbon oxygen reduction electrocatalysts. *Chem. Eur.* 2021, *27* (1), 145-157.

75. Hu, S.; Ni, W.; Yang, D.; Ma, C.; Zhang, J.; Duan, J.; Gao, Y.; Zhang, S., Fe3O4 nanoparticles encapsulated in single-atom Fe–N–C towards efficient oxygen reduction reaction: Effect of the micro and macro pores. *Carbon* 2020, *162*, 245-255.

76. Luo, E.; Chu, Y.; Liu, J.; Shi, Z.; Zhu, S.; Gong, L.; Ge, J.; Choi, C. H.; Liu, C.; Xing, W., Pyrolyzed M–Nx catalysts for oxygen reduction reaction: progress and prospects. *Energy Environ. Sci.* 2021, *14* (4), 2158-2185.

77. Hsueh, H. Y.; Yao, C. T.; Ho, R. M., Well-ordered nanohybrids and nanoporous materials from gyroid block copolymer templates. *Chem. Soc. Rev.* 2015, *44* (7), 1974-2018.

78. Liang, J.; Zhou, R. F.; Chen, X. M.; Tang, Y. H.; Qiao, S. Z., Fe–N decorated hybrids of CNTs grown on hierarchically porous carbon for high-performance oxygen reduction. *Adv. Mater*. 2014, *26* (35), 6074-6079.

79. Zhang, J.; Huang, Q.-a.; Wang, J.; Wang, J.; Zhang, J.; Zhao, Y., Supported dual-atom catalysts: preparation, characterization, and potential applications. *Chinese J. Catal.* 2020, *41* (5), 783-798.

80. Wang, J.; Liu, W.; Luo, G.; Li, Z.; Zhao, C.; Zhang, H.; Zhu, M.; Xu, Q.; Wang, X.; Zhao, C., Synergistic effect of well-defined dual sites boosting the oxygen reduction reaction. *Energy Environ. Sci.* 2018, *11* (12), 3375-3379.

Chapter 3. Methodology and experimental section

3.1 Electrochemical analysis

3.1.1 Electrochemical measurements in a standard three-electrode cell

A standard three-electrode system comprises working, reference, and counter electrodes in a batch-type electrochemical cell, which is generally used for oxygen electrocatalysis measurements. In our work, the as-prepared electrode served as the working electrode, and a graphite rod and a saturated calomel electrode (SCE) were employed as the counter electrode and the reference electrode, respectively. All electrochemical OER measurements were performed in O_2 saturated 1.0 M KOH. The HER tests were conducted in an N_2 saturated 1.0 M KOH aqueous solution. Liner sweep voltammetry (LSV) polarization and Tafel plots were obtained at a scan rate of 5 mV s^{-1} with iR compensation. The electrochemical surface area (ECSA) of the catalysts was evaluated by double-layer capacitance (C_{dl}) values (ECSA = C_{dl}/C_s cm^2, C_s =40 μF cm^{-2}), which were determined by cyclic voltammetry (CV) scans performed between a non-Faradaic region in 1.0 M KOH electrolyte at different scan rates ranging from 20 mV s^{-1} to 100 mV s^{-1} with an interval point of 20 mV s^{-1}. The electrochemical impedance spectroscopy (EIS) was performed at the overpotential of 300 mV in a frequency range of 100 kHz to 0.01 Hz. All potentials reported were corrected to the reversible hydrogen electrode (RHE) by adding $0.241 + 0.0592 \times$ pH. The Faradaic efficiency was determined by the water drainage method.

3.1.2 Electrochemical test using rotation disk electrode (RDE) and rotating ring-disk electrode (RRDE)

RDE measurements are widely used in electrochemistry to establish well-defined mass transport conditions in half-cell setups, which can be performed to screen the catalyst performance and

investigate the electron transfer mechanism in the ORR process. The RDE system consisted of a Pine Instruments rotator (PINE Research MSR Rotator, model: AFMSRCE, USA) and RDE electrode. The electrocatalysis measurement setup is shown in Figure 3.1.[1] A graphite rod and a saturated calomel electrode (SCE) were employed as the counter electrode and the reference electrode, respectively. The catalyst-coated glassy carbon RDE was used as the working electrode.
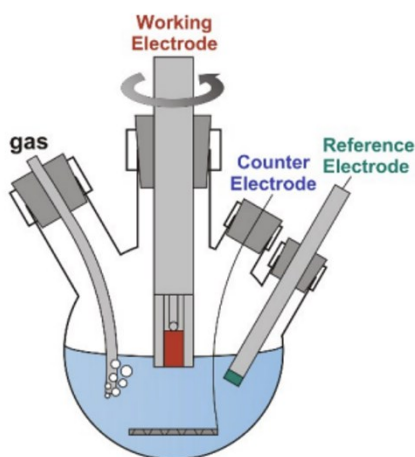
Figure 3. 1 Schematic figure of RDE test in a standard three-electrode cell.

For the preparation of the working electrode, 5 mg of catalyst was dispersed in the mixture of 495 μL isopropyl alcohol (IPA), 495 μL DI water and 10 μL Nafion (5 wt%) under sonication to form a homogeneous catalyst ink. Then 10 μL of this catalyst ink was dipped on a glassy carbon disk of RDE with a diameter of 0.5 cm, followed by drying at room temperature. The total weight loading of catalysts for both as-prepared catalysts and commercial Pt/C (20 wt%, Sigma Aldrich) was 0.255 mg cm^{-2}. The ORR test at an RDE was conducted in O$_2$-saturated 0.1 M KOH or 0.1 M HClO$_4$ electrolytes with varying rotating speeds from 400 to 2025 rpm at a scan rate of 5 mV s^{-1}. 10000 potential cycles were conducted to examine the electrocatalytic durability at the sweep speed of 50 mV s^{-1}. The ORR potentials were calculated into the reversible hydrogen electrode (RHE) by the following equation:

$$E \text{ (vs. RHE)} = E \text{ (vs. SCE)} + 0.059 \times pH + 0.241 \qquad (3.1)$$

The electron transfer number (n) per oxygen molecule for oxygen reduction can be determined by the Koutechy–Levich equations (3.2-3.3):

$$\frac{1}{J} = \frac{1}{J_L} + \frac{1}{J_K} = \frac{1}{B\omega^{0.5}} + \frac{1}{J_K} \qquad (3.2)$$

$$B = 0.62nFC_0(D_0)^{3/2}v^{-1/6} \qquad (3.3)$$

where J is the measured current density, J_L and J_K are the diffusion- and kinetic-limiting current densities, ω is the electrode rotation rate expressed in angular velocity (rad s^{-1}), n is the transferred electron number, F is the Faraday constant (96485 C mol^{-1}), C_0 is the concentration of O_2 in the electrolyte (1.26×10^{-6} mol cm^{-3}), D_0 is the diffusion coefficient of O_2 (1.93×10^{-5} cm^2 s^{-1}), and v is the kinetic viscosity of 0.1M KOH (0.01 cm^2 s^{-1}).[2]

RRDE measurements were carried out to investigate the electron selectivity of the as-prepared samples with the same catalyst loading as RDE measurement. The model of the RRDE setup is AFE6R1PT with disk OD = 5.0 mm, ring OD = 7.50 mm, ring ID = 6.50 mm. The disk electrode was scanned cathodically under the same condition of RDE at a scan rate of 5 mV s^{-1} and the ring potential was kept at 1.5 V vs RHE. The rotation rate is 1600 rpm. The following equations (3.4-3.5) were used to calculate hydrogen peroxide (H_2O_2) yield and electron transfer number (n).

$$n = \frac{4I_D}{I_D + I_R/N} \qquad (3.4)$$

$$H_2O_2\% = \frac{2I_R/N}{I_D + I_R/N} \times 100 \qquad (3.5)$$

where I_D is disk current, I_R is ring current, and N ≈ 0.25 is the current collection efficiency of the Pt ring, which was provided by the manufacturer.

The onset potential was defined as a potential value corresponding to 5 % of the diffusion-limited current density. The half-wave potential ($E_{1/2}$) is corresponding to the potential where the current density is equal to half of the limited current density. The EIS measurements were conducted from 10^5 Hz to 0.1 Hz at 50 mV vs RHE.

3.1.3 Zn–air battery (ZAB) assembly and tests.
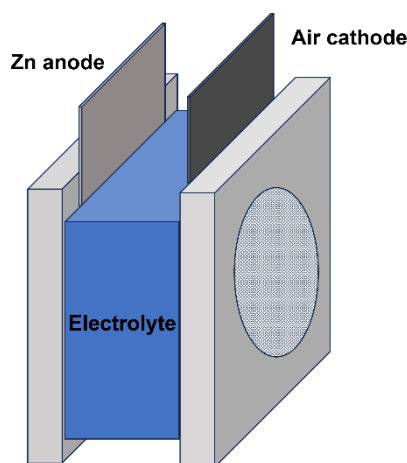
Figure 3. 2 Schematic of homemade Zinc-air battery cell.

The ZAB tests were carried out using a homemade electrochemical cell (Figure 3.2). The ability of the electrocatalysts to serve as an air electrode in ZAB was evaluated under ambient conditions. A polished zinc foil was used as the anode. 5 mg of the prepared catalyst was dispersed in 1 mL DI water, 3 mL IPA and 1 mL Nafion via probe sonication. The cathode was prepared by drop casting the catalyst inks onto the Gas Diffusion Layer (GDL) of carbon fiber paper with a mass loading of 0.5 mg cm^{-2}. For the primary Zn-air batteries, the electrolyte consists of 6 M KOH and 0.2 M zinc acetate dehydrate. Fe$_x$/Cu-N@CF+IrO$_2$ (w:w = 1:1) ink was prepared in the same way for the long-term charge-discharge cycle stability test of the ZAB device in that it was performed with a period of 10 min charge and 10 min discharge. For all-solid-state Zn–air battery assembly, the gel polymer electrolyte was prepared as follows. Polyvinyl alcohol (PVA, 1 g) was dissolved

in 10 mL DI water under continuous stirring at 95 °C to form a homogeneous gel. Then 1 mL of 18 M KOH containing 0.2 M zinc acetate dehydrate was added dropwise to form a homogeneous viscous solution. The as-prepared Fe_x/Cu-N@CF film and zinc foil were placed on the two sides of the PVA gel, followed by pressed Ni foam as the current collector. The reference cathode was made in the similar way using commercial Pt/C or Pt/C+IrO_2 (w:w=1:1).

3.2 Materials characterizations

Scanning electron microscopy (SEM): The morphologies of prepared materials were studied via Zeiss Sigma 300 VP-Field Emission Scanning Electron Microscopy (FESEM) configured with an EBSD detector.

Transmission electron microscopy (TEM): The TEM measurements were conducted on a JEOL JEMARM200CF equipped with an energy dispersive spectrometer (EDS) at an accelerating voltage of 200/300 kV.

X-ray diffraction (XRD): The XRD patterns were collected by Rigaku Ultima IV diffractometer (XRD, D8 discover diffraction system equipped with Cu Kα radiation (40 kV, 44 mA)) at a scan rate of $5° \, min^{-1}$.

X-ray photoelectron spectroscopy (XPS): XPS measurements were recorded on on Kratos Analytical AXIS 165 with a monochromatic Al Kα source. The C 1 s photoelectron peak at 284.6 eV as reference was used for spectrometer calibration.

Ultraviolet photoelectron spectroscopy (UPS): UPS measurements were carried out on a physical Electronic PHI 5000 photoelectron spectrometer with He I (21.22 eV) ultraviolet radiation.

Water contact angle: The water contact angle was characterized on Contact Angle (FTA-200) equipped with a CCD camera.

Digital microscope imaging: Bubble releasing behavior was recorded by digital microscope VHX-700F.

N$_2$ adsorption: Nitrogen adsorption-desorption isotherms were collected on an Autosorb Quantachrome 1MP at 77 K.

Raman spectroscopy: Raman spectroscopy measurements were performed using a Renishaw InVia Raman system calibrated by a standard silicon wafer (520 cm^{-1}) using a 532 nm laser. In situ Raman spectra were recorded on Renishaw InVia Raman microscope using a 532 nm laser as excitation source under the controlled potentials (1-1.5 V vs. RHE) *via* the Gamry reference 3000 in 1.0 M KOH solution.

Inductively coupled plasma optical emission spectrometry (ICP-OES): The ICP-OES mearsurements were performed on Thermo iCAP6300 Duo ICP_OES.

Atomic-resolution electron energy-loss spectroscopy (EELS): The EEELS measurements were comducted on Titan Cubed Themis G20 TEM equipped with a highly sensitive Super-X energy dispersive X-ray detector system (operated at 300 kV).

X-ray absorption spectroscopy: X-ray absorption near-edge structure (XANES) and the extended X-ray absorption fine structure (EXAFS) data at the Hard X-ray microanalysis beamline (HXMA-061D) of the Canadian Light Source. The X-ray absorption spectra were acquired in fluorescence mode using a Si(111) double-crystal monochromator to range the X-ray energy from 5–40 keV. The ring current is 250 mA. A He-filled Oxford straight ion chamber detector was used to monitor the incident X-ray, and the fluorescence yield signal was captured using a 32-element Ge detector. The energy was calibrated using Fe and Cu plate reference samples.

High-performance liquid chromatography (HPLC): The HPLC mearsurements were recorded on Shimazdu LC-20 equipped with a 4.6 mm × 150 mm 5 μm C18 detector column and an ultraviolet-visible detector set at 245 nm.

3.3 References

1.   Hong, W. T.; Risch, M.; Stoerzinger, K. A.; Grimaud, A.; Suntivich, J.; Shao-Horn, Y., Toward the rational design of non-precious transition metal oxides for oxygen electrocatalysis. *Energy Environ. Sci.* 2015, *8* (5), 1404-1427.

2.   Yang, G.; Zhu, J.; Yuan, P.; Hu, Y.; Qu, G.; Lu, B.-A.; Xue, X.; Yin, H.; Cheng, W.; Cheng, J., Regulating Fe-spin state by atomically dispersed Mn-N in Fe-NC catalysts with high oxygen reduction activity. Nat. Commun. 2021, *12* (1), 1734.

Chapter 4. Ni₃S₂-Embedded NiFe LDH Porous Nanosheets with Abundant

Heterointerfaces for High-current Water Electrolysis

Abstract: Ni$_3$S$_2$-embedded NiFe LDH heterostructured porous nanosheets were *in situ* grown on nickel foam (Ni$_3$S$_2$-NiFe LDHs /NF) *via* a one-pot solution method mediated by NaHS at room temperature in 15 min. Benefiting from the abundant Ni$_3$S$_2$-NiFe LDH interfaces, the as-prepared catalyst delivers 50, 500 and 1000 mA cm^{-2} with an overpotential of only 230, 285 and 303 mV for oxygen evolution reaction, respectively, registering as one of the best performing non-precious metal OER catalysts. *In situ* and *ex situ* analysis reveal that the Ni$_3$S$_2$ was *in situ* partially transformed under an electrooxidation environment into NiOOH over an equally important electrically conductive Ni$_3$S$_2$ to drive proficient catalysis. This strategy can be extended to fabricate Ru-Ni$_3$S$_2$-NiFe LDHs/NF electrocatalyst for high active hydrogen evolution reaction.

4.1 Introduction

Electrochemical water splitting is a promising sustainable technology to produce high-purity H$_2$ in the conversion of renewable electricity, but the energy conversion efficiency is severely restricted by the sluggish kinetics of oxygen evolution reaction (OER) in the anode.[1-2] Two-dimensional (2D) structure has sparked intensive interest in the field of energy storage/conversion due to the distinct physical and chemical properties compared with bulk and other dimensional counterparts.[3, 4] NiFe layered double hydroxides (NiFe-LDHs) nanosheets have been considered as one of the most active catalysts toward water oxidation.[5] Various strategies have been developed to further promote the OER catalytic activity of NiFe-LDHs nanosheets in terms of exposure of the more active sites. For example, tailoring LDHs into single or few-layer nanosheets exposes more surface sites and reduces the diffusion length for ions and/or electrons.[6-8] Besides, engineering nanopores is also confirmed to be a versatile strategy to enhance the

intrinsic activity of nanosheets, resulting from the abundant defects and active edge sites created in catalysts.[9] Although some encouraging developments have been made on NiFe LDHs, the electrocatalytic performance of NiFe LDHs still falls behind commercial requirements (current density, $j \geq 500$ mA cm^{-2} at overpotential, $\eta \leq 300$ mV), because of the limited exposure of active sites and low electrical conductivity.[10]

Heterostructure engineering is an effective strategy to boost OER activity benefitting from the improved electron transfer capability and tuned electronic structure. The interfaces within the heterostructure are believed to be the real catalytic active sites.[11-13] For example, NiFe(OH)$_x$/FeS and NiFeOOH/NiFe heterostructured nanomaterials exhibit enhanced OER activity as compared to the NiFe hydroxides.[14, 15] However, these reported hierarchical heterostructure possesses sparse interfacial sites, leading to inefficient utilization of catalysts because of the limited optimization of adsorption energies (Figure 4.1a). Besides, the synthesis processes (such as electrodeposition, hydrothermal and calcination) normally involve tedious multistep procedures with significant energy and time consumption. Up to now, most reported methods are difficult to realize extremely dense interfacial sites, due to the asynchronous nucleation and growth of the two heterophases. The construction of well-defined heterostructured 2D materials is expected to be an effective way to overcome the drawbacks of hierarchical heterostructure (Figure 4.1b). Recently, a powdery catalyst, Ni(0)-embedded Ni(OH)$_2$ heterostructure nanosheets, shows enhanced water oxidation due to high-density active sites exposed and modified electronic structure.[16] Nevertheless, the controllable growth of heterostructured 2D materials on a certain substrate for large-scale production is challenging because of the complex reaction kinetics.

Ni_3S_2, which occurs naturally as the mineral heazlewoodite, has intrinsic metallic behavior due to the continuous network of Ni−Ni bonds throughout its structure.[17, 18] To this end, we fabricated a robust electrode composed of Ni_3S_2-embedded NiFe LDH heterostructured nanosheets with a porous structure supported on nickel foam (NF) *via* a one-pot solution approach at room temperature in 15 min. The well-defined heterostructured Ni_3S_2-NiFe LDHs nanosheets possess both abundant interfaces and improved electron transfer capability. In addition, the porous structure not only provides nanosheets with more exposed active sites, but also facilitates ions transfer and bubble release, which benefits its stability, especially under high j_s with a large amount of gas evolved. As a result, Ni_3S_2-NiFe LDHs/NF-2 exhibits superior OER catalytic performances with small η_s of 230, 285 and 303 mV to reach j_s of 50, 500 and 1000 mA cm^{-2}, small Tafel slope of 35.6 mV dec^{-1} and excellent stability over 100 hours, outperforming most reported non-precious metal catalysts and noble-metal benchmarks. Ru-Ni_3S_2-NiFe LDHs/NF catalyst can be obtained in a similar way with only the addition of $RuCl_3$, which exhibited an enhanced hydrogen evolution reaction (HER) catalytic performance (η=61.3 mV at 10 mA cm^{-2}). The coupled Ni_3S_2-NiFe LDHs/NF-2 ‖ Ru-Ni_3S_2-NiFe LDHs/NF electrodes showed a significantly boosted overall water splitting activity with low voltages of 1.47, 1.71 and 1.85 V to deliver high j_s of 10, 100 and 500 mA cm^{-2}, respectively, far surpassing current commercial requirements (1.8-2.40 V for 200-400 mA cm^{-2}). [19]
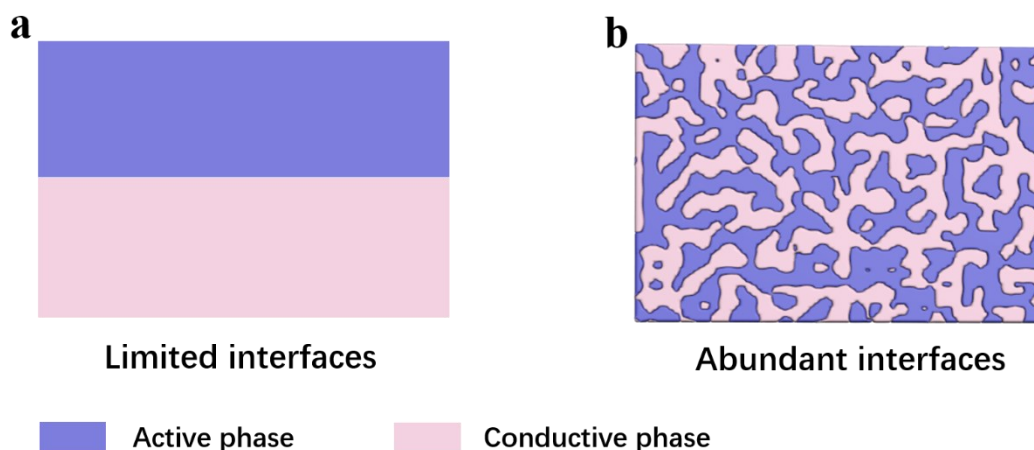
Figure 4. 1 (a) Hierarchical structure. (b) Interconnected structure.

4.2 Experimental Section

4.2.1 Materials

Fe(NO$_3$)$_3$·9H$_2$O, NaHS were purchased from Fisher scientific. Iridium oxide (IrO$_2$) and Pt/C (20%) were purchased from Sigma-Aldrich. All reagents were used as received without further purification. Ni foam was purchased from Xiamen Lith Machine Co., Ltd. Before the use, Ni foam was cleaned with HCl (3 M), acetone, and deionized water (DI) several times. Deionized water was used throughout the experimental processes.

4.2.2 Synthesis of Ni$_3$S$_2$-NiFe LDHs/NF

Typically, 0.1 M Fe(NO$_3$)$_3$·9H$_2$O solution containing 14.5 mM NaHS was prepared in 10 mL DI water. Then a piece of NF (1 × 2.5 cm^2) was immersed into the above solution. After resting for 15min at ambient conditions, Ni$_3$S$_2$-NiFe LDHs/NF-2 supported on NF was obtained by rinsing with deionized water and drying naturally. The loading of the product on NF was determined to be 1.8 mg cm^{-2}. Accordingly, Ni$_3$S$_2$-NiFe LDHs/NF-1, Ni$_3$S$_2$-NiFe LDHs/NF-3 samples were

prepared by tuning the concentration of NaHS at 8.9 and 19.6 mM, respectively. NiFe LDHs/NF was synthesized without NaHS. Ru-Ni$_3$S$_2$-NiFe LDHs/NF was synthesized similarly to that of Ni$_3$S$_2$-NiFe LDHs/NF-2 except with the addition of RuCl$_3$ (39 mg) resting for 2 h.

4.2.3 Materials characterization

SEM images were captured by Zeiss Sigma 300 VP-Field Emission Scanning Electron Microscopy (FESEM). Transmission electron microscopy (TEM) was carried out on a JEOL JEMARM200CF equipped with an energy dispersive spectrometer (EDS). X-ray diffraction (XRD) patterns were measured using a D8 discover diffraction system equipped with Cu Kα radiation (40 kV, 44 mA) at a scan rate of 5° min^{-1}. Raman spectroscopy measurements were performed using a Renishaw InVia Raman system calibrated by a standard silicon wafer (520 cm^{-1}) using a 532 nm laser. In situ Raman spectra were recorded on Renishaw InVia Raman microscope using a 532 nm laser as excitation source under the controlled potentials (1-1.5 V vs. RHE) *via* the Gamry reference 3000 in 1.0 M KOH solution. X-ray photoelectron spectroscopy (XPS) spectra were collected on a Kratos Analytical AXIS 165 with monochromatic Al Kα source. The binding energy was calibrated using the C 1s photoelectron peak at 284.6 eV as reference. The S: Fe ratio was determined by inductively coupled plasma optical emission spectrometry (ICP-OES) on Thermo iCAP6300 Duo ICP_OES. The contact angle was characterized on Contact Angle (FTA-200) equipped with a CCD camera. Bubble releasing behavior was recorded by digital microscope VHX-700F.

4.2.4 Electrochemical measurements

All electrochemical measurements were performed in a three-electrode system using Gamry reference 3000 with Ni$_3$S$_2$-NiFe LDHs/NF directly as the working electrode, graphite rod as the

counter electrode, and a saturated calomel electrode (SCE) as the reference electrode in O_2 saturated 1.0 M KOH. The HER tests were conducted in an N_2 saturated 1.0 M KOH aqueous solution. For the two-electrode electrolyzer, the Ni_3S_2-NiFe LDHs/NF and Ru-Ni_3S_2-NiFe LDHs/NF samples were used as the anode and cathode, respectively. All potentials reported were corrected to the reversible hydrogen electrode (RHE) by adding $0.241 + 0.0592 \times pH$. The stability test was performed in a 1.0 M KOH electrolyte. LSV polarization and Tafel plots were obtained at a scan rate of 5 mV s^{-1} with iR compensation. Electrochemical surface area (ECSA) of the catalysts was evaluated by double-layer capacitance (C_{dl}) values (ECSA = C_{dl}/C_s cm^2, C_s =40 μF cm^{-2}), which were determined by cyclic voltammetry (CV) scans performed between a non-Faradaic region in 1.0 M KOH electrolyte at different scan rates ranging from 20 mV s^{-1} to 100 mV s^{-1} with an interval point of 20 mV s^{-1}. The electrochemical impedance spectroscopy (EIS) was performed at the overpotential of 300 mV in a frequency range of 100 kHz to 0.01 Hz. The Faradaic efficiency was determined by the water drainage method. The RuO_2/NF and Pt/C/NF were prepared by a slurry cast method. Typically, 10 mg catalysts were ultrasonically dispersed in a 1 ml solution containing 970 μL isopropyl alcohol and 30 μL Nafion solution. To maintain the same mass loading with the Ni_3S_2-NiFe LDHs/NF, a certain amount of ink was pipetted onto the NF and dried in the air before the electrochemical measurements.

4.3 Results and Discussion

4.3.1 Synthesis and characterizations of electrocatalysts

The Ni_3S_2-embedded NiFe LDH nanosheets were in situ grown on NF *via* a one-step solution method at room temperature in only 15 min (Figure 4.2a). NF was selected as both the substrate and Ni source. The three-dimensional Ni_3S_2-NiFe LDHs/NF catalyst was prepared in the solution

containing iron (III) nitrate, NaHS, where the presence of Fe^{3+} stimulates Ni^{2+} release from NF (Eq.4.1), the NaHS hydrolyzes and generates hydroxide ions H_2S (Eq.4.2) and HS^- reacts with metal ions to produce sulfides (Eq.4.3). Meanwhile, metal ions combine with locally generated hydroxide ions to form bimetallic hydroxide NiFe LDH (Eq.4.4). [14, 20]

$$2Fe^{3+} + Ni \rightarrow Ni^{2+} + 2Fe^{2+} \qquad \text{(Eq.4.1)}$$

$$HS^- + H_2O \rightarrow OH^- + H_2S \qquad \text{(Eq.4.2)}$$

$$Ni^{2+} + HS^- \rightarrow Ni_3S_2 \qquad \text{(Eq.4.3)}$$

$$Fe^{3+} + Fe^{2+} + Ni^{2+} + OH^- \rightarrow NiFe\ LDH \qquad \text{(Eq.4.4)}$$

The color of NF changes from silvery-white to black in 15 min at room temperature without stirring. The Ni_3S_2-NiFe LDHs/NF was collected and used directly as the OER electrode. To optimize catalytic activity, electrodes were prepared by simply tuning the concentration of NaHS (0, 8.9, 14.5, 19.6 mM), which were donated as NiFe LDH/NF, Ni_3S_2-NiFe LDHs/NF-1, Ni_3S_2-NiFe LDHs/NF-2, and Ni_3S_2-NiFe LDHs/NF-3, respectively. The Ni_3S_2-NiFe LDHs/NF-2 with a large geometry size of 20x20 cm^2 was prepared (Figure 4.2b). The corresponding scanning electron microscopy (SEM) image in Figure S4.1 demonstrates that the well-defined nanosheets on NF were synthesized successfully for larger-scale preparation.

The SEM images of the Ni_3S_2-NiFe LDH/NF-2 (Figure 4.2c) show that the Ni_3S_2-NiFe LDH nanosheets are uniformly grown on NF with an average size of 186 nm (Figure S6b). Transmission electron microscopy (TEM) image of the product further corroborates the thin-layered structure (Figure 4.2d). In addition, we observed abundant pore structures from high-angle annular dark-field scanning transmission electron microscopy (HAADF-STEM) images of the Ni_3S_2-NiFe LDH nanosheet (Figure 4.2e, f). The average pore size within the nanosheet is around 3.8 nm (Figure

S4.2). Undoubtedly, the porous-structured nanosheets can provide abundant exposed active sites and facilitate electrolyte penetration and bubble release during water electrolysis. [21, 22] The high-resolution TEM (HRTEM) image (Figure 4.2g) confirms the formation of NiFe LDH and Ni_3S_2 phases in the nanosheet. In enlarged HRTEM regions (outlined in Figure 4.2g), the well-resolved lattice fringe of 0.21 nm corresponds to the (018) crystal plane of NiFe LDHs (Figure 4.2h), two sets of lattice fringes with the interplanar spacings of 0.23 and 0.24 nm, respectively, exhibit 70° interplanar angle, which agrees well with the (021) and (003) planes of the hexagonal Ni_3S_2 phase (Figure 4.2i).[17] The coexistence of NiFe LDHs and Ni_3S_2 in the nanosheet was approved by the corresponding fast Fourier transformation (FFT) pattern (Figure 4.2j). In Figure 4.2k, the STEM image and the corresponding energy-dispersive X-ray spectroscopy (EDS) mapping images clearly state the existence of the Ni, Fe, O, S elements in the catalyst. The distribution of elements confirms that Ni_3S_2 is embedded in NiFe LDHs. The atomic ratio of S/Fe determined by the EDS spectrum (Figure S4.3) is about 2.21:1, which matches well with the ICP-OES result of 2.29:1 (Table S4.1). Additionally, the mechanical integrality of as-prepared Ni_3S_2-NiFe LDHs/NF-2 catalyst is highly robust compared to self-supported catalyst (NiFe LDHs/NF) prepared by the commonly used hydrothermal method.[23] The Ni_3S_2-NiFe LDH nanosheets were hard to peel from the NF, even after sonication for 1 h in water, while the detachment of NiFe LDHs from NF occurs in 1 minute (Figure S4.4). This robust mechanical property of Ni_3S_2-NiFe LDHs/NF-2 benefits the maintenance of its activity and durability even at high j_s.
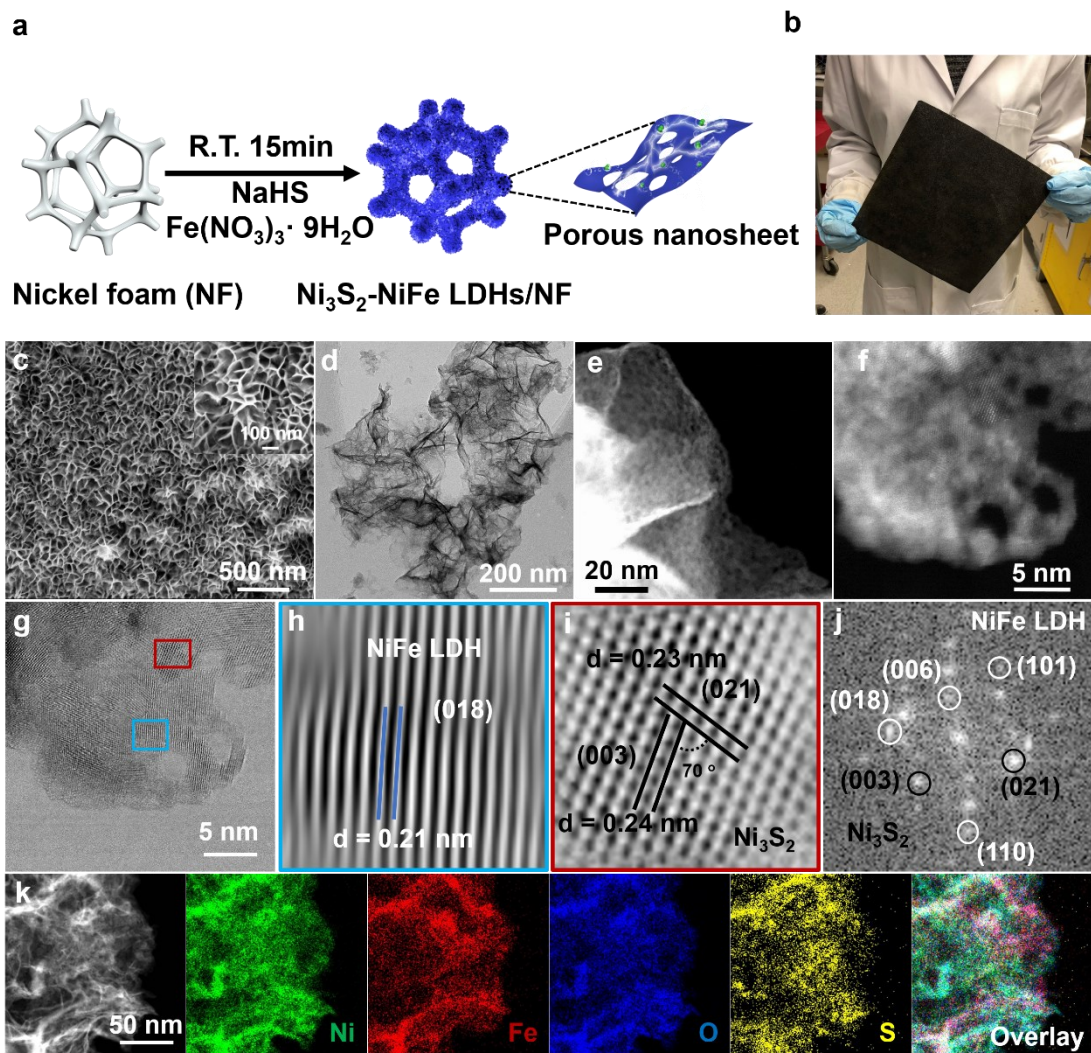
Figure 4. 2 (a) Schematic of the synthesis of Ni_3S_2-NiFe LDHs/NF. (b) Photograph of Ni_3S_2-NiFe LDHs/NF-2 with 20x20 cm^2 area. (c, d) SEM and TEM images of Ni_3S_2-NiFe LDHs/NF-2. (e, f) STEM images of Ni_3S_2-NiFe LDHs/NF-2. (g, h, i) High-resolution transmission electron microscopy (HRTEM) images of Ni_3S_2-NiFe LDHs/NF-2. (j) The corresponding fast Fourier transformation (FFT) pattern. (k) HAAD-STEM image and associated elemental mapping images.

The release of Ni species from NF is the first key step of *in situ* growth of NiFe-based hydroxides on NF. The redox reaction between Fe^{3+} and Ni in an aqueous solution ($Ni + 2Fe^{3+} \rightarrow Ni^{2+} + 2Fe^{2+}$) is slow and high temperature is needed. For most reported work, a suitable alkaline condition and high temperature are required for the synthesis of NiFe-based hydroxide with well-defined nanosheet morphology. [24, 25] In this work, NaHS in an aqueous solution provides both hydroxide ions and sulfur ions that quickly combine with metal ions, which speeds up the redox reaction rate causing *in situ* growth of Ni_3S_2-NiFe LDHs on NF in a short time. Accordingly, the synthesis of Ni_3S_2-NiFe LDHs/NF was carried out by tuning NaHS concentrations ranging from 0 to 19.6 mM. Agglomeration of particles on NF can be observed without the addition of NaHS (Figure S4.5a-c). Interestingly, Ni_3S_2-NiFe LDHs with a small nanosheet size were grown onto NF in the case of 8.9 mM NaHS (Figure S4.5d-f). The size of nanosheets increased with increasing NaHS concentration up to 14.5 mM (Figure S4.5g-i), then the opposite effect was noted when further increasing NaHS to 19.6 mM (Figure S4.5j-l). Ni_3S_2-NiFe LDHs/NF-2 prepared in 14.5 mM has the largest average size ($\bar{S}$ = 186 nm) (Figure S4.6a-c). The pore diameters between nanosheets also exhibit an apparent dependence on the concentration of NaHS. Ni_3S_2-NiFe LDHs /NF-2 has the largest pore diameter ($\bar{D}$ = 91 nm) (Figure S4.6d-f).

We suspect that the rate of Ni species release can affect the nucleation and growth processes of the product onto NF. Without the addition of NaHS, the as-produced NiFe LDH particles arise from the hydrolysis of metal ions in the solution with dissolved oxygen.[26] The addition of NaHS significantly boosts the release of Ni^{2+} from NF and provides OH^- and S^{2-} ions, which provides more nuclei and mass source for the growth process. For example, the material synthesized in 8.9 mM NaHS has embryonic-like nanosheets with small $\bar{S}$ and $\bar{D}$. Then 14.5 mM NaHS supplies more mass sources for the growth process of nanosheets, thus affording larger nanosheets.

However, at a higher NaHS concentration of 19.6 mM, the nucleation is significantly boosted resulting in small-sized nanosheets, but the atomic ratio of S/Fe is about 2.36:1 close to that of 14.5 mM (2.29:1) (Table S4.1).

The phase of the products was further identified by the X-ray diffraction (XRD) patterns. The diffraction peaks of as-synthesized catalysts match well with the standard XRD patterns of hexagonal NiFe LDH (PDF # 42-0573) and hexagonal Ni_3S_2 (PDF # 44-1418), indicating the successful formation of Ni_3S_2-NiFe LDH nanosheets on NF (Figure 4.3a).[17, 27] And the collected XRD patterns of Ni_3S_2-NiFe LDHs/NF-1 and Ni_3S_2-NiFe LDHs/NF-3 are consistent with Ni_3S_2-NiFe LDHs/NF-2 (Figure S4.7). The XRD patterns of Ni metal are from Ni foam. The Raman spectra also confirmed the chemical composition of prepared catalysts. Figure 4.3b displays a comparison of Raman spectra of NiFe LDHs/NF and Ni_3S_2-NiFe LDHs /NF-2. The peak at 194.7 cm^{-1} is related to O–M–O bending modes, including O–Ni–O and O–Fe–O.[28,29] The bands at 466 and 540 cm^{-1} correspond to the stretching vibrations of $\delta(Ni-O)$ and $\nu(Ni-O)$ in $Ni(OH)_2$, the peaks at 307, 680 cm^{-1} can be attributed to the Fe−O vibrations in disordered FeOOH.[30-32] The decrease of the ratio of peak intensities (I_δ/I_ν) can be observed in Ni_3S_2-NiFe LDHs/NF-2 compared to NiFe LDHs/NF, which means the incorporation of Fe content increased because the local structure of Ni−O is affected by the Fe content.[30, 33] In comparison, Ni_3S_2-NiFe LDHs /NF-2 exhibits additional Raman bands at 186, 200, 222, 302, 324, and 350 cm^{-1} assigned to Ni_3S_2.[17, 34] X-ray photoelectron spectroscopy (XPS) was conducted to further understand the surface chemistry and valance state of elements for the synthesized electrocatalysts. As shown in Figure 4.3c, the high resolution XPS spectrum of Ni 2p for NiFe LDHs/NF consists of two spin-orbit peaks of Ni 2p3/2 (855.6 eV) and Ni 2p1/2 (872.3 eV) along with two satellite peaks, while the minor peaks at 852.2 and 869.3 eV are indexed to metallic Ni.[35, 36] The

presence of Ni peaks suggests that NF was not fully wrapped by the products, which is consistent with the SEM images (Figure S4.6a-b). By contrast, the peaks of metallic Ni disappeared in Ni 2p for Ni_3S_2-NiFe LDHs/NF-2, which indicates that NiFe LDHs/Ni_3S_2 nanosheets are uniformly grown on the NF. For Fe 2p (Figure 4.3d), the peaks for Fe^{3+} and Fe^{2+} can be observed, indicating that the Fe^{3+} and Fe^{2+} coexist in the prepared catalyst.[37] The introduction of Fe^{2+} in NiFe LDHs has been demonstrated to be an effective strategy for the enhancement of the OER activity.[26, 38] It is noteworthy that Ni 2p3/2 shows a negative shift of approximately 0.3 eV, while Fe 2p positively shifts 0.3 eV, which could be related to the electronic interaction between Ni_3S_2 and NiFe LDH.[39-41] Correspondingly, in the O 1s spectrum (Figure 4.3e), the peaks at 529.7, 531 and 533.2 eV are attributed to metal-O, hydroxyl species and absorbed molecular water on the surface, respectively.[42-46] And the content of metal-O of Ni_3S_2-NiFe LDHs/NF-2 is about 34.4% higher than that of NiFe LDHs/NF (21.4 %), which indicates more NiFe LDH formation in Ni_3S_2-NiFe LDHs/NF-2. For the high-resolution XPS spectrum of S 2p in Figure 4.3f, the two peaks located at 167.8 and 161.9 eV originate from the sulfate groups and S-S bond, respectively, and the peak at 163.2 eV corresponds to the Ni-S bond. [47, 48]
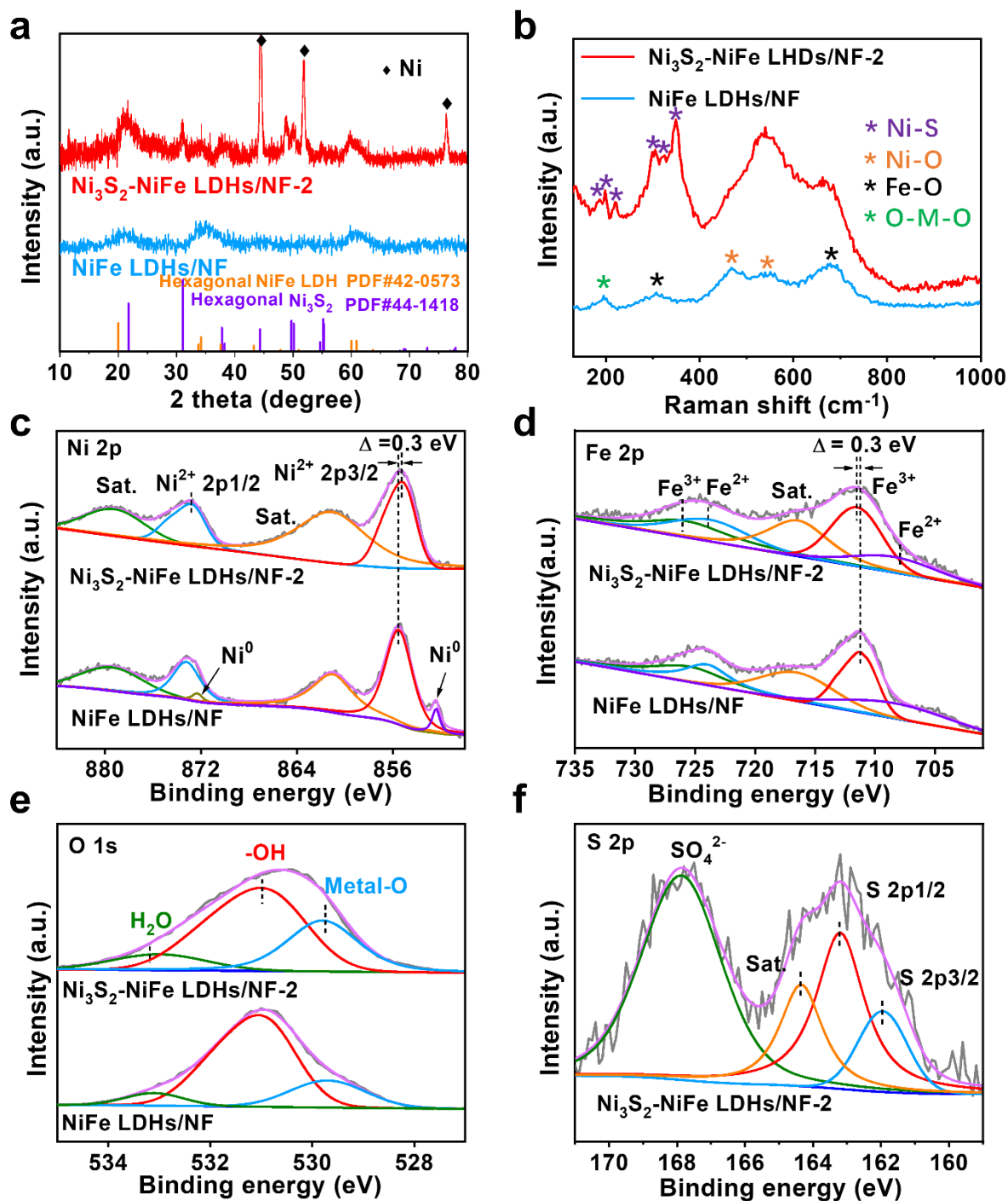
Figure 4. 3 (a) XRD patterns of NiFe LDHs/NF and Ni_3S_2-NiFe LDHs/NF-2. (b) Raman spectra of NiFe LDHs/NF and Ni_3S_2-NiFe LDHs/NF-2. (c-f) High-resolution XPS spectra of Ni 2p, Fe 2p, O 1s and S 2p for NiFe LDHs/NF and Ni_3S_2-NiFe LDHs/NF-2.

4.3.2 Electrocatalytic OER performance

The OER electrocatalytic performance of Ni_3S_2-NiFe LDHs/NF-2 is evaluated using a standard three-electrode cell in a 1.0 M KOH solution. For comparison, commercial RuO_2 loaded on NF (denoted as RuO_2/NF) and bare NF were also measured as control samples. According to the linear sweep voltammetry (LSV) curves in Figure 4.4a, the Ni_3S_2-NiFe LDHs/NF catalysts exhibit great superiority in electrocatalytic performance compared to NiFe LDHs/NF, RuO_2/NF and NF electrodes employed. It is noted that Ni_3S_2-NiFe LDHs/NF-2 exhibits the most prominent enhancement, which only requires η of 230 mV to deliver 50 mA cm^{-2}, superior to those of NiFe LDHs/NF (354 mV) and RuO_2/NF (335 mV). Specifically, the low η_s of 285 and 303 mV are needed to deliver the high j_s of 500 and 1000 mA cm^{-2}, respectively. The consistent kinetic behaviors can be observed in the Tafel plots in Figure 4.4b, Ni_3S_2-NiFe LDHs/NF-2 shows a Tafel slope of 35.6 mV dec^{-1}, which is much smaller than those of NiFe LDHs/NF (84.6 mV dec^{-1}), RuO_2/NF (83.2 mV dec^{-1}) and NF (186.4 mV dec^{-1}), suggesting boosted OER kinetics. The as-prepared 10 batches of Ni_3S_2-NiFe LDHs/NF-2 exhibit similar catalytic performance, which proves its reproduction (Figure 4.4c, S4.7). OER performances (LSV, EIS) of the prepared 20x20 cm2 catalyst. All the above experimental results state our Ni_3S_2-NiFe LDHs/NF-2 as an earth-abundant and efficient OER catalyst that is superior to most recently reported high-performance electrocatalysts (Figure 4.4d, e and Table S4.3). In addition, the facile and effective preparation method means that Ni_3S_2-NiFe LDHs/NF-2 has great potential to drive a water-splitting cell for large-scale H_2 production fulfilling the commercial criteria of the OER process in the anode. The electrochemical stability of Ni_3S_2-NiFe LDHs/NF-2 was evaluated by performing chronopotentiometry measurement under a constant j of 100 mA cm^{-2} for 240 h, which shows only 2.7 % potential decay with time (Figure 4.4f).

To elucidate the origins of disparity in the OER catalytic activity among the different catalysts, double-layer capacitance (C_{dl}) investigations were conducted, and the electrochemically active surface area (ECSA) was estimated from the C_{dl} of the electrocatalysts. The Ni$_3$S$_2$-NiFe LDHs/NF-2 shows a dramatically higher value of C_{dl} (4.57 mF cm^{-2}) than that of NiFe LDHs/NF (1.16 mF cm^{-2}), NF (0.86 mF cm^{-2}) and other investigated samples (Figure 4.4g, S4.10), which corroborates that the optimized Ni$_3$S$_2$-NiFe LDHs/NF-2 possesses a larger ECSA related to full-developed porous nanosheets with more exposure of active sites. The electrochemical impedance spectroscopy (EIS) plots reveal that the Ni$_3$S$_2$-NiFe LDHs/NF-2 catalyst exhibits the smallest semicircle diameter among all investigated samples (Figure 4.4h, S4.11, Table S4.2), revealing the lowest charge-transfer resistance of Ni$_3$S$_2$-NiFe LDHs/NF-2 during the OER process. This result suggests that the coexistence of NiFe LDHs and Ni$_3$S$_2$ in nanosheet created abundant interfaces, the metallic feature of Ni$_3$S$_2$ favors the electron transfer within the nanosheet.[39] This was further demonstrated by the work functions of the Ni$_3$S$_2$-NiFe LDHs/NF-2 and NiFe LDHs/NF determined by ultraviolet photoelectron spectroscopy (UPS). Clearly, the Ni$_3$S$_2$-NiFe LDHs/NF-2 shows a smaller work function than NiFe LDHs/NF (Figure 4.4i), confirming the better electron transferability of the former, which benefits the charge transport between the catalyst surface and reactant intermediates and thus facilitates electrocatalysis. [49-51] The OER performance (LSV, EIS) of the prepared 20 x 20 cm^2 catalyst was also examined. There is not much difference between the prepared 20 x 20 cm^2 catalyst and the small sample, confirming the scalability of this method without compromising activity (Figure S4.13).
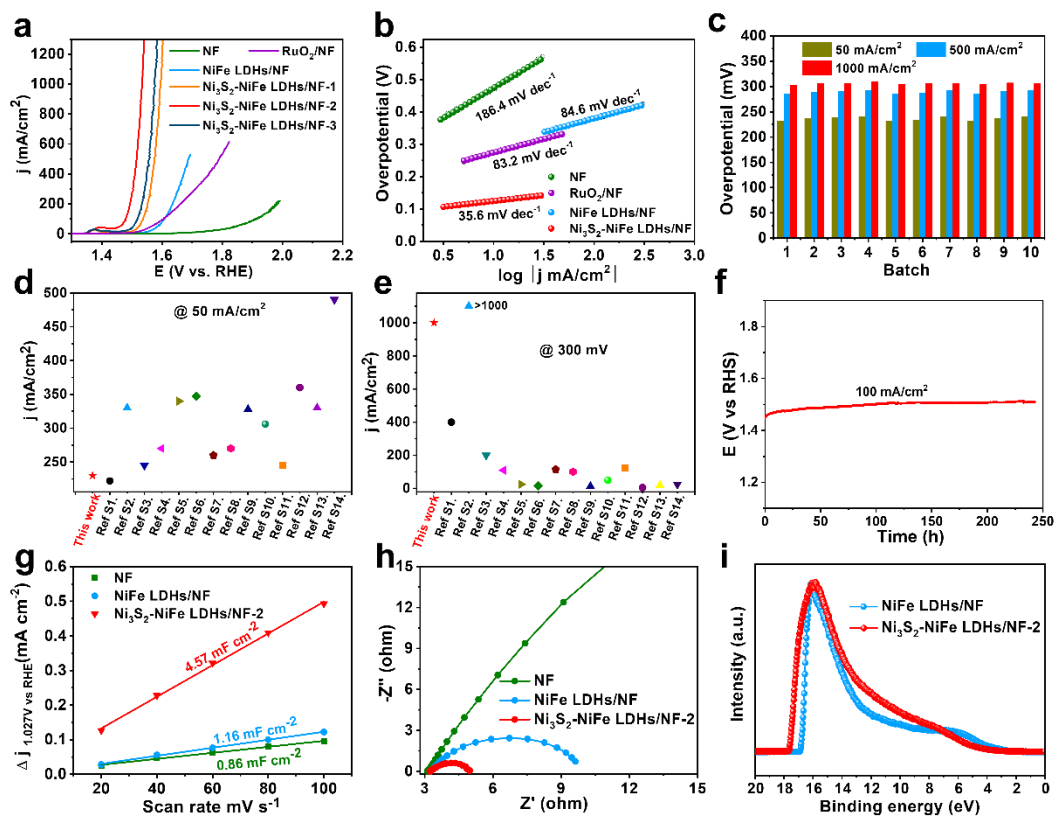
Figure 4. 4 (a) The LSV curves for OER recorded on Ni₃S₂-NiFe LDHs/NF-2, NiFe LDHs/NF, RuO₂/NF and NF. (b) The corresponding Tafel plots. (c) The overpotential histogram for ten batches of Ni₃S₂-NiFe LDHs/NF-2 at 50, 500, and 1000 mA cm⁻². (d, e) Comparison of the overpotentials required at 50 mA cm⁻² and the current densities delivered at 300 mV among our catalyst and available reported OER catalysts. (f) Chronopotentiometric curves of Ni₃S₂-NiFe LDHs/NF-2 at 100 mA cm⁻² in 1 M KOH. (g, h) ECSA and EIS plots of the Ni₃S₂-NiFe LDHs/NF-2, NiFe LDHs/NF and NF. (i) UPS spectra of Ni₃S₂-NiFe LDHs/NF-2, NiFe LDHs/NF.

4.3.3 Mechanistic analyses

We further investigated the surface wettability and oxygen bubble-releasing behavior for NF, NiFe LDHs/NF, Ni₃S₂-NiFe LDHs/NF-2 (Figure 4.5a-c, video 4.1-4.3). The NF and NiFe

64

LDHs/NF showed contact angles of 129° and 87°, respectively, while the water droplet immediately infiltrated into the Ni_3S_2-NiFe LDHs/NF-2, indicating its super hydrophilicity. The oxygen bubbles generated at the interface between electrocatalysts, and electrolytes hinder the contact of active sites and reactants, so effective bubble release is crucial for the maintenance of high activity. [52, 53] The bubble releasing behavior was recorded by a digital microscope at 25 mA cm^{-2}. The oxygen bubbles firmly stick to the surface of bare NF and grow to very large sizes (up to 400 μm) (Figure 4.5a, video 4.1). The bubbles generated from NiFe LDHs/NF show a small size (smaller than 100 μm), but the grown bubbles (more than 300 μm) can be still observed (Figure 4.5b, video 4.2). In sharp contrast, the bubbles easily leave from the surface of Ni_3S_2-NiFe LDHs/NF-2 with the smallest size (less than 30 μm) (Figure 4.5c, video 4.3), which proved fast re-exposure of active sites to surrounding electrolyte for Ni_3S_2-NiFe LDHs/NF-2. Such an efficient bubble-releasing process could be related to the high hydrophilicity and porous-structured nanosheets enhancing the mass transfer and facilitating the reaction kinetics.

To further gain insights into the mechanism of high activity of Ni_3S_2-NiFe LDHs/NF-2, the structural and compositional evolutions after the OER were investigated. SEM and TEM images show that the nanosheet structure is well maintained after the long-term electrocatalysis test. (Figure 4.5d, e). From the HR-TEM image, we can still observe the porous structure of the nanosheet, as well as some newly generated phases (Figure 4.5f). The change of surface chemical composition was further revealed by XPS, where the M-S bonds almost disappeared accompanied by an increase in M-O/OOH species (Figure 4.5g, h). The Ni^{3+} and Fe^{3+} content increased after the long-term electrocatalysis test (Figure S4.15). *In situ* Raman was measured to study the dynamic surface chemistry of the Ni_3S_2-NiFe LDHs/NF-2 during the electrochemical process. As shown in Figure 4.5i, the as-prepared catalyst immersed in electrolyte possesses the characteristic Raman

bands of Ni_3S_2 at 302 and 350 cm^{-1}. The peaks at 465 and 540 cm^{-1} are attributed to Ni^{2+}-O

vibrations in $Ni(OH)_2$ phases. It is noted that the peaks for Ni_3S_2 and Ni^{2+}-O gradually disappeared

after 1.34 V, accompanied by the rise of peaks at 477 and 557 cm^{-1} corresponding to the $\delta(Ni^{3+}$-

O) and $\nu(Ni^{3+}$-O) bonds of NiOOH phases. [54, 55] This potential is the onset of Ni oxidation peak

area in the corresponding LSV curve. In this case, the presence of Ni_3S_2 in the surfaces also creates

additional active sites for electrocatalysis, where the dynamic surface reconstruction is induced by

S leaching. Similar phenomena have been reported that metal sulfide will be transformed to metal

(oxy)hydroxides after OER, the resultant M-OOH phase is believed to be the actual active species

for OER.[56] However, the characteristic XRD peaks of Ni_3S_2 can be still observed after the long-

term electrocatalysis (Figure S4.16), dedicating that the Ni_3S_2 phases are only partially converted

into NiOOH, which preserves the conductivity of catalysts. Therefore, the *in situ* formed NiOOH

resulting from $Ni(OH)_2$ and Ni_3S_2 guarantees enough active sites, and the remaining metallic Ni_3S_2

expedites the electron transport within electrocatalysts, ensuring the catalytic process. Benefiting

from this synergistic effect, the Ni_3S_2-NiFe LDHs/NF-2 electrocatalyst exhibits superior OER

performances.
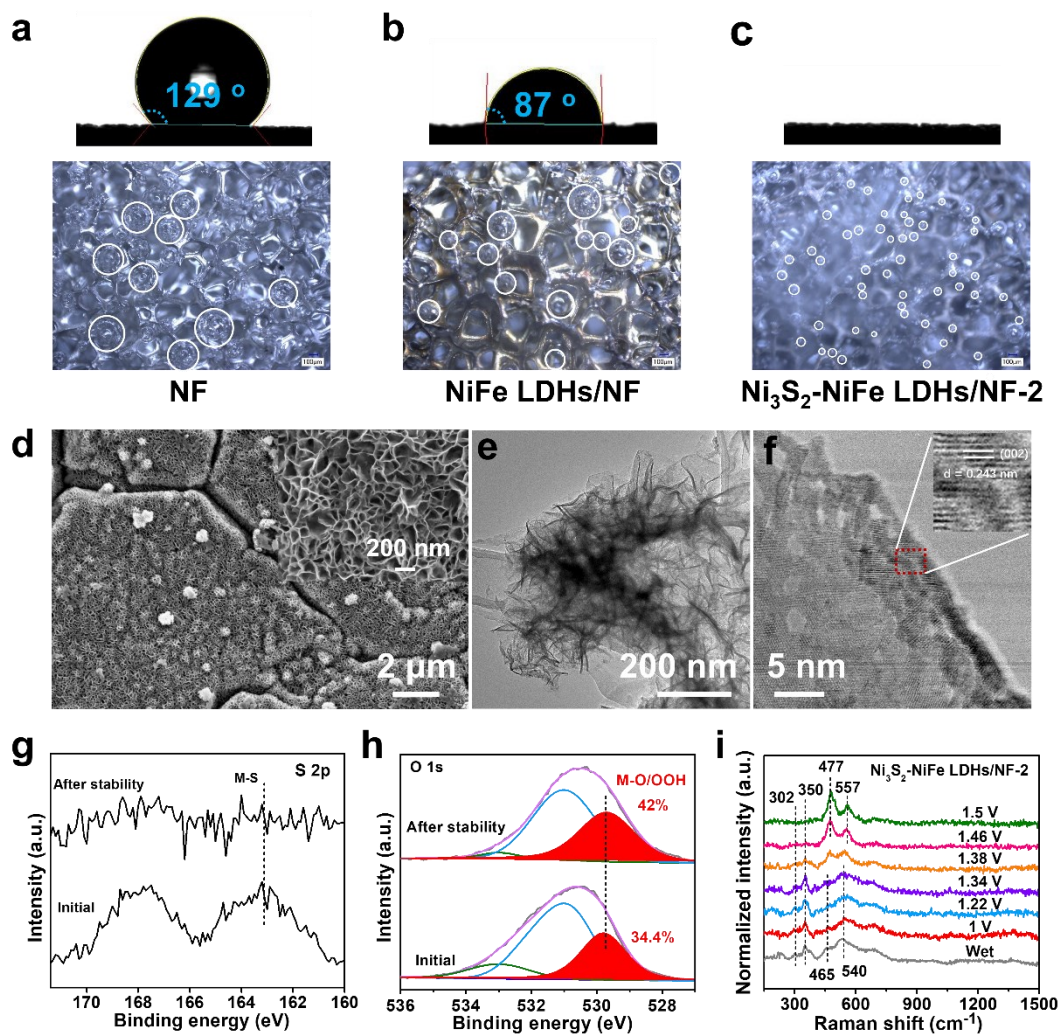
Figure 4. 5 (a-c) Surface wettability and bubble releasing behavior of the NF, NiFe LDHs/NF, and Ni₃S₂-NiFe LDHs/NF-2. (d) SEM image of Ni₃S₂-NiFe LDHs/NF-2 after electrocatalysis stability test. (e) TEM image of the products scratched from Ni₃S₂-NiFe LDHs/NF-2 after long-term stability test. (f) HR-TEM image of Ni₃S₂-NiFe LDHs/NF-2 after electrocatalysis stability test. (g) S 2p, (h) O 1s XPS spectra of the Ni₃S₂-NiFe LDHs/NF-2 electrode before reaction and after electrocatalysis stability test. (i) In situ Raman spectra of the Ni₃S₂-NiFe LDHs/NF-2 catalyst collected in the potential range 1 V–1.5 V.

4.3.4 Electrocatalytic HER and overall water splitting performances

The Ru-Ni$_3$S$_2$-NiFe LDHs/NF for HER electrocatalysis was prepared in a similar way to the preparation of Ni$_3$S$_2$-NiFe LDHs/NF-2 with the addition of RuCl$_3$. The SEM and TEM images reveal the thin-layered nanosheet structure (Figure S4.17, 4.18). The wide scanning XPS spectrum indicates the co-existence of Ni, Fe, Ru, O and S elements in the catalyst (Figure S4.20a). The high resolution spectra suggest the formation of Ru-Ni$_3$S$_2$-NiFe LDHs/NF (Figure S4.20b-f). The HER performance of the catalysts was also evaluated *via* LSV curves. The catalytic activity of as-prepared electrodes was benchmarked against Pt/C catalyst for comparison. As shown in Figure 4.6a, the Ru-Ni$_3$S$_2$-NiFe LDHs/NF electrode exhibited remarkably enhanced HER activity, which is superior to the benchmark of Pt/C, especially at high j_s. The Tafel slope of (96 mV dec^{-1}) Ru-Ni$_3$S$_2$-NiFe LDHs/NF is close to that of Pt/C catalyst (72 mV dec^{-1}) (Figure 4.6b), which is within the range of 39–116 mV/dec, indicating that the HER catalysis is governed by the charge-transfer-induced water dissociation process in alkaline electrolyte.[57] After Ru addition, the reduced Tafel slope of Ru- Ni$_3$S$_2$-NiFe LDH indicates superior HER kinetics, which is made more evident by EIS plots (Figure S4.24). The Ru- Ni$_3$S$_2$-NiFe LDHs/NF showed a much lower charge transfer resistance than that of Ni$_3$S$_2$-NiFe LDHs/NF, confirming a faster charge-transfer-induced water dissociation process in hydrogen evolution and thus a better HER kinetics on the Ru- Ni$_3$S$_2$-NiFe LDHs/NF. To deliver 10 mA cm^{-2}, the Ru-Ni$_3$S$_2$-NiFe LDHs/NF only requires an η of 61.3 mV which is comparable to previously reported HER catalysts (Table S4.4). More importantly, the Ru-Ni$_3$S$_2$-NiFe LDHs/NF electrode delivers j_s of 50 and 500 mA cm^{-2} at η_s as low as 127 and 253 mV, respectively, which is much lower than those of Pt/C (135, 400 mV), and Ni$_3$S$_2$-NiFe LDHs/NF-2 (314, 483 mV) (Figure 4.6c).

Given the superior catalytic performance of Ni_3S_2-NiFe LDHs/NF-2 and Ru-Ni_3S_2-NiFe LDHs/NF for OER and HER, respectively, the electrolyzer created by coupling a Ni_3S_2-NiFe LDHs/NF-2 anode and Ru-Ni_3S_2-NiFe LDHs/NF cathode shows a very low voltage of 1.47 V to deliver j of 10 mA cm^{-2} (Figure 4.6d), superior to the coupled state-of-the-art RuO_2 (+) || Pt/C (-) electrolyzer (1.55 V) and most existing catalysts (Table S4.5). In particular, Ni_3S_2-NiFe LDHs/NF-2 || Ru-Ni_3S_2-NiFe LDHs/NF can generate high j_s of 100 and 500 mA cm^{-2} at only 1.71 and 1.85 V, respectively, far surpassing current industrial requirements (deliver 200-400 mA cm^{-2} at 1.8-2.40 V). The bubble releasing was observed obviously when Ni_3S_2-NiFe LDHs/NF-2 || Ru-Ni_3S_2-NiFe LDHs/NF was working at 50 mA cm^{-2} (video 4.4). The Faradaic efficiency was determined to be 98% for both the HER and OER (Figure 4.6e), indicating a negligible side reaction during the electrolysis. Furthermore, the coupled cell also displays good electrochemical stability with only a 7 % decrease in activity after 210 h of continuous operation at 1.71 V (Figure 4.6f).
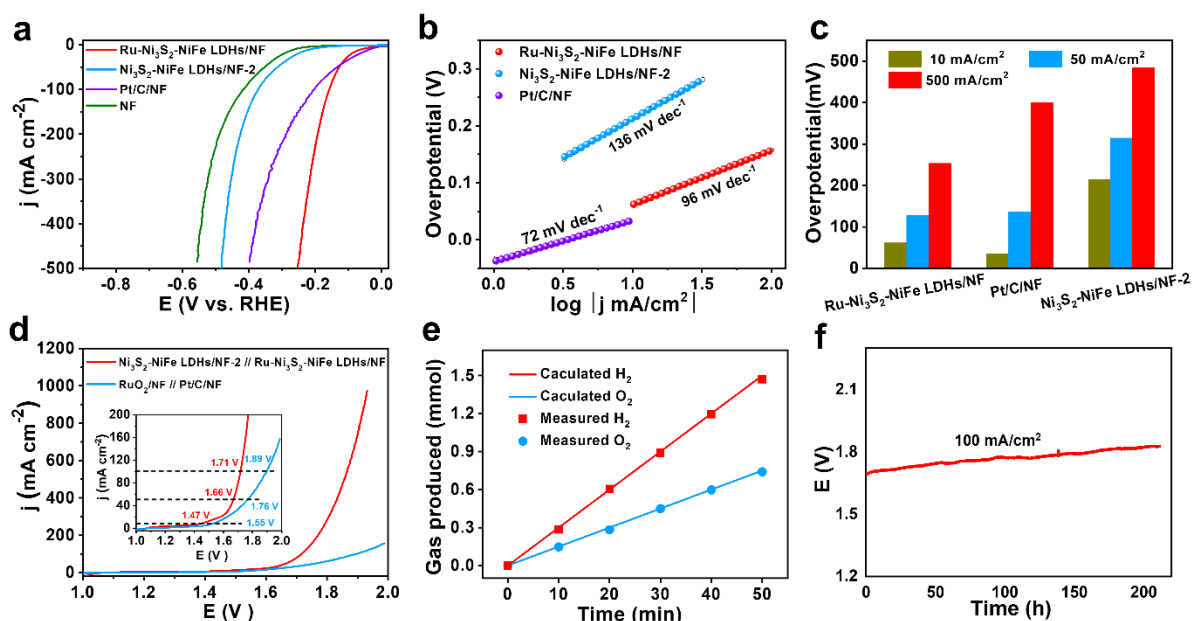
Figure 4. 6 (a) The polarization curves for HER recorded on Ru-Ni_3S_2-NiFe LDHs/NF, Ni_3S_2-NiFe LDHs/NF-2, Pt/C/NF and NF. (b) The corresponding Tafel plots. (c) The overpotential histogram

for Ru-Ni$_3$S$_2$-NiFe LDHs/NF at 10, 50, and 500 mA cm^{-2}. (d) The overall water splitting performance of coupled Ni$_3$S$_2$-NiFe LDHs/NF-2 ‖ Ru-Ni$_3$S$_2$-NiFe LDHs/NF and RuO$_2$ ‖ Pt/C electrolyzers. (e) Comparison of experimental and theoretical amounts of generated H$_2$ and O$_2$ over 50 min by Ni$_3$S$_2$-NiFe LDHs/NF-2 ‖ Ru-Ni$_3$S$_2$-NiFe LDHs/NF electrolyzer. (f) Chronopotentiometric curve of Ni$_3$S$_2$-NiFe LDHs/NF-2 ‖ Ru-Ni$_3$S$_2$-NiFe LDHs/NF electrolyzer at 100 mA cm^{-2} in 1 M KOH.

4.4 Conclusions

To achieve high-current-density oxygen evolution electrocatalysis at low overpotentials, the catalytic components should meet multiple criteria simultaneously: 1) high intrinsic catalytic activity with more exposure of active sites; 2) enhanced charge and mass transferability; 3) highly robust contact with the electrode; 4) efficient bubble release, especially under high current densities and vigorous gas evolution conditions. C_{dl} and EIS indicated a larger ECSA and low charge-transfer resistance of Ni$_3$S$_2$-NiFe LDHs/NF-2. UPS revealed the better electron transferability of Ni$_3$S$_2$-NiFe LDHs/NF-2, which benefits the charge transport between the catalyst surface and reactant intermediates and thus facilitates electrocatalysis. Herein, Ni$_3$S$_2$-embedded NiFe LDH heterostructured nanosheets with a porous structure supported on NF synthesized at room temperature in 15 min *via* a one-pot solution method, which offers abundant interface, intrinsic large surface area, high activity, efficient mass transport and fast electron transport in the electrode. More importantly, NiOOH was *in situ* formed under the electrooxidation environment by partially sacrificing Ni$_3$S$_2$, where newly formed NiOOH is equally important with remaining Ni$_3$S$_2$ to drive proficient catalysis. In 1.0 M KOH, it exhibits prominent electrochemical durability for 240 h to deliver 100 mA cm^{-2} with an overpotential of only 240 mV required. This strategy can be extended to design the Ru-Ni$_3$S$_2$-NiFe LDHs/NF catalyst for a highly efficient HER

electrocatalysis. This work provides a cost-effective and industrially compatible method to prepare water splitting catalysts, without any sophisticated process and equipment. To demonstrate the practical application, the resulting Ni_3S_2-NiFe LDHs/NF-2 and Ru-Ni_3S_2-NiFe LDHs/NF were coupled as an electrolyzer for overall water splitting and achieved a commercial-level current density of 500 mA cm^{-2} at a low voltage of 1.85 V.

4.5 References

1. J. Song, C. Wei, Z.-F. Huang, C. Liu, L. Zeng, X. Wang, Z. J. Xu, A review on fundamentals for designing oxygen evolution electrocatalysts, *Chem. Soc. Rev*. 49 (7) (2020) 2196.

2. P. Lianos, Review of recent trends in photoelectrocatalytic conversion of solar energy to electricity and hydrogen, *Appl. Catal. B* 210 (2017) 235-254.

3. H. Xu, B. Fei, G. Cai, Y. Ha, J. Liu, H. Jia, J. Zhang, M. Liu, R. Wu, Boronization-induced ultrathin 2D nanosheets with abundant crystalline–amorphous phase boundary supported on nickel foam toward efficient water splitting, *Adv. Energy Mater.* 10 (3) (2020), 1902714.

4. J. Duan, S. Chen, C. Zhao, Ultrathin metal-organic framework array for efficient electrocatalytic water splitting, *Nat. Commun.* 8 (1) (2017) 1-7.

5. Q. Chen, Z. Usman, T. Cao, S. Rafai, Z. Wang, Y. Zhu, C. Cao, J. Zhang, High-valence Ni and Fe sites on sulfated NiFe-LDH nanosheets to enhance OO coupling for water oxidation, *Chem. Eng. J.* 426 (2021) 130873.

6. V. Nicolosi, M. Chhowalla, M.G. Kanatzidis, M.S. Strano, J.N. Coleman, Liquid exfoliation of layered materials, *Science*, 340 (6139) (2013) 1226419.

7. H. Sun, W. Zhang, J.-G. Li, Z. Li, X. Ao, K.-H. Xue, K.K. Ostrikov, J. Tang, C. Wang, Rh-engineered ultrathin NiFe-LDH nanosheets enable highly-efficient overall water splitting and urea electrolysis, *Appl. Catal. B* 284 (2021) 119740.

8. F. Song, X. Hu, Exfoliation of layered double hydroxides for enhanced oxygen evolution catalysis, *Nat. Commun.* 5 (1) (2014) 1-9.

9. B. Wang, X. Han, C. Guo, J. Jing, C. Yang, Y. Li, A. Han, D. Wang, J. Liu, Structure inheritance strategy from MOF to edge-enriched NiFe-LDH array for enhanced oxygen evolution reaction, *Appl. Catal. B* 298 (2021) 120580.

10. X. Lu, C. Zhao, Electrodeposition of hierarchically structured three-dimensional nickel-iron electrodes for efficient oxygen evolution at high current densities, *Nat. Commun.* 6 (1) (2015) 1-7.

11. P.F. Liu, X. Li, S. Yang, M.Y. Zu, P. Liu, B. Zhang, L.R. Zheng, H. Zhao, H.G. Yang, Ni_2P (O)/Fe_2P (O) interface can boost oxygen evolution electrocatalysis, *ACS Energy Lett.* 2 (10) (2017) 2257-2263.

12. M. Li, X. Pan, M. Jiang, Y. Zhang, Y. Tang, G. Fu, Interface engineering of oxygen-vacancy-rich CoP/CeO_2 heterostructure boosts oxygen evolution reaction, *Chem. Eng. J.* 395 (2020): 125160.

13. J.W. Huang, K. Li, L. Wang, H. She, Q.Z. Wang, In situ conversion builds MIL-101@ NiFe-LDH heterojunction structures to enhance the oxygen evolution reaction, *Chin. Chem. Lett.* (2021).

14. S. Niu, W.J. Jiang, T. Tang, L.P. Yuan, H. Luo, J.S. Hu, Autogenous growth of hierarchical NiFe $(OH)_x$/FeS nanosheet-on-microsheet arrays for synergistically enhanced high-output water oxidation, *Adv. Funct. Mater.* 29 (36) (2019) 1902180.

15. C. Liang, P. Zou, A. Nairan, Y. Zhang, J. Liu, K. Liu, S. Hu, F. Kang, H.J. Fan, C. Yang, Exceptional performance of hierarchical Ni–Fe oxyhydroxide@ NiFe alloy nanowire array electrocatalysts for large current density water splitting, *Energy Environ. Sci.* 13 (1) (2020)

86-95.

16. L. Dai, Z.N. Chen, L. Li, P. Yin, Z. Liu, H. Zhang, Ultrathin Ni (0)-Embedded Ni (OH)$_2$ Heterostructured Nanosheets with Enhanced Electrochemical Overall Water Splitting, *Adv. Mater.* 32 (8) (2020) 1906915.

17. L.-L. Feng, G. Yu, Y. Wu, G.-D. Li, H. Li, Y. Sun, T. Asefa, W. Chen, X. Zou, High-index faceted Ni$_3$S$_2$ nanosheet arrays as highly active and ultrastable electrocatalysts for water splitting, *J. Am. Chem. Soc.* 137 (14) (2015) 14023-14026.

18. L. Chen, Y. Wang, X. Zhao, Y. Wang, Q. Li, Q. Wang, Y. Tang, Y. Lei, Trimetallic oxyhydroxides as active sites for large-current-density alkaline oxygen evolution and overall water splitting, *J. Mater. Sci. Technol.* 110 (2022): 128-135.

19. M. Carmo, D.L. Fritz, J. Mergel, D. Stolten, A comprehensive review on PEM water electrolysis, *Int. J. Hydrog. Energy.* 38 (12) (2013) 4901-4934.

20. D. Wei, K. Osseo-Asare, Aqueous synthesis of finely divided pyrite particles, *Colloids Surf. A: Physicochem. Eng. Asp.* 121 (1) (1997) 27-36.

21. F. Yu, H. Zhou, Y. Huang, J. Sun, F. Qin, J. Bao, W.A. Goddard, S. Chen, Z. Ren, High-performance bifunctional porous non-noble metal phosphide catalyst for overall water splitting, *Nat. Commun.* 9 (1) (2018) 1-9.

22. X. Peng, L. Zhang, Z. Chen, L. Zhong, D. Zhao, X. Chi, X. Zhao, L. Li, X. Lu, K. Leng, Hierarchically porous carbon plates derived from wood as bifunctional ORR/OER electrodes, *Adv. Mater.* 31 (16) (2019) 1900341.

23. H. Zhang, X. Li, A. Hähnel, V. Naumann, C. Lin, S. Azimi, S.L. Schweizer, A.W. Maijenburg, R.B. Wehrspohn, Bifunctional heterostructure assembly of NiFe LDH nanosheets on NiCoP nanowires for highly efficient and stable overall water splitting, *Adv.*

Funct. Mater. 28 (14) (2018) 1706847.

24. H. Liang, A.N. Gandi, C. Xia, M.N. Hedhili, D.H. Anjum, U. Schwingenschlögl, H.N. Alshareef, Amorphous NiFe-OH/NiFeP electrocatalyst fabricated at low temperature for water oxidation applications, *ACS Energy Lett.* 2 (5) (2017) 1035-1042.

25. S. Cao, H. Huang, K. Shi, L. Wei, N. You, X. Fan, Z. Yang, W. Zhang, Engineering superhydrophilic/superaerophobic hierarchical structures of Co-CH@ NiFe-LDH/NF to boost the oxygen evolution reaction, *Chem. Eng. J.* 422 (2021) 130123.

26. X. Meng, J. Han, L. Lu, G. Qiu, Z.L. Wang, C. Sun, Fe^{2+}-doped layered double (Ni, Fe) hydroxides as efficient electrocatalysts for water splitting and self-powered electrochemical systems, *Small* 15 (41) (2019) 1902551.

27. J.-X. Feng, J.-Q. Wu, Y.-X. Tong, G.-R. Li, Efficient hydrogen evolution on Cu nanodots-decorated Ni_3S_2 nanotubes by optimizing atomic hydrogen adsorption and desorption, *J. Am. Chem. Soc.* 140 (2) (2018) 610-617.

28. X. Meng, J. Han, L. Lu, G. Qiu, Z. Wang, C. Sun, Fe^{2+}-doped layered double (Ni, Fe) hydroxides as efficient electrocatalysts for water splitting and self-powered electrochemical systems." *Small*, 15 (41) (2019) 1902551.

29. C. Sun, T. Wang, C. Sun, F. Li, Layered double (Ni, Fe) hydroxide grown on nickel foam and modified by nickel carbonyl powder and carbon black as an efficient electrode for water splitting, *Int. J. Hydrog. Energy*, (2021).

30. X. Lu, K. Ye, S. Zhang, J. Zhang, J. Yang, Y. Huang, H. Ji. "Amorphous type FeOOH modified defective BiVO4 photoanodes for photoelectrochemical water oxidation." *Chem. Eng. J.* 428 (2022) 131027.

31. W.D. Chemelewski, H.-C. Lee, J.-F. Lin, A.J. Bard, C.B. Mullins, Amorphous FeOOH

oxygen evolution reaction catalyst for photoelectrochemical water splitting, *J. Am. Chem. Soc.* 136 (7) (2014) 2843-2850.

32. C. Liu, Y. Han, L. Yao, L. Liang, J. He, Q. Hao, J. Zhang, Y. Li, H. Liu, Engineering Bimetallic NiFe-Based Hydroxides/Selenides Heterostructure Nanosheet Arrays for Highly-Efficient Oxygen Evolution Reaction, *Small* 17 (7) (2021) 2007334.

33. Q. Xu, H. Jiang, X. Duan, Z. Jiang, Y. Hu, S.W. Boettcher, W. Zhang, S. Guo, C. Li, Fluorination-enabled Reconstruction of NiFe Electrocatalysts for Efficient Water Oxidation, *Nano Lett.* 21(1) (2020) 492-499.

34. S. Huang, Y. Meng, Y. Cao, F. Yao, Z. He, X. Wang, H. Pan, M. Wu, Amorphous $NiWO_4$ nanoparticles boosting the alkaline hydrogen evolution performance of Ni_3S_2 electrocatalysts, *Appl. Catal. B* 274 (2020) 119120.

35. N. McIntyre, M. Cook, X-ray photoelectron studies on some oxides and hydroxides of cobalt, nickel, and copper, *Anal. Chem.* 47 (13) (1975) 2208-2213.

36. X. Feng, Q. Jiao, W. Chen, Y. Dang, Z. Dai, S.L. Suib, J. Zhang, Y. Zhao, H. Li, C. Feng, Cactus-like $NiCo_2S_4@$ NiFe LDH hollow spheres as an effective oxygen bifunctional electrocatalyst in alkaline solution, *Appl. Catal. B* 286 (2021) 119869.

37. J. Huang, J. Han, R. Wang, Y. Zhang, X. Wang, X. Zhang, Z. Zhang, Y. Zhang, B. Song, S. Jin, Improving Electrocatalysts for Oxygen Evolution Using $Ni_x Fe_{3-x} O_4$/Ni Hybrid Nanostructures Formed by Solvothermal Synthesis, *ACS Energy Lett.* 3(7) (2018) 1698-1707.

38. Z. Cai, D. Zhou, M. Wang, S.M. Bak, Y. Wu, Z. Wu, Y. Tian, X. Xiong, Y. Li, W. Liu, Introducing Fe^{2+} into nickel-iron layered double hydroxide: local structure modulated water oxidation activity, *Angew. Chem., Int. Edit.* 130 (2018) 9536-9540.

39. J. Zhou, L. Yu, Q. Zhu, C. Huang, Y. Yu, Defective and ultrathin NiFe LDH nanosheets decorated on V-doped Ni_3S_2 nanorod arrays: a 3D core-shell electrocatalyst for efficient water oxidation, *J. Mater. Chem.* 7 (2019) 18118-18125.

40. C. Huang, L. Yu, W. Zhang, Q. Xiao, J. Zhou, Y. Zhang, P. An, J. Zhang, Y. Yu, "N-doped Ni-Mo based sulfides for high-efficiency and stable hydrogen evolution reaction." *Appl. Catal. B* 276 (2020): 119137.

41. O. Qi, S. Cheng, C Yang, Z. Lei, Vertically grown pn heterojunction FeCoNi LDH/CuO arrays with modulated interfacial charges to facilitate electrocatalytic oxygen evolution reaction, *J. Mater. Chem. A* (2022).

42. Y. Duan, Z.Y. Yu, S.J. Hu, X.S. Zheng, C.T. Zhang, H.H. Ding, B.C. Hu, Q.Q. Fu, Z.L. Yu, X. Zheng, Scaled-up synthesis of amorphous NiFeMo oxides and their rapid surface reconstruction for superior oxygen evolution catalysis, *Angew. Chem., Int. Edit*. 131 (2019) 15919-15924.

43. Y. Tang, Q. Liu, L. Dong, H.B. Wu, X.-Y. Yu, Activating the hydrogen evolution and overall water splitting performance of NiFe LDH by cation doping and plasma reduction, *Appl. Catal. B* 266 (2020) 118627.

44. C. Dong, T. Kou, H. Gao, Z. Peng, Z. Zhang, Eutectic-derived mesoporous Ni-Fe-O nanowire network catalyzing oxygen evolution and overall water splitting, *Adv. Energy Mater.* 8 (5) (2018) 1701347.

45. N. Gultom, H. Abdullah, C. Hsu, D. -HKuo, Activating nickel iron layer double hydroxide for alkaline hydrogen evolution reaction and overall water splitting by electrodepositing nickel hydroxide, *Chem. Eng. J.* 419 (2021) 129608.

46. Peng, Y., Y. Zhang, A. Guo, M. Mao, Y. Wang, Y. Long, G. Fan, Universal low-temperature

oxidative thermal redispersion strategy for green and sustainable fabrication of oxygen-rich carbons anchored metal nanoparticles for hydrogen evolution reactions, *Chem. Eng. J.* (2021)133648.

47. G. Zhang, Y.-S. Feng, W.-T. Lu, D. He, C.-Y. Wang, Y.-K. Li, X.-Y. Wang, F.-F. Cao, Enhanced catalysis of electrochemical overall water splitting in alkaline media by Fe doping in Ni_3S_2 nanosheet arrays, *ACS Catal.* 8 (6) (2018) 5431-5441.

48. Q. Xu, M. Chu, M. Liu, J. Zhang, H. Jiang, C. Li, Fluorine-triggered surface reconstruction of Ni3S2 electrocatalysts towards enhanced water oxidation, *Chem. Eng. J.* 411 (2021) 128488.

49. S. Liu, X.F. Lu, J. Xiao, X. Wang, X.W. Lou, Bi_2O_3 nanosheets grown on multi-channel carbon matrix to catalyze efficient CO_2 electroreduction to HCOOH, *Angew. Chem., Int. Edit.* 58 (2019) 13828-13833.

50. Y. Guo, T. Wang, Q. Yang, X. Li, H. Li, Y. Wang, T. Jiao, Z. Huang, B. Dong, W. Zhang, Highly Efficient Electrochemical Reduction of Nitrogen to Ammonia on Surface Termination Modified Ti_3C_2T x MXene Nanosheets, *ACS nano*. 14 (7) (2020) 9089-9097.

51. S.-Q Liu, M.-G Gao, R.-F Feng, L. Gong, H. Zeng, J.-L Luo. "Electronic delocalization of bismuth oxide induced by sulfur doping for efficient CO2 electroreduction to formate." *ACS Catal.* 11(12) (2021): 7604-7612.

52. K. Dastafkan, Q. Meyer, X. Chen, C. Zhao, Efficient oxygen evolution and gas bubble release achieved by a low gas bubble adhesive iron-nickel vanadate electrocatalyst, *Small* 16 (32) (2020) 2002412.

53. X. Shan, J. Liu, H. Mu, Y. Xiao, B. Mei, W. Liu, G. Lin, Z. Jiang, L. Wen, L. Jiang, An engineered superhydrophilic/superaerophobic electrocatalyst composed of the supported

CoMoS$_x$ chalcogel for overall water splitting, *Angew. Chem., Int. Edit.* 59 (4) (2020) 1659-1665.

54. B.S. Yeo, A.T. Bell, In situ Raman study of nickel oxide and gold-supported nickel oxide catalysts for the electrochemical evolution of oxygen, *J. Phys. Chem. C.* 116 (15) (2012) 8394-8400.

55. D. Friebel, M.W. Louie, M. Bajdich, K.E. Sanwald, Y. Cai, A.M. Wise, M.-J. Cheng, D. Sokaras, T.-C. Weng, R. Alonso-Mori, Identification of highly active Fe sites in (Ni, Fe) OOH for electrocatalytic water splitting, *J. Am. Chem. Soc.* 137 (3) (2015) 1305-1313.

56. L. Trotochaud, S.L. Young, J.K. Ranney, S.W. Boettcher, Nickel–iron oxyhydroxide oxygen-evolution electrocatalysts: the role of intentional and incidental iron incorporation, *J. Am. Chem. Soc.* 136 (18) (2014) 6744-6753.

57. J. H, C. Zhang, L. Jiang, H. Lin, Y. An, D. Zhou, M. Leung, and S. Yang. "Nanohybridization of MoS2 with layered double hydroxides efficiently synergizes the hydrogen evolution in alkaline media." *Joule* (2) (2017) 383-393.

4.6 Supporting Information
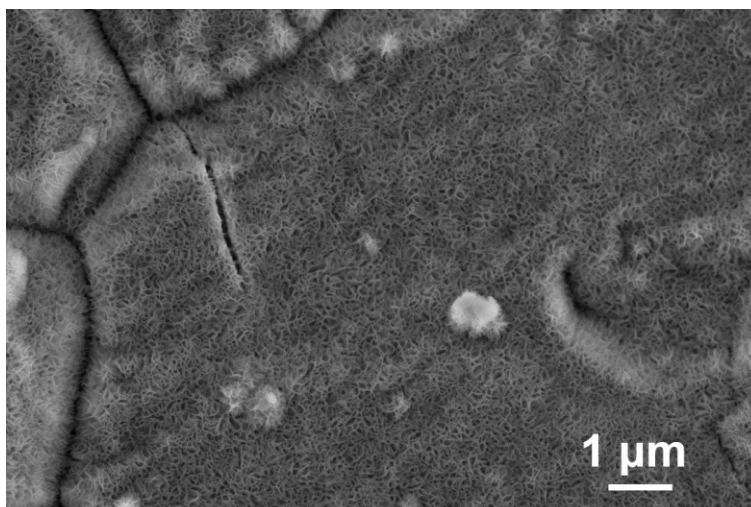
Figure S4. 1 The corresponding SEM image of Ni_3S_2-NiFe LDHs/NF-2 with 20x20 cm^2 area (Figure 4.2b).
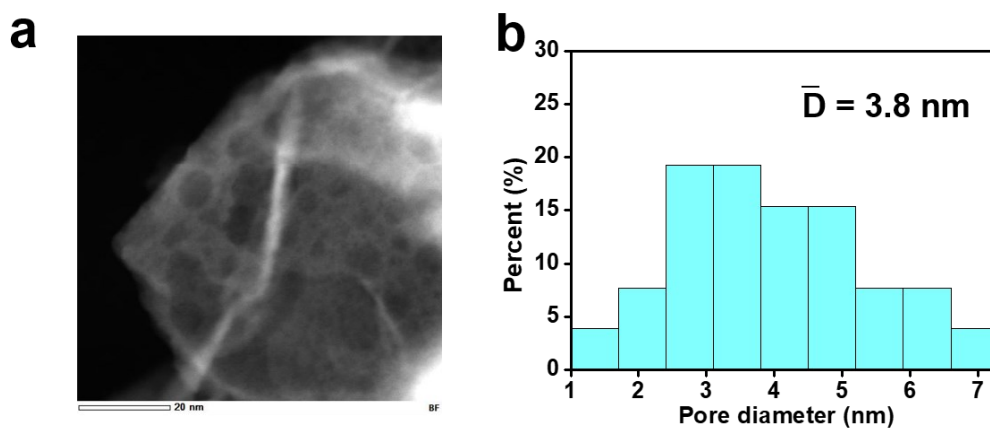
Figure S4. 2 (a) STEM image of Ni_3S_2-NiFe LDHs/NF-2. (b) The corresponding diameter histogram for pores.
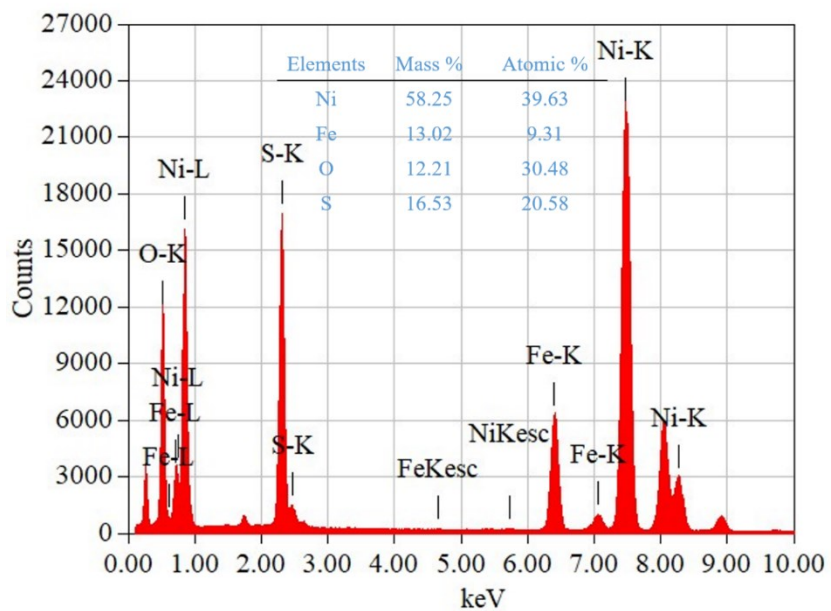
Figure S4. 3 STEM-EDS spectrum of the corresponding region in Figure S4.2.
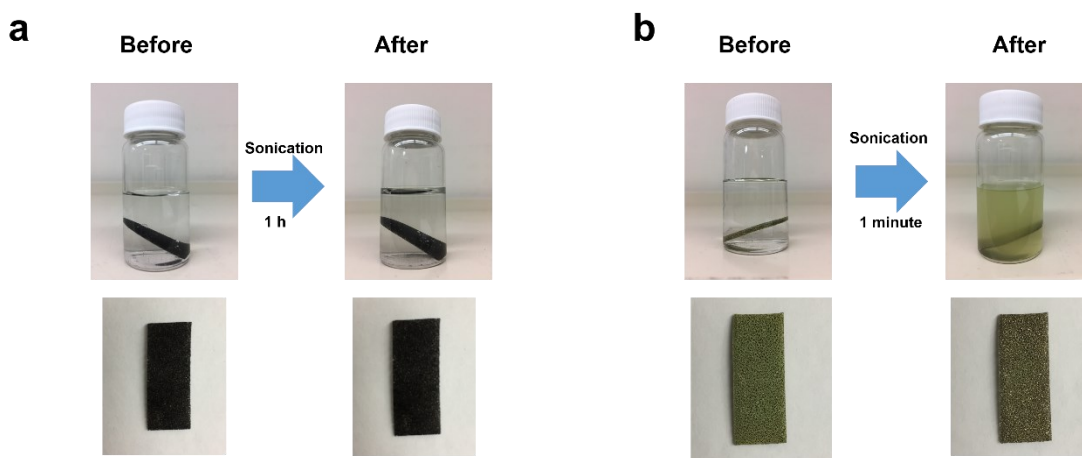
Figure S4. 4 The change of samples sonicated in water. (a) Ni_3S_2-NiFe LDHs/NF-2, (b) NiFe LDHs/NF prepared by the commonly used hydrothermal method.

Table S4. 1 Fe and S content determined by ICP-OES

Samples	Fe content (ppm)	S content (ppm)
Ni$_3$S$_2$-NiFe LDHs/NF-1	5.8	12.6
Ni$_3$S$_2$-NiFe LDHs/NF-2	17.1	22.4
Ni$_3$S$_2$-NiFe LDHs/NF-3	9.8	13.2
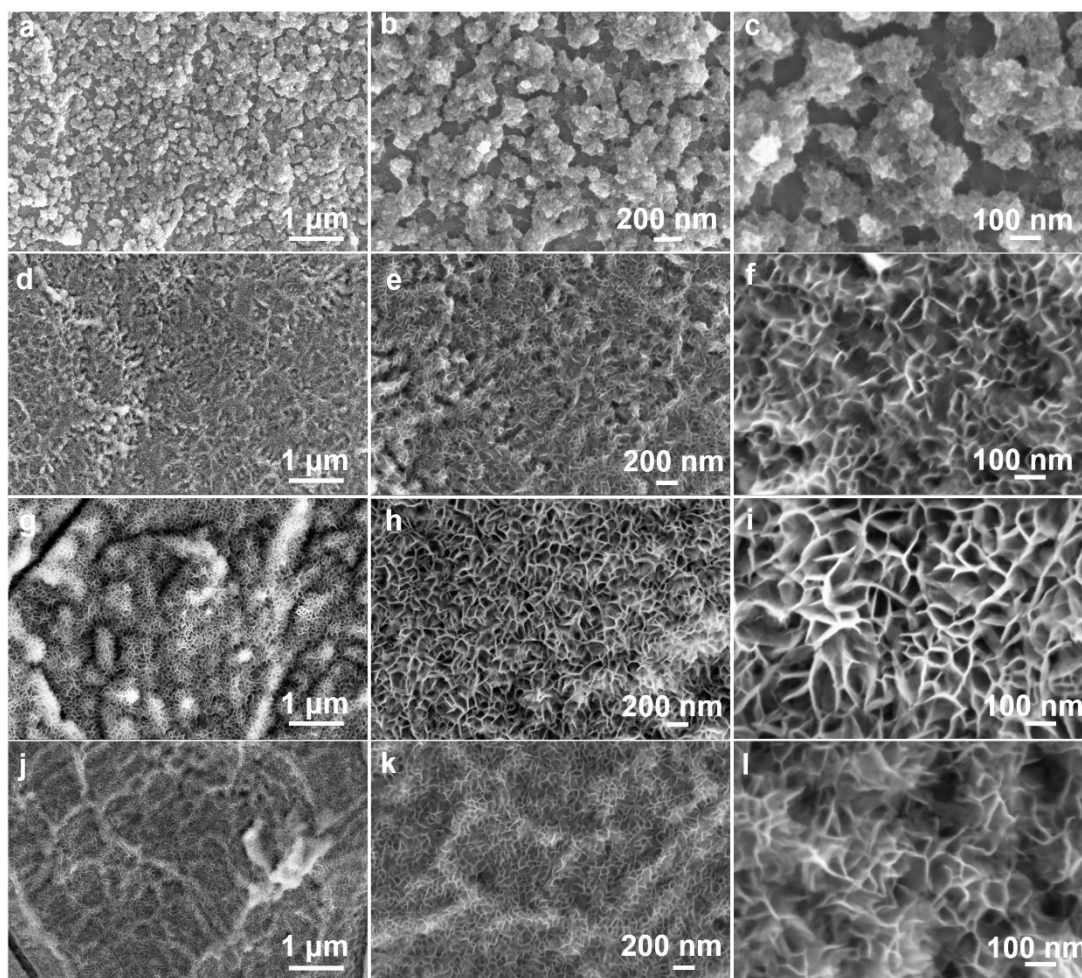
Figure S4. 5 SEM images of (a-c) NiFe LDHs/NF, (d-f) Ni_3S_2-NiFe LDHs/NF-1, (g-i) Ni_3S_2-NiFe LDHs/NF-2, (j-l) Ni_3S_2-NiFe LDHs/NF-3.
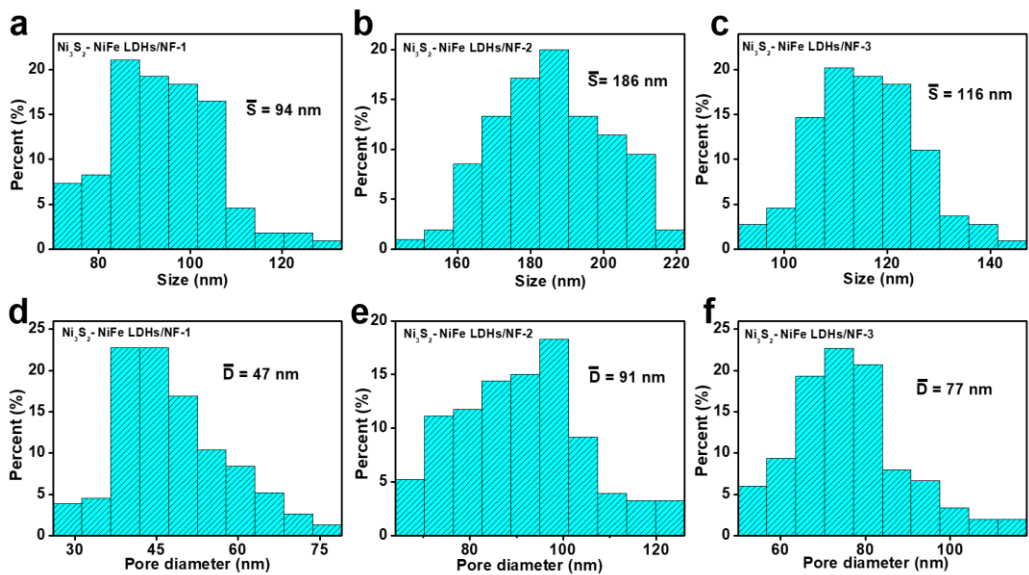
Figure S4. 6 Nanosheet size (a-c) and pore diameter (d-f) distribution histograms of Ni_3S_2-NiFe LDHs/NF-1, Ni_3S_2-NiFe LDHs/NF-2, Ni_3S_2-NiFe LDHs/NF-3.
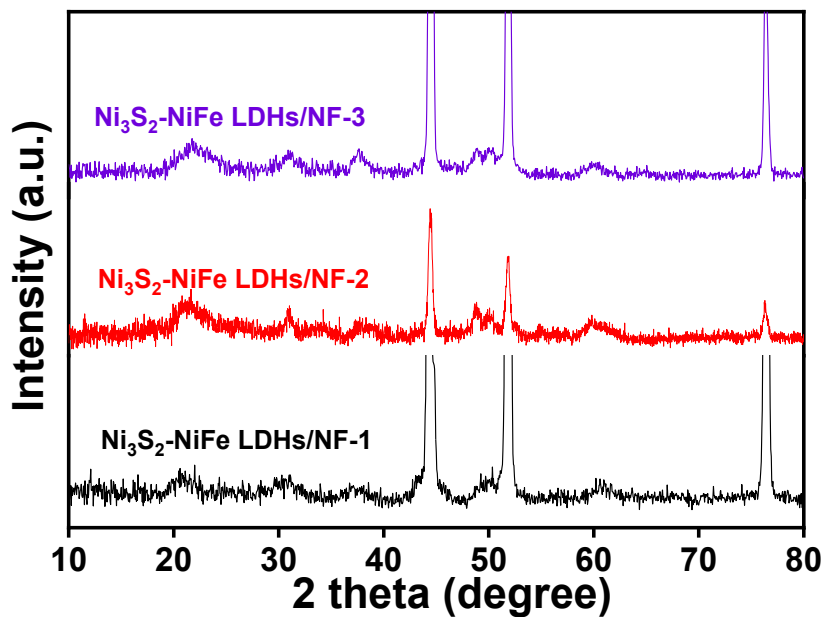
Figure S4. 7 XRD patterns of Ni_3S_2-NiFe LDHs/NF-1, Ni_3S_2-NiFe LDHs/NF-2 and Ni_3S_2-NiFe LDHs/NF-3.
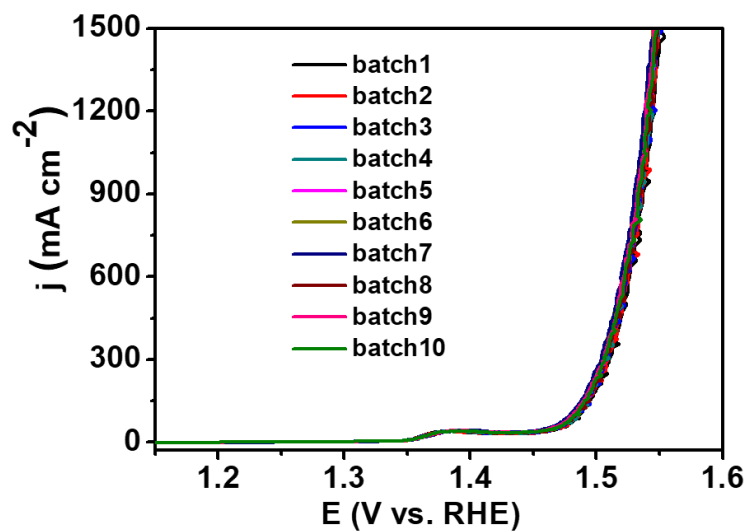
Figure S4. 8 The OER polarization curves for ten batches of Ni_3S_2-NiFe LDHs/NF-2.
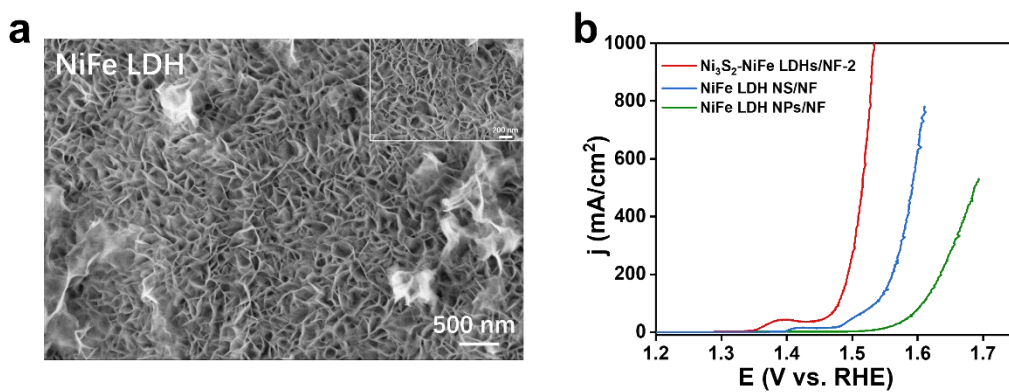
Figure S4. 9 (a) SEM images of NiFe LDH NS/NF. (b) The LSV curves for OER recorded on Ni3S2-NiFe LDHs/NF-2, NiFe LDH NS/NF and NiFe LDH NPs/NF.

In our work, the NiFe LDH synthesized at room temperature in 15 min was in nanoparticle (NP) form and not fully wrapped Ni foam (Figure S4.5a-c), which could arise from the hydrolysis of metal ions in the solution with dissolved oxygen. (Small 15.41 (2019): 1902551.) For comparison, as shown in Figure S4.9a, we prepared NiFe LDH nanosheets grown on Ni foam (NiFe LDH NS/NF) via a hydrothermal method in alkaline condition. (Applied Catalysis B: Environmental 284 (2021): 119740.) The OER performance of NiFe LDH NS/NF is higher than our NiFe LDH NPs/NF, but lower than Ni_3S_2-NiFe LDHs/NF (Figure S4.9b).
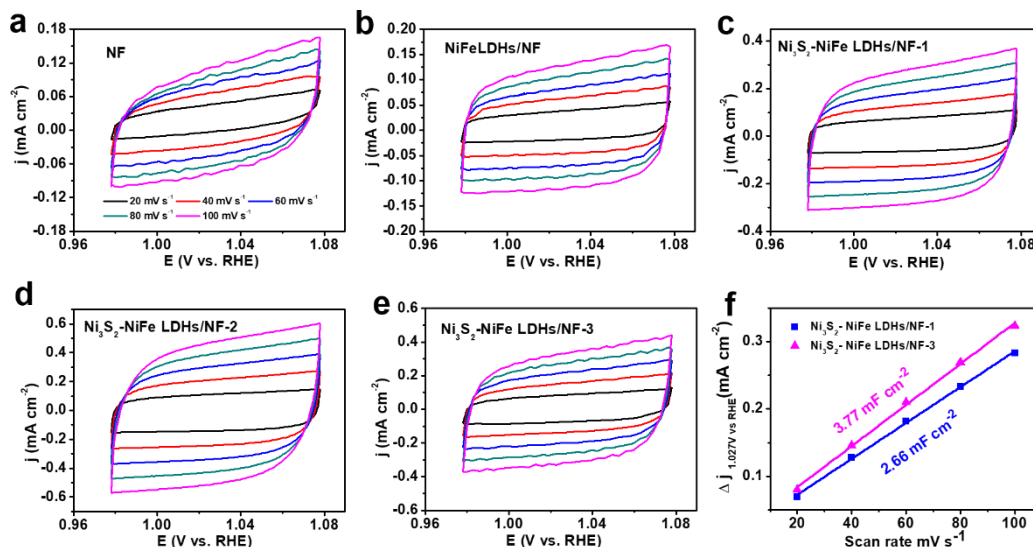
Figure S4. 10 CV curves within a non-faradaic reaction region of 0.97 ~ 1.07 V versus RHE at different scan rates for (a) NF, (b) NiFe LDHs/NF, (c) Ni_3S_2-NiFe LDHs/NF-1, (d) Ni_3S_2-NiFe LDHs/NF-2, (e) Ni_3S_2-NiFe LDHs/NF-3. (f) C_{dl} values of Ni_3S_2-NiFe LDHs/NF-1 and Ni_3S_2-NiFe LDHs/NF-3.
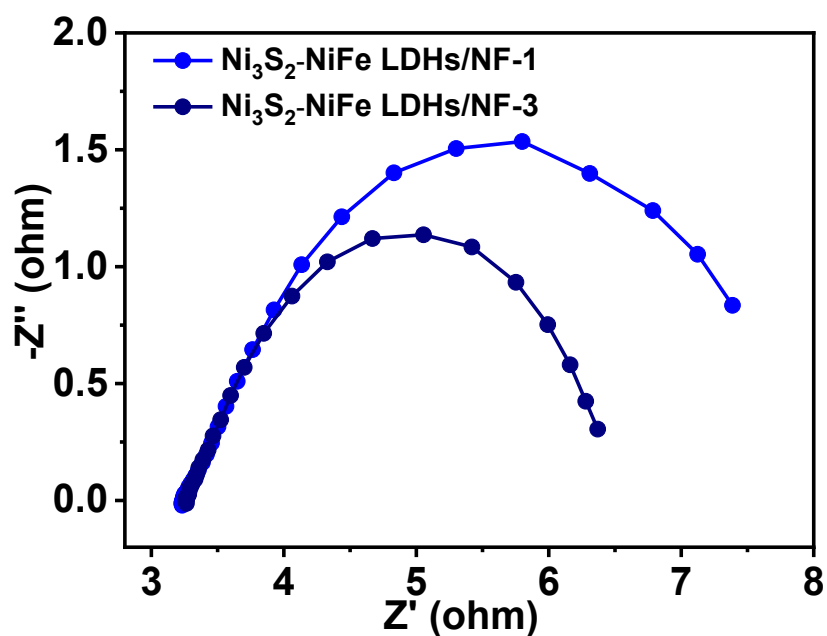
Figure S4. 11 EIS spectra of Ni₃S₂-NiFe LDHs/NF-1 and Ni₃S₂-NiFe LDHs/NF-3 toward OER.

Table S4. 2 The electrochemical impedance spectra of various catalysts fitted to equivalent electrochemical circuits.

Samples	R_{ct}	Error (%)
NF	73.36	6.266
NiFe LDHs/NF	6.244	2.578
Ni₃S₂-NiFe LDHs/NF-1	4.611	4.286
Ni₃S₂-NiFe LDHs/NF-2	1.568	2.878
Ni₃S₂-NiFe LDHs/NF-3	2.943	2.864

The electrochemical active surface area is calculated from the following formula:

$$A_{ECSA} = \frac{\text{specfic capacitance}}{40 \text{ uF } cm^{-2} \text{ per } cm^2_{ECSA}}$$

We used the double-layer capacitances (C_{dl}) to estimate the ECSAs and further normalized the geometric current density to the corresponding ECSA (Figure S4.12). When normalized to the ECSA (Figure S4.10c), the Ni$_3$S$_2$-NiFe LDHs/NF-2 still displays higher current density than other investigated samples, indicating the Ni$_3$S$_2$-NiFe LDHs/NF-2 has intrinsic high activity.
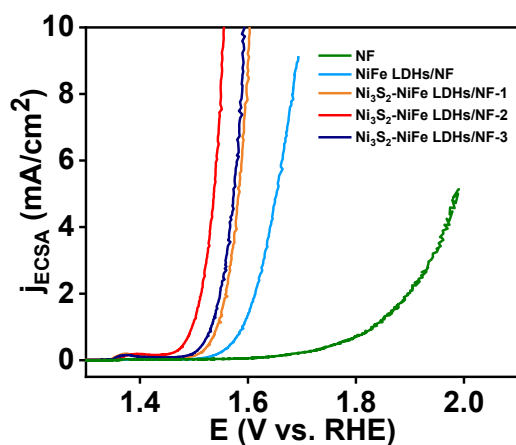
Figure S4. 12 (c) Normalized Polarization curves of investigated samples.
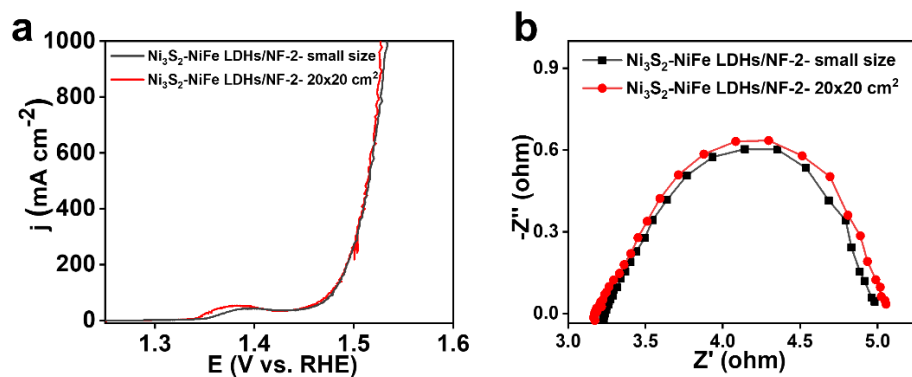
Figure S4. 13 (a) The LSV curves and (b) EIS plots for Ni$_3$S$_2$-NiFe LDHs/NF-2 in 1x2.5 cm^2 and 20x20 cm^2.
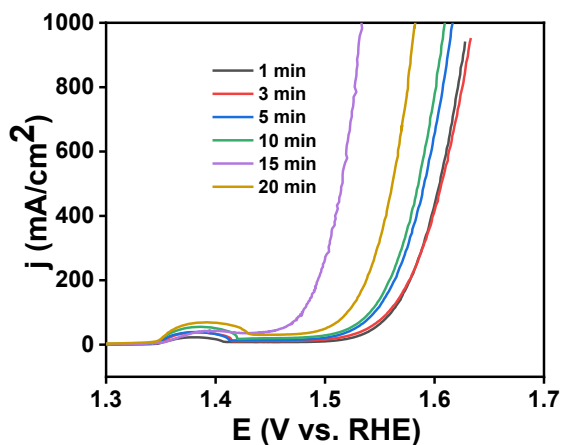
Figure S4. 14 LSV curves for OER performance on Ni$_3$S$_2$-NiFe LDHs/NF in different reaction time.

The effect of the reaction time on the catalytic performance was studied. The Ni$_3$S$_2$-NiFe LDHs/NF samples were synthesized in 10 mL 0.1 M Fe(NO$_3$)$_3$·9H$_2$O solution containing 14.5 mM NaHS at

room temperature in 1, 3, 5, 10, 15 and 20 min. Oxygen evolution performance of the samples was evaluated via LSV polarization (Figure S4.14). The Ni_3S_2-NiFe LDHs/NF-15min shows a best OER performance.
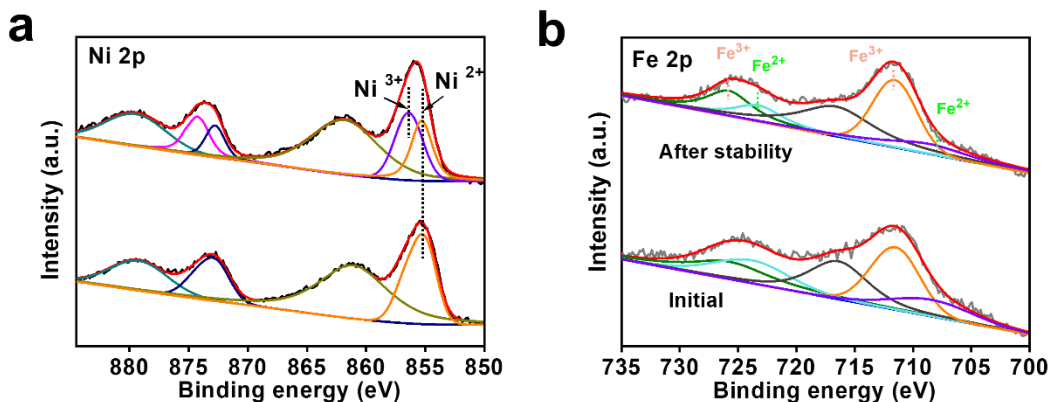
Figure S4. 15 The High-resolution (a) Ni 2p and (b) Fe 2p XPS of Ni_3S_2-NiFe LDHs/NF-2 before reaction and after electrocatalysis stability test.
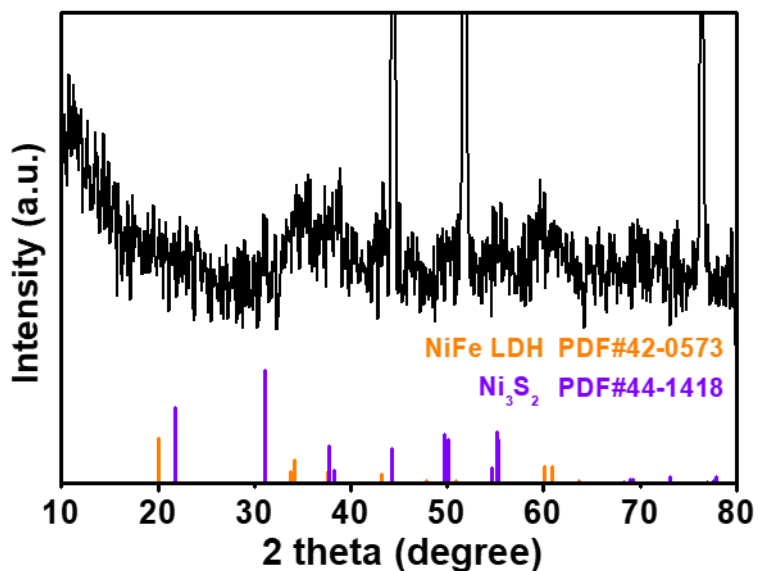
Figure S4. 16 The XRD of Ni_3S_2-NiFe LDHs/NF-2 after long-term electrocatalysis test.
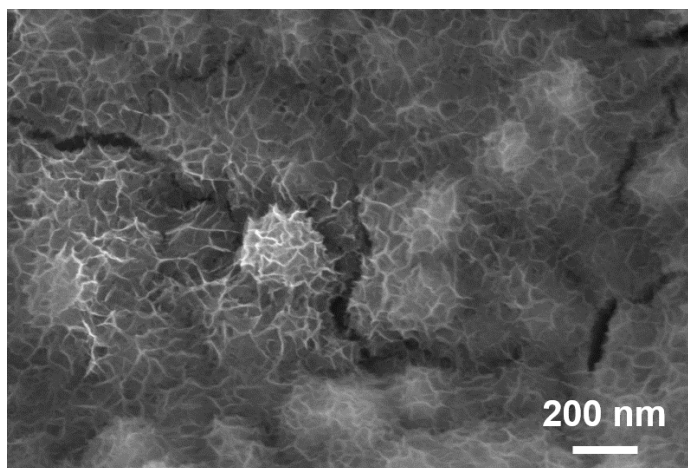
Figure S4. 17 The SEM image of Ru-Ni$_3$S$_2$-NiFe LDHs/NF.
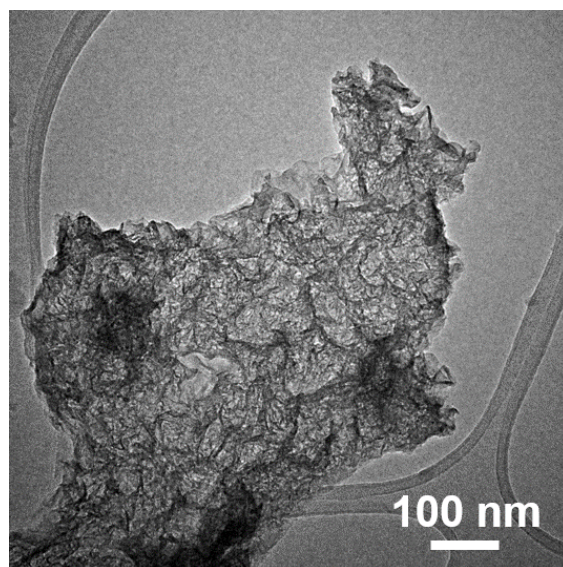
Figure S4. 18 The TEM image of Ru-Ni$_3$S$_2$-NiFe LDHs/NF.
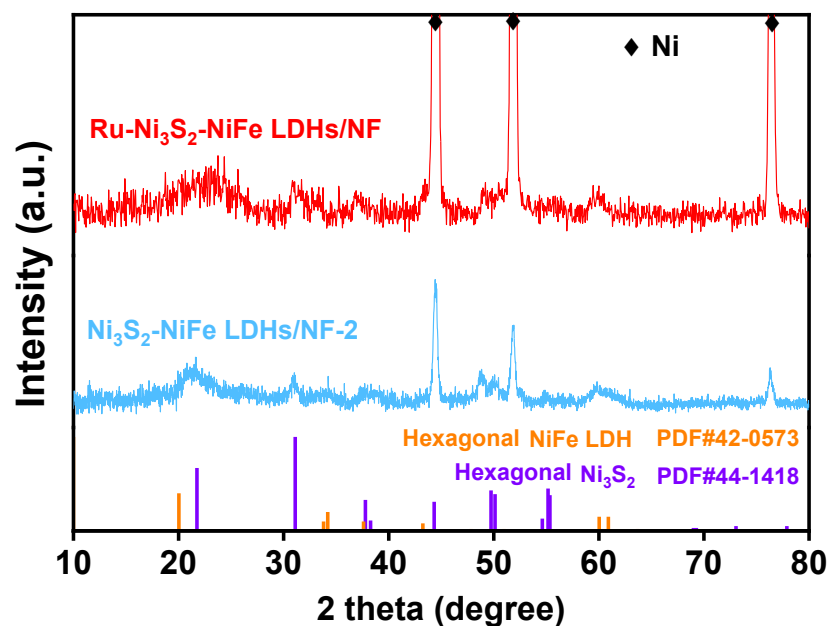
Figure S4. 19 XRD patterns of Ru-Ni$_3$S$_2$-NiFe LDHs/NF and Ni$_3$S$_2$-NiFe LDHs/NF-2.

We extended our method to synthesize Ru-doped Ni$_3$S$_2$-NiFe LDHs for HER application. The collected XRD patterns of the Ni$_3$S$_2$-NiFe LDH/NF-2 and Ru-Ni$_3$S$_2$-NiFe LDHs/NF confirmed the successful growth of the Ni$_3$S$_2$ and NiFe LDH on the Ni foam, no other Ru-based XRD diffraction signals were detected in the Ru-Ni$_3$S$_2$-NiFe LDHs/NF, suggesting that the Ru should be involved in the formation of Ni3S2-NiFe LDH (Figure S4.19).
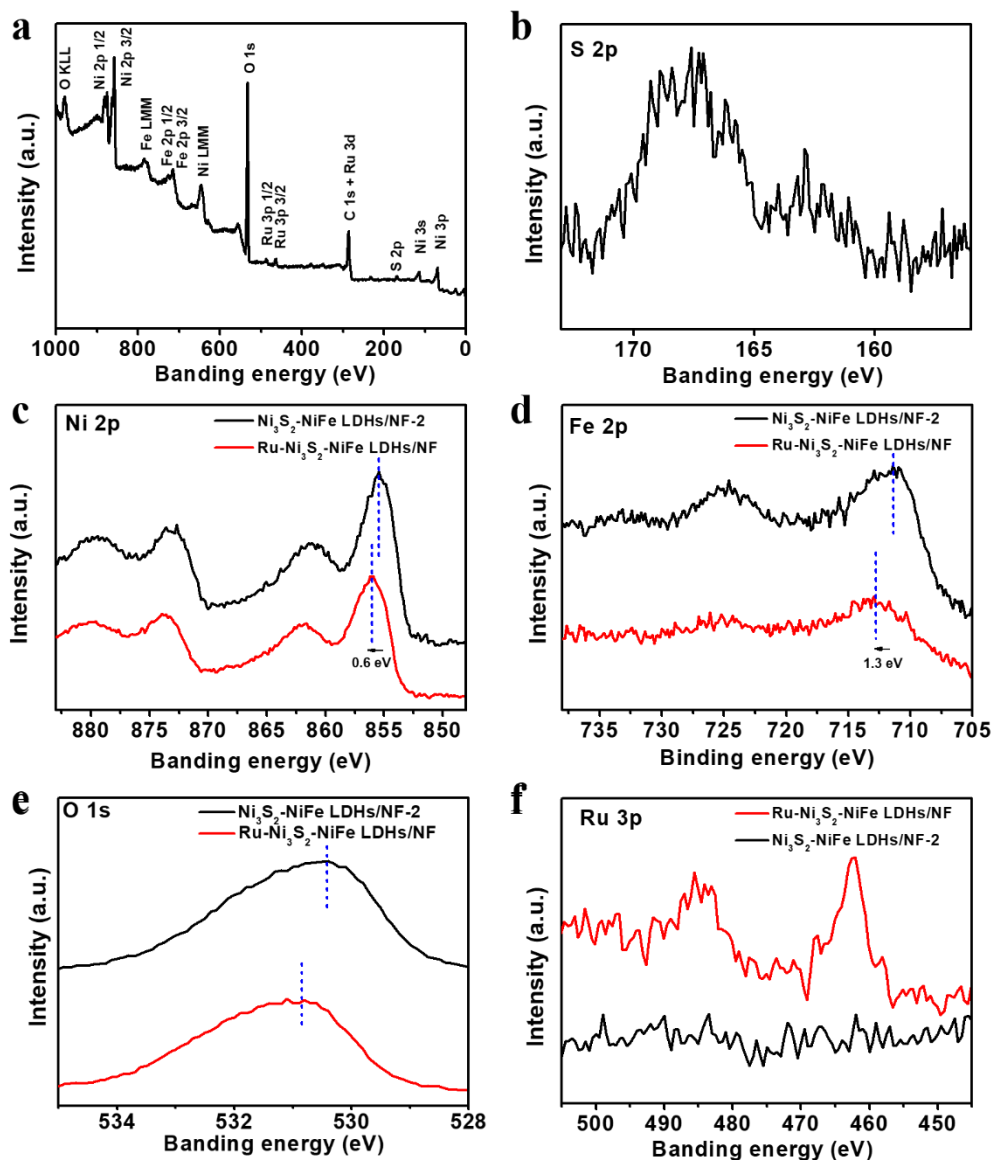
Figure S4. 20 (a) The wide-scanning XPS spectrum of Ru-Ni$_3$S$_2$-NiFe LDHs/NF. (b-f) The high resolution XPS of S, Ni, Fe, O and Ru elements in Ru-Ni$_3$S$_2$-NiFe LDHs/NF and Ni$_3$S$_2$-NiFe LDHs/NF-2.

To further confirm the introduction of the Ru, X-ray photoelectron spectroscopy (XPS) was conducted (Figure S4.20). In comparison with Ni$_3$S$_2$-NiFe-LDHs/NF, the binding energies of Ni and Fe in Ru-Ni$_3$S$_2$-NiFe LDH have a positive shift of 0.6 and 1.3 eV, respectively. Moreover, a

positive shift is observed in O 1s XPS of Ru-Ni$_3$S$_2$-NiFe LDH in comparison of Ni$_3$S$_2$-NiFe LDH, indicating that Ru atom coordinates with O atoms through an intimate interaction between Ru and Ni (Fe), where the Ru drew the electrons from Ni (Fe) atoms as a result of their different electronegativity (Nature Communications 12.1 (2021): 1-11; Advanced Materials 30.10 (2018): 1706279; A. P. Grosvenor, M. C. Biesinger, R. S. C. Smart, A. R. Gerson, in Hard X-ray Photoelectron Spectroscopy (HAXPES) (Ed.: J. Woicik), Springer International Publishing, 2016, pp. 217). All the evidence confirmed that the Ru-doped Ni$_3$S$_2$-NiFe LDH was prepared successfully.
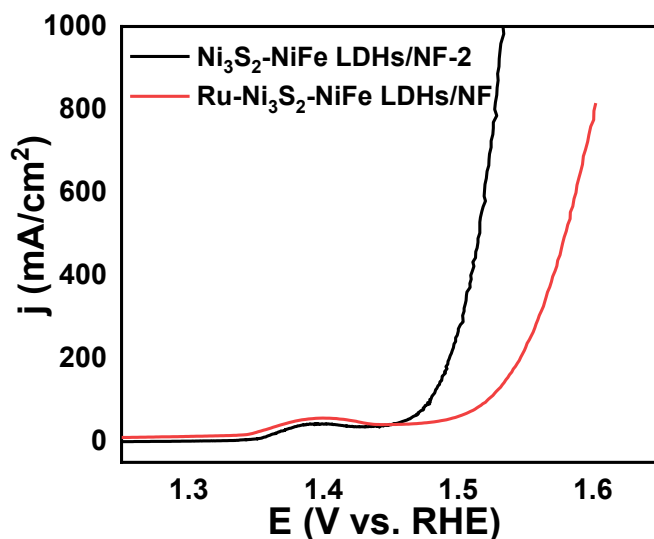
Figure S4. 21 The LSV curves for OER recorded on Ru-Ni$_3$S$_2$-NiFe LDHs/NF and Ni$_3$S$_2$-NiFe LDHs/NF-2.

Oxygen evolution performance of Ru-Ni$_3$S$_2$-NiFe LDHs/NF was evaluated via LSV polarization. As shown in Figure S4.21, the Ni$_3$S$_2$-NiFe LDHs/NF-2 showed a better OER performance than

Ru- Ni_3S_2-NiFe LDHs/NF. To gain insights into the mechanism of the OER catalytic activity, the double-layer capacitance (C_{dl}) investigations were conducted to understand the surface property of the electrocatalysts (Figure S4.22). The Ni_3S_2-NiFe LDHs/NF-2 shows a higher value of C_{dl} (4.57 mF cm^{-2}) than that of Ru- Ni_3S_2-NiFe LDHs/NF (3.6 mF cm^{-2}), indicating that the Ni_3S_2-NiFe LDHs/NF-2 possesses a larger specific surface area. The electrochemical impedance spectroscopy (EIS) plots reveal that Ni_3S_2-NiFe LDHs/NF-2 catalyst exhibits a smaller semicircle diameter than Ru-Ni_3S_2-NiFe LDHs/NF (Figure S4.23), revealing the lower charge-transfer resistance of Ni_3S_2-NiFe LDHs/NF-2 during the OER process. All these factors demonstrated that the Ru-Ni_3S_2-NiFe LDHs/NF has a low OER catalytic activity in comparison with Ni_3S_2-NiFe LDHs/NF-2.
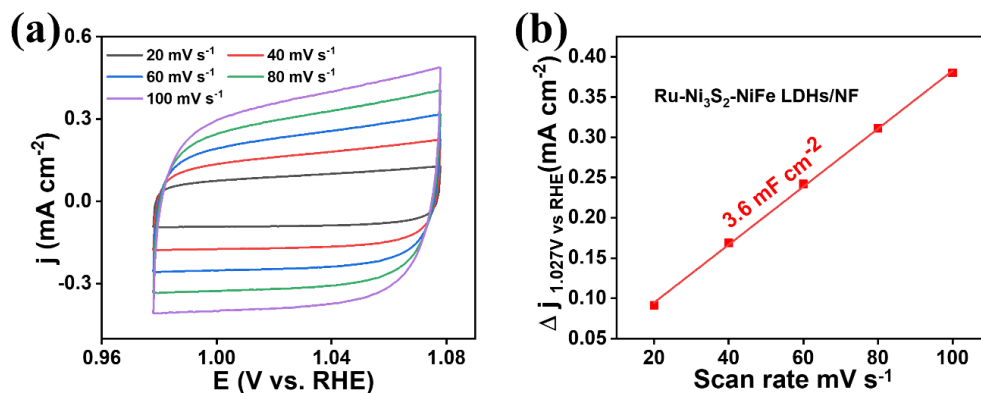
Figure S4. 22 (a) CV curves within a non-faradaic reaction region of 0.97 ~ 1.07 V versus RHE at different scan rates for Ru-Ni_3S_2-NiFe LDHs/NF. (b) C_{dl} value of Ru-Ni_3S_2-NiFe LDHs/NF.
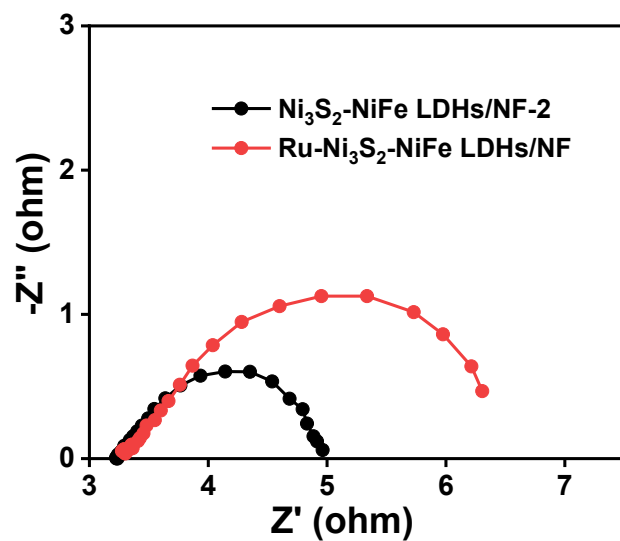
Figure S4. 23 EIS spectra of Ru-Ni$_3$S$_2$-NiFe LDHs/NF and Ni$_3$S$_2$-NiFe LDHs/NF-2 toward OER.
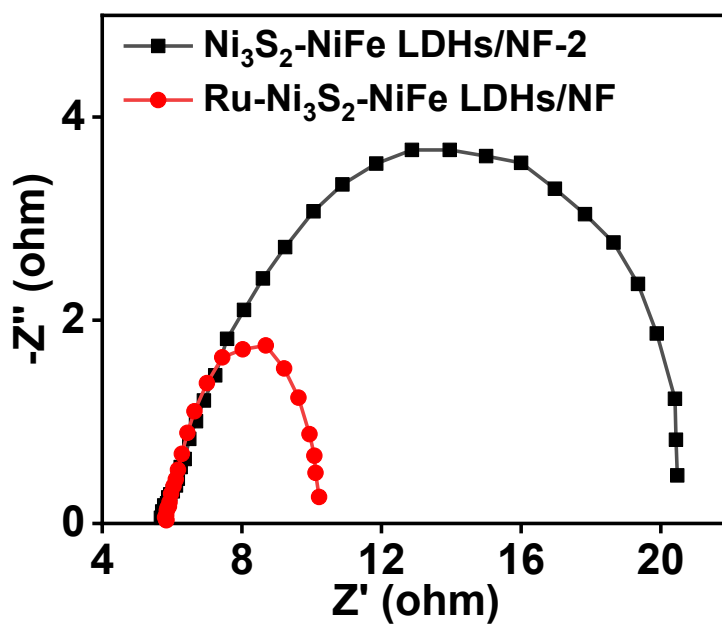
Figure S4. 24 EIS plots of Ru-Ni$_3$S$_2$-NiFe LDHs/NF and Ni$_3$S$_2$-NiFe LDHs/NF-2 toward HER.

Table S4. 3 Comparison of the OER performance and the synthesis process between the Ni_3S_2-NiFe LDHs/NF-2 catalyst and other recently reported OER electrocatalysts in 1 M KOH electrolyte. Here η_{50} represents the overpotential required to achieve current densities of 50 mA cm^{-2}. j_{300} represents the current density delivered at the overpotential of 300 mV.

Catalysts	Substrate	η_{50} (mV)	j_{300} (mA cm^{-2})	Tafel slope (mV dec^{-1})	Synthesis method	Reference
Ni_3S_2-NiFe LDHs/NF-2	Nickel foam	230	1000	35.6	One-pot solution method:15 min at room temperature	This work
NiFeOOH@NiFe nanowires [1]	Nickel foam	220	>1000	34.7	Magnetic-field-assisted chemical deposition method.	Energy Environ. Sci., 2020, 13, 86--95
S-doped NiFeOOH nanoparticles [2]	Nickel foam	250	200	48.9	One-step solution method: 5min	Energy Environ. Sci., 2020,

					at room temperature	13, 3439-- 3446
NiFe (OH))$_x$/FeS [3]	Iron foam	245	400	NA	Two steps with a hydrothermal process to synthesize FeS for 120 °C for 12 h	Adv. Funct. Mater. 2019, 29, 1902180
CoFeWO$_x$ [4]	Nickel foam	270	110	32	Two steps of electrodepositi on	Adv. Energy Mater. 2020, 10, 2002593
Se-doped FeOOH [5]	Iron foam	340	25	54	Two steps of hydrothermal process: 140 °C for 12 h; 120 °C for 12 h	J. Am. Chem. Soc. 141.17 (2019): 7005- 7013.

FeCoNi-ATNs [6]	Nickel foam	347	16	107	One-step hydrothermal method： 190 °C for 6 h	Adv. Energy Mater. 2019, 9, 1901312
ν-NiFeLDH [7]	Nickel foam	260	115	34.8	Two steps with a hydrothermal process for 150 ∘C for 24 h.	Nano Energy 81 (2021) 105606
CoFeCrOOH [8]	Glassy carbon	270	101	31	Two steps of solution phase method： 90 °C in 20 min; 90 °C for 6 h	Adv. Energy Mater. 2021, 11, 2003412
$La_{0.9}Ce_{0.1}NiO_3$ [9]	Carbon paper	328	13	45	One-step of hydrothermal method： 180 °C for 12 h	Adv. Energy Mater. 2021, 11, 2003755

Ni$_2$P-VP$_2$/NF [10]	Nickel foam	306	46	49	Two steps of hydrothermal method: 180 °C for 10 h; 600 °C for 2 h	Adv. Mater. 2019, 31, 1901174
NiCo$_2$S$_4$/FeOOH nanowires [11]	Carbon cloth	245	123	73	Two steps with a calcination: 100 °C for 10 h	Nano Energy 78 (2020) 105230
Co-Fe−N−C [12]	Glassy carbon	360	5	37	Multiple steps including: refluxed at 60 °C for 4 h; calcinated at 700 °C for 2 h	J. Am. Chem. Soc. 2019,141,14190 −14199
P/Mo-Co$_3$O$_4$ [13]	Carbon cloth	330	20	59.4	Multiple steps including: calcination at 400 °C for 2 h in air, follow	Adv. Sci. 2020, 7, 1902830

					by 300 °C for 2 h in N_2	
Pd-e-NiCo-PBA-C [14]	Glassy carbon	410	8	67	Multiple steps for 4 days at lest	Adv. Funct. Mater. 2021, 31, 2008989

Table S4. 4 Comparison of the HER performance and the synthesis process between the Ru-Ni$_3$S$_2$-NiFe LDHs/NF catalyst and other recently reported OER electrocatalysts in 1 M KOH electrolyte. Here η_{10}, η_{50} represent the overpotential needed to deliver current densities of 10, 50 mA cm^{-2}, respectively.

Catalysts	Substrate	η_{10} (mV)	η_{50} (mV)	Tafel slope (mV dec^{-1})	Synthesis method	Reference
Ru-Ni$_3$S$_2$-NiFe LDHs/NF	Nickel foam	61.3	127	96	One-pot solution method: 2 h	This work

						at room temperature
Ni₃N/C [15]	NA	64	>150	48	Two steps with a hydrothermal process at 120 °C for 16 h	Angew.Chem. Int.Ed. 2019, 58,7445 – 7449
Ni(Cu)VOₓ [16]	Nickel foam	49	75	28	Electrodeposition	Nature communications 11.1 (2020): 1-9.
Ni₂P-NiSe₂/CC [17]	Carbon cloth	66	140	72.6	Multiple steps including hydrothermal process at 120 °C for 6 h	Applied Catalysis B: Environmental 262 (2020): 118245.
MoP@NCHSs-T [18]	Glassy carbon	92	160	62	Multiple steps including	Angew. Chem. 132.23

					calcination at 900 °C for 2 h	(2020): 9067-9075.
Ni$_5$P$_4$-Ru [19]	Glassy carbon	123	220	56.7	Multiple steps including calcination at 400 °C for 2 h	Adv. Mater, 32.11 (2020): 1906972
1T-MoS$_2$ QS/Ni(OH)$_2$ [20]	carbon fiber cloth	57	105	30	Electrochemical lithiation plus water exfoliation method	Adv. Funct. Mater. 30.25 (2020): 2000551
MoS$_2$−Ni$_3$S$_2$ HNRs/NF [21]	Nickel foam	98	160	61	Hydrothermal process at 240°C for 24 h	ACS Catal. 2017, 7, 2357
Ni$_3$(S$_{0.25}$Se$_{0.75}$)$_2$@ Ni OOH/NF-8 [22]	Nickel foam	102	180	47	Hydrothermal process at 230°C for 30 min	Small 2018, 14, 1803666

					Two steps: hydrothermal process at 180 °C for 10 h, and calcination at 600 °C for 2h	Adv. Mater. 2019, 31, 1901174
Ni$_3$N-VN/NF [10]	Nickel foam	64	200	37		
NF@Ni/C-600 [23]	Nickel foam	37	110	57	Two steps: hydrothermal process at 180 °C for 24 h, and calcination at 600 °C for 2h	Energy Environ. Sci. 2018, 11, 2363

Table S4. 5 Comparison of the overall-water-splitting activities among recently reported electrocatalysts tested in 1 M KOH. V_{10} corresponds to the cell voltages of the overall-water-splitting cell operated at 10 mA cm^{-2}.

Catalysts	V_{10} (mV)	Reference
Ni$_3$S$_2$-NiFe LDHs /NF-2 || Ru-Ni$_3$S$_2$-NiFe LDHs/NF	1.47	This work
O-NiFeLDH || H-NiFe LDH [24]	1.48	Energy Environ. Sci., 2019, 12, 572-581

NF-Ni$_3$S$_2$ ‖ MnO$_2$ [25]	1.52	Applied Catalysis B: Environmental 254 (2019): 329-338.
Ni$_3$N-VN/NF ‖ Ni$_2$P-VP$_2$/NF [10]	1.51	Adv. Mater. 2019, 31, 1901174
FeNiOOH(Se)/IF‖ MoNi4/MoO2/NF [5]	>1.55	J. Am. Chem. Soc. 141.17 (2019): 7005-
NiFeOOH ‖ MoNi4 [26]	NA	Energy Environ. Sci., 2018, 11(10): 2858-2864
FeCoNi-hybrid nanotube arrays [27]	1.429	Nat. Commun., 2018, 9(1): 2452
NiO/NF ‖ Fe–NiO/NF [28]	1.73	Nano Energy 66 (2019) 104118
Ni/NiFeMoO$_x$/NF Ni/NiFeMoO$_x$/NF [29]	1.50	Adv. Sci. 2020, 7, 1902034

4.6.1 References

S1 C. Liang, P. Zou, A. Nairan, Y. Zhang, J. Liu, K. Liu, S. Hu, F. Kang, H.J. Fan, C. Yang, Exceptional performance of hierarchical Ni–Fe oxyhydroxide@ NiFe alloy nanowire array electrocatalysts for large current density water splitting, *Energy Environ. Sci*. 13 (2020) 86-95.

S2 L. Yu, L. Wu, B. McElhenny, S. Song, D. Luo, F. Zhang, Y. Yu, S. Chen, Z. Ren, Ultrafast room-temperature synthesis of porous S-doped Ni/Fe (oxy) hydroxide electrodes for oxygen evolution catalysis in seawater splitting, *Energy Environ. Sci*. 13 (2020) 3439-3446.

S3 S. Niu, W.J. Jiang, T. Tang, L.P. Yuan, H. Luo, J.S. Hu, Autogenous growth of hierarchical NiFe(OH)$_x$/FeS nanosheet-on-microsheet arrays for synergistically enhanced high-output water oxidation, *Adv. Funct. Mater.* 29 (2019) 1902180.

S4 J. Chen, H. Li, Z. Yu, C. Liu, Z. Yuan, C. Wang, S. Zhao, G. Henkelman, S. Li, L. Wei, Octahedral Coordinated Trivalent Cobalt Enriched Multimetal Oxygen-Evolution Catalysts, *Adv. Energy Mater.* 10 (2020) 2002593.

S5 S. Niu, W.-J. Jiang, Z. Wei, T. Tang, J. Ma, J.-S. Hu, L.-J. Wan, Se-doping activates FeOOH for cost-effective and efficient electrochemical water oxidation, *J. Am. Chem. Soc.* 141 (2019) 7005-7013.

S6 Q. Zhang, N.M. Bedford, J. Pan, X. Lu, R. Amal, A fully reversible water electrolyzer cell made up from FeCoNi (oxy) hydroxide atomic layers, *Adv. Energy Mater*. 9 (2019) 1901312.

S7 Y. Wang, S. Tao, H. Lin, G. Wang, K. Zhao, R. Cai, K. Tao, C. Zhang, M. Sun, J. Hu, Atomically targeting NiFe LDH to create multivacancies for OER catalysis with a small organic anchor, *Nano Energy* 81 (2021) 105606.

S8 J. Chen, H. Li, S. Chen, J. Fei, C. Liu, Z. Yu, K. Shin, Z. Liu, L. Song, G. Henkelman, Co–Fe–Cr (oxy) Hydroxides as Efficient Oxygen Evolution Reaction Catalysts, *Adv. Energy Mater.* 11 (2021) 2003412.

S9 Y. Sun, R. Li, X. Chen, J. Wu, Y. Xie, X. Wang, K. Ma, L. Wang, Z. Zhang, Q. Liao, A-Site Management Prompts the Dynamic Reconstructed Active Phase of Perovskite Oxide

OER Catalysts, *Adv. Energy Mater*. 11 (2021) 2003755.

S10 H. Yan, Y. Xie, A. Wu, Z. Cai, L. Wang, C. Tian, X. Zhang, H. Fu, Anion-Modulated HER and OER Activities of 3D Ni–V-Based Interstitial Compound Heterojunctions for High-Efficiency and Stable Overall Water Splitting, *Adv. Mater*. 31 (2019) 1901174.

S11 X. Li, Z. Kou, S. Xi, W. Zang, T. Yang, L. Zhang, J. Wang, Porous $NiCo_2S_4$/FeOOH nanowire arrays with rich sulfide/hydroxide interfaces enable high OER activity, *Nano Energy* 78 (2020) 105230.

S12 L. Bai, C.-S. Hsu, D.T. Alexander, H.M. Chen, X. Hu, A cobalt–iron double-atom catalyst for the oxygen evolution reaction, *J. Am. Chem. Soc.* 141 (2019) 14190-14199.

S13 R. Li, B. Hu, T. Yu, H. Chen, Y. Wang, S. Song, Insights into Correlation among Surface-Structure-Activity of Cobalt-Derived Pre-Catalyst for Oxygen Evolution Reaction, *Adv. Sci*. 7 (2020) 1902830.

S14 H. Zhang, Q. Jiang, J.H. Hadden, F. Xie, D.J. Riley, Pd Ion-Exchange and Ammonia Etching of a Prussian Blue Analogue to Produce a High-Performance Water-Splitting Catalyst, *Adv. Funct. Mater*. 31 (2021) 2008989.

S15 W. Ni, A. Krammer, C.S. Hsu, H.M. Chen, A. Schüler, X. Hu, Ni_3N as an active hydrogen oxidation reaction catalyst in alkaline medium, *Angew. Chem., Int. Edit*. 58 (2019) 7445-7449.

S16 Y. Li, X. Tan, R.K. Hocking, X. Bo, H. Ren, B. Johannessen, S.C. Smith, C. Zhao, Implanting Ni-O-VOx sites into Cu-doped Ni for low-overpotential alkaline hydrogen evolution, *Nat. Commun*. 11 (2020) 1-9.

S17 C. Liu, T. Gong, J. Zhang, X. Zheng, J. Mao, H. Liu, Y. Li, Q. Hao, Engineering Ni_2P-$NiSe_2$ heterostructure interface for highly efficient alkaline hydrogen evolution, *Appl.*

Catal. B. 262 (2020) 118245.

S18   D. Zhao, K. Sun, W.C. Cheong, L. Zheng, C. Zhang, S. Liu, X. Cao, K. Wu, Y. Pan, Z. Zhuang, Synergistically Interactive Pyridinic-N–MoP Sites: Identified Active Centers for Enhanced Hydrogen Evolution in Alkaline Solution, *Angew. Chem., Int. Edit.* 132 (2020) 9067-9075.

S19   Q. He, D. Tian, H. Jiang, D. Cao, S. Wei, D. Liu, P. Song, Y. Lin, L. Song, Achieving efficient alkaline hydrogen evolution reaction over a Ni_5P_4 catalyst incorporating single-atomic Ru sites, *Adv. Mater.* 32 (2020) 1906972.

S20   W. Chen, J. Gu, Y. Du, F. Song, F. Bu, J. Li, Y. Yuan, R. Luo, Q. Liu, D. Zhang, Achieving Rich and Active Alkaline Hydrogen Evolution Heterostructures via Interface Engineering on 2D 1T-MoS_2 Quantum Sheets, *Adv. Funct. Mater.* 30 (2020) 2000551.

S21   Y. Yang, K. Zhang, H. Lin, X. Li, H.C. Chan, L. Yang, Q. Gao, MoS_2–Ni_3S_2 heteronanorods as efficient and stable bifunctional electrocatalysts for overall water splitting, *Acs Catal.* 7 (2017) 2357-2366.

S22   X. Zheng, Y. Zhang, H. Liu, D. Fu, J. Chen, J. Wang, C. Zhong, Y. Deng, X. Han, W. Hu, In situ fabrication of heterostructure on nickel foam with tuned composition for enhancing water-splitting performance, *Small* 14 (2018) 1803666.

S23   H. Sun, Y. Lian, C. Yang, L. Xiong, P. Qi, Q. Mu, X. Zhao, J. Guo, Z. Deng, Y. Peng, A hierarchical nickel–carbon structure templated by metal–organic frameworks for efficient overall water splitting, *Energy Environ. Sci.* 11 (2018) 2363-2371.

S24   Z. Qiu, C.-W. Tai, G.A. Niklasson, T. Edvinsson, Direct observation of active catalyst surface phases and the effect of dynamic self-optimization in NiFe-layered double hydroxides for alkaline water splitting, *Energy Environ. Sci.* 12 (2019) 572-581.

S25 Y. Xiong, L. Xu, C. Jin, Q. Sun, Interface-engineered atomically thin Ni_3S_2/MnO_2 heterogeneous nanoarrays for efficient overall water splitting in alkaline media, *Appl. Catal. B* 254 (2019) 329-338.

S26 H. Zhou, F. Yu, Q. Zhu, J. Sun, F. Qin, L. Yu, J. Bao, Y. Yu, S. Chen, Z. Ren, Water splitting by electrolysis at high current densities under 1.6 volts, *Energy Environ. Sci.* 11 (2018) 2858-2864.

S27 H. Li, S. Chen, Y. Zhang, Q. Zhang, X. Jia, Q. Zhang, L. Gu, X. Sun, L. Song, X. Wang, Systematic design of superaerophobic nanotube-array electrode comprised of transition-metal sulfides for overall water splitting, *Nat. Commun.* 9 (2018) 1-12.

S28 Z. Qiu, Y. Ma, T. Edvinsson, In operando Raman investigation of Fe doping influence on catalytic NiO intermediates for enhanced overall water splitting, *Nano Energy* 66 (2019) 104118.

S29 Y.K. Li, G. Zhang, W.T. Lu, F.F. Cao, Amorphous Ni–Fe–Mo suboxides coupled with Ni network as porous nanoplate array on nickel foam: a highly efficient and durable bifunctional electrode for overall water splitting, *Adv. Sci.* 7 (2020) 1902034

Chapter 5. Bifunctional CoF$_2$/CoP Heterostructured Nanowires for Enhanced Electrooxidation of 5-Hydroxymethylfurfural and Hydrogen Production

Abstract: The efficiency of hydrogen production via water electrocatalytic splitting is impeded by the sluggish kinetics of anodic OER. Replacing OER with biomass electrooxidation reaction lowers driving potential and produces value-added products simultaneously is meaningful but challenging. In this study, we fabricated nanowires composed of CoF$_2$/CoP heterostructure grown on nickel foam as a robust bifunctional electrocatalyst for 5-hydroxymethylfurfural oxidation reaction (HMFOR) and hydrogen evolution reaction (HER). Thanks to its interfacial electronic structure, the optimized CoF$_2$/CoP-2 exhibits excellent HMFOR activity with a working potential of 1.33 V to deliver 100 mA cm^{-2} and a Tafel slope of 21.1 mV dec^{-1}. Meanwhile, the FDCA yield achieved 98.8 % and the faradic efficiency is 98 %. In addition, CoF$_2$/CoP-2 delivers a current density of 10 mA cm^{-2} at an overpotential of only 59 mV with a Tafel slope of 59.8 mV dec^{-1} toward HER. Furthermore, bifunctional CoF$_2$/CoP-2 exhibits excellent full-cell electrocatalytic activity when employing CoF$_2$/CoP-2 for cathodic H$_2$ and anodic FDCA production, which only requires the cell voltage of 1.33 V at 10 mA cm^{-2}, superior to the voltage of 1.54 V at 10 mA cm^{-2} for pure water splitting. This work demonstrates the great potential of CoF$_2$/CoP for energy-saving H$_2$ production with green chemical (FDCA) production in practical application.

Keywords: Heterostructured nanowires, bifunctionalities, H$_2$ production, HMFOR

5.1 Introduction

Hydrogen (H$_2$) has been regarded as a promising alternative energy carrier to traditional fossil fuels due to its high gravimetric energy density and environmental friendliness. Among various H$_2$ production methods, the electrocatalytic water splitting powdered by renewable energy is

considered as one of the most promising methods to generate high-purity H_2 in the future.[1-4] The overall water splitting (OWS) consists of a cathodic hydrogen evolution reaction (HER) and an anodic oxygen evolution reaction (OER).[5, 6] However, the overall energy efficiency of OWS is significantly limited by the sluggish kinetics of OER originating from the four-electron transfer.[7-9] Moreover, the anodic product (O_2) is of low value and does not contribute to economic feasibility.[10, 11] Replacing OER with biomass electrooxidation reactions (BEORs) is an attractive strategy to lower the full-cell potential and simultaneously produce valuable products at the anode. Biomass-derived 5-Hydroxymethylfurfural (HMF) has been emphasized as a promising anode-side reactant for coupling with cathodic HER.[12-14] Its oxidation product, 2,5-furandicarboxylic acid (FDCA), is of particular interest for the replacement of petroleum-based monomeric terephthalic acid (PET) to prepare renewable biobased plastics.[15, 16] Therefore, it is highly desirable to couple HMF oxidation reaction (HMFOR) with HER to achieve highly efficient production of H_2 and biomass upgrading. Recently, transition metal-based electrocatalysts (e.g., nitrides, phosphides, sulfides and hydroxides) have gained extensive attention for HER and HMFOR owing to their low cost as compared to noble metals.[12, 17-19] Nevertheless, most reported electrocatalysts could only deliver satisfying activity for a single HER or HMFOR. Developing low-cost transition metal-based electrocatalysts with bifunctionality for both HER and HMFOR is imperative but remains a grand challenge.

Interfacial engineering is an effective strategy to simultaneously modulate the electronic structure and active sites of catalysts.[3, 20, 21] It is demonstrated that the interfacial synergy effect between two domains has a great influence on the binding strength of reaction intermediates and the transportation of electrons, thus regulating the catalytic activity and selectivity.[22-25] These features make interfacial engineering very popular in electrochemical hydrogen and oxygen

catalysis. For example, Mu and co-workers reported that Mo-doped Ni_3S_2/Ni_xP_y hollow heterostructure exhibited remarkable stability and bifunctionality because the heterostructure can synergistically optimize the adsorption energies of H- and O-containing intermediates during HER and OER process.[20] Cobalt phosphide is an ideal HER catalyst and has also been coupled with secondary phase to achieve bifunctionality. Tian et al. synthesized a $Co_2P@Ni_2P$ core shell heterostructure arrays with efficient electrocatalytic performance toward HER and urea oxidation reaction (UOR), which can deliver 10 mA cm^{-2} at a cell voltage of 1.43 V for HER/UOR electrolyzer.[26] Cobalt (hydro)oxides (such as Co_3O_4 and CoOOH) have been adapted for HMFOR and exhibited high activity.[14, 27] However, they are not suitable for H_2 production due to their intrinsic poor HER activity, thus it is expected to explore a new bifunctional cobalt-based heterostructure catalyst to boost the efficiency of both HER and HMFOR, which has rarely been achieved.

Herein, we designed and fabricated hierarchical nanoneedle arrays with abundant CoF_2-CoP interface on Ni foam as a bifunctional electrocatalyst for both HER and HMFOR. The CoF_2-CoP is formed by in situ growth of Co $(OH)_2$ nanowire arrays on NF, followed by two-step fluorination and phosphorization process. Interfacial electron transfer between CoF_2 and CoP is important to modulate electronic environments of the active centers, where hydrogenase-like electronic structure benefits inter- and intramolecular proton/hydride exchange, the metal and base (P and F) sites exhibits an ensemble effect to act as proton-acceptor and hydride-acceptor centers. For anodic HMFOR, it only requires very low working potential of 1.33 V vs. reversible hydrogen electrode (RHE) to reach 100 mA cm^{-2} in 1.0 M KOH with 50mM HMF electrolyte. The 2,5-furandicarboxylic acid (FDCA) is obtained with the selectivity of 98.8 % and the faradic efficiency achieves 98 %. Meanwhile, due to the interfacial synergy effect of CoP and CoF_2, CoF_2-CoP-2

exhibits a current density of 10 mA cm^{-2} at low overpotential of 59 mV with small Tafel slope of 59.8 mV dec^{-1} for HER in alkaline medium. Furthermore, in an integrated electrolyzer for HMF-assisted H$_2$ production using CoF$_2$/CoP-2 as bifunctional electrocatalysts, the system requires lower cell voltage of 1.33 V at 10 mA cm^{-2} in comparison to the pure water splitting (1.54 V at 10 mA cm^{-2}), which indicates the great potential for energy-saving H$_2$ production compared to OWS system.

5.2 Experiment

5.2.1 Materials synthesis

Preparation of Co (OH)$_2$ nanowire arrays grown on Ni foam (NF): NF was cleaned with HCl (3 M), acetone, and deionized water (DI) several times. 1 mmol Co (NO$_3$)$_2$·6H$_2$O, 5 mmol CH$_4$N$_2$O and 5 mmol NH$_4$F were dispersed into 10 mL deionized water. Then a piece of CF (2 × 2 cm) was immersed into the above solution in a Teflon-lined stainless-steel autoclave and kept at 120 °C for 8 h. The products Co (OH)$_2$/NF were washed with deionized water and dried in an oven at 60 °C overnight.

Preparation of CoF$_2$/CoP nanowire arrays grown on NF: Typically, Co (OH)$_2$/NF (1 × 2 cm) and 100 mg NH$_4$F were placed in two separate porcelain crucibles with NH$_4$F at the upstream side of the furnace, following heated at 400 °C for 1h with 45 min of heating time under Ar gas to obtain CoF$_2$/Co (OH)$_2$/NF. The sample was subsequently phosphorized with 1 g NaH$_2$PO$_2$ on the upstream at 300 °C for 2 h with 3 °C/min of heating rate under Ar atmosphere. After naturally cooling to room temperature, the CoF$_2$/CoP-2 was obtained. CoF$_2$/CoP-1 and CoF$_2$/CoP-3 were prepared in the same way with 50 mg and 150 mg NH$_4$F, respectively. CoF$_2$ was synthesized in a similar way without a phosphorization process, except using 200 mg NH$_4$F. Co (OH)$_2$/NF (1 × 2 cm) was directly phosphorized with 1 g NaH$_2$PO$_2$·H$_2$O to obtain CoP.

5.2.2 Materials characterization

The morphologies of prepared materials were studied via Zeiss Sigma 300 VP-Field Emission Scanning Electron Microscopy (FESEM) and Transmission electron microscopy (TEM) on a JEOL JEMARM200CF equipped with an energy dispersive spectrometer (EDS). The crystal structure was characterized by X-ray diffractometer (XRD, D8 discover diffraction system equipped with Cu Kα radiation (40 kV, 44 mA)) at a scan rate of $5° \, min^{-1}$. X-ray photoelectron spectroscopy (XPS) spectra were performed on Kratos Analytical AXIS 165 with a monochromatic Al Kα source to study the chemical compositions. The C 1 s photoelectron peak at 284.6 eV as reference was used for spectrometer calibration. The local structures of the investigated materials were analyzed by measuring the Co K-edge X-ray absorption near-edge structure (XANES) and the extended X-ray absorption fine structure (EXAFS) data at the Hard X-ray microanalysis beamline (HXMA-061D) of the Canadian Light Source. The X-ray absorption spectra were acquired in fluorescence mode using a Si(111) double-crystal monochromator to range the X-ray energy from 5–40 keV. The ring current is 250 mA. A He-filled Oxford straight ion chamber detector was used to monitor the incident X-ray, and the fluorescence yield signal was captured using a 32-element Ge detector. The energy was calibrated using Co plate reference sample.

5.2.3 Electrochemical Measurements

The OER, BEOR and HER measurements were performed with a three-electrode system using a BioLogic SP-300 electrochemical test station with CoF_2/CoP as the working electrode. A saturated calomel electrode (SCE) electrode and a graphite rod were used as reference electrode and counter electrode, respectively. All the reported potentials were corrected to the reversible hydrogen electrode (RHE) through $E_{RHE} = E_{SCE} + 0.059 \times pH + 0.241$ V. The Pt/C/NF were prepared by a slurry cast method. Typically, 10 mg catalysts were ultrasonically dispersed in a 1 ml solution

containing 970 μL isopropyl alcohol and 30 μL Nafion solution. To maintain the same mass loading with the CoF_2/CoP, a certain amount of ink was pipetted onto the NF and dried in the air before the electrochemical measurements. The polarization curves were scanned at a scan rate of 5 mV s^{-1}. The electrochemical OER and HER tests were conducted in 1.0 M KOH solution. BEORs were similar with HER and OER, except that the electrolyte was performed in 1.0 M KOH solution with 50 mM biomass (5-hydroxymethylfurfural (HMF)). The conversion tests of catalysts for BEOR were evaluated by chronoamperometry at 1.43 V vs RHE. The stability test of HER was tested for 68 h at the current density of 20 mA cm^{-2}. The electrochemical impedance spectroscopy (EIS) measurements were carried on with frequency from 0.1 Hz to 100 kHz with an amplitude of 10 mV. The electrochemically surface area (ECSA) of the catalysts was calculated by using the double-layer capacitor. The CVs were tested with different rates from 20 to 100 mV s^{-1} in the potential interval of -0.69 to -0.59 V.

5.2.4 Product Quantification

To analyze the oxidation products of biomass quantitatively and calculate the corresponding Faradaic efficiency (FE), high-performance liquid chromatography (HPLC) on Shimazdu LC-20 was used. The HPLC was equipped with a 4.6 mm × 150 mm 5 μm C18 detector column and an ultraviolet-visible detector set at 245 nm. A mixture of eluting solvents (A and B) was utilized, comprising 70% 5 mM ammonium formate aqueous solution and 30% methanol. A 30 uL electrolyte solution was taken and mixed with 1470 uL of deionized water. An injection volume of 1 mL was applied, and the identification and quantification of reactants and oxidation products were determined from calibration curves by standard solution with known concentrations of commercially purchased compounds.

The FDCA conversion (%) and the Faradic efficiency (%) were calculated using the following equation:

$$FDCA_{yield} = \frac{mol\ of\ FDCA\ formed}{mol\ of\ initial\ HMF} \times 100\%$$

$$FE_{FDCA} = \frac{mol\ of\ FDCA\ formed \times n \times F}{Total\ passing\ charges} \times 100\%$$

Where F is the Faraday constant of 96485 C mol^{-1}, n is the electron transfer number.

5.3 Results and Discussion

5.3.1 Synthesis and characterizations of electrocatalysts
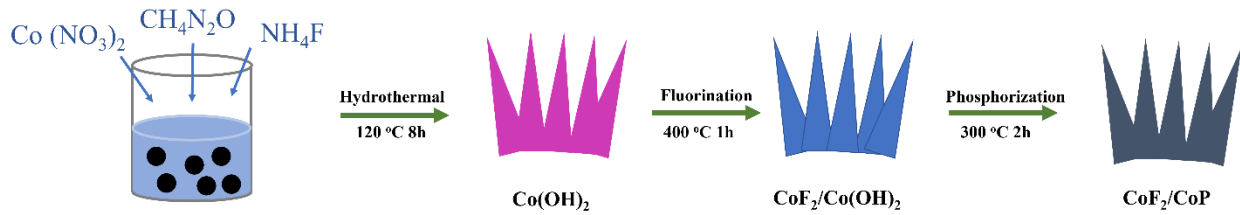
Scheme1. The synthesis procedure of CoF$_2$/CoP.

The synthetic process of CoF$_2$/CoP nanowire arrays grown on nickel foam (NF) is depicted in Scheme 1. The heterostructured CoF$_2$/CoP nanowire arrays were prepared by three steps, which involve growth of precursor and subsequent fluorination and phosphorization. Co (OH)$_2$ nanowire arrays were first vertically grown on pre-cleaned NF through facile hydrothermal synthesis with urea as precipitants to provide OH$^-$ and NH$_4$F as the morphology control reagent for selective passivation of the specific crystal surfaces. Then the vapor-phase fluorination process was conducted on the Co(OH)$_2$/NF to obtain CoF$_2$/Co(OH)$_2$ nanowire arrays at the selected temperature by reacting with hydrogen fluoride (HF) vapor resulting from the thermal decomposition of NH$_4$F. From the XRD pattern, it well indexes the presence of tetragonal CoF$_2$

(PDF#33-0417) and hexagonal $Co(OH)_2$ (PDF#30-0443) after vapor-phase fluorination process, indicating the precursor $Co(OH)_2$ was not fully transformed into CoF_2 (Figure S1). After phosphorization, the final heterostructured CoF_2/CoP nanowires were synthesized on NF, in which NaH_2PO_2 was taken as the phosphorization agent. To optimize the catalytic performance, fluorination was carried out by controlling the amount of fluorine source (0, 50, 100, 150 mg), which donates as CoP, CoF_2/CoP-1, CoF_2/CoP-2 and CoF_2/CoP-3, respectively. CoF_2 was synthesized only via fluorination with 200 mg of fluorine source. The reaction formulas are as follows:

$$Co^{2+} + 2OH^- \rightarrow Co(OH)_2 \tag{1}$$

$$NH_4F \rightarrow NH_3 + HF \tag{2}$$

$$Co(OH)_2 + HF \rightarrow CoF_2 + H_2O \tag{3}$$

$$NaH_2PO_2 \rightarrow PH_3 + H_2 + H_2O \tag{4}$$

$$Co(OH)_2 + PH_3 \rightarrow CoP + H_2O \tag{5}$$

The morphology structure of prepared products was first characterized by scanning electron microscopy (SEM). As shown in Fig. 1a, a layer of nanowires vertically and uniformly distributes on the NF, which can not only benefit the electron transfer rate during the electrocatalytic process but also enhance the specific active area. Besides, the high-resolution SEM images of the CoF_2/CoP-2 show that the nanowire morphology was formed with a diameter of 80-200 nm and several microns in length (Fig 1b, c). The transmission electron microscopy (TEM) image in Fig. 1d further confirms the straight needle-like shape. The corresponding selected area electron diffraction (SAED) pattern (Fig. 1e) indicates the polycrystalline nature instead of a single crystal, suggesting the construction of heterointerfaces. The high-resolution TEM (HRTEM) image shows

the lattice fringes of 0.196 and 0.23 nm indexed to the (112) and (111) planes of CoP and CoF_2, respectively, which reveals the presence of CoP and CoF_2 in CoF_2/CoP-2 (Fig 1f). Moreover, the elemental mapping (Fig. 1g) presents a spatial distribution of Co (red), P (green), and F (blue) elements in the typical CoF_2/CoP-2 nanowire, demonstrating the co-existence of Co, P and F in nanowires. Effects of the amount of fluorine source were investigated to evaluate on the morphology structure of the final products. As shown in Fig. S2-3 in the Supporting Information, we can observe negligible influence on the microstructures of nanowire arrays for samples prepared with different amount of fluorine source, all of them (CoF_2, CoP, CoF_2/CoP-1 and CoF_2/CoP-3) shows well-defined vertical nanowire arrays on NF.
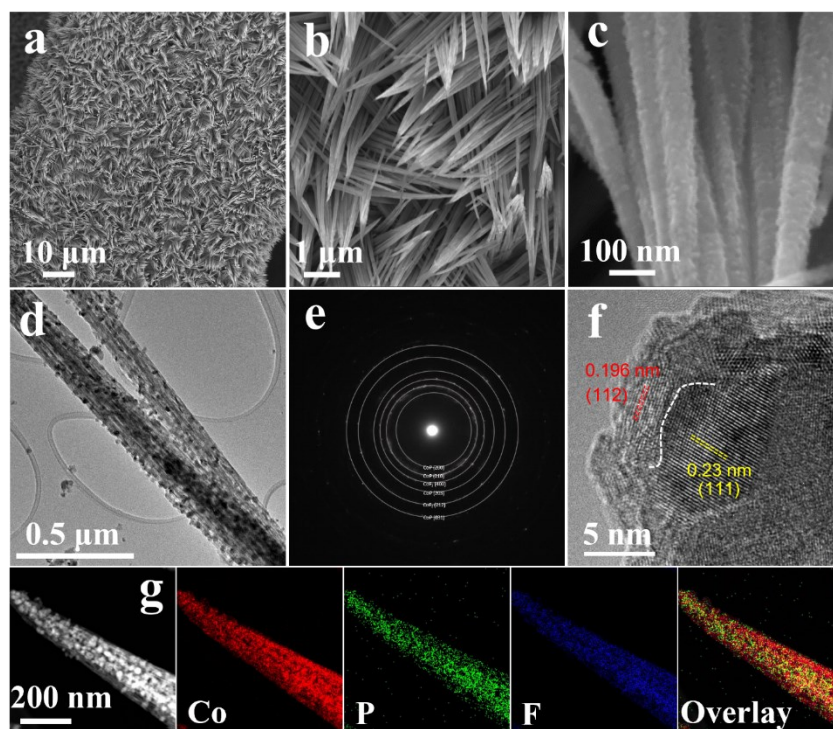
Figure 5. 1 (a, b, c) SEM images of CoF_2/CoP-2. (d) TEM image of CoF_2/CoP-2. (e) the corresponding SAED of (d). (f) High resolution transmission electron microscopy (HRTEM) image of CoF_2/CoP-2. (g) HAAD-STEM image and associated elemental mapping images.

X-ray diffraction (XRD) measurement was carried out to characterize the phase structure of the as-prepared products. As displayed in Fig. 2a, the peaks at 26.8°, 34.2°, 39.2° and 54.9° match with the (110), (101), (111) and (220) planes of tetragonal CoF_2 (PDF#33-0417), respectively. The peaks at 48.7°, 56.2° and 57.1° can also be differentiated, which can be indexed to (202), (212) and (301) planes of orthorhombic CoP (PDF#29-0497), respectively. The peaks of metallic Ni are derived from the substrate. The CoF_2/CoP-2 involves both the CoF_2 and CoP phase patterns, implying again the formation of CoF_2 and CoP in the CoF_2/CoP-2 sample. Besides, it is well indexed that the single phase CoF_2 (PDF#33-0417) and CoP (PDF#29-0497) can be observed in prepared products of CoF_2 and CoP, respectively, which indicates that precursor Co $(OH)_2$ was thoroughly transformed. Similarly, the XRD patterns of CoF_2/CoP-1 and CoF_2/CoP-3 also involve the crystal structure of both CoF_2 and CoP (Fig. S4).

X-ray photoelectron spectroscopy (XPS) was conducted to further understand the surface chemistry and valance state of elements for the synthesized electrocatalysts. In the wide-scanning XPS spectra, the signals for Co, F and P elements can be observed in CoF_2/CoP-1, CoF_2/CoP-2 and CoF_2/CoP-3 (Fig. S5), consistent with the EDS elemental mapping. In Fig. 2b, the high-resolution XPS spectrum of Co 2p for CoP consists of peaks at 778.7 eV and 793.7 eV assigned to Co^0 in CoP, as well as peaks at 781.6 eV and 797.8 eV corresponding to Co^{2+} in the surface oxidation.[28, 29] The Co 2p spectrum of CoF_2 only shows Co-F/O peaks along with two satellite peaks, where the binding energies of Co 2p negatively shifted in comparison to CoP. After phosphorization, the Co^0 belonging to CoP appears in CoF_2/CoP-2, in addition, the binding energies of the Co 2p spectrum in CoF_2/CoP-2 are also negatively shifted in comparison to that of CoP. F 1s XPS spectrum of CoF_2/CoP-2 exhibits the F-P signal that is absent in CoF_2 (Fig. 3c), indicating P and F atoms form a transitional interface and penetrate each other between the two

lattice structures. As shown in Fig. 3d, the binding energies of P $2p_{1/2}$ (129.93 eV) and P $2p_{3/2}$ (129.04 eV) of CoF_2/CoP-2 also show a positive shift in contrast to those of CoP (0.49 eV for P $2p_{1/2}$ and 0.36 eV for P $2p_{3/2}$), since the high electronegativity of F. [30] The broad peak at about 134 eV owns to the P-O due to the air exposure. The above results suggest the pronounced electron transfer in CoF_2/CoP-2 due to the interaction between CoP and CoF_2 in the closely contacted heterointerface. Besides, introduction of the base F (δ^-) into Co-P complex results in the formation of hydrogenase-like electronic structure, facilitating inter- and intramolecular proton/hydride exchange, where metal and base (P and F) sites exhibit an ensemble effect to act as proton-acceptor and hydride-acceptor centers, benefiting the catalytic process.[31-33] Synchrotron XAFS spectroscopy was used to further investigate the electronic property and coordination information of as-prepared products. The valence of Co in CoF_2/CoP-2 is between that of CoP and CoF_2, but lower than that of Co_3O_4, suggesting the electron redistribution in the heterointerfaces (Fig. 2e). The extended X-ray absorption fine structure (EXAFS) spectroscopy was used to explore the coordination configurations. As shown in Fig. 2f, the R-space EXAFS spectrum of Co K-edge in CoF_2/CoP-2 presents peaks at 1.47 Å and 1.82 Å, corresponding to the Co-F and Co-P shells, respectively, in reference to CoF_2 and CoP.[34, 35] This evidences again the presence of CoF_2 and CoP in the prepared CoF_2/CoP-2.
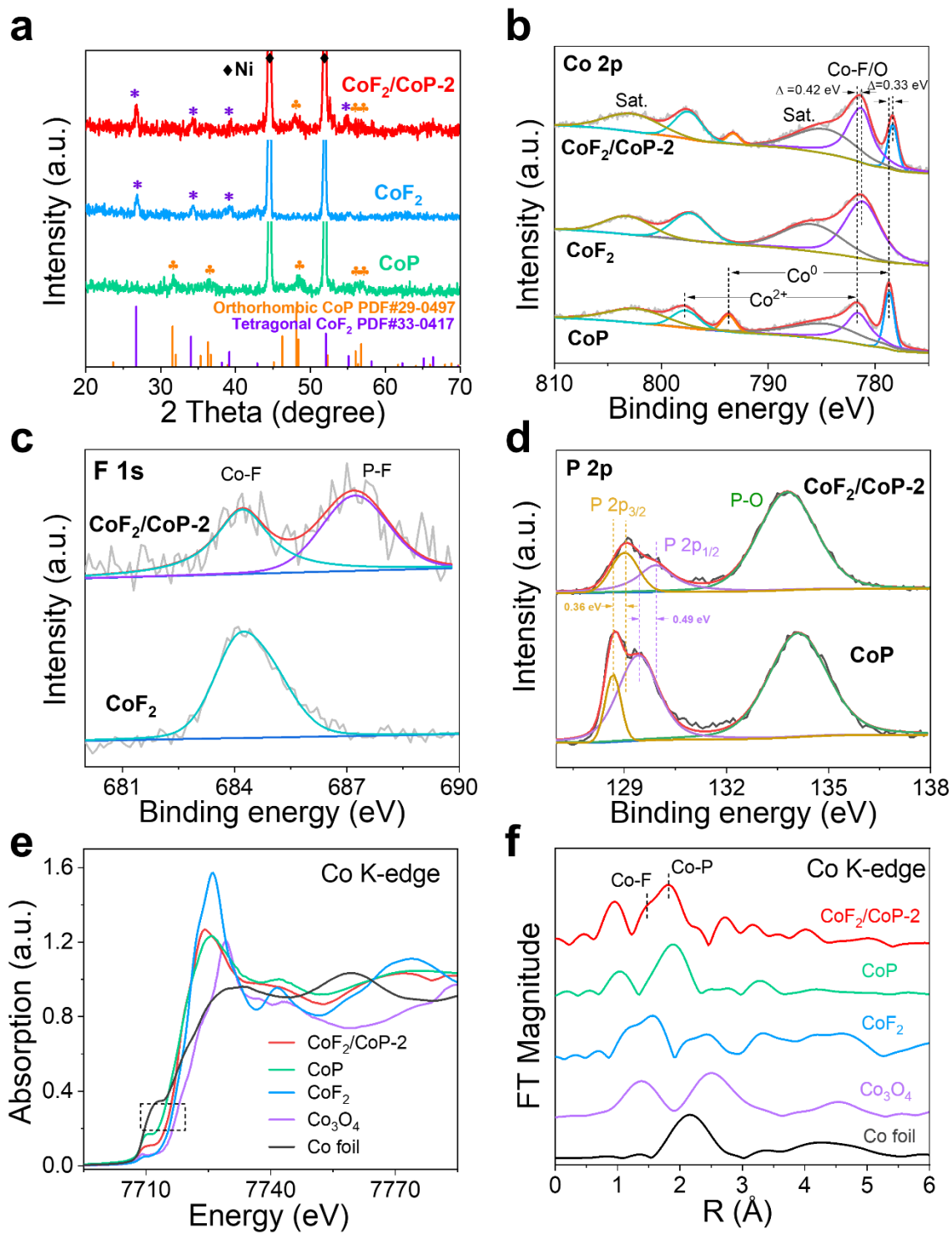
Figure 5. 2 (a) XRD patterns of CoF_2, CoP and CoF_2/CoP-2. (b) High-resolution XPS spectra of Co for CoF_2, CoP and CoF_2/CoP-2. (c) High-resolution XPS spectra of F 1s for CoF_2 and

CoF$_2$/CoP-2. (d) High-resolution XPS spectra of P 2p for CoP and CoF$_2$/CoP-2. (e) Co K-edge XANES spectra and (f) Fourier-transform EXAFS curves of CoF$_2$, CoP and CoF$_2$/CoP-2 and references (Co foil and Co$_3$O$_4$).

5.3.2 Electrocatalytic performance

The advantages of CoF$_2$/CoP-2 could render it a promising robust electrocatalyst, considering the active heterointerface and good mass/electron transfer ability. FDCA as one of the oxidation products of HMF is a promising chemical for synthesis of polymeric materials with different industrial applications. The electrochemical HMFOR activity of prepared electrodes was determined in 1M KOH with 50 mM HMF electrolyte. Since OER is the major competing reaction to HMFOR, the Cyclic voltammetry (CV) and polarization curves of water oxidation in the absence of HMF were also investigated for comparison at a scan rate of 5 mV s^{-1}. In Fig. S6, it is noted that Co^{2+}/Co^{3+} transformation occurs in CoF$_2$ at potentials around 1.2-1.3 V (vs RHE).[36] The transformation of Co^{3+}/Co^{4+} (1.36-1.5 V vs RHE) was boosted with the co-existence of CoF$_2$ and CoP in CoF$_2$/CoP-1.[37, 38] With the increase of CoF$_2$, the CoF$_2$/CoP-2 shows the most abroad oxidation peak area including Co^{2+}↔Co^{3+}↔Co^{4+} transformations. It was clearly observed from the CV profiles that OER occurred after the redox peak positions. The electrochemical HMFOR activity was examined shown in Fig. S7. The CoF$_2$/CoP-2 manifests a prominent enhanced performance for HMF oxidation relative to CoF$_2$/CoP-1 and CoF$_2$/CoP-3. In addition, as depicted in Fig. 3a, without HMF, the CoF$_2$/CoP-2 electrode presents the potential of 1.60 V (vs RHE) to deliver 100 mA cm^{-2} resulting from the OER. In contrast, the potential was decreased to 1.33 V (vs RHE) at 100 mA cm^{-2} after 50 mM HMF was introduced, indicating that the oxidation of HMF was significantly favored over water oxidation. Subsequently, the HMFOR activity of CoF$_2$, CoP and CoF$_2$/CoP-2 were also evaluated for comparison (Fig. 3b). The CoF$_2$/CoP-2 presents a better

activity than CoF_2 and CoP for HMF oxidation. The consistent kinetic behaviors can be observed in the Tafel plots. The CoF_2/CoP-2 exhibits a Tafel slope of 21.1 mV dec^{-1}, smaller than CoF_2 (26.7 mV dec^{-1}) and CoP (29.7 mV dec^{-1}), implying a boosted HMFOR kinetics for practical applications. The above results indicate that the presence of both Co^{2+} and Co^{3+} contributes to the electrocatalytic activity for HMF electrooxidation, which is consistent with the previous report.[14]

HMF is a highly functionalized platform chemical derived from biomass, composed of a furan ring, a hydroxymethyl group, and an aldehyde group. Both the hydroxymethyl and aldehyde groups can be oxidized into carboxyl groups. Thus, the HMF oxidation has two possible pathways, due to the sequential oxidation order of the two groups. As shown in Fig. 3d, the initial alcohol group of HMF is oxidized into 2,5-diformylfuran (DFF) intermediate and the oxidation of aldehyde group yields 5-hydroxymethyl-2-furancarboxylic acid (HMFCA) intermediate. Both DFF and HMFCA can be further oxidized into 2-formyl-5-furancarboxylic acid (FFCA), which can turn into the end-product of FDCA. In addition to the above process, the ring-opening reaction of HMF can also easily be occurred to generate by-products such as levulinic acid and formic acid.[39, 40] Given the complex transformation network of HMF, achieving a high selectivity of HMF transformation to FDCA is still considered to be a challenging technical objective. The electrochemical HMF oxidation of CoF_2/CoP-2 was conducted in 20 mL 1.0 M KOH with the concentration of 10 mM HMF under an applied potential of 1.43 V in a H-cells. To fully convert the HMF into FDCA, nearly 116 C of the theoretical passed charge is required (Fig. S8). The high-performance liquid chromatography (HPLC) was used to analyze the HMF oxidation products during electrocatalysis process, including HMFCA, FDCA, DFF and FFCA. Calibration with standard solutions of HMF and the intermediates allows to quantify the possible compounds during electrolysis (Fig. S9). The concentration of HMF and oxidation products are depicted in Fig. 3e.

We can clearly see the decreased concentration of HMF and an increase in FDCA over time, suggesting the gradual conversion of HMF into FDCA during the electrochemical HMF oxidation. The trace amounts of HMFCA, FFCA and DFF were also detected during the process. It is noted that the intermediates do not accumulate and the HPLC trace of end-product FDCA increases to the maximum while that of HMF almost disappears, when the passing charge reaches 116 C. Above results indicate the fast transformation of HMFCA, FFCA and DFF into FDCA. The durability test of CoF_2/CoP-2 for HMF oxidation was performed at an applied constant potential of 1.43 V in the presence of 10 mM HMF. The one sample was tested in 5 bathes of 10 mM HMF subsequently under the same electrocatalysis condition. The superior FDCA yield (~ 98.8%) and faradic efficiency (~ 98%) were achieved, due to the efficient synergistic effect between CoF_2 and CoP (Fig. 3f). The catalytic activity of CoF_2/CoP-2 is well maintained after five runs. Notably, CoF_2/CoP-2 still retains superior FDCA yield and faradic efficiency after five successive constant electrocatalysis cycles, illustrating the outstanding stability for HMF oxidation.

To evaluate the hydrogen generation application of the prepared CoF_2/CoP electrodes, the electrocatalytic HER performance of the synthesized samples was examined in 1 M KOH electrolyte using a standard three-electrode system. The HER catalytic activity of the electrodes was benchmarked against Pt/C catalyst for comparison. According to the linear sweep voltammetry (LSV) curves in Fig. S10, the optimized CoF_2/CoP-2 presents a better electrocatalytic activity than the counterparts. As shown in Fig. 3g, Pt/C displays excellent activity at current density of 10 mA cm^{-2} with overpotential of only 15.9 mV, and the onset potential is near zero, Tafel slope is 18.2 mV dec^{-1}. CoF_2/CoP-2 exhibited remarkably enhanced HER activity among investigated samples (such as CoF_2 and CoP), which only requires overpotentials of 59 and 114.1 mV to deliver 10 and 100 mA cm^{-2}, respectively, superior to those of CoF_2 (218.7 and 308 mV)

and CoP (120.5 and 215.4 mV). Moreover, its activity is also better than that of Pt/C when the absolute value of current density is above 123.8 mA cm^{-2}. The Tafel slope of CoF$_2$/CoP-2 is 59.8 mV dec^{-1}, which is smaller than that of CoF$_2$ (99 mV dec^{-1}) and CoP (88 mV dec^{-1}), demonstrating more rapid HER kinetics of CoF$_2$/CoP-2 (Fig. 3h). Such Tafel slope suggests the Volmer–Heyrovsky mechanism of CoF$_2$/CoP-2 for HER, indicating that the HER catalysis is governed by the charge-transfer-induced water dissociation process in alkaline electrolyte.[41, 42] Furthermore, electrochemical impedance spectroscopy (EIS) test was also performed (Fig. S11). In accordance with the order of HER activity, the CoF$_2$/CoP-2 shows smallest semicircle diameter among the investigated samples (CoF$_2$ and CoP), confirming the enhanced conductivity and rapid electron transfer in the CoF$_2$-CoP interfaces and a better HER kinetics of CoF$_2$/CoP-2. Additionally, the electrochemical active surface area (ECSA) was estimated by measuring the double-layer capacitance (C_{dl}) of catalysts via cyclic voltammetry. The CoF$_2$/CoP-2 presents a dramatically higher value of C_{dl} (44.28 mF cm^{-2}) than that of CoF$_2$ (4.66 mF cm^{-2}) and CoP (10.13 mF cm^{-2}) (Fig. S12), which corroborates that the optimized CoF$_2$/CoP-2 possesses a larger ECSA related to the construction of heterointerfaces in CoF$_2$/CoP-2 with high exposure of the active sites. In addition to the high activity, a desirable catalyst should be able to achieve substantial long-term stability, which endows its potential in practical application. The electrochemical stability of CoF$_2$/CoP-2 was evaluated by performing chronopotentiometry measurement at a constant current density of 20 mA cm^{-2} for 68 h. CoF$_2$/CoP-2 displays the long-term stability without obvious potential shift with time (Fig. S13).

In view of the above encouraging catalytic performance, we expect that CoF$_2$/CoP-2 can catalyze both HER and HMFOR simultaneously. A two-electrode electrolyzer was constructed using CoF$_2$/CoP-2 as both the anode and cathode in H-cells. The pure water splitting electrolyzer was

also evaluated for comparison. The polarization curves are illustrated in Fig. 3i. CoF_2/CoP-2 catalyst exhibits a voltage of 1.54 V at 10 mA cm^{-2} for pure water splitting. In contrast, the voltage is obviously reduced to 1.33 V at 10 mA cm^{-2} when 50 mM HMF is introduced, highlighting pairing HER with HMFOR is an effective strategy to realize the highly efficient generation of hydrogen and the synthesis of value-added products.
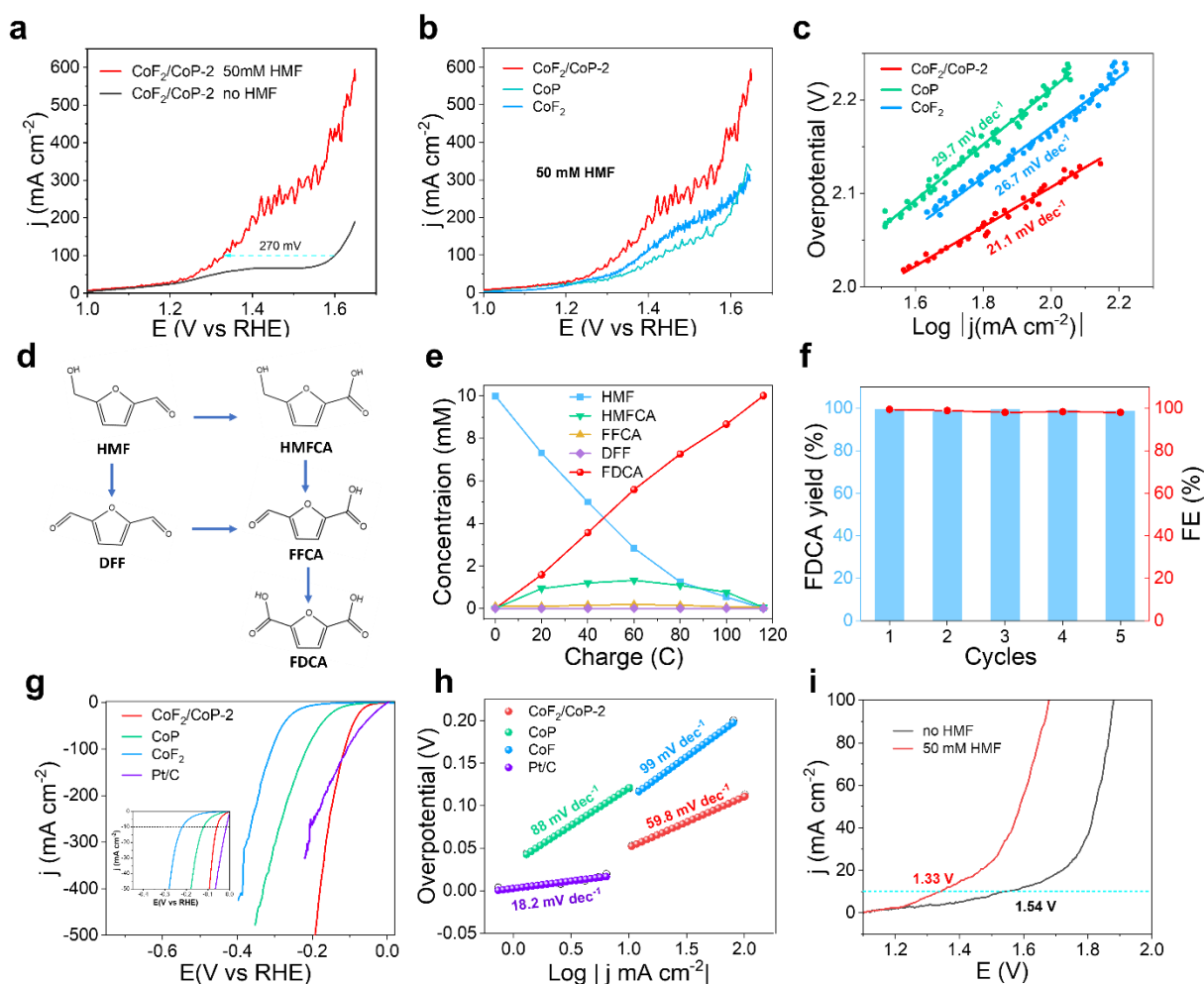
Figure 5. 3 (a) Polarization curves of CoF_2/CoP-2 in 1 M KOH with and without 50 mM HMF at a scan rate of 5 mV s^{-1}. (b) Polarization curves of CoF_2, CoP and CoF_2/CoP-2. (c) The corresponding Tafel slopes of (b). (d) Two possible pathways of HMF oxidation to FDCA. (e) Concentration changes of HMF, FDCA and the intermediates during the HMFOR process. (f)

125

FDCA yield and FE (%) of CoF_2/CoP-2 under five successive cycles. (g) The HER polarization curves of CoF_2, CoP, CoF_2/CoP-2 and Pt/C. (h) The corresponding Tafel slopes of (g). (i) Polarization curves of CoF_2/CoP-2 couple in 1M KOH with and without 50 mM HMF.

5.3.3 Mechanism Analysis

To explore the HMFOR/HER activity–structure relationship, the morphology and compositional changes were investigated before and after long term electrocatalysis. The change of phase structure in HMFOR was revealed by XRD, where apart from CoF_2 diffraction peaks, the new crystallization peaks corresponding to γ-CoOOH also appear in the XRD pattern, but no peaks for CoP can be observed, suggesting that bias potential could mainly promote the transformation of CoP into γ-CoOOH (Fig. 4 a). The morphological evolution after HMFOR was unveiled by SEM and TEM. As shown in Fig. S14a-c, the nanowires were converted into nanosheets with rough thin film on the surface after the anion reconstruction. In TEM image (Fig. S15), we can see that the nanosheets are vertically grown on a single nanowire, forming a core–shell nanostructure with a rough surface, where the core should be the preserved CoF_2, which could explain the presence of CoF_2 diffraction peaks in the XRD pattern. The high-resolution TEM images further corroborate the newly formed thin-layered structure (Fig. 4b, c). The formation of thin-layered structure results in large surface area, favoring the contact with more electrolytes for mass transfer. In addition, the (101) crystal face of γ-CoOOH can also be observed in the nanosheet, which evidenced again the phase of γ-CoOOH mainly contributing to the HMFOR catalytic activity (Fig. 4c). The sustained vertical nanostructure and integrated nanosheets after anion reconstruction endow fast ion diffusion and electron conduction throughout the electrode, further optimizing the electrocatalytic activity and durability of the composites.[43] The XRD pattern of electrode after HER reveals the diffraction peaks of Co $(OH)_2$ without CoF_2 and CoP peaks observed (Fig. 4d). The SEM images

of CoF$_2$/CoP-2 after HER test are also compared to the pristine electrode before testing, as exhibited in Fig. S14d-f. It appears that the NF is uniformly covered by newly formed nanosheets with a smooth surface after long term electrocatalysis. It can be concluded that Co species are mainly transformed into Co (OH)$_2$ and the newly converted phase is obtained by anion reconstruction as well, which benefits the catalytic performance for HER.[44] The nanosheet morphology can be demonstrated again by the TEM images (Fig. 4e, f). From the HR-TEM image, the newly generated phases are matching well with the (100) and (001) crystal planes of Co (OH)$_2$. Thus, the actual active phases between the two electrodes are clearly different, which stems from the different reaction mechanisms for the HMFOR and HER.

The change of surface chemical composition was also investigated by XPS. For the post- HMFOR catalyst, the two new peaks of the Co 2p spectrum are assigned to the Co^{3+} species in CoOOH (Fig. 4g). In F 1s, the Co-F peak can be obviously observed, while F-P peak disappears (Fig 4h). Meanwhile, the Co-P peak in P 2p spectrum also vanishes and the P-O peak has a negative shift and decreases in comparison with initial electrode (Fig. 4i). These results illustrate the successive reconstruction of CoP into metal (oxy)hydroxide during HMFOR, which is the true active species, consistent with previous reports.[45, 46] For the post-HER catalyst, we can observe the disappearance of Co^0 peaks belonging to CoP and only Co^{2+} peaks along with two satellite peaks in Co 2p spectrum. The F1s peaks of the electrode thoroughly vanish (Fig. 5h). The peak of Co-P in P 2p also disappears and P-O peak show a negative shift, which indicates that the leaching of anion triggers the phase reconstruction during HER.[47]
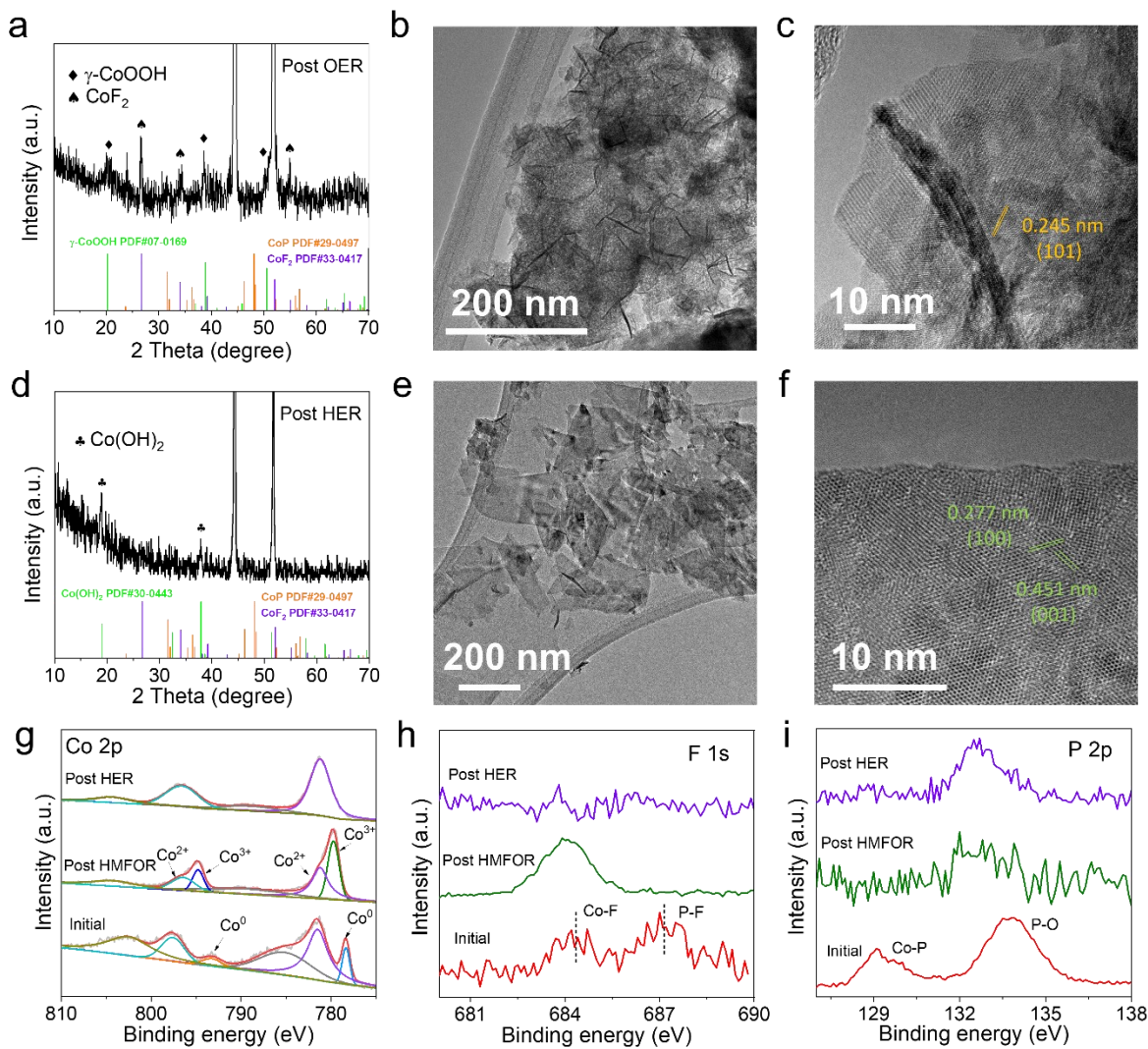
Figure 5. 4 (a) XRD patterns of CoF$_2$/CoP-2 after long term electrocatalysis test under HMFOR condition. (b, c) TEM image of CoF$_2$/CoP-2 after long-term stability test under HMFOR condition. (d) XRD patterns of CoF$_2$/CoP-2 after long term electrocatalysis test under HER condition. (e, f) TEM image of CoF$_2$/CoP-2 after long-term stability test under HER condition. (g) Co 2p, (h) F 1s, (i) P 2p XPS spectra of the CoF$_2$/CoP-2 electrode before and after electrocatalysis HMFOR/HER stability test.

5.4 Conclusion

In summary, we developed an electrode with CoF_2/CoP nanowire arrays grown on NF, which possesses good mass/electron transfer ability. The construction of heterointerfaces between CoF_2 and CoP results in the more exposure of active sites, modulating the catalytic activity for HMFOR and HER. As a result, a high electrocatalytic performance for both HMFOR and HER is achieved. Since the different reaction mechanisms for the HMFOR and HER, the newly formed γ-CoOOH after the anion reconstruction contributes to the HMFOR activity with low driving potential, high biomass conversion and selectivity, and enhanced cycle durability. The Co $(OH)_2$ is the actual active phase benefiting the catalytic performance for HER with low overpotential and good electrocatalysis stability. The CoF_2/CoP-2 was used to catalyze cathodic H_2 and anodic FDCA production synchronously, which only requires a low voltage of 1.33 V to afford 10 mA cm^{-2}. Thus, the construction of heterostructure between CoF_2 and CoP has been identified as promising strategy for both electrocatalytic HMF oxidation and HER to enhance hydrogen generation efficiency and the production of value-added products, paving a way for "green chemistry".

5.5 References

1. A. Hayat, M. Sohail, H. Ali, T.A. Taha, H.I.A. Qazi, N. Ur Rahman, Z. Ajmal, A. Kalam, A.G. Al-Sehemi, S. Wageh, M.A. Amin, A. Palamanit, W.I. Nawawi, E.F. Newair, Y. Orooji, Recent Advances and Future Perspectives of Metal-Based Electrocatalysts for Overall Electrochemical Water Splitting, *Chem. Rec*. 23 (2023) e202200149.

2. S.Y. Tee, K.Y. Win, W.S. Teo, L.D. Koh, S. Liu, C.P. Teng, M.Y. Han, Recent Progress in Energy-Driven Water Splitting, *Adv. Sci*. 4 (2017) 1600337.

3. S.-Q. Liu, M.-R. Gao, S. Liu, J.-L. Luo, Hierarchically assembling cobalt/nickel carbonate hydroxide on copper nitride nanowires for highly efficient water splitting, *Appl. Catal. B*

292 (2021) 120148.

4. Z. Wang, C. Li, K. Domen, Recent developments in heterogeneous photocatalysts for solar-driven overall water splitting, *Chem. Soc. Rev*. 48 (2019) 2109-2125.

5. C. Xing, Y. Xue, B. Huang, H. Yu, L. Hui, Y. Fang, Y. Liu, Y. Zhao, Z. Li, Y. Li, Fluorographdiyne: A Metal-Free Catalyst for Applications in Water Reduction and Oxidation, *Angew. Chem., Int. Ed*. 58 (2019) 13897-13903.

6. Y. Zhang, X. Zheng, X. Guo, J. Zhang, A. Yuan, Y. Du, F. Gao, Design of modified MOFs electrocatalysts for water splitting: High current density operation and long-term stability, *Appl. Catal. B* 336 (2023) 122891.

7. R. Frydendal, E.A. Paoli, B.P. Knudsen, B. Wickman, P. Malacrida, I.E.L. Stephens, I. Chorkendorff, Benchmarking the Stability of Oxygen Evolution Reaction Catalysts: The Importance of Monitoring Mass Losses, *Chem. Electro. Chem*. 1 (2014) 2075-2081.

8. T. Reier, H.N. Nong, D. Teschner, R. Schlögl, P. Strasser, Electrocatalytic Oxygen Evolution Reaction in Acidic Environments - Reaction Mechanisms and Catalysts, *Adv. Energy Mater*. 7 (2017) 1601275.

9. T. ul Haq, Y. Haik, A roadmap towards sustainable anode design for alkaline water electrolysis, *Appl. Catal. B* 334 (2023) 122853.

10. R. Li, K. Xiang, Z. Liu, Z. Peng, Y. Zou, S. Wang, Recent Advances in Upgrading of Low-Cost Oxidants to Value-Added Products by Electrocatalytic Reduction Reaction, *Adv. Funct. Mater*. 32 (2022) 2208212.

11. H.Y. Wang, M.L. Sun, J.T. Ren, Z.Y. Yuan, Circumventing Challenges: Design of Anodic Electrocatalysts for Hybrid Water Electrolysis Systems, *Adv. Energy Mater*. 13 (2022) 2203568.

12. N. Zhang, Y. Zou, L. Tao, W. Chen, L. Zhou, Z. Liu, B. Zhou, G. Huang, H. Lin, S. Wang, Electrochemical Oxidation of 5-Hydroxymethylfurfural on Nickel Nitride/Carbon Nanosheets: Reaction Pathway Determined by In Situ Sum Frequency Generation Vibrational Spectroscopy, *Angew. Chem., Int. Ed*. 58 (2019) 15895-15903.

13. B. You, X. Liu, N. Jiang, Y. Sun, A General Strategy for Decoupled Hydrogen Production from Water Splitting by Integrating Oxidative Biomass Valorization, *J. Am. Chem. Soc*. 138 (2016) 13639-13646.

14. Y. Lu, C.L. Dong, Y.C. Huang, Y. Zou, Z. Liu, Y. Liu, Y. Li, N. He, J. Shi, S. Wang, Identifying the Geometric Site Dependence of Spinel Oxides for the Electrooxidation of 5-Hydroxymethylfurfural, *Angew. Chem., Int. Ed*. 59 (2020) 19215-19221.

15. S.H. Swan, Environmental phthalate exposure in relation to reproductive outcomes and other health endpoints in humans, *Environ. Res*. 108 (2008) 177-184.

16. Y. Xie, L. Sun, X. Pan, Z. Zhou, G. Zhao, Selective two-electron electrocatalytic conversion of 5-Hydroxymethylfurfural boosting hydrogen production under neutral condition over $Co(OH)_2$-CeO_2 catalyst, *Appl. Catal. B* 338 (2023) 123068.

17. T. Wang, X. Cao, L. Jiao, Progress in Hydrogen Production Coupled with Electrochemical Oxidation of Small Molecules, *Angew. Chem., Int. Ed*. 61 (2022) e202213328.

18. B. You, N. Jiang, X. Liu, Y. Sun, Simultaneous H_2 Generation and Biomass Upgrading in Water by an Efficient Noble-Metal-Free Bifunctional Electrocatalyst, *Angew. Chem., Int. Ed*. 55 (2016) 9913-9917.

19. Y. Wang, M. Zhang, Y. Liu, Z. Zheng, B. Liu, M. Chen, G. Guan, K. Yan, Recent Advances on Transition-Metal-Based Layered Double Hydroxides Nanosheets for Electrocatalytic Energy Conversion, *Adv. Sci*. 10 (2023) e2207519.

20. X. Luo, P. Ji, P. Wang, R. Cheng, D. Chen, C. Lin, J. Zhang, J. He, Z. Shi, N. Li, S. Xiao, S. Mu, Interface Engineering of Hierarchical Branched Mo-Doped Ni_3S_2/Ni_xP_y Hollow Heterostructure Nanorods for Efficient Overall Water Splitting, *Adv. Energy Mater*., 10 (2020) 1903891.

21. J. Shan, Y. Zheng, B. Shi, K. Davey, S.-Z. Qiao, Regulating Electrocatalysts via Surface and Interface Engineering for Acidic Water Electrooxidation, *ACS Energy Lett*. 4 (2019) 2719-2730.

22. Y.J. Sa, C.W. Lee, S.Y. Lee, J. Na, U. Lee, Y.J. Hwang, Catalyst-electrolyte interface chemistry for electrochemical CO_2 reduction, *Chem. Soc. Rev*. 49 (2020) 6632-6665.

23. G. Yang, Y. Jiao, H. Yan, Y. Xie, A. Wu, X. Dong, D. Guo, C. Tian, H. Fu, Interfacial Engineering of MoO_2 -FeP Heterojunction for Highly Efficient Hydrogen Evolution Coupled with Biomass Electrooxidation, *Adv. Mater*. 32 (2020) e2000455.

24. Y. Zhang, Y. Lin, T. Duan, L. Song, Interfacial engineering of heterogeneous catalysts for electrocatalysis, *Mater. Today*, 48 (2021) 115-134.

25. S.-Q. Liu, H.-R. Wen, G. Ying, Y.-W. Zhu, X.-Z. Fu, R. Sun, C.-P. Wong, Amorphous $Ni(OH)_2$ encounter with crystalline CuS in hollow spheres: A mesoporous nano-shelled heterostructure for hydrogen evolution electrocatalysis, *Nano Energy*, 44 (2018) 7-14.

26. W. Yuan, T. Jiang, X. Fang, Y. Fan, S. Qian, Y. Gao, N. Cheng, H. Xue, J. Tian, Interface engineering of S-doped $Co_2P@Ni_2P$ core–shell heterostructures for efficient and energy-saving water splitting, *Chem. Eng. J*. 439 (2022) 135743.

27. H. Wang, Y. Zhou, S. Tao, CoP-CoOOH heterojunction with modulating interfacial electronic structure: A robust biomass-upgrading electrocatalyst, *Appl. Catal. B* 315 (2022) 121588.

28. T. Liu, P. Li, N. Yao, G. Cheng, S. Chen, W. Luo, Y. Yin, CoP-Doped MOF-Based Electrocatalyst for pH-Universal Hydrogen Evolution Reaction, *Angew. Chem., Int. Ed*. 58 (2019) 4679-4684.

29. Z. Liang, W. Zhou, S. Gao, R. Zhao, H. Zhang, Y. Tang, J. Cheng, T. Qiu, B. Zhu, C. Qu, W. Guo, Q. Wang, R. Zou, Fabrication of Hollow CoP/TiO$_x$ Heterostructures for Enhanced Oxygen Evolution Reaction, *Small*, 16 (2020) e1905075.

30. J.X. Feng, S.Y. Tong, Y.X. Tong, G.R. Li, Pt-like Hydrogen Evolution Electrocatalysis on PANI/CoP Hybrid Nanowires by Weakening the Shackles of Hydrogen Ions on the Surfaces of Catalysts, *J. Am. Chem. Soc*. 140 (2018) 5118-5126.

31. A.D. Wilson, R.H. Newell, M.J. McNevin, J.T. Muckerman, M. Rakowski DuBois, D.L. DuBois, Hydrogen oxidation and production using nickel-based molecular catalysts with positioned proton relays, *J. Am. Chem. Soc*. 128 (2006) 358-366.

32. E.J. Popczun, J.R. McKone, C.G. Read, A.J. Biacchi, A.M. Wiltrout, N.S. Lewis, R.E. Schaak, Nanostructured nickel phosphide as an electrocatalyst for the hydrogen evolution reaction, *J. Am. Chem. Soc*. 135 (2013) 9267-9270.

33. Y. Lin, K. Sun, S. Liu, X. Chen, Y. Cheng, W.C. Cheong, Z. Chen, L. Zheng, J. Zhang, X. Li, Y. Pan, C. Chen, Construction of CoP/NiCoP Nanotadpoles Heterojunction Interface for Wide pH Hydrogen Evolution Electrocatalysis and Supercapacitor, *Adv. Energy Mater.* 9 (2019) 1901213.

34. P.A. O'Day, J.J. Rehr, S.I. Zabinsky, G.E. Brown, Jr., Extended X-ray Absorption Fine Structure (EXAFS) Analysis of Disorder and Multiple-Scattering in Complex Crystalline Solids, *J. Am. Chem. Soc*. 116 (2002) 2938-2949.

35. K. Xu, H. Cheng, H. Lv, J. Wang, L. Liu, S. Liu, X. Wu, W. Chu, C. Wu, Y. Xie,

Controllable Surface Reorganization Engineering on Cobalt Phosphide Nanowire Arrays for Efficient Alkaline Hydrogen Evolution Reaction, *Adv. Mater*. 30 (2018) 1703322.

36. Z. Chen, C.X. Kronawitter, B.E. Koel, Facet-dependent activity and stability of Co_3O_4 nanocrystals towards the oxygen evolution reaction, *Phys. Chem. Chem. Phys*. 17 (2015) 29387-29393.

37. G. Rajeshkhanna, E. Umeshbabu, G.R. Rao, In situ grown nano-architectures of Co_3O_4 on Ni-foam for charge storage application, *J. Chem. Sci*. 129 (2016) 157-166.

38. T.I. Singh, G. Rajeshkhanna, U.N. Pan, T. Kshetri, H. Lin, N.H. Kim, J.H. Lee, Alkaline Water Splitting Enhancement by MOF-Derived Fe-Co-Oxide/Co@NC-mNS Heterostructure: Boosting OER and HER through Defect Engineering and In Situ Oxidation, *Small*, 17 (2021) e2101312.

39. X. Wan, C. Zhou, J. Chen, W. Deng, Q. Zhang, Y. Yang, Y. Wang, Base-Free Aerobic Oxidation of 5-Hydroxymethyl-furfural to 2,5-Furandicarboxylic Acid in Water Catalyzed by Functionalized Carbon Nanotube-Supported Au–Pd Alloy Nanoparticles, *ACS Catal*. 4 (2014) 2175-2185.

40. M.-M. Zhu, X.-L. Du, Y. Zhao, B.-B. Mei, Q. Zhang, F.-F. Sun, Z. Jiang, Y.-M. Liu, H.-Y. He, Y. Cao, Ring-Opening Transformation of 5-Hydroxymethylfurfural Using a Golden Single-Atomic-Site Palladium Catalyst, *ACS Catal*. 9 (2019) 6212-6222.

41. J. Hu, C. Zhang, L. Jiang, H. Lin, Y. An, D. Zhou, M.K.H. Leung, S. Yang, Nanohybridization of MoS_2 with Layered Double Hydroxides Efficiently Synergizes the Hydrogen Evolution in Alkaline Media, *Joule*, 1 (2017) 383-393.

42. S.-W. Wu, S.-Q. Liu, X.-H. Tan, W.-Y. Zhang, K. Cadien, Z. Li, Ni_3S_2-embedded NiFe LDH porous nanosheets with abundant heterointerfaces for high-current water electrolysis,

Chem. Eng. J. 442 (2022) 136105.

43. Q. Dong, T. Su, W. Ge, Y. Ren, Y. Liu, W. Wang, Q. Wang, X. Dong, Atomic Doping and Anion Reconstructed CoF_2 Electrocatalyst for Oxygen Evolution Reaction, *Adv. Mater. Interfaces* 7 (2020) 1901939.

44. P. Ji, R. Yu, P. Wang, X. Pan, H. Jin, D. Zheng, D. Chen, J. Zhu, Z. Pu, J. Wu, S. Mu, Ultra-Fast and In-Depth Reconstruction of Transition Metal Fluorides in Electrocatalytic Hydrogen Evolution Processes, *Adv. Sci.* 9 (2022) e2103567.

45. X. Deng, G.Y. Xu, Y.J. Zhang, L. Wang, J. Zhang, J.F. Li, X.Z. Fu, J.L. Luo, Understanding the Roles of Electrogenerated Co^{3+} and Co^{4+} in Selectivity-Tuned 5-Hydroxymethylfurfural Oxidation, *Angew. Chem., Int. Ed.* 60 (2021) 20535-20542.

46. Q. Fu, T. Wu, G. Fu, T. Gao, J. Han, T. Yao, Y. Zhang, W. Zhong, X. Wang, B. Song, Skutterudite-Type Ternary $Co_{1-x}Ni_xP_3$ Nanoneedle Array Electrocatalysts for Enhanced Hydrogen and Oxygen Evolution, *ACS Energy Lett.* 3 (2018) 1744-1752.

47. J. Liu, Y. Gao, X. Tang, K. Zhan, B. Zhao, B.Y. Xia, Y. Yan, Metal–organic framework-derived hierarchical ultrathin CoP nanosheets for overall water splitting, *J. Mater. Chem A*, 8 (2020) 19254-19261.

5.6 Supporting information
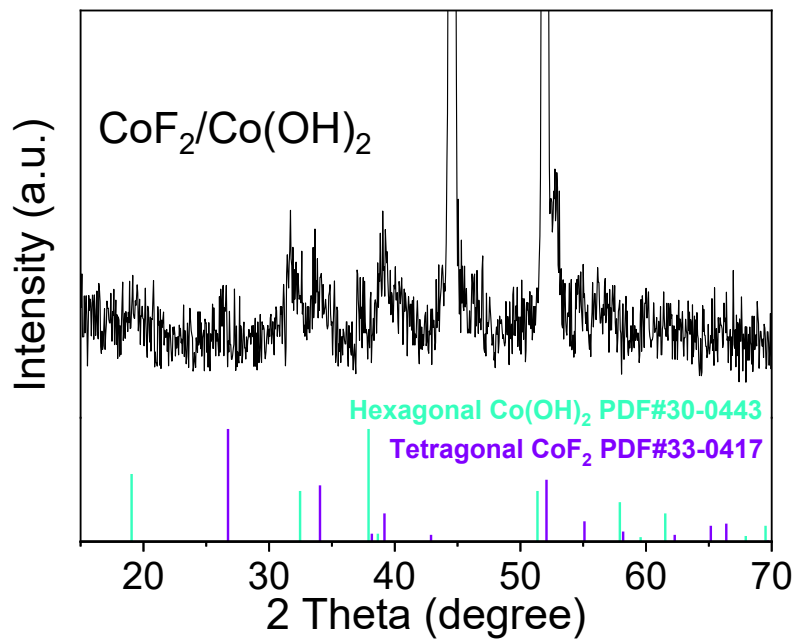
Figure S5. 1 XRD pattern of the product after fluorination process
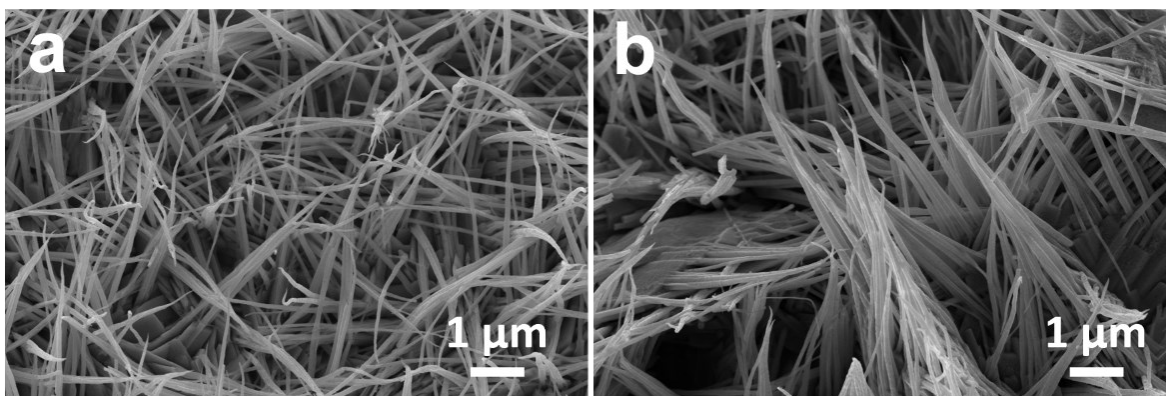
Figure S5. 2 SEM images of CoP (a), CoF$_2$ (b).
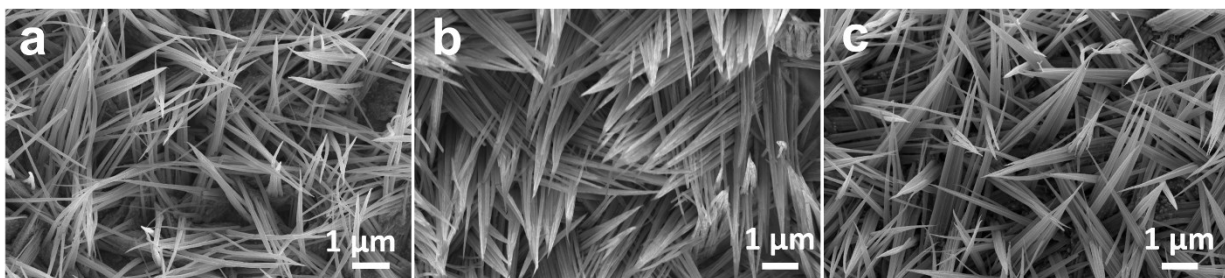
Figure S5. 3 SEM images of CoF$_2$/CoP-1 (a), CoF$_2$/CoP-2 (b) and CoF$_2$/CoP-3(c)
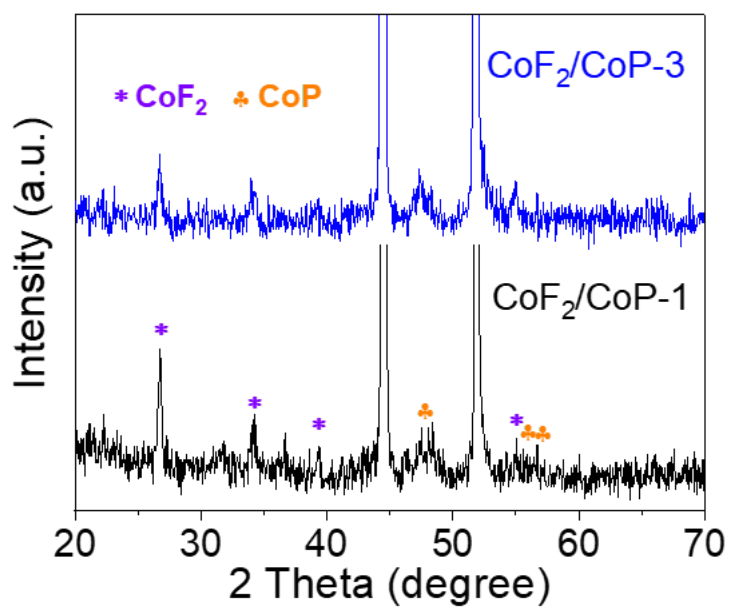
Figure S5. 4 XRD patterns of CoF$_2$/CoP-1 and CoF$_2$/CoP-3.
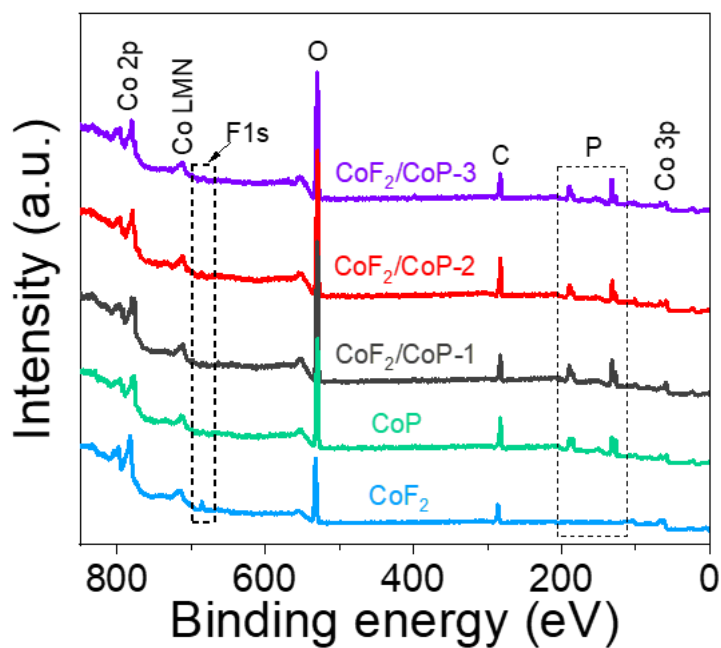
Figure S5. 5 The wide-scanning XPS spectra of CoF_2, CoP, CoF_2/CoP-1, CoF_2/CoP-2 and CoF_2/CoP-3.
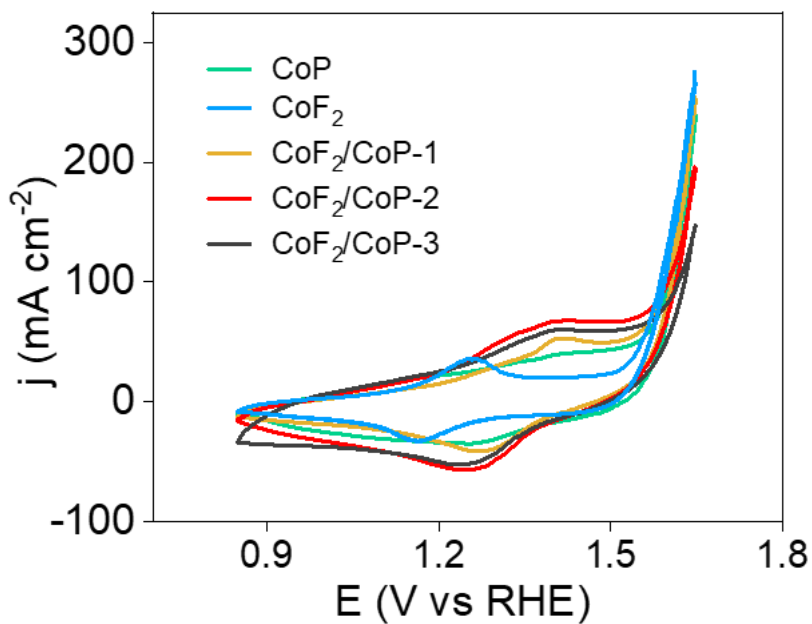
Figure S5. 6 The CV of CoF_2, CoP, CoF_2/CoP-1, CoF_2/CoP-2 and CoF_2/CoP-3 toward OER.
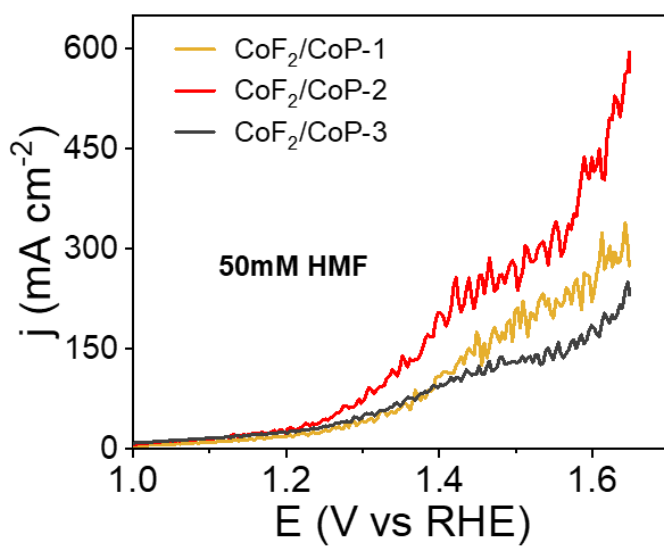
Figure S5. 7 The polarization curves of CoF$_2$/CoP-1, CoF$_2$/CoP-2 and CoF$_2$/CoP-3 toward HMFOR.
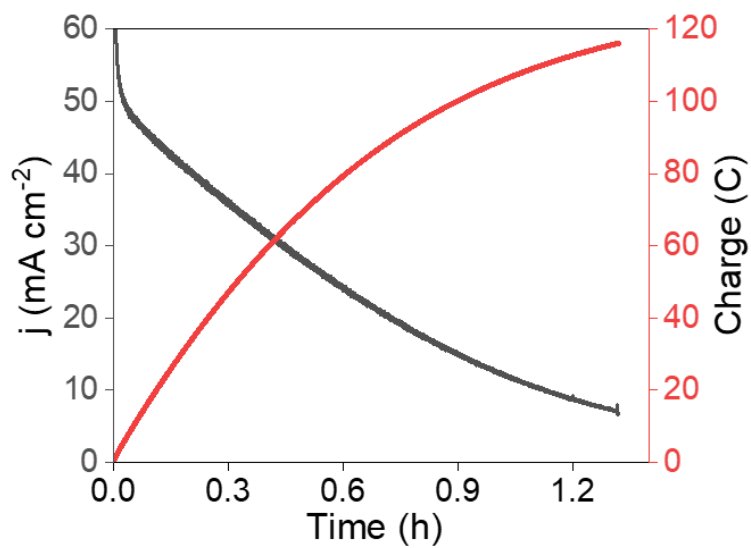
Figure S5. 8 I-t curve for CoF$_2$/CoP-2 at a constant potential of 1.43 V in 1.0 M KOH with 10 mM HMF by passing the charge of 116 C.
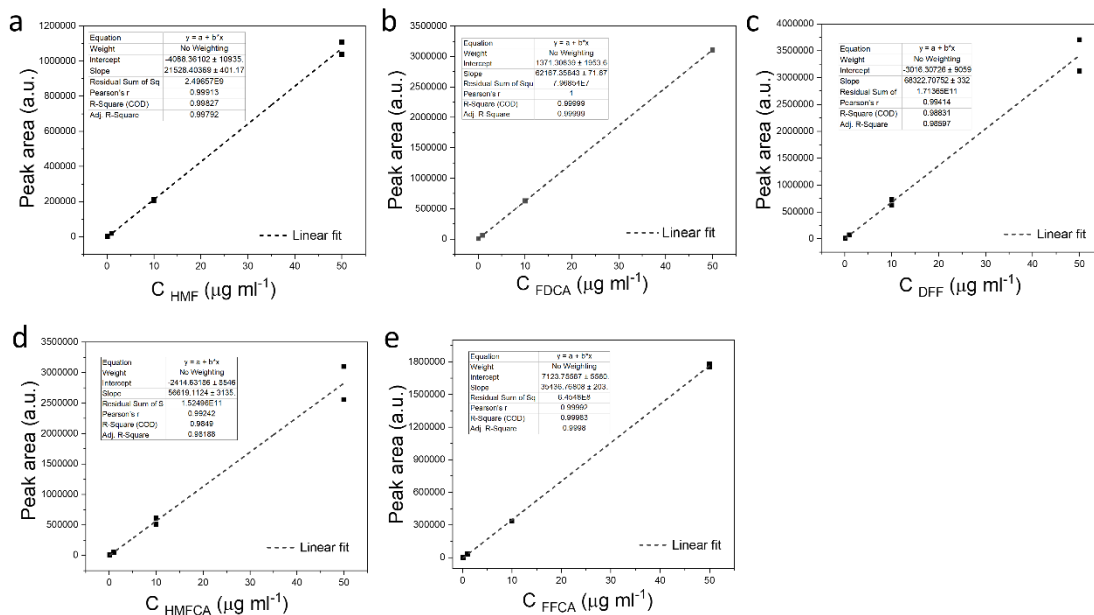
Figure S5. 9 Calibration of the HPLC for HMF (a), FDCA (b), DFF (c), HMFCA (d) and FFCA (e).
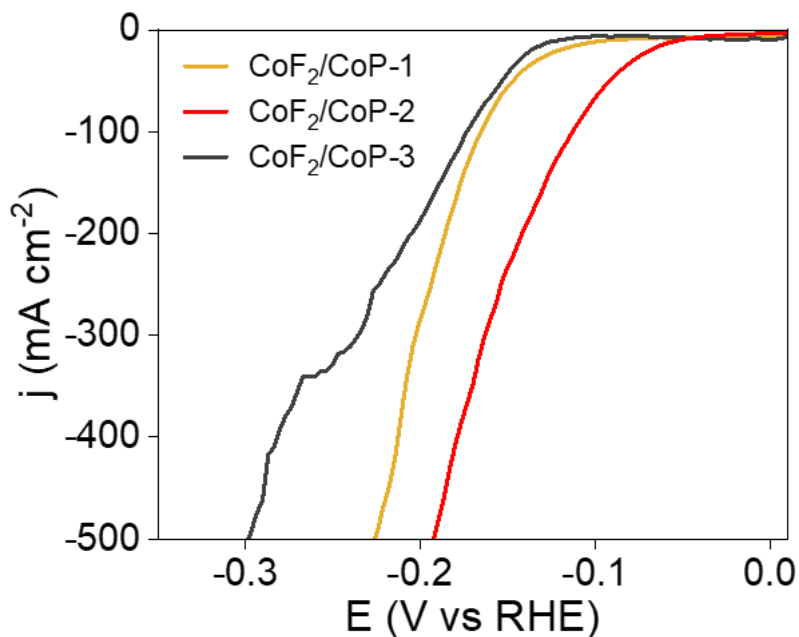
Figure S5. 10 The polarization curves of CoF$_2$/CoP-1, CoF$_2$/CoP-2 and CoF$_2$/CoP-3 toward HER.
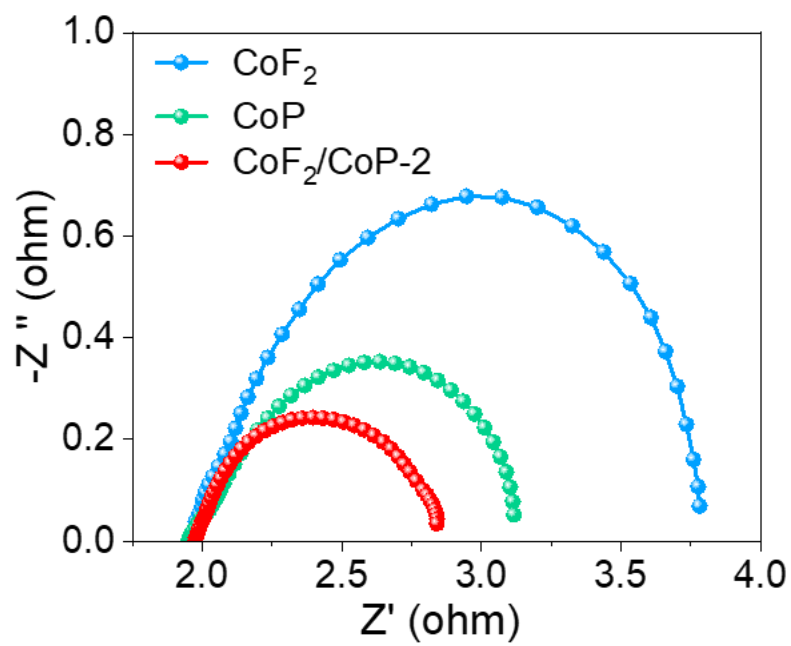
Figure S5. 11 EIS spectra of CoF_2, CoP and CoF_2/CoP-2 towards HER.
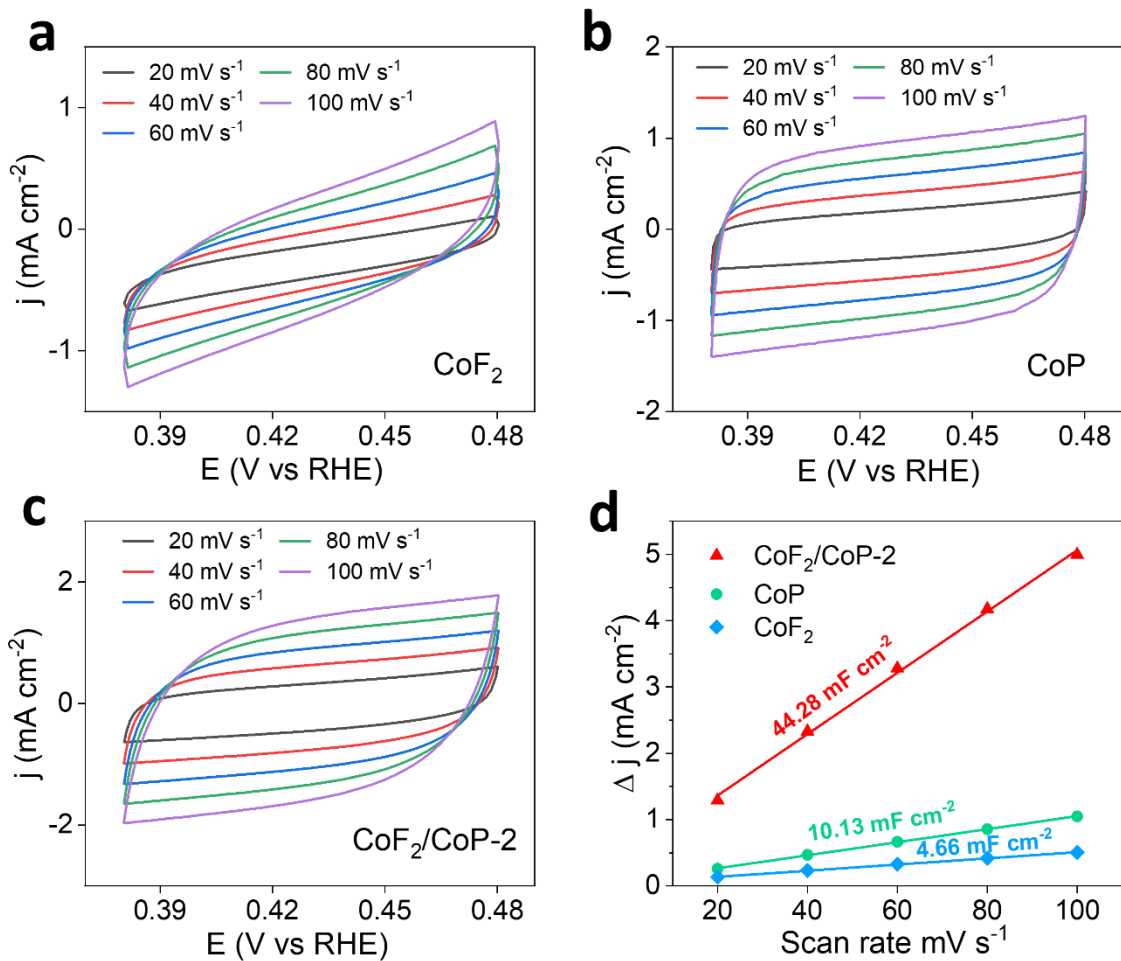
Figure S5. 12 (a-c) CV curves within a non-faradaic reaction region of -0.69 ~ -0.59 V versus RHE at different scan rates for CoF_2, CoP and CoF_2/CoP-2. (d) The corresponding C_{dl} value.
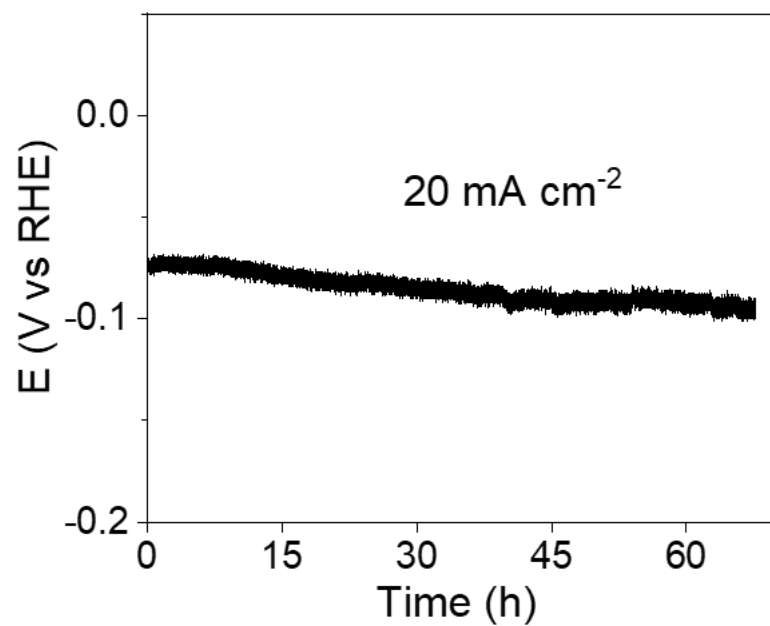
Figure S5. 13 Chronopotentiometry of CoF$_2$/CoP-2 under the current density of 20 mA cm^{-2}.
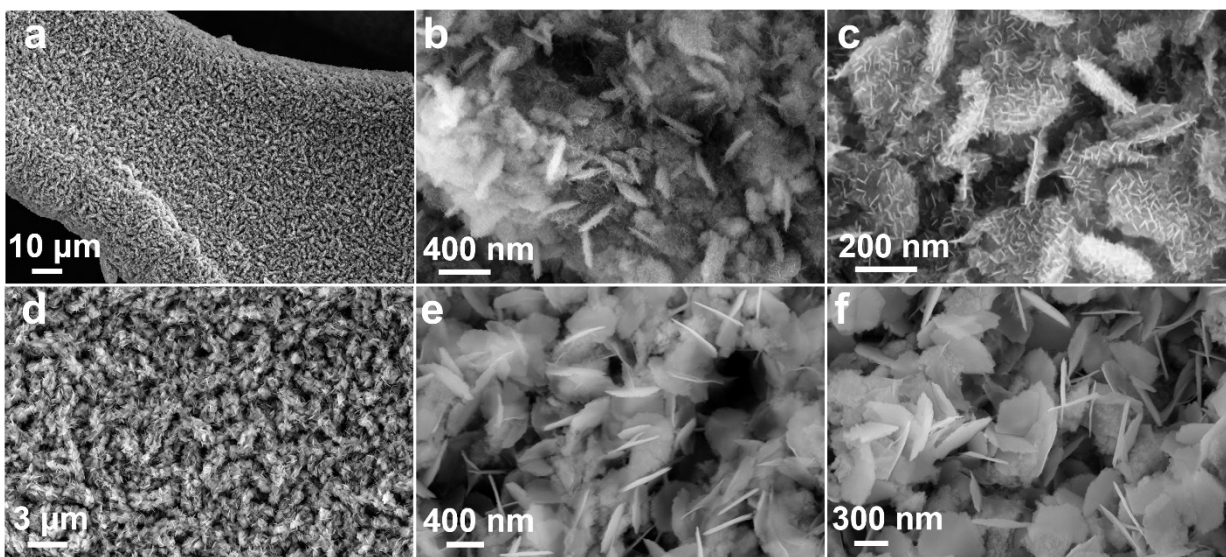
Figure S5. 14 SEM images of CoF$_2$/CoP-2 after long-term electrocatalysis under HMFOR condition (a-c) and HER condition (d-f).
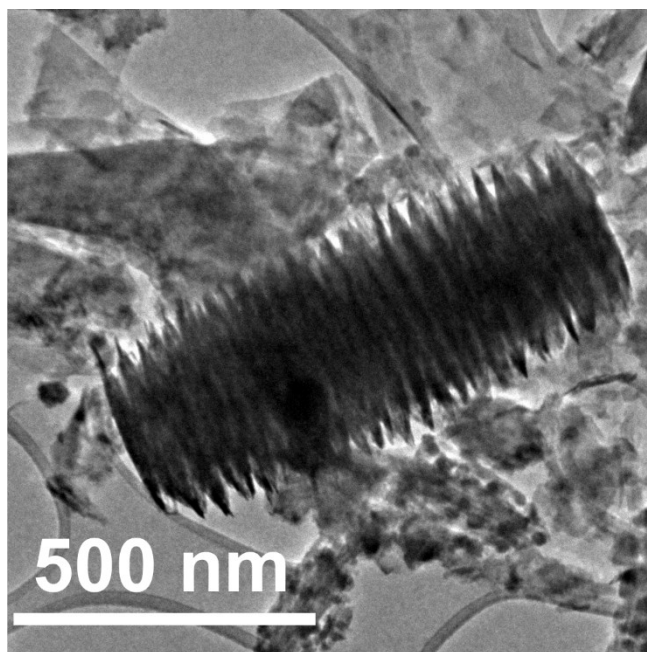
Figure S5. 15 TEM image of CoF$_2$/ CoP-2 after long term HMFOR electrocatalysis.

Chapter 6. Single Cu–N₄ sites enable atomic Fe clusters with high-performance oxygen reduction reaction

Abstract: Atomically dispersed Fe–N₄ catalysts are proved as promising alternatives to commercial Pt/C for the oxygen reduction reaction. Most reported Fe–N₄ catalysts suffer from inferior O–O bond-breaking capability due to superoxo-like O_2 adsorption, though the isolated dual-atomic metal sites strategy is extensively adopted. Atomic Fe clusters hold greater promise for promoting O–O bond cleavage by forming peroxo-like O_2 adsorption. However, the excessively strong binding strength between Fe clusters and oxygenated intermediates sacrifices the activity. Here, we first report a Fe_x/Cu–N@CF catalyst with atomic Fe clusters functionalized by adjacent single Cu–N₄ sites anchoring on porous carbon nanofiber membrane. The theoretical calculation indicates that the single Cu–N₄ sites can modulate the electronic configuration of Fe clusters to reduce O_2* protonation reaction free energy which ultimately enhances the electrocatalytic performance. Particularly, the Cu–N₄ sites can increase the overlaps between d orbitals of Fe and p orbitals of O to accelerate O–O cleavage in OOH*. As a result, this unique atomic catalyst exhibits a half potential ($E_{1/2}$) of 0.944 V in an alkaline medium exceeding that of commercial Pt/C, whereas acidic performance $E_{1/2}$ = 0.815 V is comparable to Pt/C. This work shows the great potential of single atoms for improvements of atomic cluster catalysts.

6.1 Introduction

The development of highly efficient and low-cost electrocatalysts for oxygen reduction reaction (ORR) is significantly urgent for fuel cells and metal-air batteries.[1-6] However, the high energy needs of O=O bond breaking and sluggish kinetics of the $4e^-/4H^+$ transfer process result in most electrocatalysts suffering from unsatisfactory ORR performance.[7-9] Although platinum-group-metal (PGM)-based catalysts exhibit state-of-the-art activity toward ORR, their scalable

implementation is restricted to the price and scarcity.[10-13] Fe–N–C single-atom catalysts (SACs) with Fe–N$_4$ moieties dispersed on carbon matrix have been considered as promising alternatives to PGM due to the maximized atomic utilization and low cost.[14-16] Despite this, substituting PGM catalysts with Fe–N$_4$ catalysts while achieving superior activity and robust stability for practical applications still remains a grand challenge.

An ideal ORR catalyst for substitution of PGM catalysts firstly should possess favourable O$_2$ activation sites for efficient O=O bond cleavage due to the very high O=O bond energy of 498 kJ mol^{-1}.[17] Fe–N$_4$ tends to bond only one oxygen atom of O$_2$ to form superoxo-like adsorption because of its simple and symmetric structure.[18-20] This adsorption configuration will result in two-electron side reaction (O$_2$ reaction to H$_2$O$_2$) and slow catalytic kinetics due to high energy barrier of O–O bond cleavage. As compared with Fe–N$_4$, multinuclear Fe sites (such as atomic Fe clusters) could accelerate O–O bond cleavage by forming a stretched peroxo-like O$_2$ adsorption (two oxygen atoms of O$_2$ bonded to two adjacent Fe atoms).[21] However, the peroxo-like adsorption results in relatively strong binding strength with *O$_2$,[22] which may be an obstacle for the next hydrogenation step. An effective way to solve this problem is to adjust the electronic structure of the active sites by introducing another metallic center. For example, various secondary metal sites, such as Ni–N$_4$,[23] Mn–N$_4$,[24] Pt–N$_4$,[25] Co–N$_4$,[26] and Cu–N$_4$,[27] have been introduced to modulate the electronic structure of Fe–N$_4$. However, the electronic modification of atomic Fe clusters by another single metal atom has been overlooked as compared with Fe–N$_4$, let alone the in-depth understanding of the interaction between them.

Another key factor for efficient Fe–N–C catalysts is that they should possess well-defined pore structure.[28, 29] To date, most reported Fe–N–C catalysts are prepared by direct pyrolysis of zeolitic imidazolate frameworks (ZIFs) with abundant micropores. Unfortunately, only the FeN$_x$ sites near

the external surface of the ZIF-derived catalysts could contribute to ORR, whereas those interior

FeN_x sites buried in the dense carbon matrix are inactive.[30, 31] This is because protons and O_2

molecules can hardly penetrate these micropores with small openings (1–2 nm).[32, 33] Such an

obstacle can be mitigated by constructing crosslinked one-dimensional (1D) carbon nanofibers

(CNF) with sufficient microporosity for hosting active FeN_x sites as well as interconnected meso-

and macropores for efficient mass and charge transfer. Electrospinning has been proved a practical

strategy to introduce large meso- and macropores.[34] Hence, we hypothesized that introducing

single atom sites (i.e., CuN_4) into atomic Fe clusters and simultaneously integrating them with

hierarchical porous CNF is particularly appealing for ORR.

Herein, we report an effective strategy of Cu–N_4 sites functionalizing atomic Fe clusters on a

hierarchical porous carbon nanofiber (Fe_x/Cu–N@CNF) via electrospinning for high performance

ORR. Density of functional theory (DFT) calculations reveal that the single Cu–N_4 sites assist the

activation of O_2 to reduce the energy barrier of O_2* protonation, as well as modulate the overlap

of Fe d orbitals and O p orbitals to facilitate O–O bond cleavage in OOH*, thus significantly

boosting the overall ORR. Concurrently, the interconnected micro- and mesopores within Fe_x/Cu–

N@CNF enable abundant accessible active sites and fast mass transport. Electrochemical

measurements show that Fe_x/Cu–N@CNF exhibits superior performances with an onset potential

(E_{onset}) of 1.03 V, an ultrahigh half-wave potential ($E_{1/2}$) of 0.944 V, and remarkable durability in

alkaline medium, outperforming commercial Pt/C and most reported catalysts. Moreover, when

applied in zinc-batteries, it achieves an impressive specific capacity (1110.4 mA h g^{-1} at 100 mA

cm^{-2}) and long-cycling over 400 h, exceeding those Pt/C-based devices. This work not only

highlights the influence of single atoms on atomic metal clusters but also provides a new and

efficient strategy for designing highly active catalysts.

6.2 Results and Discussion

6.2.1 Sample synthesis and structural characterization

The fabrication approach of $Fe_x/Cu–N@CF$ is described in Scheme 6.1, which involves electrospinning process, thermal treatment, and chemical vapor deposition (CVD). Typically, Cu doped zeolitic imidazolate framework-8 (Cu/ZIF–8) nanoparticles (NPs) with an average size of ~ 50 nm were first prepared (Figure S6.1). Then, these Cu/ZIF–8 NPs and melamine were well-dispersed into polyacrylonitrile (PAN) solution. This mixture solution was electrospun into a three-dimensional (3D) membrane consisting of Cu/ZIF–8 embedded 1D polymeric fibers (Cu/ZIF–8@PF). A rough surface was observed over Cu/ZIF–8@PF precursor due to the presence of Cu/ZIF–8 in the PF (Figure S6.2). Afterward, pre-oxidation and carbonization two-step thermal treatments were implemented to form atomically dispersed Cu anchored N-doped porous carbon fibers (Cu–N@CF). The pre-oxidation in air was used to stabilize the microstructure and avoid the fusion of CFs in the later subsequent carbonization step. During the carbonization process in argon, the Zn species were evaporated from Cu/ZIF-8 and created carbon defects. Meanwhile, $Cu–N_4$ species were in situ formed by coordinating with four N atoms. Finally, atomic Fe clusters were introduced into Cu–N@CF to form $Fe_x/Cu–N@CF$ via a CVD process using anhydrous $FeCl_3$ as the Fe source. Solid $FeCl_3$ with a low boiling point of ~316 °C will become a Fe_2Cl_6 vapour and directly deposit on the defect sites of Cu–N@CF. The sample only contained atomic Fe clusters on CF ($Fe_x–N@CF$) was prepared by using pristine ZIF–8 for electrospinning.
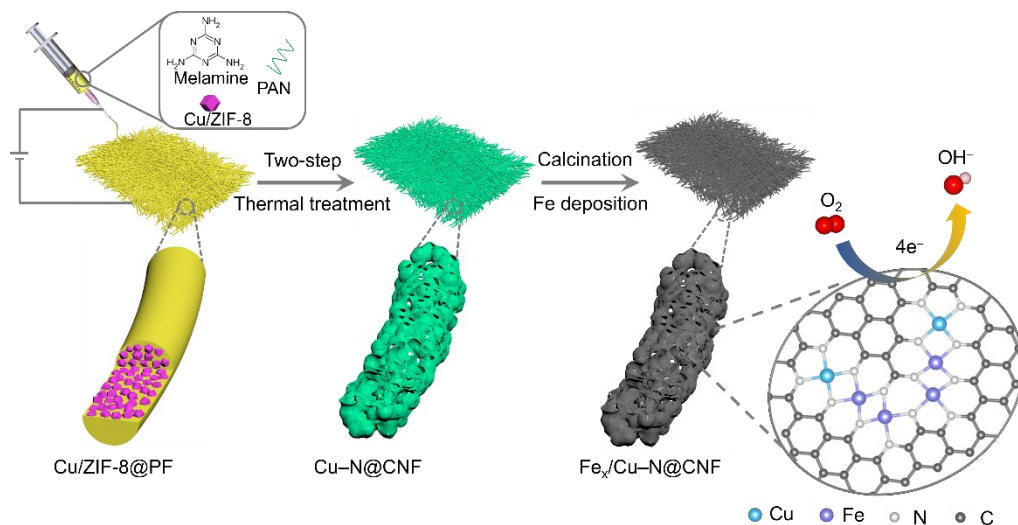
Scheme 6.1. The synthesis procedure of Fe_x/Cu–N@CF.

The morphology of Fe_x/Cu–N@CF was revealed by scanning electron microscopy and transmission electron microscopy. Clearly, the CFs of Fe_x/Cu–N@CF formed a 3D interconnected network with the diameter of CF ranging from 200 to 500 nm (Figure 6.1a). The higher-resolution SEM and TEM images (Figure 6.1b-e and Figure S6.3a, b) show that a large amount of mesopores is uniformly distributed throughout these nanofibers. The size of these mesopores is about 50 nm, close to the size of Cu/ZIF–8 nanoparticles. This well-distributed pore structure could facilitate the electrolyte penetration and O_2 reactants diffusion for ORR. A similar morphology is also observed for Fe_x–N@CF and Cu–N@CF (Figure S6.4). The textural porosity of samples was further inspected by N_2 adsorption-desorption isotherms measurement (Figure S6.5). The surface area of Fe_x/Cu–N@CF was up to 478 m^2 g^{-1} based on the BET measurement. The pore size distribution curves show that the as-prepared catalysts possess dominate micropores of 1–2 nm and mesopores of 2–50 nm, which agrees well with SEM and TEM results. The mesoporous structure was expected to enhance mass transportation and utilization of active sites, causing the remarkable O_2 adsorption capacity of the catalyst under the O_2-saturated electrolyte.[32, 35, 36] It is

149

noteworthy that no metallic particles exist in the $Fe_x/Cu-N@CF$ (Figure 6.1f). The X-ray diffraction (XRD) patterns of prepared samples show only two broad diffraction peaks assigned to the (002) and (100) planes of carbon (Figure S6.6). Peaks of the crystalline metal (oxide) species could not be resolved within the resolution of the used diffractometer.
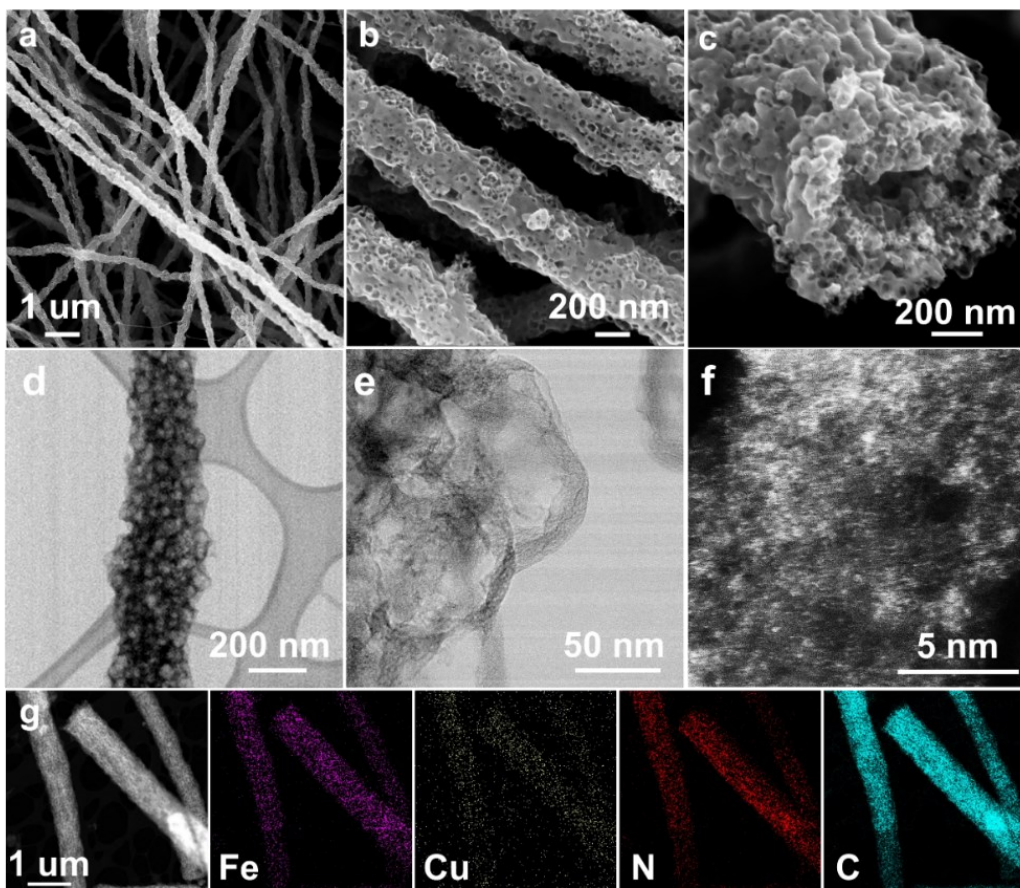
Figure 6. 1 (a) Low-resolution and (b-c) high-resolution SEM images of $Fe_x/Cu-N@CF$. (d-f) HAADF-STEM images of $Fe_x/Cu-N@CF$. (g) HAADF-STEM image and corresponding EDS mapping of $Fe_x/Cu-N@CF$.

Energy dispersive X-ray spectroscopy (EDS) elemental mapping shows the coexistence of Fe, Cu, N, and C elements over $Fe_x/Cu-N@CF$ (Figure 6.1g). To figure out how the metal species exist in the CF, aberration-corrected HADDF-STEM was utilized. As shown in Figure 6.2a, the HRTEM

image of Cu–N@CF displays individual bright dots (marked with blue circles), indicating the atomic distribution of Cu atoms. The HAADF-STEM image in magnified scale further indicates the single atomic Cu in Cu–N@CF (Figure S6.7). After the CVD process, plentiful larger spots (marked with pink circles) were observed (Figure 6.2b), which can be assigned to Fe clusters. The high magnitude image more clearly shows the atomic cluster close to single atoms (Figure S6.8). The HADDF-STEM and EDS mapping images in magnified scale further reveal the existence of Fe clusters and homogenous distribution of Cu, N, and C elements (Figure S6.9). For Fe_x–N@CF, Fe clusters are randomly distributed on the carbon support (Figure S6.10). Furthermore, the atomic-resolution elemental analysis via electron energy-loss spectroscopy (EELS) line scan clearly reveals that only Fe elements can be detected in the bright cluster (Figure S6.11). As shown in Figure S6.11a, the bright cluster is surrounded by single atoms. When the beam was moved to the cluster edge area, both Fe and Cu elements can be detected, but the intensity of the signal of Cu is much weaker than that of Fe, suggesting the single atomic Cu distribution. It is demonstrated that the bright cluster spots are comprised of only Fe, and Cu single atoms are distributed on the edge of Fe clusters. Inductively coupled plasma optical emission spectrometer (ICP-OES) tests determined that the mass loading of Fe and Cu in Fe_x/Cu–N@CF is about 2.23 and 0.57 wt%, respectively (Table S6.1). X-ray photoelectron spectroscopy (XPS) was adopted to further detect the surface chemical composition of as-prepared catalysts. Signals for Fe, Cu, N and C elements are observed in the survey XPS spectrum of Fe_x/Cu–N@CF (Figure S6.12), consistent with the EDS elemental mapping. The high resolution of the N 1s spectra of prepared catalysts (Figure S6.13a) can deconvolute into pyridinic N (398.5 eV), metal–N (399.8 eV), pyrrolic N (400.8 eV) and graphitic N (401.5 eV).[37-39] It is noted that the peak energy of metal–N bond obviously increased after the deposition of Fe atoms on the Cu–N@CF, demonstrating the formation of Fe–

N moieties in Fe_x/Cu–N@CF. Besides, as shown in Figure S6.13b, c, the binding energy of Fe shows a positive shift of approximately 0.5 eV, while Cu negatively shifts 0.5 eV, which could be attributed to the electronic interaction between Cu and Fe, indicating the higher oxidation state of Fe and lower valence of Cu in Fe_x/Cu–N@CF in comparison to that of Fe_x–N@CF and Cu–N@CF, respectively.[40]
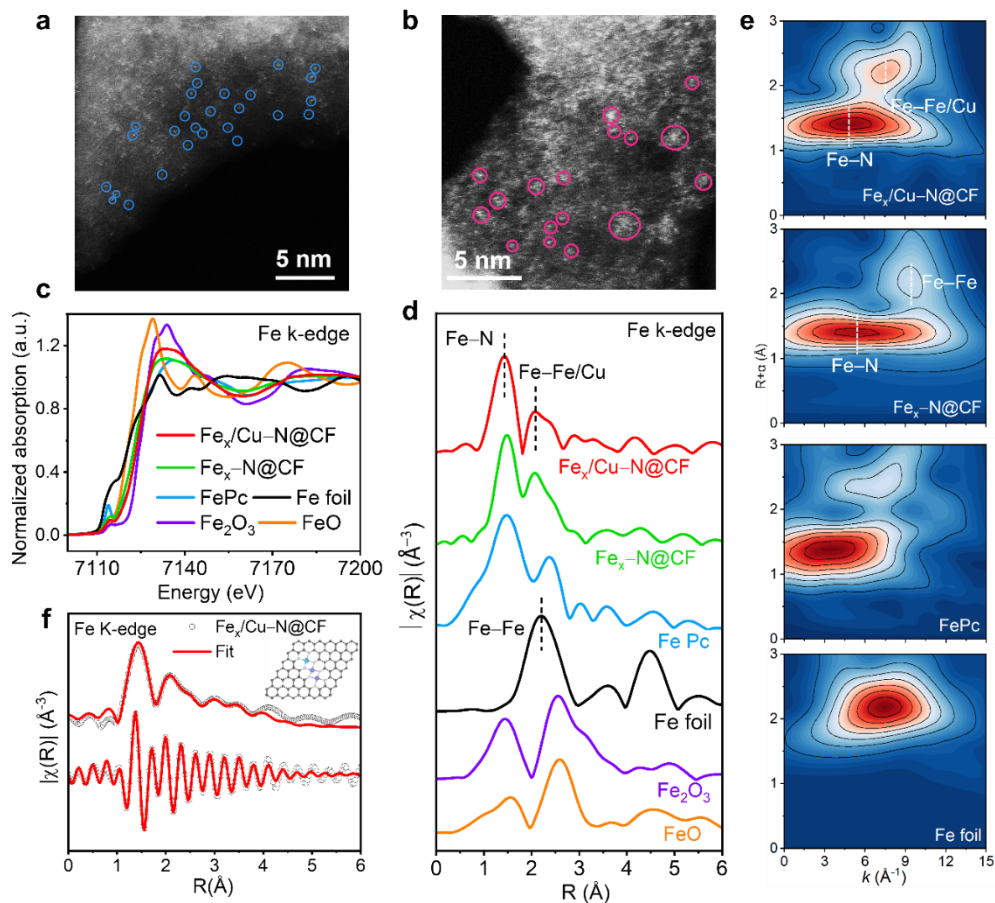
Figure 6. 2 HAADF-STEM images of (a) Cu-N@CF and (b) Fe_x/Cu-N@CF. (c) Fe K-edge XANES spectra and (d) Fourier-transform EXAFS curves of Fe_x/Cu–N@CF, Fe_x–N@CF and references (Fe Pc, Fe foil, Fe_2O_3, FeO). (e) WT-EXAFS of Fe_x/Cu–N@CF, Fe_x–N@CF, Fe Pc and Fe foil. (f) Fe K-edge experimental and FT-EXAFS fitting curves of Fe_x/Cu–N@CF in R-space (FT magnitude and imaginary component) (inset is the corresponding structure model).

To resolve the chemical states and coordination configurations of Fe and Cu sites in $Fe_x/Cu–N@CF$, $Fe_x–N@CF$ and $Cu–N@CF$, X-ray absorption near-edge structure (XANES) and extended X-ray absorption fine structure (EXAFS) measurements were conducted at the K-edge in reference to Fe foil, FePc, Fe_2O_3, FeO, Cu foil, CuPc, CuO and Cu_2O. The Fe K-edge XANES spectra (Figure 6.2c) show that the adsorption threshold position of $Fe_x/Cu–N@CF$ and $Fe_x–N@CF$ located between FeO and Fe_2O_3 reveals the oxidation state of Fe in $Fe_x/Cu–N@CF$ and $Fe_x–N@CF$ is between +2 and +3. Yet, the position of the adsorption threshold for $Fe_x/Cu–N@CF$ shows a slight positive shift in comparison with $Fe_x–N@CF$, suggesting a somewhat higher Fe valence state in $Fe_x/Cu–N@CF$, in good agreement with results from XPS measurements. Notably, the pre-edge peak at around 7113 eV, arising from the square-planar or centrosymmetric FeN_4 configuration, shows a weaker intensity in $Fe_x/Cu–N@CF$ than in $Fe_x–N@CF$ and Fe Pc, indicating the decreased symmetry of FeN_4 in $Fe_x/Cu–N@CF$ in the presence of Cu in contrast to $Fe_x–N@CF$.[41, 42] In Figure 6.2d, the R-space EXAFS spectrum of Fe K-edge in $Fe_x/Cu– N@CF$ presents a primary peak located at ~1.43 Å, corresponding to the Fe−N scattering, similar to that in $Fe_x–N@CF$ and FePc. It is noteworthy that a secondary peak can be also observed at 2.10 Å in both $Fe_x/Cu–N@CF$ and $Fe_x–N@CF$, but absent in FePc, implying the existence of coupling effect between Fe–metal atoms in addition to Fe-N bonding. The profiles of $Fe_x/Cu–N@CF$ and $Fe_x–N@CF$ are markedly different from Fe foil, suggesting no Fe particles in our prepared catalysts. Additionally, the Fe K-edge wavelet transform (WT)-EXAFS was also analyzed to identify the atomic configuration of back scatterers, which provides the resolution in both R-space and k-space. In the WT contour plots of reference samples (Fe Pc and Fe foil), the intensity maximum at R ≈ 2.4 Å and k ≈ 7.4 $Å^{−1}$ in Fe Pc assigns to the Fe–C distance of the second neighbor shell, which is different from that of Fe foil (R ≈ 2.2 Å and k ≈ 7.6 $Å^{−1}$) (Figure 6.2e).[43,44] As shown in Fig. 2e, the WT contour plots in $Fe_x/Cu–$

N@CF exhibited two intensity maximums at 4.5 $Å^{-1}$ and 7.8 $Å^{-1}$, corresponding to the Fe-N and Fe-metal scattering paths, respectively. It should be noted that the intensity of Fe-metal was obviously enhanced, and the position in k-space shifted with the addition of Cu in comparison to Fe_x–N@CF, which could arise from the formation of coordination between Fe–Cu. But these two WT contour plots are clearly different from the Fe foil, indicating the isolated Fe atoms are in clusters rather than the Fe-based crystalline structure in Fe_x/Cu–N@CF and Fe_x–N@CF. The Cu K-edge XANES profiles of the specimens (Figure S6.14a) exhibit the absorption edge of Cu in Fe_x/Cu–N@CF negatively shifted in comparison to Cu–N@CF, suggesting a lower Cu valency, as revealed by XPS spectra. In the Fe_x/Cu–N@CF and Cu–N@CF EXAFS spectra (Figure S6.14b), a predominant peak at about 1.45 Å is very close to that in CuPc, confirming the presence of atomically dispersed Cu–N_4 sites. In addition, a Cu–metal peak (≈ 2.43 Å) shows up in the R-space EXAFS spectrum of Fe_x/Cu–N@CF, but absent in Cu–N@CF, which could illustrate the coupling effect between Cu and Fe after the deposition of Fe. This was also confirmed by the WT contour plots (Figure S6.14c), where the intensity maximum of Cu–Fe appeared in Fe_x/Cu–N@CF, but no Cu-metal peak can be observed in Cu–N@CF, further demonstrating the coupling effect of Cu–Fe in Fe_x/Cu–N@CF.

The EXAFS fitting analysis was performed to quantitatively determine the local structure of Fe in as-prepared materials. Based on the CVD synthesis process of $FeCl_3$ evaporation, $FeCl_3$ exists in the binuclear form of Fe_2Cl_6 in the gas phase, indicating the smallest Fe clusters could be Fe dimers.[45,46] The Fe_2 dimer is considered as the model of ultra-small Fe clusters in different configurations (Figure S6.15a, b). Based on the simulated Fe K-edge spectra of EXAFS, the theoretically calculated Fe_2–N_6–1 was consistent with the experimental spectra (Figure S6.16a-d, Table S6.2). Therefore, the proposed Fe_2–N_6–1 model is suggested as the most possible structure

of Fe_x–N@CF. In addition, the EXAFS spectrum of Cu–N@CF can be perfectly fitted to the proposed Cu–N shell with the coordination number of 4, indicating the formation of Cu–N_4 moieties in Cu–N@CF (Figure S6.15c, Figure S6.17 and Table S6.3). To confirm the atomic configurations of Fe_x/Cu–N@CF, density functional theory (DFT) was used to deduce the possible structure of Fe_x/Cu–N–C (Figure S6.18). Among these three types of configurations, Cu K-edge EXAFS fitting curves based on Cu–N_4/Fe_2–N_6–3 model fit the experimental data best in R-space (Figure S6.19, 20a and Table S6.4-6.5). In addition, the Fe K-edge fitting curves based on Cu–N_4/Fe_2–N_6–3 model also match well with the experimental data in R-space (Figure 6.2f, Table S6.6). The Cu/Fe K-edge fitting curves exhibit very similar oscillation to the experimental spectra in k-space (Figure S6.20b, c), further confirming the rationality of the selected Cu–N_4/Fe_2–N_6–3 model.

The computational calculations have made XANES spectroscopy able to confirm or discard a structure model for the environment of the X-ray absorbing atom, thus forming a fundamental diagnostic tool in condensed matter physics and chemistry.[47] Therefore, DFT guided XANES modelling is also used to verify the Cu-Fe coordination configuration, based on the predicted structural models (Cu–N_4/Fe_2–N_6–1, Cu–N_4/Fe_2–N_6–2 and Cu–N_4/Fe_2–N_6–3). For Cu-K edge (Figure S6.21a, b, ESI†), the Cu–N_4/Fe_2–N_6–3 reproduces most of the features of experimental spectrum upon "a" the chemical shift for XANES edge jump, "b" whiteline peak drafting and "c" signal intensity on high energy wing of whiteline. The Cu–N_4/Fe_2–N_6–1 is least supported by XANES modeling, considering the feature "d". Moreover, the simulated Fe K-edge XANES spectra show that Cu–N_4/Fe_2–N_6–3 well reproduces the pre-edge feature (Figure S6.21c). While the Cu–N_4/Fe_2–N_6–1 and Cu–N_4/Fe_2–N_6–2 exhibit whiteline intensity loss and whiteline peak drifting. Thus, a better consistency between experimental and simulated Cu–N_4/Fe_2–N_6–3 XANES

spectra on Fe K-edge was obtained. The simulated XANES on Cu/Fe K edge again evidenced that

Cu–N$_4$/Fe$_2$–N$_6$–3 could be the most reasonable structure model in Fe$_x$/Cu–N@CF.
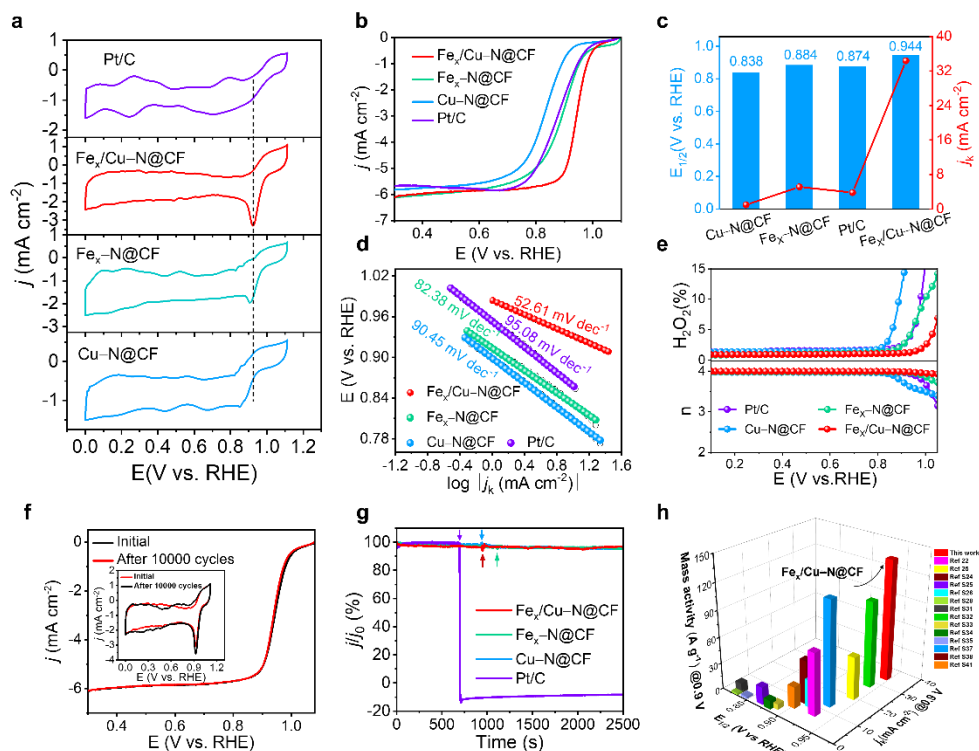
Figure 6. 3 (a) CV curves of Fe$_x$/Cu–N@CF, Fe$_x$–N@CF, Cu–N@CF and Pt/C in O$_2$-saturated 0.1 M KOH solution at a sweep rate of 5 mV s^{-1}. (b) LSV curves recorded in 0.1 M KOH with a rotation rate of 1600 rpm. (c) E$_{1/2}$ and j$_k$ at 0.85 V. (d) The corresponding Tafel plots. (e) Electron transfer number and peroxide yield calculated from RRDE measurements. (f) LSV and CV curves of Fe$_x$/Cu–N@CF before and after 10000 potential cycles at the scan rate of 5 mV s^{-1} with the rotation speed of 1600 and 0 rpm, respectively. (g) Methanol tolerance tests. (h) The comparison of performance to literature.

6.2.2 Electrocatalytic ORR performance

To verify the oxygen reduction reactivity of $Fe_x/Cu–N@CF$ with single Cu atoms functionalized Fe nanoclusters, the electrocatalytic performance of $Fe_x/Cu–N@CF$ in O_2-saturated 0.1 M KOH solution was first demonstrated in comparison to $Fe_x–N@CF$, $Cu–N@CF$ and commercial Pt/C (20%) by Cyclic voltammetry (CV) and Linear scan voltammetry (LSV) measurements. The CV of $Fe_x/Cu–N@CF$ curve reveals a significant reduction peak at 0.93 V while $Cu–N@CF$ and $Fe_x–N@CF$ show a lower one at 0.88 and 0.91 V (Figure 6.3a), suggesting the significant role of coexistence of Fe and Cu in boosting ORR electrocatalytic activity. In addition, the LSV curves recorded at a scan rate of 5 mV s^{-1} and a rotating rate of 1600 rpm further present the highest activity of $Fe_x/Cu–N@CF$ with the most positive onset potential (E_{onset} = 1.03 V) and half-wave potential ($E_{1/2}$ = 0.944 V) among all investigated catalysts (Figure 6.3b), outperforming the catalysts containing only $Fe_x–N$ moieties (E_{onset} = 1.01 V, $E_{1/2}$ = 0.884 V) or only Cu–N moieties (E_{onset} = 0.95 V, $E_{1/2}$ = 0.838 V) and even commercial Pt/C (E_{onset} = 0.997 V, $E_{1/2}$ = 0.874 V), indicating that the adjacent Cu-N could remarkably enhance the ORR activity of $Fe_x–N$. As shown in Figure 6.3c, $Fe_x/Cu–N@CF$ also shows the highest kinetic current density (j_k) of 34.37 mA cm^{-2} at 0.9 V, compared to Pt/C (3.81 mA cm^{-2}), $Fe_x–N@CF$ (5.12 mA cm^{-2}), and $Cu–N@CF$ (0.97 mA cm^{-2}), manifesting the fast ORR kinetic process. Moreover, $Fe_x/Cu–N@CF$ shows the smallest Tafel slope (52.61 mV dec^{-1}) among all prepared catalysts (Figure 6.3d). Koutecky–Levich (K–L) plots were used to probe the electron transfer number during ORR process (Figure S6.22).[48] The results suggest that the first-order reaction kinetics of the dissolved oxygen and the electron transfer number is n ≈ 4, which signifies a high $4e^-$ selectivity for reduction of O_2 to H_2O. The rotating ring-disk electrode (RRDE) measurements (Figure 6.3e) suggest that the H_2O_2 yield of $Fe_x/Cu–N@CF$ remains below 2% over the potential range of 0.1 to 0.8 V, where the direct four-electron transfer mediated ORR process is confirmed again in alkaline media (n ≈ 3.99). The

electron transfer number for other investigated samples is 3.98 (Fe_x–N@CF), 3.96 (Cu–N@CF) and 3.97 (Pt/C). The electrochemical impedance spectra (EIS) plots reveal the smallest charge-transfer resistance of Fe_x/Cu–N@CF during the ORR process, suggesting the enhanced reaction kinetics by adjacent Cu–N (Figure S6.23).

In addition to the high activity, a desirable ORR catalyst should also be able to achieve substantial long-term stability. This was first assessed by the continuous repetitive CV cycling. As evidenced by Figure 6.3f, the $E_{1/2}$ of Fe_x/Cu–N@CF only negatively shifts ≈ 6 mV after 10000 continuous potential cycles in O_2-saturated 0.1M KOH. The outstanding stability of Fe_x/Cu–N@CF is also supported by the chronoamperometry measurement with 95% current retention after 72 h continuous operation (Figure S6.24). The high-resolution TEM and XRD analysis show that the clusters and single atoms still can be observed on the carbon supports without forming any crystalline species after the long-term stability test (Figure S6.25a-c). The R-space EXAFS spectra of Fe K-edge in Fe_x/Cu–N@CF still present a primary peak of Fe−N and a secondary peak of Fe-Fe/Cu (Figure S6.25d), and Cu-N and Cu-Fe peaks can also be observed in Cu K-edge (Figure S25e), indicating the preserved atomic Fe clusters and Cu single atoms in Fe_x/Cu–N@CF after long-term electrolysis. All these results reflect the structural robustness of Fe_x/Cu–N@CF during electrocatalysis process. Furthermore, Fe_x/Cu–N@CF possesses a superior methanol tolerance with a negligible current drop, while a sharp current recession of commercial Pt/C catalyst occurs after methanol crossover (Figure 6.3g), implying strong resistance to poisoning in alkaline electrolyte. In comparison to the performance metrics of literature benchmarks, our catalyst is superior to most recently reported Fe-N based ORR electrocatalysts (Figure 6.3h and Table S6.9). The ORR performance was also examined in acidic media. Fe_x/Cu–N@CF shows an outstanding ORR activity with $E_{1/2}$ of 0.815 V, superior to the Fe_x–N@CF and Cu–N@CF, close to that of

commercial Pt/C (0.845 V) with only -30 mV of disparity (Figure S6.27). In addition, the stability test of $Fe_x/Cu–N@CF$ and Pt/C was conducted in the O_2-saturated 0.1M $HClO_4$ solution, where $Fe_x/Cu–N@CF$ shows better stability than commercial Pt/C in the acidic media (Figure S6.28). These results suggest its potential application in acidic solution. It is worth mentioning that Cu-interacted Fe clusters dominate on $Fe_x/Cu–N@CF$, while Fe clusters without Cu modification could exist based on the microscopic characterizations. As we discussed above, $Fe_x/Cu–N@CF$ shows much enhanced electrocatalytic activity in comparison to $Fe_x–N@C$, which indicates Cu modified-Fe clusters mainly contribute to the activity enhancement, the effect of Fe clusters without Cu modification on activity enhancement should be limited.

6.2.3 Performance in ZABs

Inspired by the outstanding ORR performance of $Fe_x/Cu–N@CF$ catalyst in alkaline electrolyte, a two-electrode primary Zn-air battery (ZAB) was assembled using $Fe_x/Cu–N@CF$ catalyst as air cathode and a Zn plate as the anode for the practical application, where the open-circuit voltage is up to 1.4 V, the peak-power density is 156 mW cm^{-2}, superior to commercial Pt/C (98.7 mW cm^{-2}, Figure 6.4a). In Figure 6.4b, the specific capacities of as-assembled ZABs normalized by the mass of consumed Zn were estimated by the galvanostatic discharge at the current density of 100 mA cm^{-2}. The specific capacity of $Fe_x/Cu–N@CF$ was calculated to be 1110.4 mA h g^{-1} with a corresponding energy density of 1032.7 Wh kg^{-1}, which is higher than that of commercial Pt/C (1076.2 mA h g^{-1}, 925.5 Wh kg^{-1}). The solid-state ZABs were further fabricated using $Fe_x/Cu–N@CF$ membrane as the air cathode directly and poly (vinyl alcohol) (PVA)-KOH-Zn $(CH_3COO)_2$ hydrogel as the electrolyte, delivering an open-circuit voltage of 1.34 V (Figure 6.4c). These two assembled solid-state ZABs in a series connection can effectively power a series of LED lamps, demonstrating the promising practical application in power energy devices. As shown in Figure

6.4d, the galvanostatic discharge curves were first obtained continuously at different current densities (5, 10 and 20 mA cm^{-2}) each with 18 h discharge voltage plateaus of Fe$_x$/Cu–N@CF-based ZAB. The discharge voltage plateaus can be well recovered when the current density is returned to 10 mA cm^{-2}, continuously discharging for 100 h with only 70 mV of voltage decay, signifying a good rate capability. To further examine the electrochemical stability of Fe$_x$/Cu–N@CF in the rechargeable battery, the cycling performance of rechargeable ZAB with Fe$_x$/Cu–N@CF was investigated by long-term galvanostatic charge-discharge tests with a duration of 20 min per cycle. Considering promoting the efficiency for oxygen evolution reaction (OER) during charging, the commercial IrO$_2$ was additionally added into the catalytic layers of Fe$_x$/Cu–N@CF.[49,50] The rechargeable ZAB was assembled by using Fe$_x$/Cu–N@CF + IrO$_2$ as the cathode and Zn foil as the anode. From Figure 6.4e, we can observe the negligible change of both charge and discharge voltage by over 240 h at 5 mA cm^{-2}. Then the cycling performance of Fe$_x$/Cu–N@CF + IrO$_2$-based ZAB was continuously examined at 10 mA cm^{-2} for 160 h, where the discharge potential of Fe$_x$/Cu–N@CF cathode barely changes. These results confirm the remarkable stability of Fe$_x$/Cu–N@CF in practical ZAB.
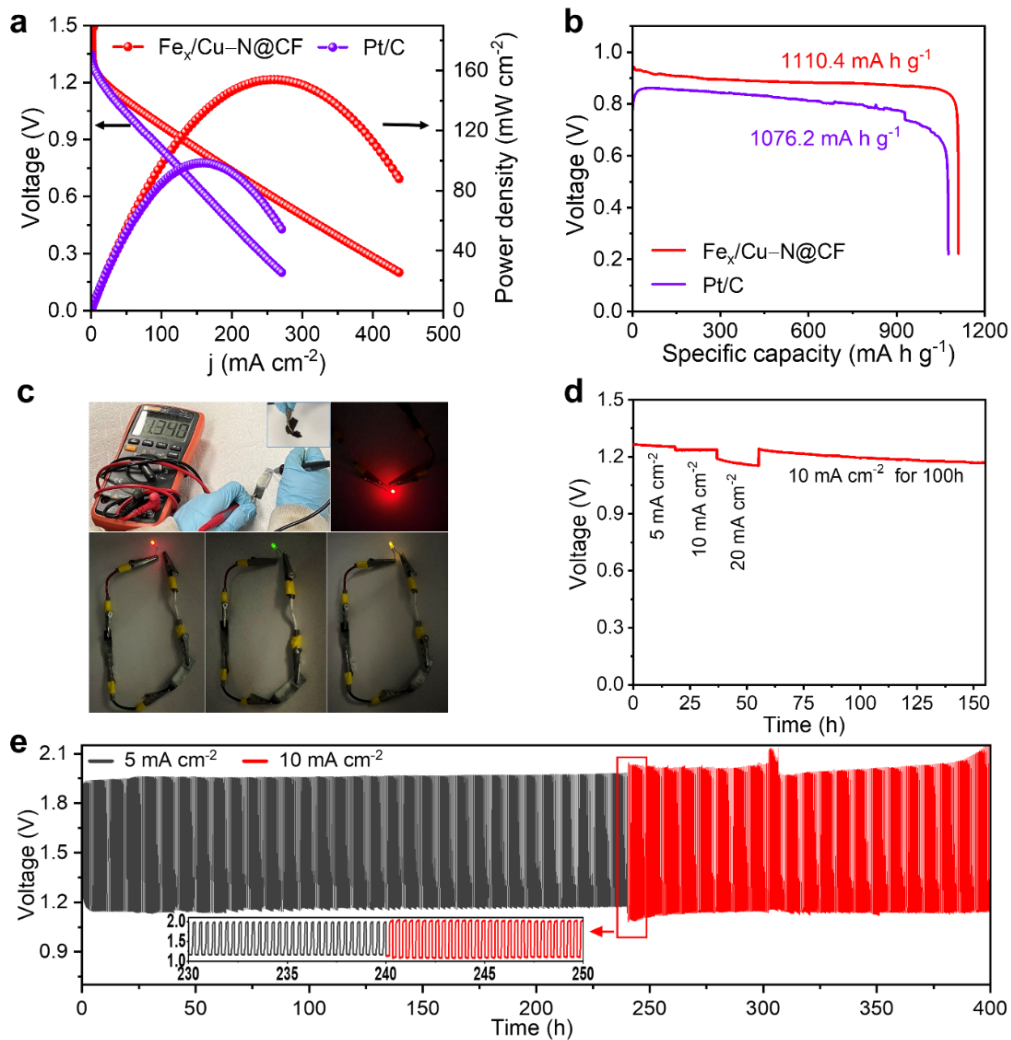
Figure 6. 4 (a) Polarization and power density curves of the primary Zn–air batteries of the Fe_x/Cu–N@CF and Pt/C catalyst in O_2-saturated 6 M KOH solution and 0.2 M zinc acetate. (b) Specific capacity normalized by the consumed Zn of Fe_x/Cu–N@CF and Pt/C at 100 mA cm^{-2}. (c) LED lamps lighted by the solid-state ZABs. (d) Galvanostatic discharge curves at different current densities (5, 10 and 20 mA cm^{-2}). (e) Galvanostatic discharge–charge cycle profiles of the Zn-air battery based on Fe_x/Cu–N@CF + IrO_2 at 5 mA cm^{-1} and 10 mA cm^{-1}.

6.2.4 Theoretical analysis

To further shed light on the critical role of Cu–N_4 in boosting ORR activity of atomic Fe clusters, density functional theory (DFT) calculations were performed. The Fe_2 dimer is considered as the model of ultra-small Fe clusters, considering computational resources and time. Based on the synchrotron XAFS experimental data and fitting results, we used Cu–N_4, Fe_2–N_6, and Cu–N_4/Fe_2–N_6 graphene as the model reference to represent the difference of Cu–N@CF, Fe_x–N@CF, and Fe_x/Cu–N@CF, respectively (Figure 6.5a, b). Generally, the absorption of O_2 and O–O bond cleavage are key factors determining the ORR performance of metal–N–based catalysts.[51] The O–O bond length is related to the activation of O_2 molecules, and metal–O bond length reflects the strength of interaction between *O_2 and metal–N site. For Cu–N@CF, the O_2 molecule is adsorbed on the Cu–N_4 site in a superoxo-like configuration with O–O bond length of only 1.26 Å and Cu–O bond length of 2.44 Å (Figure S6.29), indicating the interaction between Cu atom and oxygen is under-activated on Cu-N_4.[52] This could limit the kinetic rate because the following protonation of O_2* requires extra energy.[53] In contrast, a peroxo-like adsorption is formed on Fe_2–N_6 and Cu–N_4/Fe_2–N_6 both containing Fe_2–N_6 site. The Fe–O bond lengths over these two structures are distributed between 1.83–1.85 Å, which are shorter than Cu–O bond over Cu–N_4 (2.44 Å). Moreover, the peroxo-like adsorption elongates the O–O bond (1.39 Å). Therefore, the Fe_2–N_6 facilitates the activation of O_2 molecule due to the unique adjacent Fe_2 structure, which is consistent with previous reports.[22, 54] Since *OOH is another important reaction intermediate of ORR, the adsorption configuration of *OOH over Fe_2–N_6 and Cu–N_4/Fe_2–N_6 was also checked (Figure 6.5b). Compared with the Fe_2–N_6, the adjacent Cu-N strengthens bridge-cis absorption of *OOH on Fe atoms, where both adjacent Fe atoms in Cu–N_4/Fe_2–N_6 bind an O atom of OOH* to form dual-side adsorption which stretches the O–O bond to a slightly longer distance (1.48 Å), manifesting an easier O–O bond cleavage.[55] He et al. reported that the introduction of single Cu

atoms (CuN$_4$) to single Fe–N$_4$ sites manipulated the magnetic moment, exhibiting reduced $\triangle G_{OH*}$, benefitting the catalytic activity.[27] In our work, the proposed reaction pathways are shown in Figure S6.30.
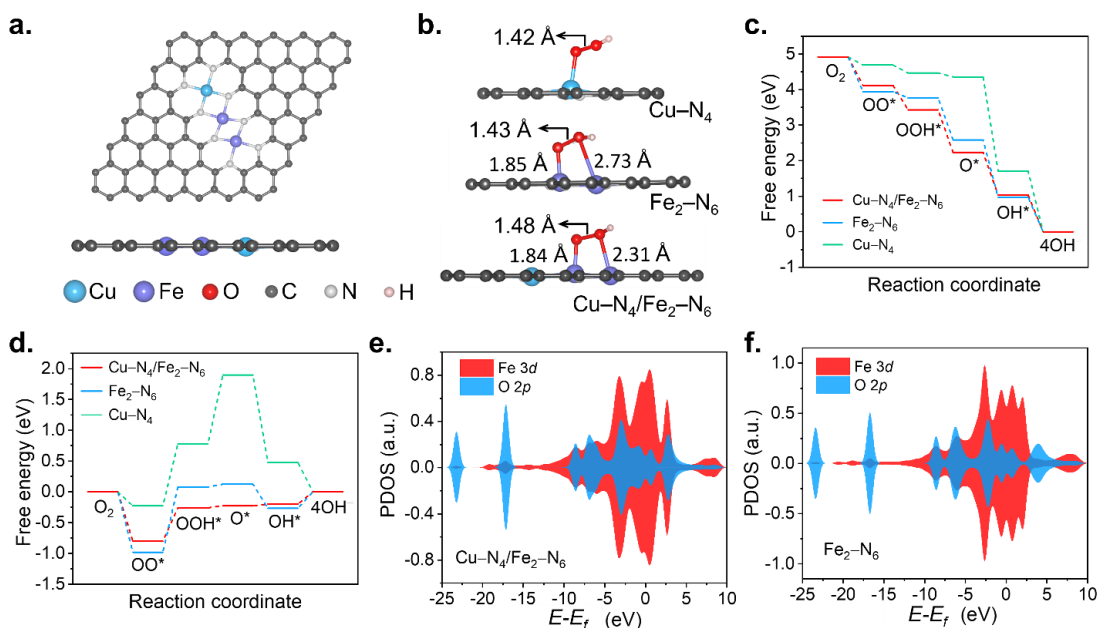
Figure 6. 5 (a) Constructed Cu–N$_4$/Fe$_2$–N$_6$ model for the calculations. (b) Optimized geometry of OOH adsorption configuration on Cu–N$_4$, Fe$_2$–N$_6$, and Cu–N$_4$/Fe$_2$–N$_6$. (c) ORR free energy diagrams for Cu–N$_4$, Fe$_2$–N$_6$ and Cu–N$_4$/Fe$_2$–N$_6$ at U=0 V. (d) ORR free energy diagrams for Cu–N$_4$, Fe$_2$–N$_6$, and Cu–N$_4$/Fe$_2$–N$_6$ at U=1.23 V. Fe 3d and O 2p PDOS of Cu–N$_4$/Fe$_2$–N$_6$ (e) and Fe$_2$–N$_6$ (f) after OOH* adsorption.

The intrinsic activity of the catalysts was further evaluated by comparing the free energy of the intermediate steps of the electrochemical reactions. The Gibbs free energy diagrams for ORR over Cu–N$_4$, Fe$_2$–N$_6$ and Cu–N$_4$/Fe$_2$–N$_6$ were then calculated and shown in Figure 6.5c. At U = 0 V, the energy pathway for all these three samples is downhill, indicating a spontaneous and exothermic process. According to Noskov et al., when detailed kinetic data is not available, the largest of the free energy differences in the reaction mechanism can be used as an indicator of the activation

barrier of the rate limiting step.[56] Upon increasing the potential to 1.23 V, the dissociative step from OOH* to O* on Cu–N$_4$ structure has the largest free energy difference as 1.12 eV (Figure 6.5d). This can explain the poor ORR activity observed on Cu–N@CF. For Fe$_2$–N$_6$ and Cu–N$_4$/Fe$_2$–N$_6$, the protonation of O$_2$* step has the largest free energy difference, instead of the dissociation of OOH*. Moreover, the free energy difference between OOH* and OO* on Cu–N$_4$/Fe$_2$–N$_6$ (0.54 eV) is much lower compared on pure Fe$_2$–N$_6$ (1.06 eV), suggesting that the introduction of Cu–N$_4$ site facilitates the protonation of O$_2$*, significantly boosting ORR activity of Fe$_2$–N$_6$. To further elucidate how the Cu–N$_4$ site affects the electronic structure of Fe$_2$–N$_6$ and the consequent interactions with ORR intermediates, the projected density of states (PDOS) from the 3d state of Fe atom in Fe$_2$–N$_6$ and Cu–N$_4$/Fe$_2$–N$_6$ was investigated. As observed in Figure S6.31, the d-band center of Cu–N$_4$/Fe$_2$–N$_6$ (–0.96 eV) negatively shifts to lower energy level compared to Fe$_2$–N$_6$ (–0.92 eV). Lee et al.[57] suggested that such slight downshift of d-band center might increase the filling degree of antibonding orbitals and thus in turn weaken the adsorption of O$_2$*. As such, the introduction of Cu–N$_4$ site can potentially increase the filling degree of partially occupied d orbitals of Fe$_2$–N$_6$ and lead to weakened binding strength of the overly strong adsorption of O$_2$*, consequently facilitating the ORR process. Since the formation of OOH* is the reaction step with the largest reaction free energy difference for both Fe$_2$–N$_6$ and Cu– N$_4$/Fe$_2$–N$_6$. The PDOS for d orbitals of Fe and p orbitals of O for the two structures after OOH* adsorption was calculated. As shown in Figure 6.5e, f, the overlap (especially for energy level from 2.5-5 eV) between d orbitals of Fe and p orbitals of O over Cu–N$_4$/Fe$_2$–N$_6$ is significantly larger than that over Fe$_2$–N$_6$. This could be an indicator for a stronger σ-bond between the d orbital of Fe and p orbital of the O in OOH on Cu–N$_4$/Fe$_2$–N$_6$, which strengthens the adsorption of OOH* and weakens the O–O bond.[58] This could facilitate the O–O bond breaking, which is in agreement with

the adsorption configuration analysis. These comparative studies show that the introduction of Cu–N_4 modulates the electronic structure of Fe_2–N_6 sites, and at the same time, reduces the reaction free energy of the protonation of O_2* step to enhance the ORR catalytic activity. A larger model consisting of Fe_4–N_{11} with single Cu atoms located on the edges (Figure S6.32) was further investigated. As shown in Figure S6.33, the energy profile of this large model is similar to the Cu–N_4/Fe_2–N_6 mode, with a similar limiting step of 0.62 eV (the reaction energy for *OO to *OOH). This suggests that the combination of multiple Cu–N_4/Fe_2–N_6 models could potentially form a large Fe cluster in the center with single Cu atoms on the edges, while still maintaining active sites on Fe atoms that are enhanced by single Cu atoms.

Based on the findings and results from this study, it is worth mentioning that our work differs from some previous studies on FeN_4-based bimetallic catalysts for ORR application, in which secondary metal sites were introduced to regulate the electronic configuration of the FeN_4 sites.[23-27] However, the intrinsic poor activation of O-O* on FeN_4 could still result in slow catalytic kinetics. In addition, most reported M–N–C catalysts are prepared by direct pyrolysis of zeolitic imidazolate frameworks (ZIFs) with micropores, which leads to limited active site exposure and mass transfer.[32, 33] In contrast, we here demonstrated Cu–N_4 sites functionalizing atomic Fe clusters on hierarchical porous carbon nanofibers (Fe_x/Cu–N@CNF), which shows reduced O_2* protonation reaction free energy and boosted O–O cleavage during the catalysis process. Moreover, the hierarchical porous construction possesses interconnected micropores and mesopores, enabling abundant accessible active sites and fast mass transport. As a result, this unique atomic catalyst exhibits outstanding catalytic activity and durability for ORR, superior to most recently reported transition metallic ORR electrocatalysts. This work could pave a new avenue for the design of earth-abundant metal-based catalysts for efficient ORR.

6.3 Conclusion

In summary, we for the first time have reported atomic Fe clusters functionalized by single Cu atoms anchoring on interconnected porous CFs (Fe$_x$/Cu-N@CF) through electrospinning and subsequent pyrolysis process. The configurations of atomic Fe clusters and single Cu sites in Fe$_x$/Cu-N@CF have been identified by HADDF-STEM, XAFS, and DFT calculations. The unique atomic interaction between single Cu atoms and Fe clusters renders significantly enhanced ORR catalytic activity compared to monometal counterparts. DFT calculations show that the increased filling degree of d orbitals of Fe clusters with the introduction of Cu–N$_4$ sites in Fe$_x$/Cu–N@CF leads to a reduced energy barrier of rate determining step (O$_2$* protonation) in comparison to Fe$_x$–N@CF. The strong σ bonds resulted from the overlap of the Fe d orbital and p orbital of O in OOH enhance the adsorption of OOH*, facilitating the O–O bond breaking. Thus, the boosted intrinsic activity of Fe$_x$/Cu–N@CF results from the optimized oxygen intermediate adsorption and strong driving force for O-O bond breaking in OOH*. As for practical applications, the free-standing Fe$_x$/Cu-N@CF membrane was successfully incorporated as an effective air cathode in a Zn–air battery device with long-term work stability. This work paves the way to optimizing transition-metal cluster catalysts via heterogeneous single metal atoms to achieve high-efficient and stable ORR catalysts for metal–air batteries, fuel cells and other renewable energy devices.

6.4 References

1. M. Lefèvre, E. Proietti, F. Jaouen and J.-P. Dodelet, *science*, 2009, 324, 71-74.

2. S. Liu, C. Li, M. J. Zachman, Y. Zeng, H. Yu, B. Li, M. Wang, J. Braaten, J. Liu and H. M. Meyer, *Nat. Energy*, 2022, 7, 652-663.

3. J. Li, M. Chen, D. A. Cullen, S. Hwang, M. Wang, B. Li, K. Liu, S. Karakalos, M. Lucero and H. Zhang, *Nat. Catal.*, 2018, 1, 935-945.

4. W. Li, D. Wang, Y. Zhang, L. Tao, T. Wang, Y. Zou, Y. Wang, R. Chen and S. Wang, *Adv. Mater.*, 2020, 32, 1907879.

5. M. Zhao, H. Liu, H. Zhang, W. Chen, H. Sun, Z. Wang, B. Zhang, L. Song, Y. Yang and C. Ma, *Energy Environ. Sci.*, 2021, 14, 6455-6463.

6. F. Luo, A. Roy, L. Silvioli, D. A. Cullen, A. Zitolo, M. T. Sougrati, I. C. Oguz, T. Mineva, D. Teschner and S. Wagner, *Nat. Mater.*, 2020, 19, 1215-1223.

7. J. Wang, Z. Huang, W. Liu, C. Chang, H. Tang, Z. Li, W. Chen, C. Jia, T. Yao and S. Wei, *J. Am. Chem. Soc.*, 2017, 139, 17281-17284.

8. L. Xie, X. P. Zhang, B. Zhao, P. Li, J. Qi, X. Guo, B. Wang, H. Lei, W. Zhang and U. P. Apfel, *Angew. Chem. Int. Ed.*, 2021, 133, 7654-7659.

9. X.-P. Zhang, A. Chandra, Y.-M. Lee, R. Cao, K. Ray and W. Nam, *Chem. Soc. Rev.*, 2021, 50, 4804-4811.

10. V. R. Stamenkovic, B. Fowler, B. S. Mun, G. Wang, P. N. Ross, C. A. Lucas and N. M. Markovic, *science*, 2007, 315, 493-497.

11. H. Ze, X. Chen, X.-T. Wang, Y.-H. Wang, Q.-Q. Chen, J.-S. Lin, Y.-J. Zhang, X.-G. Zhang, Z.-Q. Tian and J.-F. Li, *J. Am. Chem. Soc.*, 2021, 143, 1318-1322.

12. Y. Guo, M. Wang, Q. Zhu, D. Xiao and D. Ma, *Nature Catal.*, 2022, 5, 766-776.

13. S. Li, J. Liu, Z. Yin, P. Ren, L. Lin, Y. Gong, C. Yang, X. Zheng, R. Cao, S. Yao and Y. Deng, *ACS Catal.,* 2019, 10, 907-913.

14. L. Yang, X. Zhang, L. Yu, J. Hou, Z. Zhou and R. Lv, *Adv. Mater.*, 2022, 34, 2105410.

15. X. Xie, L. Peng, H. Yang, G. I. Waterhouse, L. Shang and T. Zhang, *Adv. Mater.*, 2021, 33, 2101038.

16. Y. Chen, S. Ji, Y. Wang, J. Dong, W. Chen, Z. Li, R. Shen, L. Zheng, Z. Zhuang and D. Wang, *Angew. Chem. Int. Ed.*, 2017, 129, 7041-7045.

17. A. Han, X. Wang, K. Tang, Z. Zhang, C. Ye, K. Kong, H. Hu, L. Zheng, P. Jiang and C. Zhao, *Angew. Chem. Int. Ed.,* 2021, 60, 19262-19271.

18. A. Kulkarni, S. Siahrostami, A. Patel and J. K. Nørskov, *Chemical Reviews*, 2018, 118, 2302-2312.

19. S. Kattel and G. Wang, *J. Phys. Chem. Lett.*, 2014, 5, 452-456.

20. L. Huang, J. Chen, L. Gan, J. Wang and S. Dong, *Sci. Adv.*, 2019, 5, eaav5490.

21. N. Zhang, T. Zhou, J. Ge, Y. Lin, Z. Du, W. Wang, Q. Jiao, R. Yuan, Y. Tian and W. J. M. Chu, *Matter*, 2020, 3, 509-521.

22. W. Ye, S. Chen, Y. Lin, L. Yang, S. Chen, X. Zheng, Z. Qi, C. Wang, R. Long and M. J. C. Chen, *Chem*, 2019, 5, 2865-2878.

23. Z. Zhu, H. Yin, Y. Wang, C. H. Chuang, L. Xing, M. Dong, Y. R. Lu, G. Casillas-Garcia, Y. Zheng and S. Chen, *Adv. Mater.*, 2020, 32, 2004670.

24. G. Yang, J. Zhu, P. Yuan, Y. Hu, G. Qu, B.-A. Lu, X. Xue, H. Yin, W. Cheng and J. Cheng, *Nat. Commun.*, 2021, 12, 1-10.

25. A. Han, X. Wang, K. Tang, Z. Zhang, C. Ye, K. Kong, H. Hu, L. Zheng, P. Jiang and C. Zhao, *Angew. Chem. Int. Ed.*, 2021, 60, 19262-19271.

26. H. Li, Y. Wen, M. Jiang, Y. Yao, H. Zhou, Z. Huang, J. Li, S. Jiao, Y. Kuang and S. Luo, *Adv. Funct. Mater.*, 2021, 31, 2011289.

27. T. He, Y. Chen, Q. Liu, B. Lu, X. Song, H. Liu, M. Liu, Y. N. Liu, Y. Zhang and X. Ouyang, *Angew. Chem. Int. Ed.*, 2022, 61, e202201007.

28. S. H. Lee, J. Kim, D. Y. Chung, J. M. Yoo, H. S. Lee, M. J. Kim, B. S. Mun, S. G. Kwon, Y.-E. Sung and T. Hyeon, *J. Am. Chem. Soc.*, 2019, 141, 2035-2045.

29. X. Wan, X. Liu, Y. Li, R. Yu, L. Zheng, W. Yan, H. Wang, M. Xu and J. Shui, *Nat. Catal.*, 2019, 2, 259-268.

30. X. Fu, P. Zamani, J. Y. Choi, F. M. Hassan, G. Jiang, D. C. Higgins, Y. Zhang, M. A. Hoque and Z. Chen, *Adv. Mater.*, 2017, 29, 1604456.

31. Y. Ye, F. Cai, H. Li, H. Wu, G. Wang, Y. Li, S. Miao, S. Xie, R. Si and J. Wang, *Nano Energy*, 2017, 38, 281-289.

32. S. H. Lee, J. Kim, D. Y. Chung, J. M. Yoo, H. S. Lee, M. J. Kim, B. S. Mun, S. G. Kwon, Y.-E. Sung and T. Hyeon, *J. Am. Chem. Soc.*, 2019, 141, 2035-2045.

33. H.-W. Liang, X. Zhuang, S. Brüller, X. Feng and K. J. N. c. Müllen, *Nat. Commun.*, 2014, 5, 1-7.

34. Y. He, H. Guo, S. Hwang, X. Yang, Z. He, J. Braaten, S. Karakalos, W. Shan, M. Wang and H. Zhou, *Adv. Mater.*, 2020, 32, 2003577.

35. X. Xie, L. Peng, H. Yang, G. I. Waterhouse, L. Shang and T. J. A. M. Zhang, *Adv. Mater.*, 2021, 33, 2101038.

36. Y. He, H. Guo, S. Hwang, X. Yang, Z. He, J. Braaten, S. Karakalos, W. Shan, M. Wang and H. J. A. M. Zhou, *Adv. Mater.*, 2020, 32, 2003577.

37. Z. Wang, X. Jin, C. Zhu, Y. Liu, H. Tan, R. Ku, Y. Zhang, L. Zhou, Z. Liu and S. J. Hwang, *Adv. Mater.*, 2021, 33, 2104718.

38. M. Tong, F. Sun, Y. Xie, Y. Wang, Y. Yang, C. Tian, L. Wang and H. Fu, *Angew. Chem. Int. Ed.*, 2021, 60, 14005-14012.

39. H. Yang, Y. Wu, G. Li, Q. Lin, Q. Hu, Q. Zhang, J. Liu and C. He, *J. Am. Chem. Soc.*, 2019, 141, 12717-12723.

40. F. Huang, Y. Deng, Y. Chen, X. Cai, M. Peng, Z. Jia, J. Xie, D. Xiao, X. Wen, N. Wang and Z. Jiang, *Nat. commun.,* 2019, 10, 4431.

41. T. He, Y. Chen, Q. Liu, B. Lu, X. Song, H. Liu, M. Liu, Y. N. Liu, Y. Zhang, X. Ouyang and S Chen, *Angew. Chem. Int. Ed.*, 2022, 61, e202201007.

42. J. Zhou, P. N. Duchesne, Y. Hu, J. Wang, P. Zhang, Y. Li, T. Regier and H. Dai, *Phys. Chem. Chem. Phys*., 2014, 16, 15787-15791.

43. W.-J. Jiang, L. Gu, L. Li, Y. Zhang, X. Zhang, L.-J. Zhang, J.-Q. Wang, J.-S. Hu, Z. Wei and L. Wan, *J. Am. Chem. Soc.*, 2016, 138, 3570-3578.

44. X. Guo, H. Xu, W. Li, Y. Liu, Y. Shi, Q. Li and H. Pang, *Adv. Sci.,* 2023, 10, 2206084.

45. L. Ouyang, E. S. Thrall, M. M. Deshmukh and H. Park, *Adv. Mater.,* 2006, 18, 1437-1440.

46. F. A. Cotton, G. Wilkinson, C. A. Murillo and M. Bochmann, *Advanced inorganic chemistry*, John Wiley and Sons, Inc., 1999.

47. S. A. Guda, A. A. Guda, M. A. Soldatov, K. A. Lomachenko, A. L. Bugaev, C. Lamberti, W. Gawelda, C. Bressler, G. Smolentsev, A. V. Soldatov, Y. Joly, *J. Chem. Theory Comput*., 2015, 11, 4512-4521.

48. S. Xu, Y. Kim, D. Higgins, M. Yusuf, T. F. Jaramillo and F. B. Prinz, *Electrochim. Acta*, 2017, 255, 99-108.

49. Y. Tian, X. Liu, L. Xu, D. Yuan, Y. Dou, J. Qiu, H. Li, J. Ma, Y. Wang, D. Su and S. Zhang, *Adv. Funct. Mater.*, 2021, 31, 2101239.

50. W. Zhai, S. Huang, C. Lu, X. Tang, L. Li, B. Huang, T. Hu, K. Yuan, X. Zhuang and Y. Chen, *Small*, 2022, 18, 2107225.

51. R. Cao, R. Thapa, H. Kim, X. Xu, M. Gyu Kim, Q. Li, N. Park, M. Liu and J. Cho, *Nat. Commun.*, 2013, 4, 1-7.

52. R. Pal, L.-M. Wang, Y. Pei, L.-S. Wang and X. C. Zeng, *J. Am. Chem. Soc.*, 2012, 134, 9438-9445.

53. Y. Sun, L. Silvioli, N. R. Sahraie, W. Ju, J. Li, A. Zitolo, S. Li, A. Bagger, L. Arnarson and X. Wang, *J. Am. Chem. Soc.*, 2019, 141, 12372-12381.

54. X. Ao, W. Zhang, Z. Li, J.-G. Li, L. Soule, X. Huang, W.-H. Chiang, H. M. Chen, C. Wang, M. Liu and X.C. Zeng, *ACS nano*, 2019, 13, 11853-11862.

55. T. Cui, Y. P. Wang, T. Ye, J. Wu, Z. Chen, J. Li, Y. Lei, D. Wang and Y. Li, *Angew. Chem. Int. Ed.*, 2022, 61, e202115219.

56. J. K. Nørskov, J. Rossmeisl, A. Logadottir, L. Lindqvist, J. R. Kitchin, T. Bligaard and H. Jónsson, *J. Phys. Chem. B.*, 2004, 108, 17886-17892.

57. H. Lee, O. Gwon, K. Choi, L. Zhang, J. Zhou, J. Park, J.-W. Yoo, J.-Q. Wang, J. H. Lee and G. Kim, *ACS Catal.*, 2020, 10, 4664-4670.

58. K. Liu, J. Fu, Y. Lin, T. Luo, G. Ni, H. Li, Z. Lin and M. Liu, *Nat. Commun.*, 2022, 13, 1-8.

6.5 Supporting information

6.5.1 Experimental section

Synthesis of Cu/ZIFs-8. 1.041 g $Zn(NO_3)_2 \cdot 6H_2O$ and 0.0954 g $Cu(NO_3)_2 \cdot 3H_2O$ were dissolved in 8 mL deionized (DI) water. 22.7 g 2-methylimidazole was dissolved in 80 mL DI water. Then these two aqueous solutions were purified by filter paper before mixing. The purified nitrate solution was subsequently poured into the above 80 mL of the solution containing 22.7 g 2-

methylimidazole with magnetically stirring for 5 min at room temperature. The products were collected by centrifugation (12000 rpm, 30 min) and washed by DI water at least three times. The product was dried at 60 °C overnight in a vacuum drying oven.

Synthesis of Fe$_x$/Cu-N@CF, Cu-N@CF and Fe$_x$-N@CF. The main membrane was synthesized via an electrospinning process. First, 330 mg of polyacrylonitrile (PAN, Mw = 150,000), 770 mg of Cu/ZIFs-8 and 200 mg of melamine were dissolved in 8 mL of N, N-dimethylformamide (DMF) in a round bottom flask via vigorously stirring at 60 °C overnight to get a homogenous precursor mixture. The precursor solution was diverted into a syringe with a stainless tip needle for the subsequent electrospun process. The processing condition was 0.7 mL/h of solution flow rate, 21 kV of applied potential and 15 cm of spin distance. The as-spun fibers were peroxidized in the air at 250 °C for 1 h, following carbonized under Ar gas at a high temperature of 900 °C for 2 h with 5 °C min^{-1} heating rate. After this carbonization, the atomically dispersed Cu anchored N-doped porous carbon fibers (Cu–N@CF) was formed. Then, the deposition of Fe atoms was conducted on the above resultant material. In a typical process, 40 mg of anhydrous FeCl$_3$ was placed in a boat sitting in the tube upstream of the gas flow; 40 mg of the carbonized material was placed in another boat sitting in the tube downstream of the gas flow. The furnace was heated to 750 °C with a ramping rate of 10 °C min^{-1} and maintained at this temperature for 3 h under the continuous Ar gas flow (100 mL min^{-1} of flow rate). Then the Fe$_x$/Cu-N@CF was collected. Fe$_x$-N@CF was prepared in a similar way by using pristine ZIF–8 for electrospinning.

Materials characterization. The morphologies of prepared materials were studied via Zeiss Sigma 300 VP-Field Emission Scanning Electron Microscopy (FESEM) and Transmission electron microscopy (TEM) on a JEOL JEMARM200CF equipped with an energy dispersive spectrometer (EDS). Atomic-resolution electron energy-loss spectroscopy (EELS) images were

taken with a Titan Cubed Themis G20 TEM equipped with a highly sensitive Super-X energy dispersive X-ray detector system (operated at 300 kV). The crystal structure was characterized by X-ray diffractometer (XRD, D8 discover diffraction system equipped with Cu Kα radiation (40 kV, 44 mA)) at a scan rate of 5° min^{-1}. Nitrogen adsorption-desorption isotherms were collected on an Autosorb Quantachrome 1MP at 77 K. X-ray photoelectron spectroscopy (XPS) spectra were performed on Kratos Analytical AXIS 165 with a monochromatic Al Kα source to study the chemical compositions. The C 1 s photoelectron peak at 284.6 eV as reference was used for spectrometer calibration. The Fe/Cu ratio was determined by inductively coupled plasma optical emission spectrometry (ICP-OES) on Thermo iCAP6300 Duo ICP_OES.

XAFS measurements and data analysis. The local structures of the investigated materials were analyzed by measuring the Fe K-edge and Cu K-edge X-ray absorption near-edge structure (XANES) and the extended X-ray absorption fine structure (EXAFS) data at the Hard X-ray microanalysis beamline (HXMA-061D) of the Canadian Light Source. The X-ray absorption spectra were acquired in fluorescence mode using a Si(111) double-crystal monochromator to range the X-ray energy from 5–40 keV. The ring current is 250 mA. A He-filled Oxford straight ion chamber detector was used to monitor the incident X-ray, and the fluorescence yield signal was captured using a 32-element Ge detector. The energy was calibrated using Fe and Cu plate reference samples. The obtained XAFS raw data were normalized, background-subtracted, and Fourier transformed based on the standard procedures using the ATHENA program.[1, 2] The k^2-weighted EXAFS spectra were obtained by normalizing to the edge-jump step and subtracting the post-edge background from the overall absorption. Then, χ (k) data of Fe and Cu K edge in the k-space was Fourier transformed to real (R) space using a Hanning window (dk = 1.0 Å^{-1}) to separate the EXAFS contributions from different coordination shells in k range 3–11 Å^{-1}. The

EXAFS fitting analysis was performed using the ARTEMIS program according to standard procedures to get the quantitative structural parameters.[2] The WT of EXAFS data was performed by using the Hama Fortran code. The parameters were R range: 1–3 Å, k range: 0–15 Å^{-1}. Morlet function with $\kappa = 10$, $\sigma = 1$ was used as the mother wavelet to provide the overall distribution.[3, 4] The theoretical calculation for XANES data was performed with the FDMNES code under the Molecule model with "Quadrupole" and "SCF" included in the calculation.[5, 6]

Electrochemical measurements of ORR. Electrochemical measurements were conducted by BioLogic SP-300 electrochemical test station. A Pine instrument (PINE Research MSR Rotator, model: AFMSRCE, USA) was used for ORR measurements by a standard three-electrode system in an O_2-saturated 0.1 M KOH or 0.1 M $HClO_4$ electrolyte. A standard three-electrode system comprises working, reference, and counter electrodes in a batch-type electrochemical cell.[7, 8] In our work, a graphite rod and a saturated calomel electrode (SCE) were employed as the counter electrode and the reference electrode, respectively. For the preparation of the working electrode, 5 mg of catalyst was dispersed in the mixture of 495 μL isopropyl alcohol (IPA), 495 μL DI water and 10 μL Nafion (5 wt%) under sonication to form a homogeneous catalyst ink. Then 10 μL of this catalyst ink was dipped on a glassy carbon disk of RDE with a diameter of 0.5 cm, followed by drying at room temperature. The total weight loading of catalysts for both as-prepared catalysts and commercial Pt/C (20 wt%, Sigma Aldrich) was 0.255 mg cm^{-2}. The ORR test at an RDE was conducted in O_2-saturated 0.1 M KOH electrolytes with varying rotating speeds from 400 to 2025 rpm at a scan rate of 5 mV s^{-1}. The onset potential was defined as a potential value corresponding to 5 % of the diffusion-limited current density. 10000 potential cycles were conducted to examine the electrocatalytic durability at the sweep speed of 50 mV s^{-1}. The ORR potentials were calculated into the reversible hydrogen electrode (RHE) by the following equation:

$$E \text{ (vs. RHE)} = E \text{ (vs. SCE)} + 0.059 \times \text{pH} + 0.241 \qquad \text{(S6.1)}$$

The electron transfer number (n) per oxygen molecule for oxygen reduction can be determined by the Koutechy–Levich equations (S6.2-6.3):

$$\frac{1}{J} = \frac{1}{J_L} + \frac{1}{J_K} = \frac{1}{B\omega^{0.5}} + \frac{1}{J_K} \qquad \text{(S6.2)}$$

$$B = 0.62nFC_0(D_0)^{3/2}v^{-1/6} \qquad \text{(S6.3)}$$

where J is the measured current density, J_L and J_K are the diffusion- and kinetic-limiting current densities, ω is the electrode rotation rate expressed in angular velocity (rad s^{-1}), n is the transferred electron number, F is the Faraday constant (96485 C mol^{-1}), C_0 is the concentration of O_2 in the electrolyte (1.26×10^{-6} mol cm^{-3}), D_0 is the diffusion coefficient of O_2 (1.93×10^{-5} cm^2 s^{-1}), and v is the kinetic viscosity of 0.1M KOH (0.01 cm^2 s^{-1}).[9]

RRDE measurements were carried out to investigate the electron selectivity of the as-prepared samples with the same catalyst loading as RDE measurement. The model of the RRDE setup is AFE6R1PT with disk OD = 5.0 mm, ring OD = 7.50 mm, ring ID = 6.50 mm. The disk electrode was scanned cathodically under the same condition of RDE at a scan rate of 5 mV s^{-1} and the ring potential was kept at 1.5 V vs RHE. The rotation rate is 1600 rpm. The following equations (S6.4-6.5) were used to calculate hydrogen peroxide (H_2O_2) yield and electron transfer number (n).

$$n = \frac{4I_D}{I_D + I_R/N} \qquad \text{(S6.4)}$$

$$H_2O_2\% = \frac{2I_R/N}{I_D + I_R/N} \times 100 \qquad \text{(S6.5)}$$

where I_D is disk current, I_R is ring current, and N ≈ 0.25 is the current collection efficiency of the Pt ring, which was provided by the manufacturer.

Zn–air battery (ZAB) performance test. The ZAB tests were carried out using a homemade electrochemical cell. The ability of the electrocatalysts to serve as an air electrode in ZAB was evaluated under ambient conditions. A polished zinc foil was used as the anode. 5 mg of the prepared catalyst was dispersed in 1 mL DI water, 3 mL IPA and 1 mL Nafion via probe sonication. The cathode was prepared by drop casting the catalyst inks onto the Gas Diffusion Layer (GDL) of carbon fiber paper with a mass loading of 0.5 mg cm^{-2}. For the primary Zn-air batteries, the electrolyte consists of 6 M KOH and 0.2 M zinc acetate dehydrate. $Fe_x/Cu-N@CF+IrO_2$ (w:w = 1:1) ink was prepared in the same way for the long-term charge-discharge cycle stability test of the ZAB device in that it was performed with a period of 10 min charge and 10 min discharge. For all-solid-state Zn–air battery assembly, the gel polymer electrolyte was prepared as follows. Polyvinyl alcohol (PVA, 1 g) was dissolved in 10 mL DI water under continuous stirring at 95 °C to form a homogeneous gel. Then 1 mL of 18 M KOH containing 0.2 M zinc acetate dehydrate was added dropwise to form a homogeneous viscous solution. The as-prepared $Fe_x/Cu-N@CF$ film and zinc foil were placed on the two sides of the PVA gel, followed by pressed Ni foam as the current collector. The reference cathode was made in the similar way using commercial Pt/C or $Pt/C+IrO_2$ (w:w=1:1).

6.5.2 Computational methods

DFT calculations were performed with the periodic plane-wave implementation (with the plane-wave cutoff energy of 450 eV) of DFT using the Vienne Ab-initio Simulation Package (VASP)[10-13] with the projector augmented wave (PAW) scheme.[14,15] The Perdew-Burke-Ernzerhof (PBE) exchange correlation functional[16] with the vdW-DFT[17,18] was used as the Generalized gradient approximation (GGA). $3 \times 3 \times 1$ K-point sampling and within the Monkhorst-Pack scheme was used for integration over the Brillouin zone. The convergence criteria for total energy and inter-

atomic forces of all calculations were 10^{-6} eV per unit cell and 0.01 eV Å^{-1}, respectively. A 15 Å

vacuum thickness above the top layer was used to prevent the interaction between repeated

periodic unit cells. To obtain the free energies of the ORR reaction intermediates, the entropy,

zero-point energy and enthalpy correction were computed from statistical thermodynamics for all

adsorbed structures, while those values for gas-phase molecules were taken from the standard

thermodynamics NIST-JANAF table.[19] The reaction energy of the entire ORR process is

calculated according to the method proposed by Norskov et al. [20]

The four-electron ORR pathway was simulated as follows:

$$O_2 + * \rightarrow {}^*OO$$

$$^*OO + H_2O + e^- \rightarrow {}^*OOH + OH^-$$

$$^*OOH + e^- \rightarrow {}^*O + OH^-$$

$$^*O + H_2O + e^- \rightarrow {}^*OH + OH^-$$

$$^*OH + e^- \rightarrow * + OH^-$$
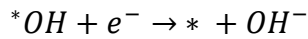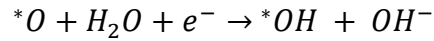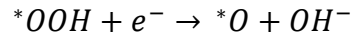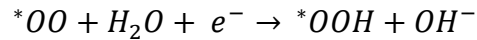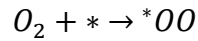
The asterisk * represents the adsorption site.

For each reaction step, the Gibbs reaction free energy is calculated as

$$\Delta G = \Delta E + \Delta ZPE - T\Delta S - eU + \Delta E_{pH}$$

where ΔE is the reaction energy between the reactants and products; ΔZPE is the change in zero-

point energy due to the reaction; T is the temperature and ΔS is the change in entropy ; $-eU$

includes the bias effect on all states involving the electron in the electrode, where e is the

transferred charge and U is the electrode potential; ΔE_{pH} is the energy correction due to pH value of the electrolyte, which depends on the concentration of H^+:

$$\Delta G_{pH} = -kTln[H^+]$$

where k is the Boltzmann constant and T is the temperature. The Gibbs reaction free energy were calculated for each reaction step.

The free energy of gas-phase O_2 molecule was determined as

$$G_{O_{2(g)}} = 4 \times 1.23eV + 2G_{H_2O} - 2G_{H_2}$$

The zero-point energies were obtained by vibrational frequency calculations and the zero-point energy of the adsorption site was assumed negligible. The thermodynamic properties of gas-phase molecules were taken from the standard thermodynamics NIST-JANAF table, and the entropies of adsorbates and adsorption site were assumed to be negligible. All reported free energies of gas phase and reaction free energies were computed at 20 °C.
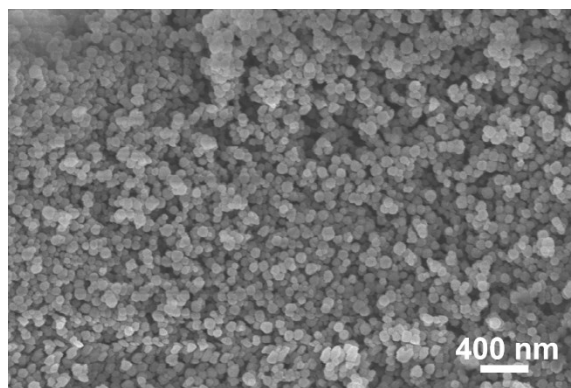
Figure S6. 1 SEM image of Cu/ZIF-8.
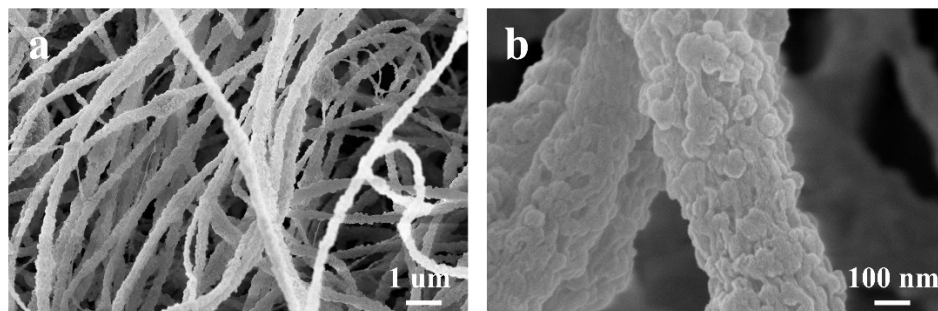
Figure S6. 2 SEM images of Cu/ZIF–8@PF.
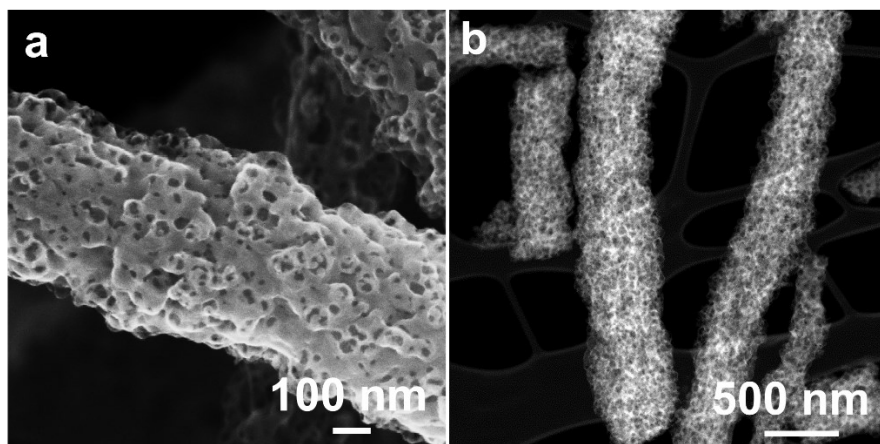
Figure S6. 3 (a) high resolution SEM image, (b) HAADF-STEM image of Fe$_x$/Cu–N@CF.
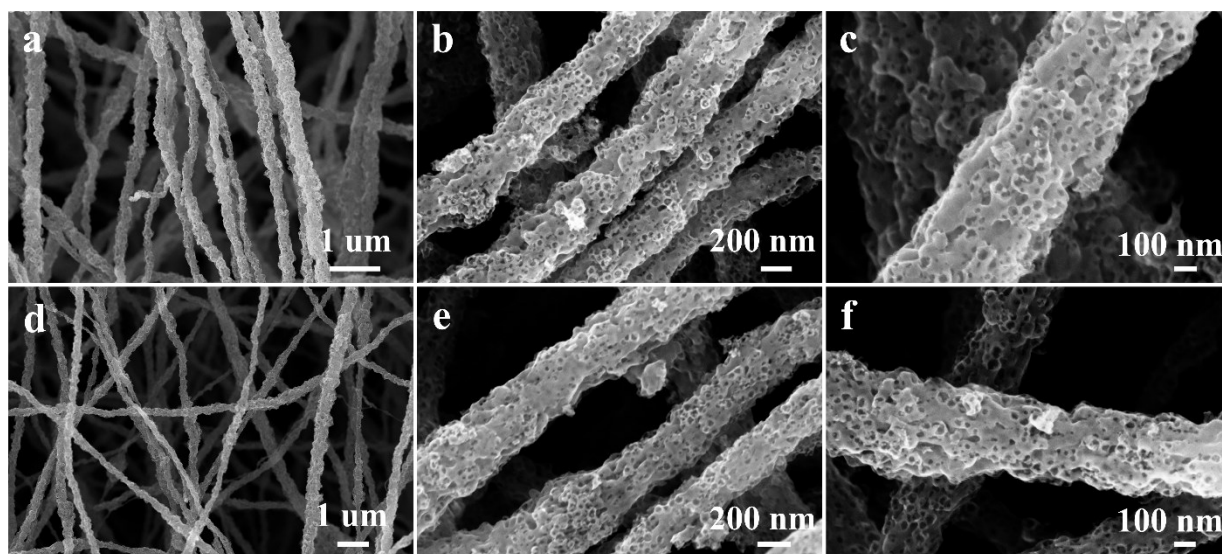
Figure S6. 4 SEM images of (a-c) Cu-N@CF and (d-f) Fe$_x$-N@CF.
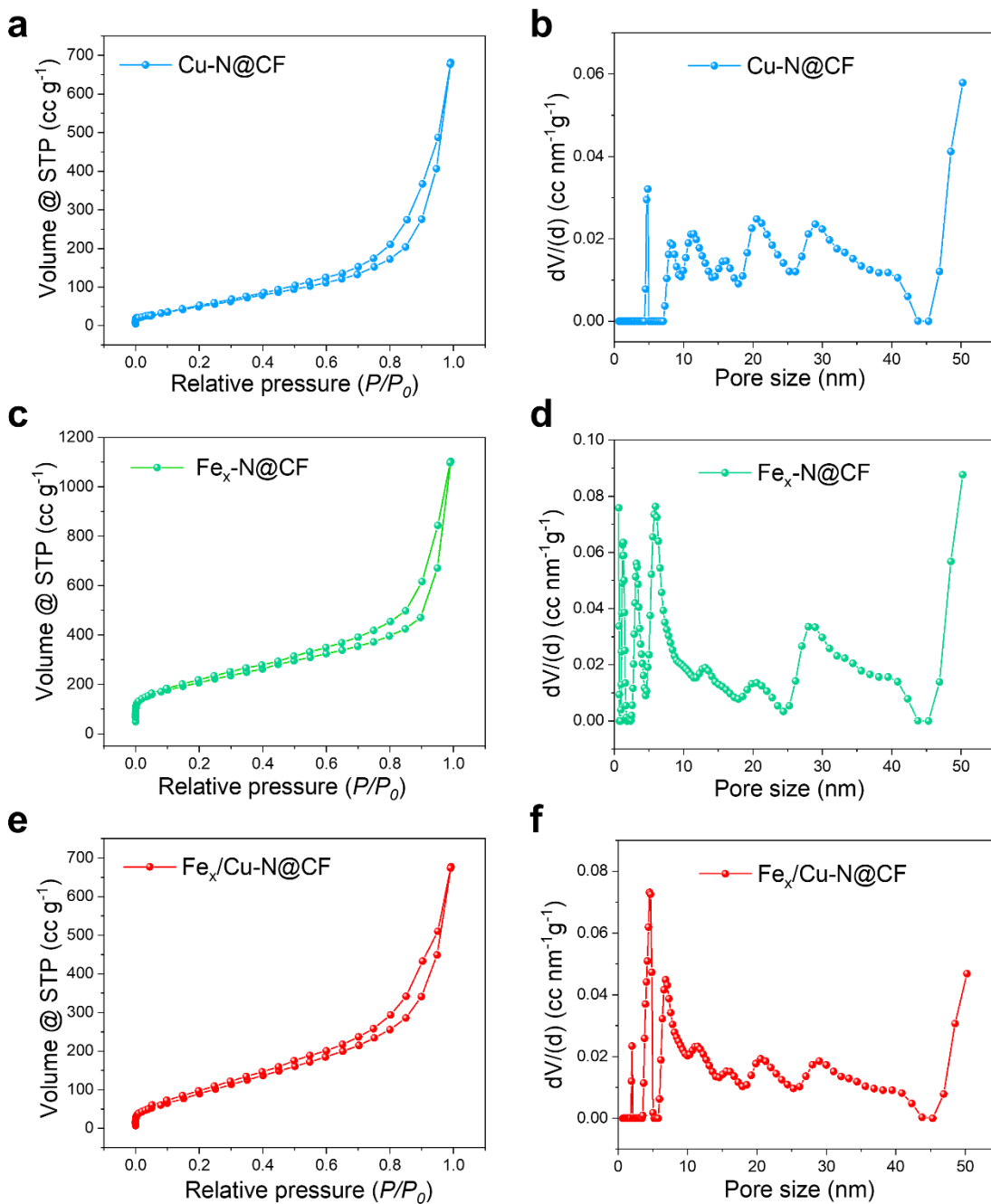
Figure S6. 5 N_2 adsorption isotherms and pore size distributions of (a, b) Cu-N@CF, (c, d) Fe_x-N@CF and (e, f) Fe_x/Cu-N@CF.
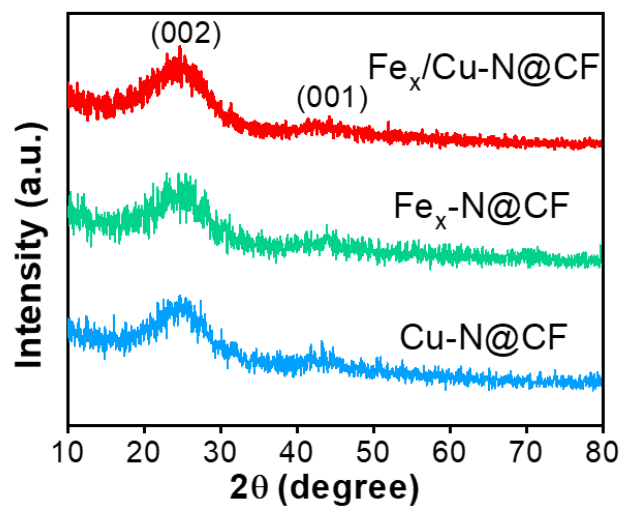
Figure S6. 6 XRD patterns of Cu–N@CF, Fe$_x$–N@CF and Fe$_x$/Cu–N@CF.
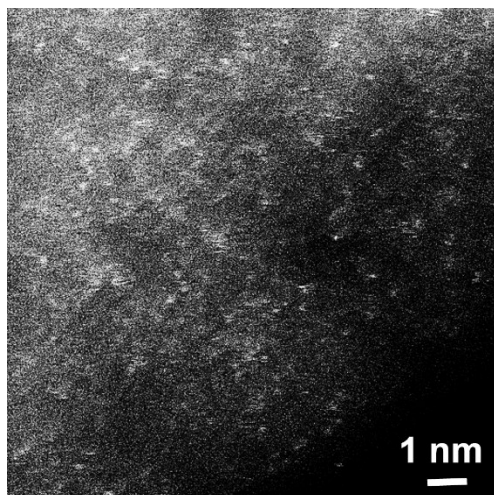
Figure S6. 7 The magnified HAADF-STEM image of Cu–N@C.
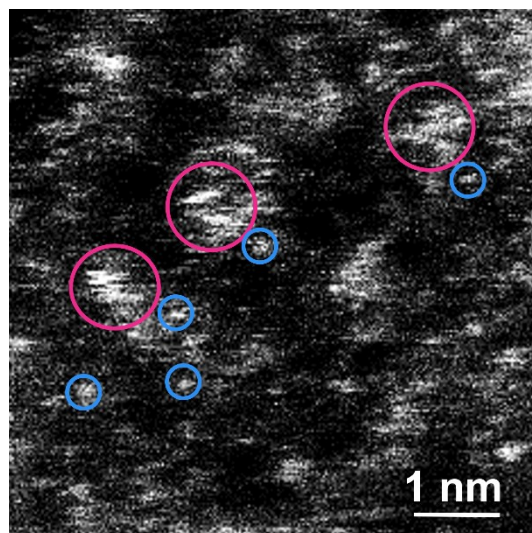
Figure S6. 8 HAADF-STEM image showing the coexistence Fe clusters (marked by pink circles) and single Cu atoms (marked by blue circles) of $Fe_x/Cu–N@CF$.
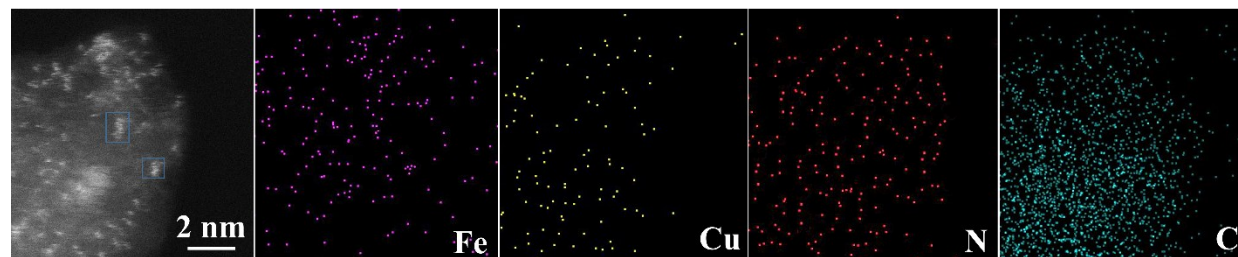
Figure S6. 9 The magnified HAADF-STEM image and corresponding EDS mapping of $Fe_x/Cu–N@CF$. Blue rectangles indicate Fe nanoclusters.
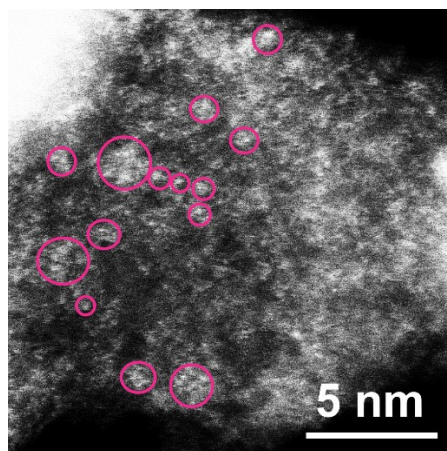
Figure S6. 10 HAADF-STEM image of Fe_x–N@CF (marked larger spots with pink circles).
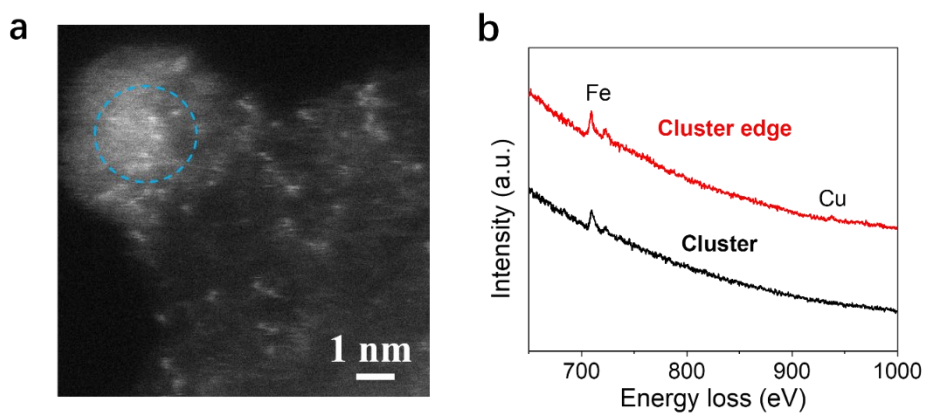
Figure S6. 11 (a) Atomic-level HAADF-STEM image (marked the bright cluster with the blue circle), (b) corresponding EEL spectra.

Table S6. 1 Fe and Cu content determined by ICP-OES.

Samples	Fe content (wt. %)	Cu content (wt. %)
Fe$_x$/Cu-N@CF	2.23%	0.57%
Fe$_x$-N@CF	2.01%	0.06%
Cu-N@CF	0.05%	0.62%
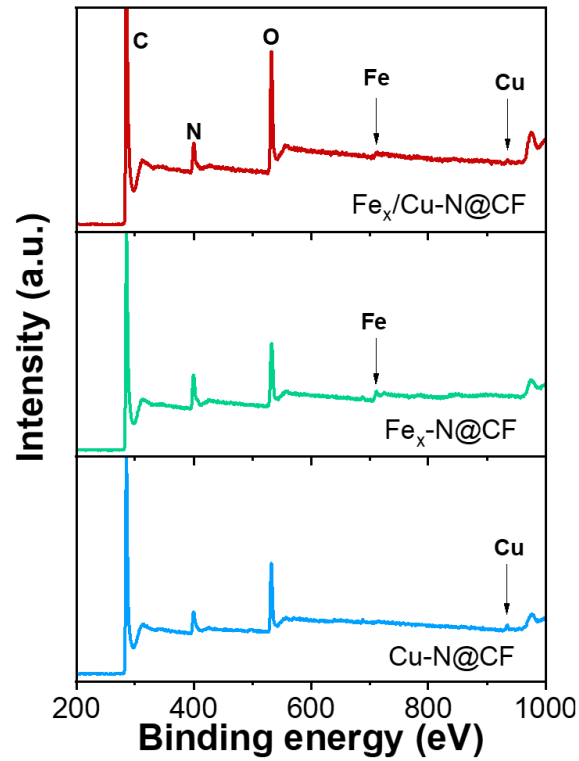
Figure S6. 12 The wide-scanning XPS spectra of Cu–N@CF, Fe$_x$–N@CF and Fe$_x$/Cu–N@CF.
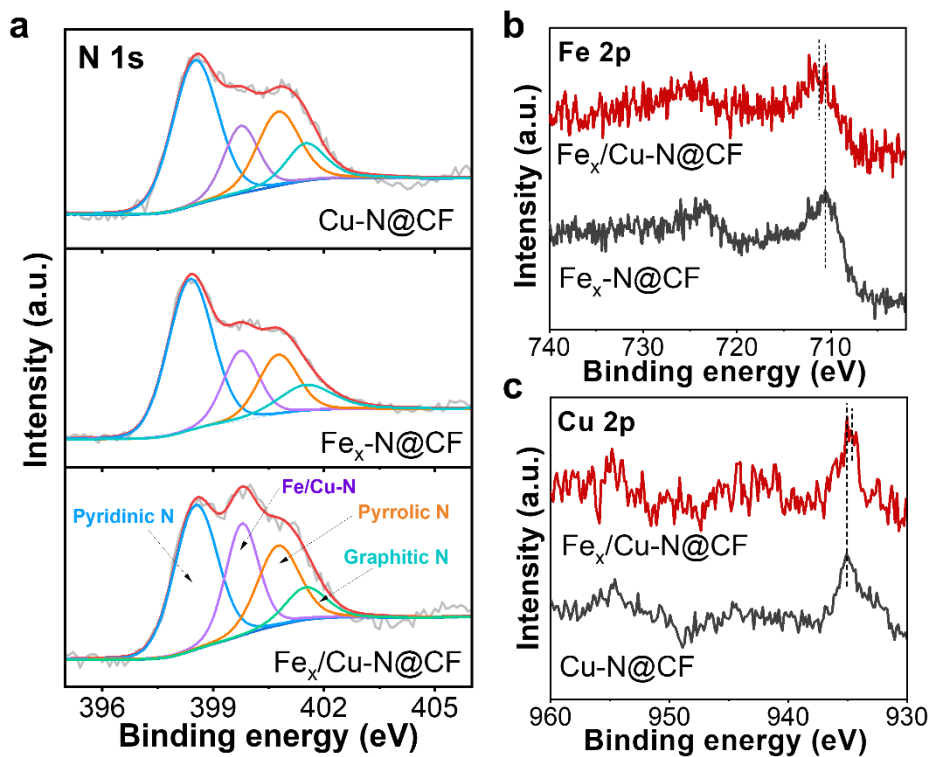
Figure S6. 13 XPS spectra of N 1s, Fe 2p, and Cu 2p in Cu–N@CF, Fe_x–N@CF and Fe_x/Cu–N@CF.
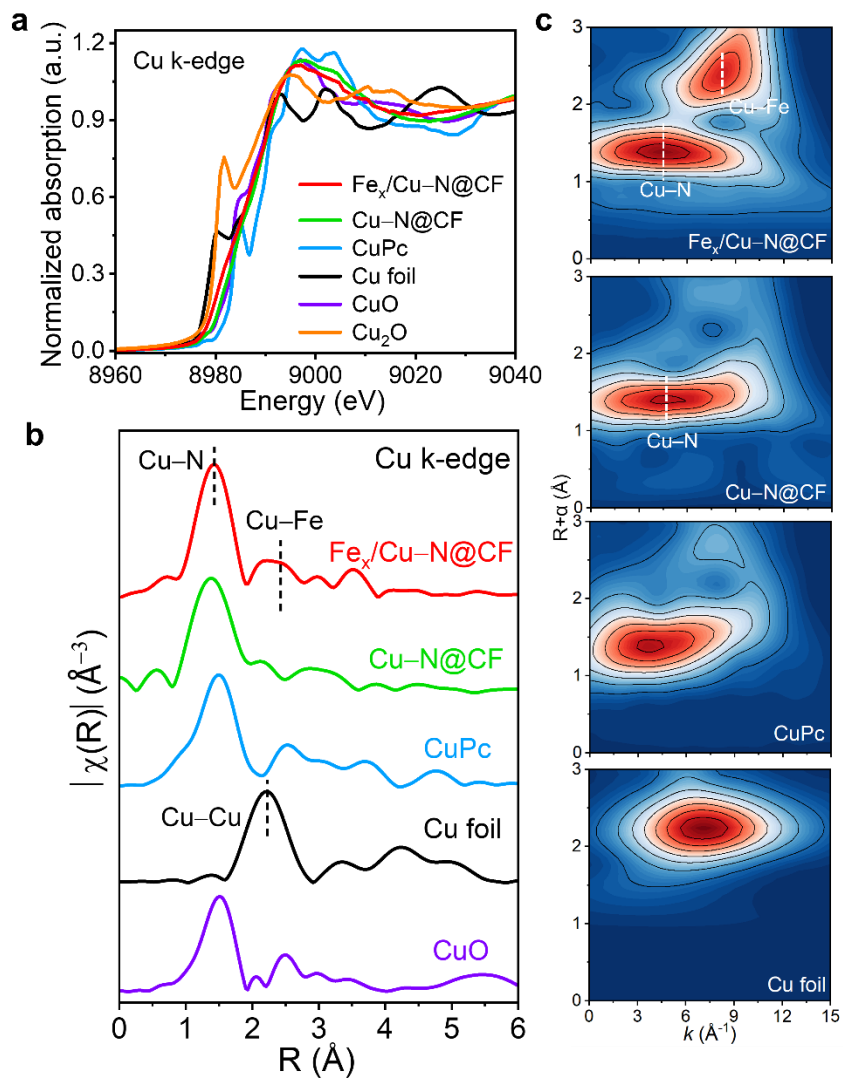
Figure S6. 14 (a) Cu K-edge XANES spectra and (b) EXAFS curves of Fe$_x$/Cu–N@CF, Cu–N@CF and references (Cu Pc, Cu foil, CuO, Cu$_2$O). (c) WT-EXAFS of Fe$_x$/Cu–N@CF, Cu–N@CF, Cu Pc, Cu foil and CuO.
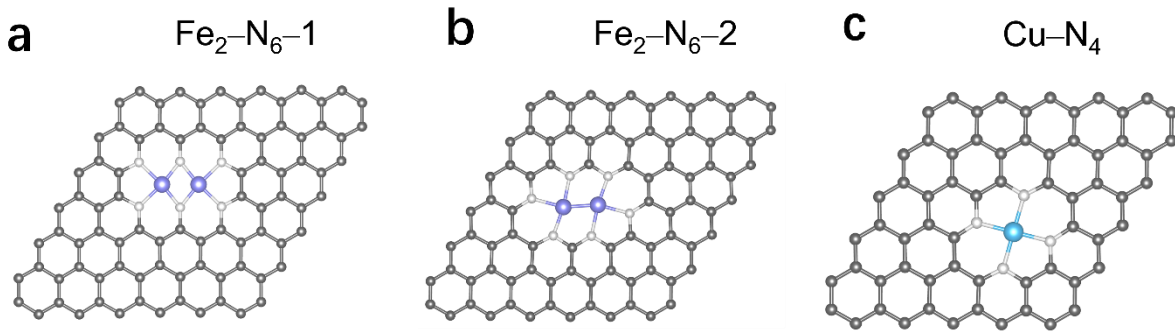
Figure S6. 15 The proposed possible structural models of Fe_x-N@CF (a-b) and Cu-N@CF (c).
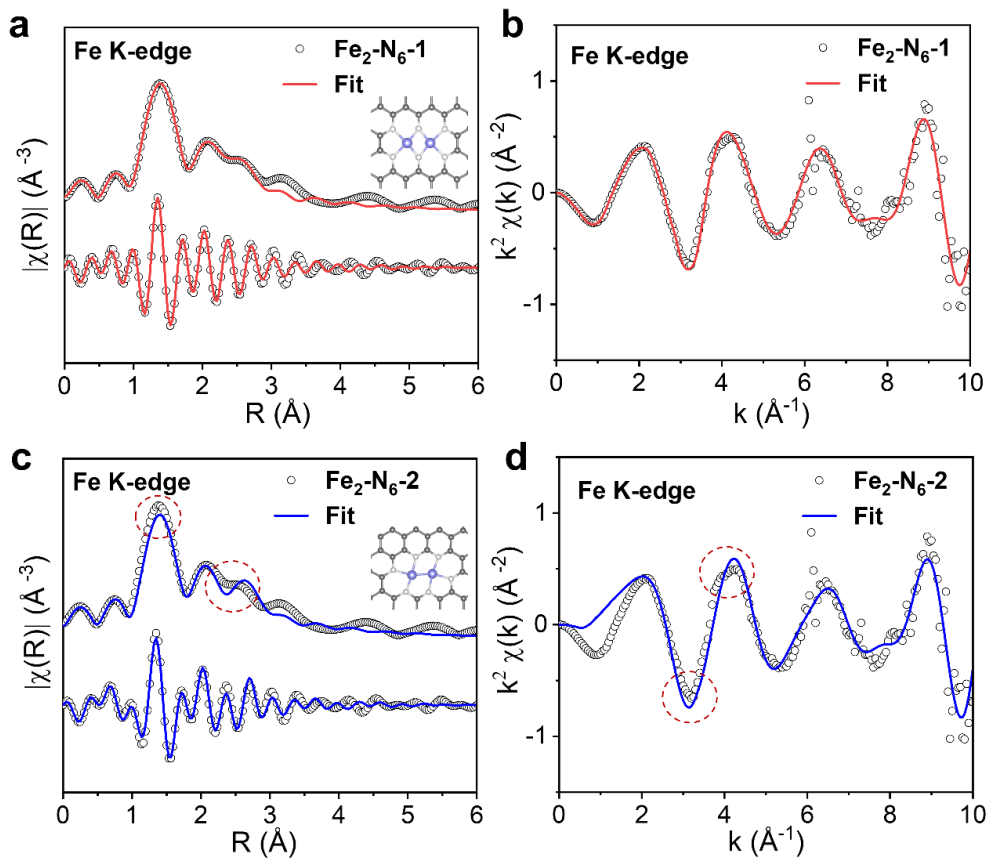
Figure S6. 16 (a, b) Fe K-edge experimental and FT-EXAFS fitting curves of Fe_x-N@CF and the corresponding fitting curves of k^2-weighted k-space based on Fe_2–N_6–1 and (c, d) Fe_2–N_6–2 models.

Table S6. 2 The Fe K-edge EXAFS curves fitting parameters of Fe_x-N@CF based on Fe_2–N_6–1, Fe_2–N_6–2 models.

Sample	Scattering pair	Coordination number	R(Å)	σ^2	$\triangle E_0$	S_0^2	R factor
	Fe-N1	1.98 ± 0.126	1.72	0.005			
Fe_2-N_6-1	Fe-N2	1.89 ± 0.367	1.94	0.004	3.9	0.83	0.0032
	Fe-Fe	0.91 ± 0.161	2.18	0.003			
	Fe-N	2.81 ± 0.69	1.99	0.003			
Fe_2-N_6-2					4.5	0.83	0.029
	Fe-Fe	0.94 ± 0.39	2.22	0.003			
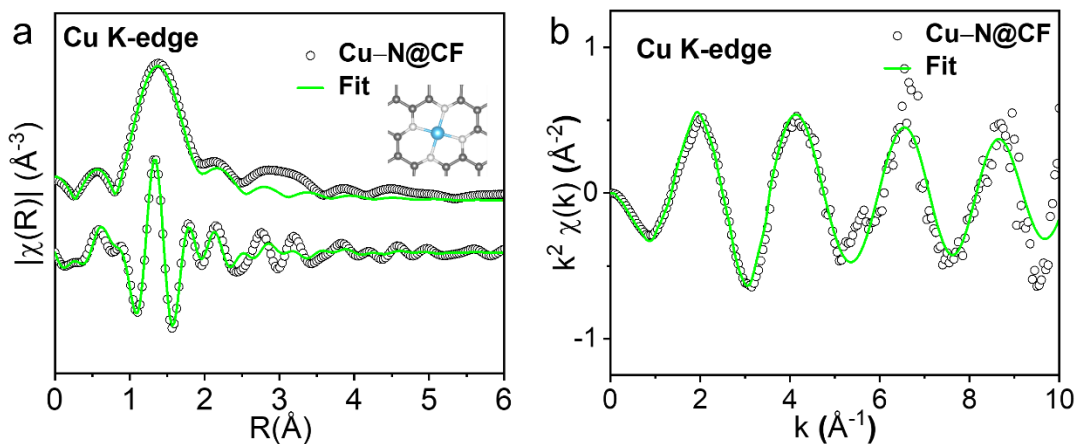
Figure S6. 17 (a) Cu K-edge experimental and FT-EXAFS fitting curves of Cu-N@CF based on Cu-N_4 model. (b) The corresponding fitting curves are shown in k^2-weighted k-space.

Table S6. 3 The Cu K-edge EXAFS curves fitting parameters of Cu-N@CF.

Sample	Scattering pair	Coordination number	$R(Å)$	σ^2	$\triangle E_0$	S_0^2	R factor
Cu-N@CF	Cu-N	3.91 ± 0.221	1.89	0.004	3.6	0.9	0.0044
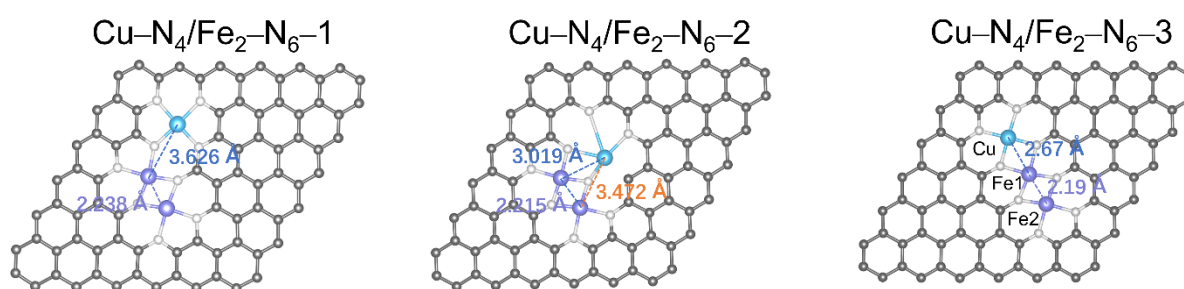
Figure S6. 18 The possible structural models of Fe_x/Cu-N@CF.
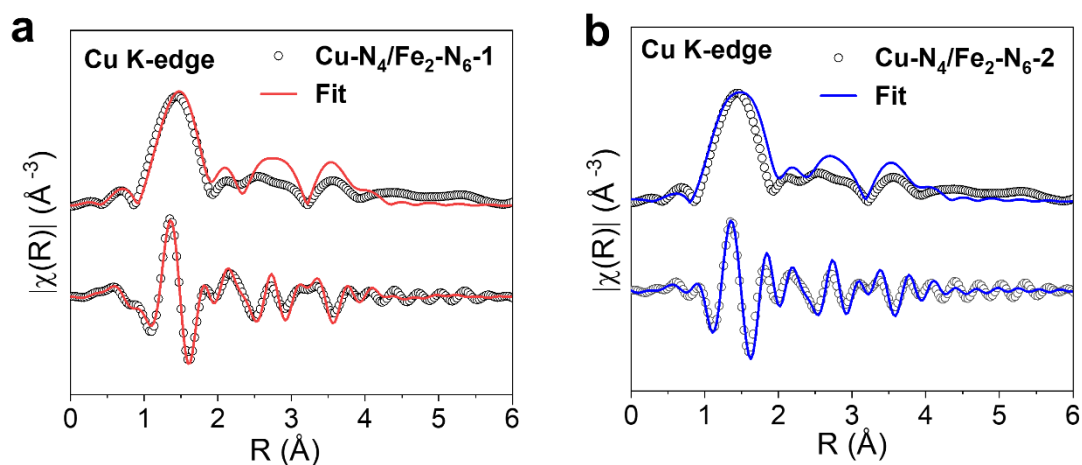
Figure S6. 19 Cu K-edge experimental and FT-EXAFS fitting curves of Cu-N@CF based on Cu-N_4/Fe_2-N_6-1 model (a) and Cu-N_4/Fe_2-N_6-2 model (b).

Table S6. 4 The Cu K-edge EXAFS curves fitting parameters of Cu-N@CF based on Cu-N_4/Fe_2-N_6-1 and Cu-N_4/Fe_2-N_6-2 models.

Sample	Scattering pair	Coordination number	R(Å)	σ^2	$\triangle E_0$	S_0^2	R factor
	Cu-N1	3.13 ± 0.132	1.95	0.003			
Cu-N_4/Fe_2-N_6-1	Cu-N2	1.02 ± 0.571	1.80	0.004	4.2	0.9	0.043
	Cu-Fe	0.55 ± 0.461	3.23	0.006			
	Cu-N1	2.11 ± 0.159	1.97	0.004			
Cu-N_4/Fe_2-N_6-2	Cu-N2	1.74 ± 0.436	1.80	0.004	5.5	0.9	0.031
	Cu-Fe	0.67 ± 0. 387	2.89	0.006			
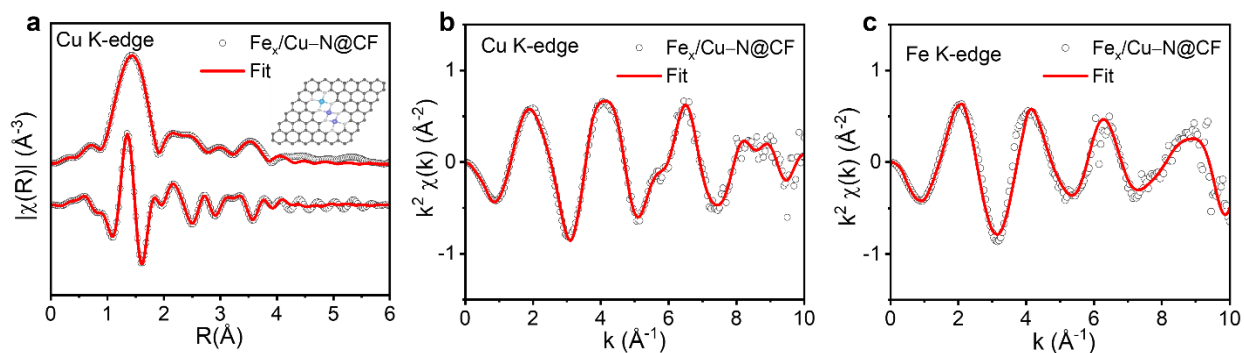
Figure S6. 20 (a) Cu K-edge experimental and FT-EXAFS fitting curves of Fe_x/Cu–N@CF in R-space (inset shows the corresponding structure model), and (b) the corresponding fitting curve shown in k^2-weighted k-space. (c) Fe K-edge experimental and FT-EXAFS fitting curves of Fe_x/Cu–N@CF shown in k^2-weighted k-space.

Table S6. 5 The Cu K-edge EXAFS curves fitting parameters of $Fe_x/Cu-N@CF$.

Sample	Scattering pair	Coordination number	R(Å)	σ^2	$\triangle E_0$	S_0^2	R factor
$Fe_x/Cu-N@CF$	Cu-N1	2.99 ± 0.041	1.95	0.005			
	Cu-N2	0.98 ± 0.083	1.80	0.004	3.6	0.9	0.001
	Cu-Fe	1.05 ± 0.062	2.77	0.003			

Table S6. 6 The Fe K-edge EXAFS curves fitting parameters of $Fe_x/Cu-N@CF$.

Sample	Scattering pair	Coordination number	R(Å)	σ^2	$\triangle E_0$	S_0^2	R factor
$Fe_x/Cu-N@CF$	Fe-N1	2.22 ± 0.361	1.77	0.005			
	Fe-N2	1.85 ± 0.123	1.95	0.004	3.9	0.83	0.012
	Fe-Fe	1.13 ± 0.345	2.17	0.003			
	Fe-Cu	1.15 ± 0.514	2.77	0.003			

R is the distance between absorber and backscatter atoms, $\sigma2$ is Debye-Waller factor to account for both thermal and structural disorders, ΔE_0 is inner potential correction; R factor indicates the goodness of the fit. S_0^2 for Fe K-edge fitting was fixed to 0.83 determined from Fe foil fitting. S_0^2 for Cu K-edge fitting was fixed to 0.9 determined from Cu foil. Fitting range: $3 \leq k (/Å) \leq 11$ and $1 \leq R (Å) \leq 3$.
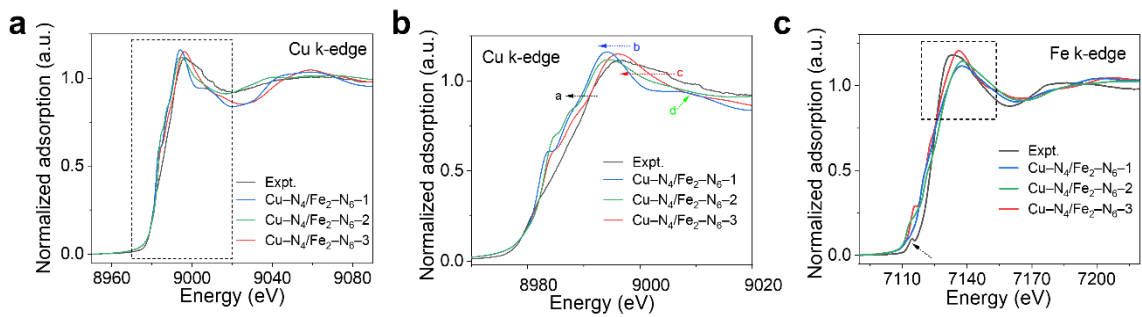
Figure S6. 21 (a) Comparison between the experimental Cu K-edge XANES spectrum of Fe_x/Cu-N@CF and the simulated spectra. (b) The spectra from dash box of (a). (c) Comparison between the experimental Fe K-edge XANES spectrum of Fe_x/Cu-N@CF and the simulated spectra.
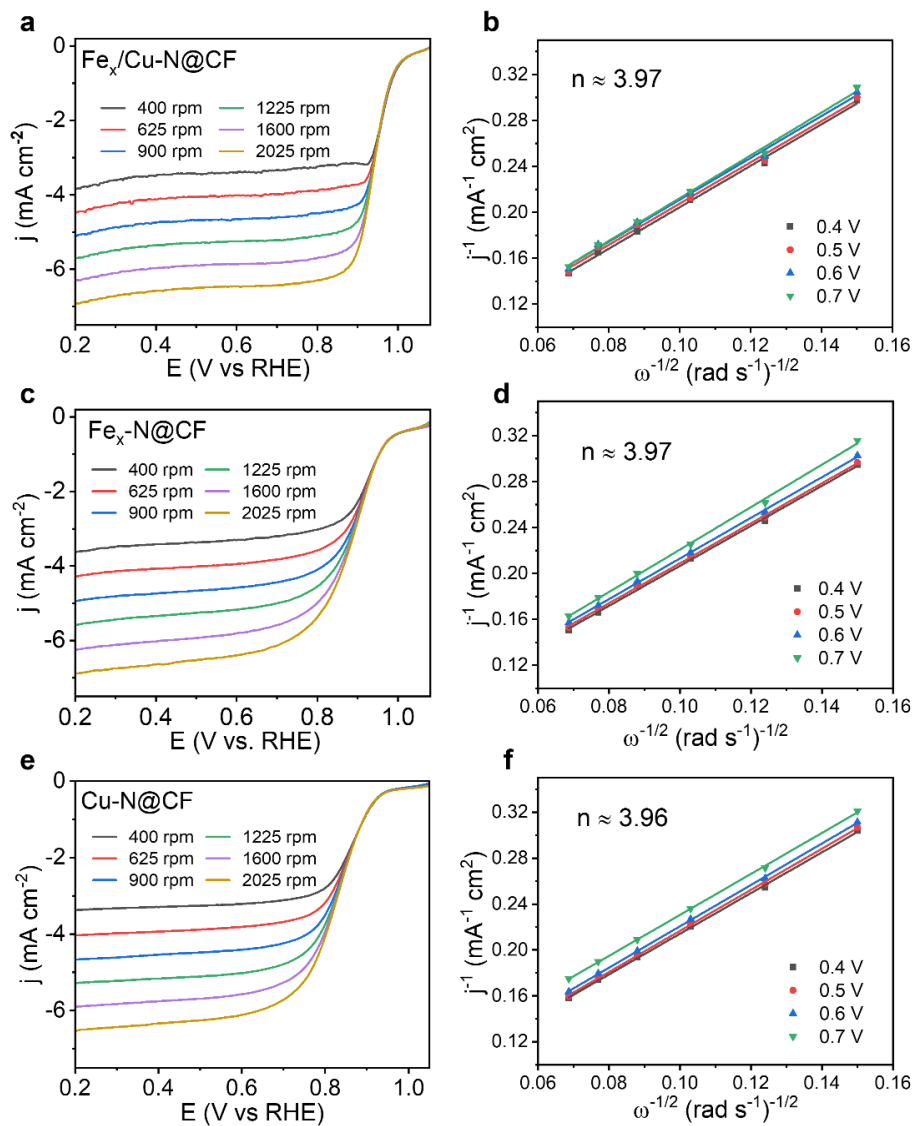
Figure S6. 22 LSV curves of (a) Fe_x/Cu-N@CF, (c) Fe_x-N@CF and (e) Cu-N@CF at different rotating rates. (b, d, f) The corresponding K-L plots and electron transfer number.
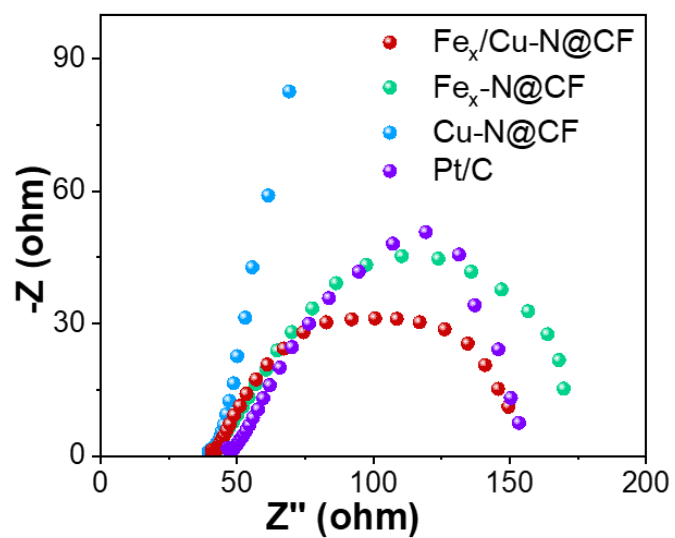
Figure S6. 23 EIS plots of Fe$_x$/Cu-N@CF, Fe$_x$-N@CF, Cu-N@CF and Pt/C.
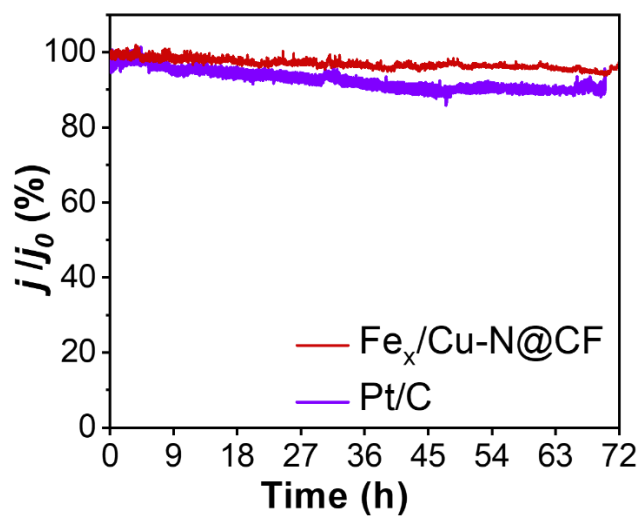
Figure S6. 24 Stability test at 0.6 V for Fe$_x$/Cu-N@CF and Pt/C in 0.1 M KOH.

195
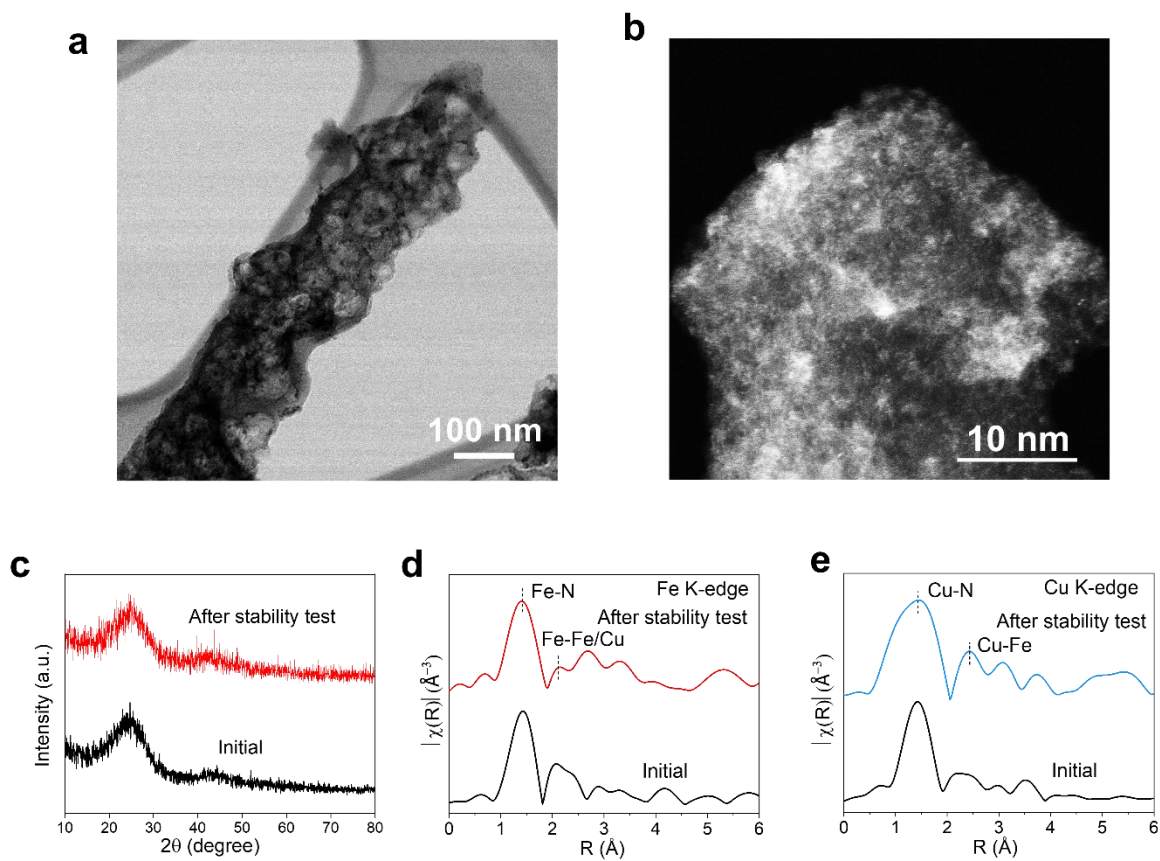
Figure S6. 25 (a-b) HR-TEM image, (c) XRD pattern, (d-e) Fourier-transform EXAFS curves of Fe$_x$/Cu-N@CF before and after stability test.
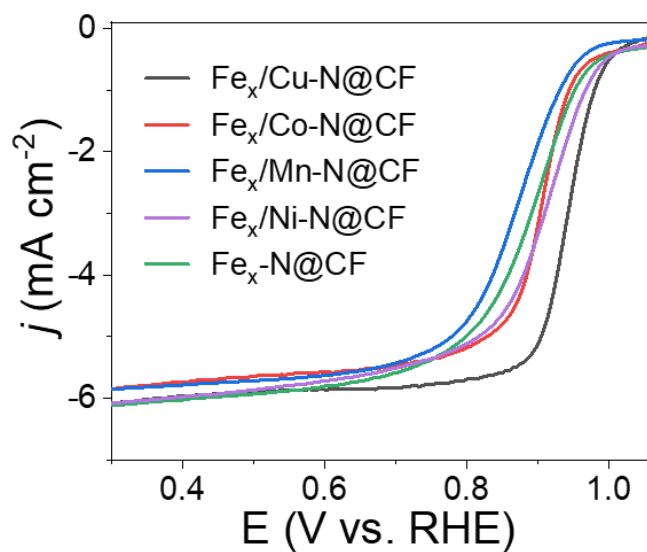
Figure S6. 26 LSV curves were recorded in 0.1 M KOH with a rotation rate of 1600 rpm.

The ORR performance of other $M-N_4$ (e.g., CoN_4, MnN_4, and NiN_4) decorated atomic Fe clusters was also examined. As shown in Figure S26, the CuN_4 is the most effective one in improving the ORR performance of Fe clusters.
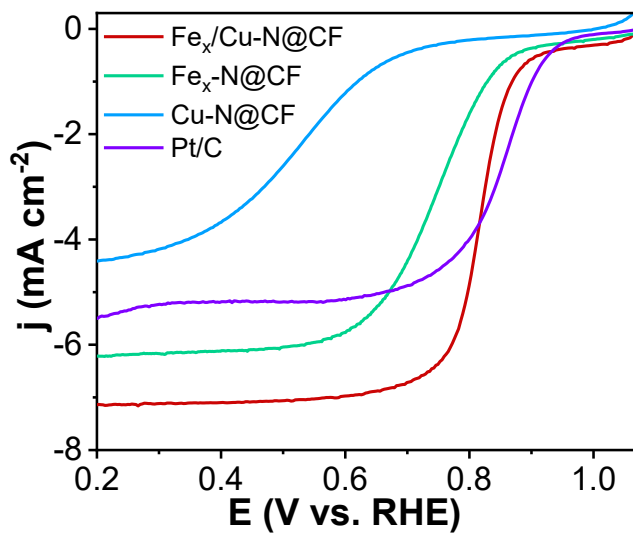
Figure S6. 27 LSV curves in O_2-saturated 0.1 M $HClO_4$.
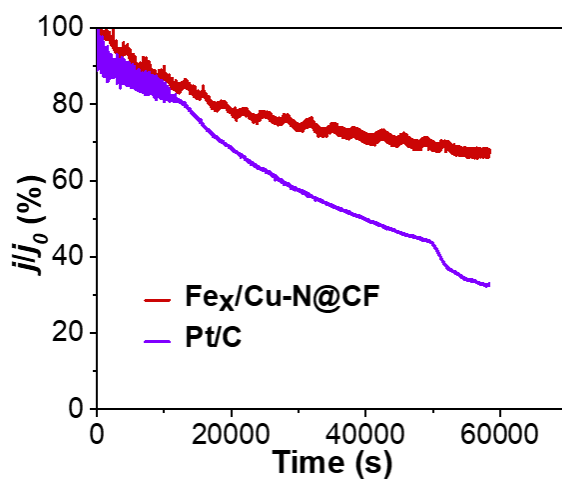
Figure S6. 28 Stability test at 0.6 V in 0.1 M HClO$_4$.
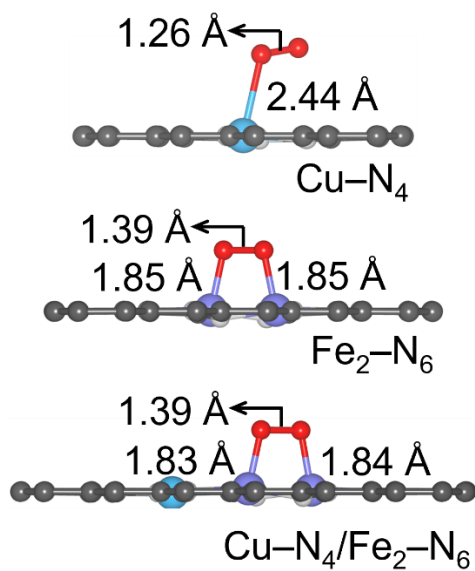
Figure S6. 29 Optimized geometry of OO* adsorption configuration on Cu–N$_4$, Fe$_2$–N$_6$ and Cu–N$_4$/Fe$_2$–N$_6$.
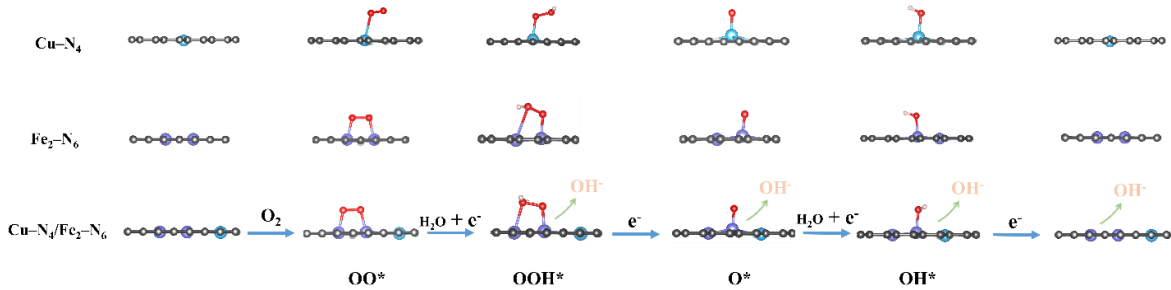
Figure S6. 30 The ORR reaction pathways of Cu–N$_4$, Fe$_2$–N$_6$ and Cu–N$_4$/Fe$_2$–N$_6$.
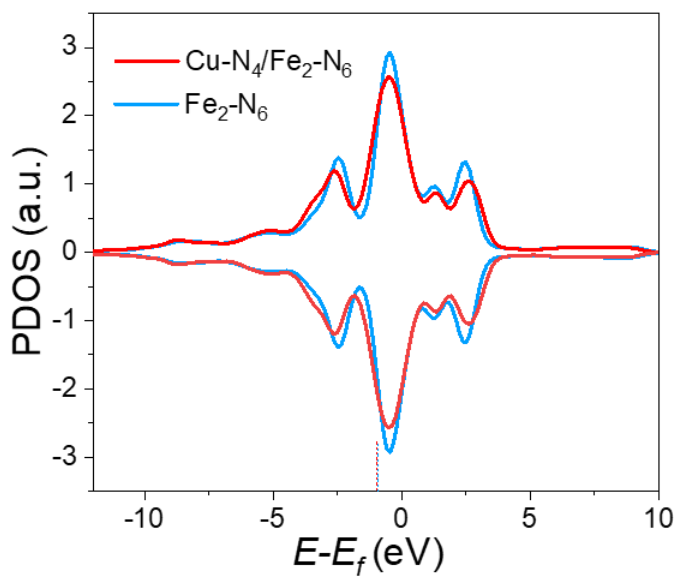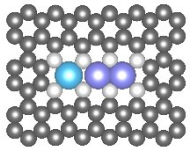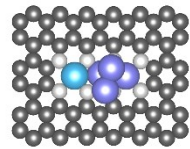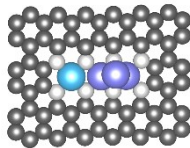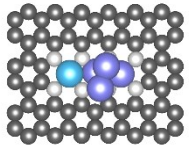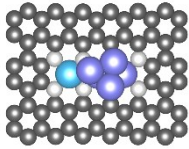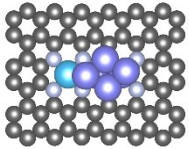
Figure S6. 31 The PDOS of Fe d orbitals in Fe$_2$–N$_6$ and Cu–N$_4$/Fe$_2$–N$_6$.

Additional DFT calculations were performed to investigate the possible structure of the catalyst. To investigate the thermodynamic feasibility of Fe forming a cluster with a larger number of atoms, we calculated the reaction energy of adding Fe to the CNF structure, starting from $Cu-N_4/N_6$ and progressing to $Cu-N_4/Fe_2-N_6$, and all the way to $Cu-N_4/Fe_6-N_6$. Table S6.7 reports the reaction energies. The comparison of reactions i and ii reveals that the addition of first two Fe atoms close to Cu is energetically favorable (-3.50 eV). However, if $Cu-N_4/Fe_2-N_6$ is already formed, adding two more Fe atoms is significantly less favorable, suggesting it is unlikely to occur on the catalytic surface. As Fe atoms are added one by one to the previous structures in reactions iii-vi, the reaction energies increase from +2.53 to +2.93 eV, indicating that during the catalyst synthesis, Fe atoms are more likely to form a new $Cu-N_4/Fe_2-N_6$ structure near a single Cu with the formation of Fe–N moieties on the CNF rather than aggregating into larger Fe-Fe clusters.

Table S6. 7 The Fe cluster formation reactions and corresponding reaction energies

	Hypothetical reactions	Reaction energy(eV)	Structures
i	$Cu-N_4/N_6 + 2Fe = Cu-N_4/Fe_2-N_6$	-3.50	
ii	$Cu-N_4/Fe_2-N_6 + 2Fe = Cu-N_4/Fe_4-N_6$	+5.27	
iii	$Cu-N_4/Fe_2-N_6 + Fe = Cu-N_4/Fe_3-N_6$	+2.53	

iv	Cu–N$_4$/Fe$_3$–N$_6$ + Fe = Cu–N$_4$/Fe$_4$–N$_6$	+2.73	
v	Cu–N$_4$/Fe$_4$–N$_6$ + Fe = Cu–N$_4$/Fe$_5$–N$_6$	+2.70	
vi	Cu–N$_4$/Fe$_5$–N$_6$ + Fe = Cu–N$_4$/Fe$_6$–N$_6$	+2.93	

*The energy of Fe is taken from pure iron lattice unit cell.

The use of simplified models with a few Fe atoms to represent an iron cluster is common in the literature.[21,22] We believe that the Cu–N$_4$/Fe$_2$–N$_6$ model is appropriate as a basic unit for representing the catalyst structure. To validate this model, we calculated the free energy pathway of a larger model consisting of Cu–N$_4$/Fe$_4$–N$_{11}$ (Figure S6.32). The Cu–N$_4$/Fe$_4$–N$_{11}$ model has single Cu atoms located on the edges of the observed "Fe cluster."
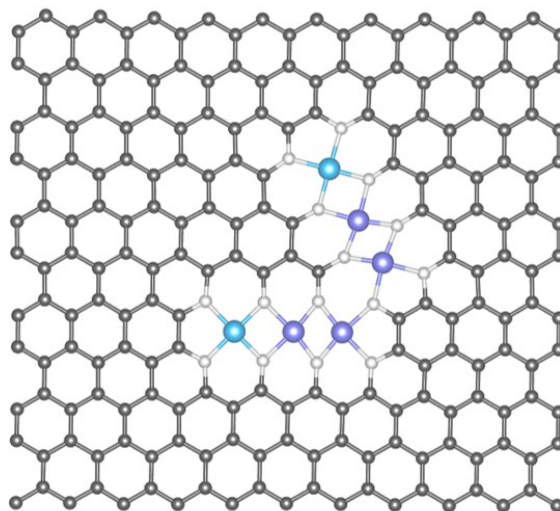
Figure S6. 32 The Cu–N$_4$/Fe$_4$–N$_{11}$ model.

We found that the active site remains on the Fe atoms that are closest to the Cu atoms, confirming the enhancing effect of Cu on the reactivity of the Fe cluster. As shown in Figure S6.33, the energy profile of this large model is similar to the $Cu-N_4/Fe_2-N_6$ model proposed in the manuscript, with a similar limiting step of 0.62 eV (the reaction energy for *OO to *OOH). This suggests that the combination of multiple $Cu-N_4/Fe_2-N_6$ models could potentially form a large Fe cluster in the center with single Cu atoms on the edges, while still maintaining active sites on Fe atoms that are enhanced by Cu atoms. Therefore, we conclude that the $Cu-N_4/Fe_2-N_6$ model proposed is suitable for representing the catalyst structure.
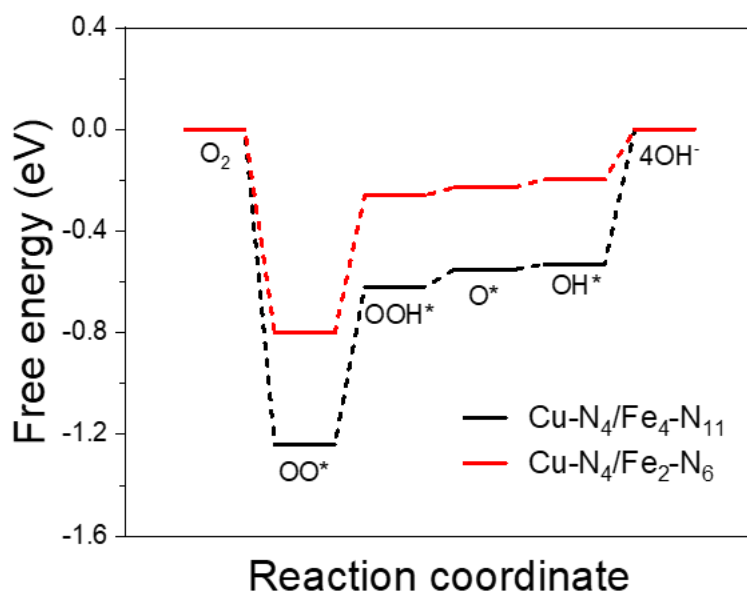
Figure S6. 33 ORR free energy diagrams for $Cu-N_4/Fe_2-N_6$, and $Cu-N_4/Fe_4-N_{11}$ at U=1.23 V.

Table S6. 8 Bader's charge of Fe atom on Fe_2–N_6 and Cu–N_4/Fe_2–N_6 model

Model	Fe #1	Fe #2	Average
Fe_2–N_6	0.959	0.956	0.958
Cu–N_4/Fe_2–N_6	1.015	0.984	1.000

Bader's charge analysis was performed to further investigate the impact of Cu on Fe_2–N_6. Table S6.8 shows the Bader's charge for Fe on both Fe_2–N_6 and Cu–N_4/Fe_2–N_6 models. On Fe_2–N_6 model, two Fe atoms have the same neighbor atoms, resulting in their Bader's charges being similar, with an average value of 0.958. On Cu–N_4/Fe_2–N_6 model, the Bader's charges of Fe are slightly increased to 1.015 and 0.984, respectively. We observed Fe #1 is in between Cu and another Fe atom (Fe #2). As Fe #1 is closer to Cu, its Bader's charge increased more significantly, resulting in a stronger bond with O-containing adsorbates. This is qualitatively in agreement with configuration analysis and free energy calculation results.

Table S6. 9 ORR activities of various transition metal singe-atom electrocatalysts in 0.1 M KOH.

Catalysts	$E_{1/2}$ (V vs RHE)	Tafel slope (mV dec^{-1})	J_k (mA cm^{-2}) @0.9 (V vs RHE)*	MA(A g^{-1})@ @0.9 (V vs RHE)*	Reference
Fe$_x$/Cu-N@CF	**0.944**	**52.61**	**34.37**	**137.5**	**This work**
NCAG/Fe-Cu	0.94	55	20	49.1	23
Fe/Zn-N-C	0.906	47	10	26.3	24
Fe-Te$_n$	0.867	86	2.3	20.3	25
Co$_2$/Fe-N@CHC	0.915	62	9.44	31.46	26
Fe,Mn/N-C	0.928	86	7.1	71	27
Cu/Zn-NC	0.83	54.8	1.1	2.71	28
Zn/Fe–N–C	0.86	84	5.49@0.85V	16.1@0.85V	29
Fe-N$_4$/Pt-N$_4$@NC	0.93	78	13.1	NA	30
Ni-N$_4$/GHSs/Fe-N$_4$	0.83	55	2.8	11.2	31
Fe/Ni-N$_x$/OC	0.938	59.9	28.1	98.6	32
FeCoNiCuMn	0.887	81	3.2	6.27	33
Fe-NC-S	0.88	49	2	10	34
Fe-N/P-C-700	0.844	NA	1.56	2.6	35
Fe/SNCFs-NH$_3$	0.89	70.82	38.36 @ 0.82 V	100.2@0.82	36
Fe-Pc-O defect	0.929	30	13	118.4	37
Fe-N-C-900	0.905	76.6	10	50	38
Fe-N-C/Fe NP	0.885	56	55.1 @ 0.8 V	162.1@0.8V	39
FeAC@FeSA−N−C	0.912	61	61.1@0.85	165@0.85	40
Fe-ACSA@NC	0.90	76	6.45	24.81	41
P/Fe-N-C	0.90	NA	25.4@0.85	40.7@0.85	42
5-PtNi$_x$/NiNC	0.86	NA	NA	26	43
Pd$_{50}$Ag$_{50}$	0.81	45.7	NA	NA	44

*The value of J_k and Mass activity (MA) are recorded at 0.9 V, except specifically noted.

6.5.3 References

1. D. C. Koningsberger and R. Prins, 1987.

2. B. Ravel and M. Newville, *J. Synchrotron Radiat*, 2005, **12**, 537-541.

3. H. Funke, A. Scheinost and M. Chukalina, *Phys. Rev. B*, 2005, **71**, 094110.

4. H. Funke, M. Chukalina and A. Scheinost, *J. Synchrotron Radiat*, 2007, **14**, 426-432.

5. O. Bunău, A. Y. Ramos and Y. Joly, *Wiley*, 2021.

6. Y. Joly, A. Y. Ramos and O. Bunău, *Wiley*, 2022.

7. S. Niu, S. Li, Y. Du, X. Han and P. Xu, *ACS Energy Lett*, 2020, **5**, 1083-1087.

8. S. G. Ji, H. Kim, C. Park, W. Kim and C. Choi, *ACS Catal.*, 2020, **10**, 10773-10783.

9. G. Yang, J. Zhu, P. Yuan, Y. Hu, G. Qu, B.-A. Lu, X. Xue, H. Yin, W. Cheng, J. Cheng and W. Xu, *Nat. Commun.*, 2021, **12**, 1734.

10. G. Kresse and J. Furthmüller, *Comput. Mater. Sci.*, 1996, **6**, 15-50.

11. G. Kresse and J. Furthmüller, *Phys. Rev. B*, 1996, **54**, 11169-11186.

12. G. Kresse and J. Hafner, *J. Phys. Condens. Matter*, 1994, **6**, 8245-8257.

13. G. Kresse and D. Joubert, *Phys. Rev. B*, 1999, **59**, 1758-1775.

14. G. Kresse and J. Hafner, *Phys. Rev. B*, 1993, **47**, 558-561.

15. P. E. Blöchl, *Phys. Rev. B,* 1994, **50**, 17953-17979.

16. J. P. Perdew, K. Burke and M. Ernzerhof, *Phys. Rev. Lett.*, 1996, **77**, 3865-3868.

17. J. Klimeš, A. Bowler Dr Fau - Michaelides and A. Michaelides, *Condens. Matter*, 2009, **22**, 022201.

18. J. Klimeš, D. R. Bowler and A. Michaelides, *Phys. Rev. B*, 2011, **83**, 195131.

19. Malcolm W. Chase, Jr., *NIST-JANAF thermochemical tables*, Fourth edition. Washington, DC : American Chemical Society ; New York : American Institute of Physics for the National Institute of Standards and Technology, 1998.

20. J. K. Nørskov, J. Rossmeisl, A. Logadottir, L. Lindqvist, J. R. Kitchin, T. Bligaard and H. Jónsson, *J. Phys. Chem. B*, 2004, **108**, 17886-17892.

21. X. Wan, Q. Liu, J. Liu, S. Liu, X. Liu, L. Zheng, J. Shang, R. Yu and J. Shui, *Nat. commun.*, 2022, **13**, 2963.

22. S. An, G. Zhang, T. Wang, W. Zhang, K. Li, C. Song, J. T. Miller, S. Miao, J. Wang and X. Guo, *ACS nano*, 2018, **12**, 9441-9450.

23. T. He, Y. Chen, Q. Liu, B. Lu, X. Song, H. Liu, M. Liu, Y. N. Liu, Y. Zhang and X. Ouyang,

Angew. Chem. Int. Ed., 2022, **61**, e202201007.

24. H. Li, S. Di, P. Niu, S. Wang, J. Wang, L. Li, Energy Environ. Sci., 2022, **15**, 1601-
    a. 1610.

25. B. Ji, J. Gou, Y. Zheng, X. Zhou, P. Kidkhunthod, Y. Wang, Q. Tang and Y. Tang, *Adv. Mater.,* 2022, **34**, 2202714.

26. Z. Wang, X. Jin, C. Zhu, Y. Liu, H. Tan, R. Ku, Y. Zhang, L. Zhou, Z. Liu, S. J. Hwang and H.J. Fan, Adv. Mater., 2021, **33**, 2104718.

27. G. Yang, J. Zhu, P. Yuan, Y. Hu, G. Qu, B.-A. Lu, X. Xue, H. Yin, W. Cheng, J. Cheng and W. Xu, *Nat. Commun.,* 2021, **12**, 1-10.

28. M. Tong, F. Sun, Y. Xie, Y. Wang, Y. Yang, C. Tian, L. Wang and H. Fu, *Angew. Chem. Int. Ed.,* 2021, **60**, 14005-14012.

29. J. Xue, Y. Li and J. Hu, J. Mater. Chem. A, 2020, 8, 7145-7157.

30. A. Han, X. Wang, K. Tang, Z. Zhang, C. Ye, K. Kong, H. Hu, L. Zheng, P. Jiang, C. Zhao and Q. Zhang *Angew. Chem. Int. Ed.,* 2021, **60**, 19262-19271.

31. J. Chen, H. Li, C. Fan, Q. Meng, Y. Tang, X. Qiu, G. Fu, T. Ma., *Adv. Mater.,* 2020, **32**, 2003134.

32. Z. Zhu, H. Yin, Y. Wang, C. H. Chuang, L. Xing, M. Dong, Y. R. Lu, G. Casillas-Garcia, Y. Zheng, S. Chen and Y. Dou, *Adv. Mater.,* 2020, 32, 2004670.

33. Rao, P., Deng, Y., Fan, W. *et al.* Movable type printing method to synthesize high-
    a. entropy single-atom catalysts. *Nat Commun.,* 2022, **13**, 5071.

34. X. Li, C.-S. Cao, S.-F. Hung, Y.-R. Lu, W. Cai, A. I. Rykov, S. Miao, S. Xi, H. Yang, Z. Hu, J. Wang, *Chem* 2020, 6, 3440-3454.

35. K. Yuan, D. Lützenkirchen-Hecht, L. Li, L. Shuai, Y. Li, R. Cao, M. Qiu, X. Zhuang, M. K. Leung, Y. Chen, U. Scherf, *J. Am. Chem. Soc.* 2020, 142, 2404-2412.

36. L. Yang, X. Zhang, L. Yu, J. Hou, Z. Zhou and R. Lv, *Adv. Mater.,* 2022, **34**, 2105410.

37. X. Tan, H. Li, W. Zhang, K. Jiang, S. Zhai, W. Zhang, N. Chen, H. Li and Z. Li, *Chem Catal.,* 2022, **2**, 816-835.

38. C. Zhu, Q. Shi, B. Z. Xu, S. Fu, G. Wan, C. Yang, S. Yao, J. Song, H. Zhou, D. Du and S.P. Beckman, *Adv. Energy Mater.,* 2018, **8**, 1801956.

39. S. N. Zhao, J. K. Li, R. Wang, J. Cai and S. Q. Zang, *Adv. Mater*., 2022, **34**, 2107291.

40. X. Ao, W. Zhang, Z. Li, J.-G. Li, L. Soule, X. Huang, W.-H. Chiang, H. M. Chen, C. Wang,

M. Liu and X.C. Zeng, *ACS nano,* 2019, **13**, 11853-11862.

41. H. Huang, D. Yu, F. Hu, S. C. Huang, J. Song, H. Y. Chen, L. L. Li and S. J. A. C. Peng, *Angew. Chem. Int. Ed.,* 2022, **134**, e202116068.

42. Y. Zhou, R. Lu, X. Tao, Z. Qiu, G. Chen, J. Yang, Y. Zhao, X. Feng, K. J. J. o. t. A. C. S. Müllen, *J. Am. Chem. Soc.*, 2023, **145**, 3647-3655.

43. Q. Feng, X. Wang, M. Klingenhof, M. Heggen and P. Strasser, *Angew. Chem. Int. Ed.,* 2022, 61, e202203728.

44. W. He, X. Li, Z. Qian, Z. Liu and Z. Tang, *Int. J. Electrochem. Sci*, 2019, 14, 8781-8792.

Chapter 7 Summary and prospects

7.1 Summary

In this thesis, I present the strategies in developing transition metal-based catalysts for electrochemical devices. The advances and ideas presented herein are described as below:

In chapter 4, the integration of two-phase-coexisting nanosheets on three-dimensional substrates offers new and fascinating opportunities for the design of electrocatalysts. The catalyst composed of Ni_3S_2-embedded NiFe LDH porous nanosheets in situ grown on nickel foam (Ni_3S_2-NiFe LDHs /NF) was fabricated via a one-pot solution method mediated by NaHS at room temperature in 15 min, without any sophisticated equipment involved. The NaHS plays a critical role in the growing process by manipulating the Ni^{2-} release from nickel foam and providing OH^- and S^{2+}. The preparation process is fully controllable and scalable to deliver commercial-level performance. This study reveals the enhanced catalytic activity by offering the following advantages: 1) The Ni_3S_2-embedded NiFe LDH porous nanosheet possesses remarkably more interfaces than the traditional hierarchical structure. 2) Ni_3S_2 was *in situ* partially transformed into NiOOH under electrooxidation environment, the newly formed NiOOH is equally important with remaining electrically conductive Ni_3S_2 to drive proficient catalysis. 3) This integrated 3D electrode significantly facilitates the charge and mass transfer. For instance, the bubbles can be released much more efficiently, according to our *in situ* microscope analysis. The resulting catalyst only requires an η of 303 mV to deliver 1000 mA cm^{-2} toward OER. It can continuously work for at least 240 h at 100 mA cm^{-2}. This strategy can be extended to prepare a highly active HER catalyst (Ru-Ni_3S_2-NiFe LDHs/NF). A full electrolytic cell coupling Ni_3S_2-NiFe LDH/NF-2 and Ru-Ni_3S_2-NiFe LDHs/NF catalysts achieved remarkable j_s of 10, 100 and 500 mA cm^{-2} at low voltages of

1.47, 1.71 and 1.85 V upon driving overall water splitting, far surpassing current commercial requirements (200-400 mA cm^{-2} at 1.8-2.40 V).

In chapter 5, I developed hierarchical nanoneedle arrays with abundant CoF$_2$-CoP interface on Ni foam as a bifunctional electrocatalyst for HER and HMFOR. Interfacial electron transfer between CoF$_2$ and CoP modulates the electronic environments of the active centers, boosting the activity and stability of both HER/HMFOR. The modulated electronic structure benefits the Co^{2+}↔Co^{3+}↔Co^{4+} transformations under the bias potential. The post-investigation reveals that γ-CoOOH and Co (OH)$_2$ were formed via anion reconstruction under the HMFOR and HER, respectively, which serve as the real active phases contributing to the electrocatalytic activity. As a result, CoF$_2$/CoP-2 exhibits excellent HMFOR activity with a working potential of only 1.33 V to deliver 100 mA cm^{-2}. Meanwhile, the FDCA yield achieved 98.8 % and the faradic efficiency is 98 %. CoF$_2$/CoP-2 also exhibits outstanding HER activity delivering 10 mA cm^{-2} at an overpotential of only 59 mV. Furthermore, the electrolyzer employing CoF$_2$/CoP-2 for cathodic H$_2$ and cathodic FDCA production only requires the cell voltage of 1.33 V at 10 mA cm^{-2}, superior to the voltage of 1.54 V at 10 mA cm^{-2} for pure water splitting. This work demonstrates a promising strategy of the construction of CoF$_2$/CoP heterostructure for both electrocatalytic HMF oxidation and HER to promote H$_2$ generation efficiency and the production of value-added products, paving a way for "green chemistry".

In chapter 6, I demonstrated a Fe$_x$/Cu–N@CF catalyst with atomic Fe clusters functionalized by adjacent single Cu–N$_4$ sites anchoring on porous carbon nanofiber membrane. The theoretical calculation indicates that the single Cu–N$_4$ sites can modulate the electronic configuration of Fe clusters to trigger optimized oxygen intermediates absorption and strong driving force for O–O cleavage, because the introduction of Cu-N$_4$ sites increases the filling degree of d orbitals of Fe

and the overlaps between d orbitals of Fe and p orbitals of O in OOH*. In addition, the construction of crosslinked one-dimensional carbon nanofibers provides sufficient microporosity for hosting active sites and interconnected micro- and mesopores for efficient mass and charge transfer. As a result, this unique atomic catalyst exhibits excellent ORR activity with 0.944 V of half-wave potential ($E_{1/2}$) in 0.1M KOH, registering as one of the best performing ORR catalysts. And 0.815 V of $E_{1/2}$ in 0.1M $HClO_4$ is comparable with commercial Pt/C. For practical applications, the free-standing Fe_x/Cu-N@CF membrane was successfully incorporated as an effective air cathode in Zn–air battery device with long-term work stability. Besides the outstanding catalytic activity, the two key achievements of this work are (1) having developed a feasible strategy (single atom functionalizes atomic clusters) to overcome the obstacle of poor O–O cleavage and (2) having understood the interplay between single atoms and atomic clusters on ORR. This work shows the great potential of single atoms for improvements in atomic cluster catalysts.

7.2 Future prospects

Understanding the dynamic reconstruction of electrocatalysts under the working conditions is critical for the design of highly efficient catalysts, since most electrocatalysts undergo structural reconstruction and surface rearrangement under the bias potential. Similarly, the catalysts presented in this thesis undergo the transformation in terms of composition and morphology during the electrocatalytic process. *In situ* characterizations provide the information of understanding reconstruction process, real active sites, and catalytic intermediates. Recently, *in situ* investigations have been explored by various techniques, including Raman, X-ray diffraction (XRD), infrared (IR) spectroscopy, X-ray photoelectron spectroscopy (XPS), X-ray absorption spectroscopy (XAS), transmission electron microscopy (TEM) and other methods, in tracking the reconstruction of electrocatalysts in realistic reaction conditions. However, employing a single *in situ* technique

could provide limited reconstruction information of catalysts. Thus, using *in situ* techniques will provide deep insights into reaction progress under applied potential, which should be central position for this research direction.

HMFOR have been regarded to as an ideal reaction for the replacement of OER coupling with HER for hydrogen generation with low driving voltage and production of value-added chemicals. Chapter 5 has shown that the construction of heterointerface creates a robust bifunctional electrocatalyst for HER and HMFOR. The mechanistic understanding associated with HMF electrocatalytic oxidation is still not clear enough so far. The development of innovative catalytic materials should be accompanied by the theoretical investigations to elaborate structure-performance relationships in-depth, such as molecular dynamics simulation and electronic calculation.

Transition metal-based catalysts for oxygen reduction reaction still are restricted by the low activity and durability in acidic media. Chapter 6 has shown that transition metal cluster anchored on N-doped carbon (M_x-N-C) is a promising alternative to Pt, which even outperform Pt/C in terms of both ORR activity and durability. However, the catalytic performance in acidic media is still far from satisfactory for practical application. Many efforts have been devoted to improving the catalytic activity of carbon based electrocatalysts, including regulation of the N dopant species, co-doping of heteroatoms (e.g., N/P and N/S), and morphological structure engineering. Further research effort should be made in this direction to promote catalytic performance of M_x-N-C for catalytic activity and stability in acidic media.

Bibliography

1. Cozzi, L.; Gould, T.; Bouckart, S.; Crow, D.; Kim, T.; Mcglade, C.; Olejarnik, P.; Wanner, B.; Wetzel, D., World energy outlook 2020. *International Energy Agency: Paris, France*, 2020, 1-461.

2. Yang, Z.; Zhang, J.; Kintner-Meyer, M. C.; Lu, X.; Choi, D.; Lemmon, J. P.; Liu, J., Electrochemical energy storage for green grid. *Chem. Rev.* 2011, *111* (5), 3577-613.

3. Chen, H.; Cong, T. N.; Yang, W.; Tan, C.; Li, Y.; Ding, Y., Progress in electrical energy storage system: A critical review. *Prog. Nat. Sci.* 2009, *19* (3), 291-312.

4. Zhang, F.; Liu, J.; Yang, W.; Logan, B. E., A thermally regenerative ammonia-based battery for efficient harvesting of low-grade thermal energy as electrical power. *Energy Environ. Sci.* 2015, *8* (1), 343-349.

5. Peng, L.; Zhu, Y.; Chen, D.; Ruoff, R. S.; Yu, G., Two-Dimensional Materials for Beyond-Lithium-Ion Batteries. *Adv. Energy Mater.* 2016, *6* (11), 1600025.

6. Thakur, V. K.; Ding, G.; Ma, J.; Lee, P. S.; Lu, X., Hybrid materials and polymer electrolytes for electrochromic device applications. *Adv. Mater.* 2012, *24* (30), 4071-96.

7. Lu, X. F.; Fang, Y.; Luan, D.; Lou, X. W. D., Metal-Organic Frameworks Derived Functional Materials for Electrochemical Energy Storage and Conversion: A Mini Review. *Nano Lett.* 2021, *21* (4), 1555-1565.

8. Chen, J.; Wei, L.; Mahmood, A.; Pei, Z.; Zhou, Z.; Chen, X.; Chen, Y., Prussian blue, its analogues and their derived materials for electrochemical energy storage and conversion. *Energy Stor. Mater.* 2020, *25*, 585-612.

9. Yang, Z.; Liu, J.; Baskaran, S.; Imhoff, C. H.; Holladay, J. D., Enabling renewable energy—and the future grid—with advanced electricity storage. Jom. 2010, *62*, 14-23.

10. Subinas Seco de Herrera, J. M., Development of a microgrid with renewable energy sources and electrochemical storage system integration. 2015.

11. Song, J.; Wei, C.; Huang, Z. F.; Liu, C.; Zeng, L.; Wang, X.; Xu, Z. J., A review on fundamentals for designing oxygen evolution electrocatalysts. *Chem. Soc. Rev.* 2020, *49* (7), 2196-2214.

12. Li, Y.; Wei, X.; Chen, L.; Shi, J., Electrocatalytic Hydrogen Production Trilogy. *Angew. Chem. Int. Ed.* 2021, *60* (36), 19550-19571.

13. Gopalakrishnan, M.; Mohamad, A. A.; Nguyen, M. T.; Yonezawa, T.; Qin, J.; Thamyongkit, P.; Somwangthanaroj, A.; Kheawhom, S., Recent advances in oxygen electrocatalysts based on tunable structural polymers. *Mater. Today Chem.* 2022, *23*, 100632.

14. Rodionova, M. V.; Poudyal, R. S.; Tiwari, I.; Voloshin, R. A.; Zharmukhamedov, S. K.; Nam, H. G.; Zayadan, B. K.; Bruce, B. D.; Hou, H. J. M.; Allakhverdiev, S. I., Biofuel production: Challenges and opportunities. *Int. J. of Hydrog. Energy* 2017, *42* (12), 8450-8461.

15. Yang, G.; Jiao, Y.; Yan, H.; Xie, Y.; Wu, A.; Dong, X.; Guo, D.; Tian, C.; Fu, H., Interfacial Engineering of MoO2 -FeP Heterojunction for Highly Efficient Hydrogen Evolution Coupled with Biomass Electrooxidation. *Adv. Mater.* 2020, *32* (17), e2000455.

16. Yang, G.; Jiao, Y.; Yan, H.; Tian, C.; Fu, H., Electronic Structure Modulation of Non-Noble-Metal-Based Catalysts for Biomass Electrooxidation Reactions. *Small Structures* 2021, *2* (10), 2100095.

17. Yang, C.; Wang, C.; Zhou, L.; Duan, W.; Song, Y.; Zhang, F.; Zhen, Y.; Zhang, J.; Bao, W.; Lu, Y.; Wang, D.; Fu, F., Refining d-band center in Ni0.85Se by Mo doping: A strategy

for boosting hydrogen generation via coupling electrocatalytic oxidation 5-hydroxymethylfurfural. *Chem. Eng. J.* 2021, *422*, 130125.

18. Singh, S. K.; Takeyasu, K.; Nakamura, J., Active Sites and Mechanism of Oxygen Reduction Reaction Electrocatalysis on Nitrogen-Doped Carbon Materials. *Adv. Mater.* 2019, *31* (13), e1804297.

19. Vanysek, P., Electrochemical series. *CRC handbook of chemistry and physics* 2000, *8*, 8-33.

20. McNaught, A. D.; Wilkinson, A., Compendium of chemical terminology. *Blackwell Science Oxford*: 1997; Vol. 1669.

21. Sawyer, D. T.; Roberts, J. L., Experimental electrochemistry for chemists. Wiley: 1974.

22. Woo, J.; Lim, J. S.; Kim, J. H.; Joo, S. H., Heteroatom-doped carbon-based oxygen reduction electrocatalysts with tailored four-electron and two-electron selectivity. *Chem. Commun.* 2021, *57* (60), 7350-7361.

23. Jiao, Y.; Zheng, Y.; Jaroniec, M.; Qiao, S. Z., Design of electrocatalysts for oxygen- and hydrogen-involving energy conversion reactions. *Chem. Soc. Rev.* 2015, *44* (8), 2060-86.

24. Xia, W.; Mahmood, A.; Liang, Z.; Zou, R.; Guo, S., Earth-Abundant Nanomaterials for Oxygen Reduction. *Angew. Chem. Int. Ed.* 2016, *55* (8), 2650-76.

25. Zhang, L.; Jiang, S.; Ma, W.; Zhou, Z., Oxygen reduction reaction on Pt-based electrocatalysts: Four-electron vs. two-electron pathway. *Chin. J. Catal.* 2022, *43* (6), 1433-1443.

26. Che, M., Nobel Prize in chemistry 1912 to Sabatier: Organic chemistry or catalysis? *Catal. Today* 2013, *218-219*, 162-171.

27. Strasser, P.; Kühl, S., Dealloyed Pt-based core-shell oxygen reduction electrocatalysts.

Nano Energy 2016, *29*, 166-177.

28. Shi, Y.; Zhang, B., Recent advances in transition metal phosphide nanomaterials: synthesis and applications in hydrogen evolution reaction. *Chem. Soc. Rev*. 2016, *45* (6), 1529-1541.

29. Zheng, Y.; Jiao, Y.; Vasileff, A.; Qiao, S. Z., The Hydrogen Evolution Reaction in Alkaline Solution: From Theory, Single Crystal Models, to Practical Electrocatalysts. *Angew. Chem. Int. Ed.* 2018, *57* (26), 7568-7579.

30. Zou, X.; Zhang, Y., Noble metal-free hydrogen evolution catalysts for water splitting. *Chem. Soc. Rev.* 2015, *44* (15), 5148-80.

31. Suen, N. T.; Hung, S. F.; Quan, Q.; Zhang, N.; Xu, Y. J.; Chen, H. M., Electrocatalysis for the oxygen evolution reaction: recent development and future perspectives. *Chem. Soc. Rev.* 2017, *46* (2), 337-365.

32. Liu, Y.; Tang, A.; Zhang, Q.; Yin, Y., Seed-mediated growth of anatase TiO2 nanocrystals with core–antenna structures for enhanced photocatalytic activity. *J. Am. Chem. Soc.* 2015, *137* (35), 11327-11339.

33. Wang, Z.; Yang, G.; Zhang, Z.; Jin, M.; Yin, Y., Selectivity on Etching: Creation of High-Energy Facets on Copper Nanocrystals for CO2 Electrochemical Reduction. *ACS Nano* 2016, *10* (4), 4559-64.

34. Zhang, S.; Ma, Y.; Zhang, H.; Zhou, X.; Chen, X.; Qu, Y., Additive-Free, Robust H2 Production from H2O and DMF by Dehydrogenation Catalyzed by Cu/Cu2O Formed In Situ. *Angew. Chem. Int. Ed.* 2017, *56* (28), 8245-8249.

35. Shi, R.; Cao, Y.; Bao, Y.; Zhao, Y.; Waterhouse, G. I. N.; Fang, Z.; Wu, L. Z.; Tung, C. H.; Yin, Y.; Zhang, T., Self-Assembled Au/CdSe Nanocrystal Clusters for Plasmon-Mediated Photocatalytic Hydrogen Evolution. *Adv. Mater.* 2017, *29* (27), 1700803.

36. Xu, W.; Lyu, F.; Bai, Y.; Gao, A.; Feng, J.; Cai, Z.; Yin, Y., Porous cobalt oxide nanoplates enriched with oxygen vacancies for oxygen evolution reaction. *Nano Energy* 2018, *43*, 110-116.

37. Ding, D.; Liu, K.; He, S.; Gao, C.; Yin, Y., Ligand-exchange assisted formation of Au/TiO2 Schottky contact for visible-light photocatalysis. *Nano Lett.* 2014, *14* (11), 6731-6.

38. Zhang, Q.; Lima, D. Q.; Lee, I.; Zaera, F.; Chi, M.; Yin, Y., A highly active titanium dioxide based visible-light photocatalyst with nonmetal doping and plasmonic metal decoration. *Angew. Chem. Int. Ed.* 2011, *50* (31), 7088-92.

39. Popczun, E. J.; Roske, C. W.; Read, C. G.; Crompton, J. C.; McEnaney, J. M.; Callejas, J. F.; Lewis, N. S.; Schaak, R. E. J. J. o. M. C. A., Highly branched cobalt phosphide nanostructures for hydrogen-evolution electrocatalysis. *J. Mater. Chem. A* 2015, *3* (10), 5420-5425.

40. Seo, B.; San Baek, D.; Sa, Y. J.; Joo, S. H., Shape effects of nickel phosphide nanocrystals on hydrogen evolution reaction. *Cryst. Eng. Comm.* 2016, *18* (32), 6083-6089.

41. Tan, C.; Chen, J.; Wu, X.-J.; Zhang, H., Epitaxial growth of hybrid nanostructures. *Nat. Rev. Mater.* 2018, *3* (2), 1-13.

42. Xia, Y.; Xiong, Y.; Lim, B.; Skrabalak, S. E., Cover Picture: Shape-Controlled Synthesis of Metal Nanocrystals: Simple Chemistry Meets Complex Physics? *Angew. Chem. Int. Ed.* 2009, *48* (1), 1-1.

43. Wu, X. J.; Chen, J.; Tan, C.; Zhu, Y.; Han, Y.; Zhang, H., Controlled growth of high-density CdS and CdSe nanorod arrays on selective facets of two-dimensional semiconductor nanoplates. *Nat. Chem.* 2016, *8* (5), 470-5.

44. Gao, C.; Goebl, J.; Yin, Y., Seeded growth route to noble metal nanostructures. *J. Mater. Chem. C* 2013, *1* (25), 3898-3909.

45. Chen, J.; Wu, X. J.; Gong, Y.; Zhu, Y.; Yang, Z.; Li, B.; Lu, Q.; Yu, Y.; Han, S.; Zhang, Z.; Zong, Y.; Han, Y.; Gu, L.; Zhang, H., Edge Epitaxy of Two-Dimensional MoSe(2) and MoS(2) Nanosheets on One-Dimensional Nanowires. *J. Am. Chem. Soc.* 2017, *139* (25), 8653-8660.

46. Guo, W.; Xia, W.; Cai, K.; Wu, Y.; Qiu, B.; Liang, Z.; Qu, C.; Zou, R., Kinetic-Controlled Formation of Bimetallic Metal–Organic Framework Hybrid Structures. *Small* 2017, *13* (41), 1702049.

47. Araki, T.; Serra, F.; Tanaka, H. J., Defect science and engineering of liquid crystals under geometrical frustration. *Soft Matter* 2013, *9* (34), 8107-8120.

48. Jia, Y.; Jiang, K.; Wang, H.; Yao, X., The role of defect sites in nanomaterials for electrocatalytic energy conversion. *Chem* 2019, *5* (6), 1371-1397.

49. Yan, X.; Jia, Y.; Yao, X., Defects on carbons for electrocatalytic oxygen reduction. *Chem. Soc. Rev.* 2018, *47* (20), 7628-7658.

50. Yan, D.; Li, Y.; Huo, J.; Chen, R.; Dai, L.; Wang, S., Defect Chemistry of Nonprecious-Metal Electrocatalysts for Oxygen Reactions. *Adv. Mater.* 2017, *29* (48), 1606459.

51. Jia, Y.; Chen, J.; Yao, X., Defect electrocatalytic mechanism: concept, topological structure and perspective. *Mater. Chem. Front.* 2018, *2* (7), 1250-1268.

52. Sun, Y.; Liu, Q.; Gao, S.; Cheng, H.; Lei, F.; Sun, Z.; Jiang, Y.; Su, H.; Wei, S.; Xie, Y., Pits confined in ultrathin cerium(IV) oxide for studying catalytic centers in carbon monoxide oxidation. *Nat. Commun.* 2013, *4* (1), 2899.

53. Xu, L.; Jiang, Q.; Xiao, Z.; Li, X.; Huo, J.; Wang, S.; Dai, L., Plasma-engraved Co3O4

nanosheets with oxygen vacancies and high surface area for the oxygen evolution reaction. *Angew. Chem. Int. Ed.* 2016, *128* (17), 5363-5367.

54. Kim, J.; Yin, X.; Tsao, K.-C.; Fang, S.; Yang, H., Ca2Mn2O5 as oxygen-deficient perovskite electrocatalyst for oxygen evolution reaction. *J. Am. Chem. Soc.* 2014, *136* (42), 14646-14649.

55. Jia, Y.; Zhang, L.; Du, A.; Gao, G.; Chen, J.; Yan, X.; Brown, C. L.; Yao, X., Defect graphene as a trifunctional catalyst for electrochemical reactions. *Adv. mater.* 2016, *28* (43), 9532-9538.

56. Liu, T.; Bai, L.; Tian, N.; Liu, J.; Zhang, Y.; Huang, H. J. I., Interfacial engineering in two-dimensional heterojunction photocatalysts. *Int. J. Hydrog. Energy* 2023.

57. Hu, L.; Zeng, X.; Wei, X.; Wang, H.; Wu, Y.; Gu, W.; Shi, L.; Zhu, C., Interface engineering for enhancing electrocatalytic oxygen evolution of NiFe LDH/NiTe heterostructures. *Appl. Catal. B* 2020, *273*, 119014.

58. Borah, B. J.; Yamada, Y.; Bharali, P., Unravelling the role of metallic Cu in Cu-CuFe2O4/C nanohybrid for enhanced oxygen reduction electrocatalysis. *ACS Appl. Energy Mater.* 2020, *3* (4), 3488-3496.

59. Niu, Y.; Xiao, M.; Zhu, J.; Zeng, T.; Li, J.; Zhang, W.; Su, D.; Yu, A.; Chen, Z., A" trimurti" heterostructured hybrid with an intimate CoO/CoxP interface as a robust bifunctional air electrode for rechargeable Zn–air batteries. *J. Mater. Chem. A* 2020, *8* (18), 9177-9184.

60. An, L.; Zhang, Z.; Feng, J.; Lv, F.; Li, Y.; Wang, R.; Lu, M.; Gupta, R. B.; Xi, P.; Zhang, S., Heterostructure-promoted oxygen electrocatalysis enables rechargeable zinc– air battery with neutral aqueous electrolyte. *J. Am. Chem. Soc.* 2018, *140* (50), 17624-

17631.

61. Chen, G. F.; Ma, T. Y.; Liu, Z. Q.; Li, N.; Su, Y. Z.; Davey, K.; Qiao, S. Z., Efficient and stable bifunctional electrocatalysts Ni/NixMy (M= P, S) for overall water splitting. *Adv. Funct. Mater.* 2016, *26* (19), 3314-3323.

62. Yan, Z.; Sun, H.; Chen, X.; Liu, H.; Zhao, Y.; Li, H.; Xie, W.; Cheng, F.; Chen, J., Anion insertion enhanced electrodeposition of robust metal hydroxide/oxide electrodes for oxygen evolution. *Nat. Commun.* 2018, *9* (1), 2373.

63. Jin, T.; Han, Q.; Jiao, L., Binder-Free Electrodes for Advanced Sodium-Ion Batteries. *Adv. Mater.* 2020, *32* (3), e1806304.

64. Wu, S.-W.; Liu, S.-Q.; Tan, X.-H.; Zhang, W.-Y.; Cadien, K.; Li, Z, Ni3S2-embedded NiFe LDH porous nanosheets with abundant heterointerfaces for high-current water electrolysis. *Chem. Eng. J.* 2022, *442*, 136105.

65. Liu, S.-Q.; Gao, M.-R.; Liu, S.; Luo, J.-L., Hierarchically assembling cobalt/nickel carbonate hydroxide on copper nitride nanowires for highly efficient water splitting. *Appl. Catal. B* 2021, *292*, 120148.

66. Quan, X.; Yang, S.; Ruan, X.; Zhao, H., Preparation of titania nanotubes and their environmental applications as electrode. *Environ. Sci. Technol.* 2005, *39* (10), 3770-3775.

67. Lee, C.; Min, K., Effects of heat treatment on the microstructure and properties of HVOF-sprayed Ni–Cr–W–Mo–B alloy coatings. *Surf. Coat. Technol.* 2000, *132* (1), 49-57.

68. Kong, D.; Wang, H.; Lu, Z.; Cui, Y., CoSe2 nanoparticles grown on carbon fiber paper: an efficient and stable electrocatalyst for hydrogen evolution reaction. *J. Am. Chem. Soc.* 2014, *136* (13), 4897-900.

69. Liu, S. Q.; Shahini, E.; Gao, M. R.; Gong, L.; Sui, P. F.; Tang, T.; Zeng, H.; Luo, J. L.,

Bi(2)O(3) Nanosheets Grown on Carbon Nanofiber with Inherent Hydrophobicity for High-Performance CO2 Electroreduction in a Wide Potential Window. *ACS Nano* 2021, *15* (11), 17757-17768.

70. Fan, X.-Z.; Pang, Q.-Q.; Yi, S.-S.; Du, X.; Zhang, S.; Liu, Z.-Y.; Yue, X.-Z., Intrinsic-structural-modulated carbon cloth as efficient electrocatalyst for water oxidation. *Appl. Catal. B* 2021, *292*, 120152.

71. Kunimoto, T.; Naya, S.-i.; Tada, H., Hydrogen Peroxide Production from Oxygen and Water by Two-electrode Electrolytic Cell Using a Gold Nanoparticle-loaded Fluorine-doped Tin Oxide Cathode. *Chem. Lett.* 2021, *50* (8), 1589-1591.

72. Liu, B.; Zhao, Y. F.; Peng, H. Q.; Zhang, Z. Y.; Sit, C. K.; Yuen, M. F.; Zhang, T. R.; Lee, C. S.; Zhang, W. J., Nickel-Cobalt Diselenide 3D Mesoporous Nanosheet Networks Supported on Ni Foam: An All-pH Highly Efficient Integrated Electrocatalyst for Hydrogen Evolution. *Adv. Mater.* 2017, *29* (19), 1606521.

73. Pi, Y.; Shao, Q.; Wang, P.; Lv, F.; Guo, S.; Guo, J.; Huang, X., Trimetallic Oxyhydroxide Coralloids for Efficient Oxygen Evolution Electrocatalysis. *Angew. Chem. Int. Ed.* 2017, *56* (16), 4502-4506.

74. Gopalakrishnan, A.; Durai, L.; Ma, J.; Kong, C. Y.; Badhulika, S., Vertically aligned few-layer crumpled MoS2 hybrid nanostructure on porous Ni foam toward promising binder-free methanol electro-oxidation application. *Energy Fuels* 2021, *35* (12), 10169-10180.

75. Chen, H.; Jiang, J.; Zhang, L.; Zhao, Y.; Guo, D.; Ruan, Y.; Xia, D., One-Pot Fabrication of Layered α-Phase Nickel–Cobalt Hydroxides as Advanced Electrode Materials for Pseudocapacitors. *ChemPlusChem* 2015, *80* (1), 181-187.

76. Li, H.; Han, X.; Zhao, W.; Azhar, A.; Jeong, S.; Jeong, D.; Na, J.; Wang, S.; Yu, J.; Yamauchi, Y., Electrochemical preparation of nano/micron structure transition metal-based catalysts for the oxygen evolution reaction. *Mater, Horiz,* 2022, *9* (7), 1788-1824.

77. Li, R.; Li, Y.; Yang, P.; Wang, D.; Xu, H.; Wang, B.; Meng, F.; Zhang, J.; An, M., Electrodeposition: synthesis of advanced transition metal-based catalyst for hydrogen production via electrolysis of water. *J. Energy Chem.* 2021, *57*, 547-566.

78. Wang, Y.; Zhang, G.; Xu, W.; Wan, P.; Lu, Z.; Li, Y.; Sun, X., A 3D nanoporous Ni–Mo electrocatalyst with negligible overpotential for alkaline hydrogen evolution. *ChemElectroChem* 2014, *1* (7), 1138-1144.

79. Pierson, H. O., *Handbook of chemical vapor deposition: principles, technology and applications*. William Andrew: 1999.

80. Xu, K.; Wang, F.; Wang, Z.; Zhan, X.; Wang, Q.; Cheng, Z.; Safdar, M.; He, J., Component-controllable WS2(1–x) Se2x nanotubes for efficient hydrogen evolution reaction. *ACS nano* 2014, *8* (8), 8468-8476.

81. Liu, X.; Wang, X.; Yuan, X.; Dong, W.; Huang, F., Rational composition and structural design of in situ grown nickel-based electrocatalysts for efficient water electrolysis. *J. Mater. Chem. A* 2016, *4* (1), 167-172.

82. Zou, X.; Liu, Y.; Li, G. D.; Wu, Y.; Liu, D. P.; Li, W.; Li, H. W.; Wang, D.; Zhang, Y.; Zou, X., Ultrafast Formation of Amorphous Bimetallic Hydroxide Films on 3D Conductive Sulfide Nanoarrays for Large-Current-Density Oxygen Evolution Electrocatalysis. *Adv. Mater.* 2017, *29* (22), 1700404.

83. Li, P.; Duan, X.; Kuang, Y.; Li, Y.; Zhang, G.; Liu, W.; Sun, X., Tuning electronic structure of NiFe layered double hydroxides with vanadium doping toward high efficient

electrocatalytic water oxidation. *Adv. Energy Mater.* 2018, *8* (15), 1703341.

84. Nie, Y.; Li, L.; Wei, Z., Recent advancements in Pt and Pt-free catalysts for oxygen reduction reaction. *Chem. Soc. Rev.* 2015, *44* (8), 2168-201.

85. Doyle, R. L.; Godwin, I. J.; Brandon, M. P.; Lyons, M. E., Redox and electrochemical water splitting catalytic properties of hydrated metal oxide modified electrodes. *Phys. Chem. Chem. Phys.* 2013, *15* (33), 13737-83.

86. Ma, T. Y.; Dai, S.; Jaroniec, M.; Qiao, S. Z., Metal–organic framework derived hybrid Co3O4-carbon porous nanowire arrays as reversible oxygen evolution electrodes. *J. Am. Chem. Soc.* 2014, *136* (39), 13925-13931.

87. Jin, Y.; Wang, H.; Li, J.; Yue, X.; Han, Y.; Shen, P. K.; Cui, Y., Porous MoO2 nanosheets as non-noble bifunctional electrocatalysts for overall water splitting. *Adv. Mater.* 2016, *28* (19), 3785-3790.

88. Zhao, Y.; Chang, C.; Teng, F.; Zhao, Y.; Chen, G.; Shi, R.; Waterhouse, G. I.; Huang, W.; Zhang, T., Defect-engineered ultrathin δ-MnO2 nanosheet arrays as bifunctional electrodes for efficient overall water splitting. *Adv. Energy Mater.* 2017, *7* (18), 1700005.

89. Kölbach, M.; Fiechter, S.; van de Krol, R.; Bogdanoff, P., Evaluation of electrodeposited α-Mn2O3 as a catalyst for the oxygen evolution reaction. *Catal. Today* 2017, *290*, 2-9.

90. Ye, Z.; Li, T.; Ma, G.; Dong, Y.; Zhou, X., Metal-Ion (Fe, V, Co, and Ni)-doped MnO2 ultrathin nanosheets supported on Carbon fiber paper for the oxygen evolution reaction. *Adv. Funct. Mater.* 2017, *27* (44), 1704083.

91. Zhang, T.; Cheng, F.; Du, J.; Hu, Y.; Chen, J., Efficiently enhancing oxygen reduction electrocatalytic activity of MnO2 using facile hydrogenation. *Adv. Energy Mater.* 2015, *5* (1), 1400654.

92. Zhou, M.; Weng, Q.; Zhang, X.; Wang, X.; Xue, Y.; Zeng, X.; Bando, Y.; Golberg, D., In situ electrochemical formation of core–shell nickel–iron disulfide and oxyhydroxide heterostructured catalysts for a stable oxygen evolution reaction and the associated mechanisms. *J. Mater. Chem. A* 2017, *5* (9), 4335-4342.

93. Xu, X.; Song, F.; Hu, X., A nickel iron diselenide-derived efficient oxygen-evolution catalyst. *Nat. Commun.* 2016, *7* (1), 12324.

94. Gao, Q.; Huang, C. Q.; Ju, Y. M.; Gao, M. R.; Liu, J. W.; An, D.; Cui, C. H.; Zheng, Y. R.; Li, W. X.; Yu, S. H., Phase-Selective Syntheses of Cobalt Telluride Nanofleeces for Efficient Oxygen Evolution Catalysts. *Angew. Chem. Int. Ed.* 2017, *56* (27), 7769-7773.

95. Ullah, N.; Ullah, R.; Khan, S.; Xu, Y., Boron nitride-based electrocatalysts for HER, OER, and ORR: A mini-review. *Front. Mater.* 2021, 1-10.

96. Parra-Puerto, A.; Ng, K. L.; Fahy, K.; Goode, A. E.; Ryan, M. P.; Kucernak, A., Supported transition metal phosphides: activity survey for HER, ORR, OER, and corrosion resistance in acid and alkaline electrolytes. *ACS Catal.* 2019, *9* (12), 11515-11529.

97. Stern, L.-A.; Feng, L.; Song, F.; Hu, X., Ni2P as a Janus catalyst for water splitting: the oxygen evolution activity of Ni2P nanoparticles. *Energy Environ. Sci.* 2015, *8* (8), 2347-2351.

98. Zhou, H.; Yu, F.; Sun, J.; He, R.; Chen, S.; Chu, C.-W.; Ren, Z., Highly active catalyst derived from a 3D foam of Fe (PO3) 2/Ni2P for extremely efficient water oxidation. *PNAS.* 2017, *114* (22), 5607-5611.

99. Shao, M.; Chang, Q.; Dodelet, J. P.; Chenitz, R., Recent Advances in Electrocatalysts for Oxygen Reduction Reaction. *Chem. Rev.* 2016, *116* (6), 3594-657.

100. Tang, J.; Su, C.; Shao, Z., Covalent Organic Framework (COF)-Based Hybrids for

Electrocatalysis: Recent Advances and Perspectives. *Small Methods* 2021, *5* (12), e2100945.

101.   Chen, M. X.; Tong, L.; Liang, H. W., Understanding the catalytic sites of metal–nitrogen–carbon oxygen reduction electrocatalysts. *Chem. Eur.* 2021, *27* (1), 145-157.

102.   Hu, S.; Ni, W.; Yang, D.; Ma, C.; Zhang, J.; Duan, J.; Gao, Y.; Zhang, S., Fe3O4 nanoparticles encapsulated in single-atom Fe–N–C towards efficient oxygen reduction reaction: Effect of the micro and macro pores. *Carbon* 2020, *162*, 245-255.

103.   Luo, E.; Chu, Y.; Liu, J.; Shi, Z.; Zhu, S.; Gong, L.; Ge, J.; Choi, C. H.; Liu, C.; Xing, W., Pyrolyzed M–Nx catalysts for oxygen reduction reaction: progress and prospects. *Energy Environ. Sci.* 2021, *14* (4), 2158-2185.

104.   Hsueh, H. Y.; Yao, C. T.; Ho, R. M., Well-ordered nanohybrids and nanoporous materials from gyroid block copolymer templates. *Chem. Soc. Rev.* 2015, *44* (7), 1974-2018.

105.   Liang, J.; Zhou, R. F.; Chen, X. M.; Tang, Y. H.; Qiao, S. Z., Fe–N decorated hybrids of CNTs grown on hierarchically porous carbon for high-performance oxygen reduction. *Adv. Mater*. 2014, *26* (35), 6074-6079.

106.   Zhang, J.; Huang, Q.-a.; Wang, J.; Wang, J.; Zhang, J.; Zhao, Y., Supported dual-atom catalysts: preparation, characterization, and potential applications. *Chinese J. Catal.* 2020, *41* (5), 783-798.

107.   Wang, J.; Liu, W.; Luo, G.; Li, Z.; Zhao, C.; Zhang, H.; Zhu, M.; Xu, Q.; Wang, X.; Zhao, C., Synergistic effect of well-defined dual sites boosting the oxygen reduction reaction. *Energy Environ. Sci.* 2018, *11* (12), 3375-3379.

108.   Hong, W. T.; Risch, M.; Stoerzinger, K. A.; Grimaud, A.; Suntivich, J.; Shao-

Horn, Y., Toward the rational design of non-precious transition metal oxides for oxygen electrocatalysis. *Energy Environ. Sci.* 2015, *8* (5), 1404-1427.

109.   Yang, G.; Zhu, J.; Yuan, P.; Hu, Y.; Qu, G.; Lu, B.-A.; Xue, X.; Yin, H.; Cheng, W.; Cheng, J., Regulating Fe-spin state by atomically dispersed Mn-N in Fe-NC catalysts with high oxygen reduction activity. *Nat. Commun.* 2021, *12* (1), 1734.

110.   J. Song, C. Wei, Z.-F. Huang, C. Liu, L. Zeng, X. Wang, Z. J. Xu, A review on fundamentals for designing oxygen evolution electrocatalysts, *Chem. Soc. Rev.* 49 (7) (2020) 2196.

111.   P. Lianos, Review of recent trends in photoelectrocatalytic conversion of solar energy to electricity and hydrogen, *Appl. Catal. B* 210 (2017) 235-254.

112.   H. Xu, B. Fei, G. Cai, Y. Ha, J. Liu, H. Jia, J. Zhang, M. Liu, R. Wu, Boronization-induced ultrathin 2D nanosheets with abundant crystalline–amorphous phase boundary supported on nickel foam toward efficient water splitting, *Adv. Energy Mater.* 10 (3) (2020), 1902714.

113.   J. Duan, S. Chen, C. Zhao, Ultrathin metal-organic framework array for efficient electrocatalytic water splitting, *Nat. Commun.* 8 (1) (2017) 1-7.

114.   Q. Chen, Z. Usman, T. Cao, S. Rafai, Z. Wang, Y. Zhu, C. Cao, J. Zhang, High-valence Ni and Fe sites on sulfated NiFe-LDH nanosheets to enhance OO coupling for water oxidation, *Chem. Eng. J.* 426 (2021) 130873.

115.   V. Nicolosi, M. Chhowalla, M.G. Kanatzidis, M.S. Strano, J.N. Coleman, Liquid exfoliation of layered materials, *Science*, 340 (6139) (2013) 1226419.

116.   H. Sun, W. Zhang, J.-G. Li, Z. Li, X. Ao, K.-H. Xue, K.K. Ostrikov, J. Tang, C. Wang, Rh-engineered ultrathin NiFe-LDH nanosheets enable highly-efficient overall water

splitting and urea electrolysis, *Appl. Catal. B* 284 (2021) 119740.

117.   F. Song, X. Hu, Exfoliation of layered double hydroxides for enhanced oxygen evolution catalysis, *Nat. Commun.* 5 (1) (2014) 1-9.

118.   B. Wang, X. Han, C. Guo, J. Jing, C. Yang, Y. Li, A. Han, D. Wang, J. Liu, Structure inheritance strategy from MOF to edge-enriched NiFe-LDH array for enhanced oxygen evolution reaction, *Appl. Catal. B* 298 (2021) 120580.

119.   X. Lu, C. Zhao, Electrodeposition of hierarchically structured three-dimensional nickel-iron electrodes for efficient oxygen evolution at high current densities, *Nat. Commun.* 6 (1) (2015) 1-7.

120.   P.F. Liu, X. Li, S. Yang, M.Y. Zu, P. Liu, B. Zhang, L.R. Zheng, H. Zhao, H.G. Yang, Ni_2P (O)/Fe_2P (O) interface can boost oxygen evolution electrocatalysis, *ACS Energy Lett.* 2 (10) (2017) 2257-2263.

121.   M. Li, X. Pan, M. Jiang, Y. Zhang, Y. Tang, G. Fu, Interface engineering of oxygen-vacancy-rich CoP/CeO2 heterostructure boosts oxygen evolution reaction, *Chem. Eng. J.* 395 (2020): 125160.

122.   J.W. Huang, K. Li, L. Wang, H. She, Q.Z. Wang, In situ conversion builds MIL-101@ NiFe-LDH heterojunction structures to enhance the oxygen evolution reaction, *Chin. Chem. Lett.* (2021).

123.   S. Niu, W.J. Jiang, T. Tang, L.P. Yuan, H. Luo, J.S. Hu, Autogenous growth of hierarchical NiFe $(OH)_x$/FeS nanosheet-on-microsheet arrays for synergistically enhanced high-output water oxidation, *Adv. Funct. Mater.* 29 (36) (2019) 1902180.

124.   C. Liang, P. Zou, A. Nairan, Y. Zhang, J. Liu, K. Liu, S. Hu, F. Kang, H.J. Fan, C. Yang, Exceptional performance of hierarchical Ni–Fe oxyhydroxide@ NiFe alloy

nanowire array electrocatalysts for large current density water splitting, *Energy Environ. Sci.* 13 (1) (2020) 86-95.

125.   L. Dai, Z.N. Chen, L. Li, P. Yin, Z. Liu, H. Zhang, Ultrathin Ni (0)-Embedded Ni $(OH)_2$ Heterostructured Nanosheets with Enhanced Electrochemical Overall Water Splitting, *Adv. Mater.* 32 (8) (2020) 1906915.

126.   L.-L. Feng, G. Yu, Y. Wu, G.-D. Li, H. Li, Y. Sun, T. Asefa, W. Chen, X. Zou, High-index faceted Ni_3S_2 nanosheet arrays as highly active and ultrastable electrocatalysts for water splitting, *J. Am. Chem. Soc.* 137 (14) (2015) 14023-14026.

127.   L. Chen, Y. Wang, X. Zhao, Y. Wang, Q. Li, Q. Wang, Y. Tang, Y. Lei, Trimetallic oxyhydroxides as active sites for large-current-density alkaline oxygen evolution and overall water splitting, *J. Mater. Sci. Technol.* 110 (2022): 128-135.

128.   M. Carmo, D.L. Fritz, J. Mergel, D. Stolten, A comprehensive review on PEM water electrolysis, *Int. J. Hydrog. Energy.* 38 (12) (2013) 4901-4934.

129.   D. Wei, K. Osseo-Asare, Aqueous synthesis of finely divided pyrite particles, *Colloids Surf. A: Physicochem. Eng. Asp.* 121 (1) (1997) 27-36.

130.   F. Yu, H. Zhou, Y. Huang, J. Sun, F. Qin, J. Bao, W.A. Goddard, S. Chen, Z. Ren, High-performance bifunctional porous non-noble metal phosphide catalyst for overall water splitting, *Nat. Commun.* 9 (1) (2018) 1-9.

131.   X. Peng, L. Zhang, Z. Chen, L. Zhong, D. Zhao, X. Chi, X. Zhao, L. Li, X. Lu, K. Leng, Hierarchically porous carbon plates derived from wood as bifunctional ORR/OER electrodes, *Adv. Mater.* 31 (16) (2019) 1900341.

132.   H. Zhang, X. Li, A. Hähnel, V. Naumann, C. Lin, S. Azimi, S.L. Schweizer, A.W. Maijenburg, R.B. Wehrspohn, Bifunctional heterostructure assembly of NiFe LDH

nanosheets on NiCoP nanowires for highly efficient and stable overall water splitting, *Adv. Funct. Mater.* 28 (14) (2018) 1706847.

133.   H. Liang, A.N. Gandi, C. Xia, M.N. Hedhili, D.H. Anjum, U. Schwingenschlögl, H.N. Alshareef, Amorphous NiFe-OH/NiFeP electrocatalyst fabricated at low temperature for water oxidation applications, *ACS Energy Lett.* 2 (5) (2017) 1035-1042.

134.   S. Cao, H. Huang, K. Shi, L. Wei, N. You, X. Fan, Z. Yang, W. Zhang, Engineering superhydrophilic/superaerophobic hierarchical structures of Co-CH@ NiFe-LDH/NF to boost the oxygen evolution reaction, *Chem. Eng. J.* 422 (2021) 130123.

135.   X. Meng, J. Han, L. Lu, G. Qiu, Z.L. Wang, C. Sun, Fe^{2+}-doped layered double (Ni, Fe) hydroxides as efficient electrocatalysts for water splitting and self-powered electrochemical systems, *Small* 15 (41) (2019) 1902551.

136.   J.-X. Feng, J.-Q. Wu, Y.-X. Tong, G.-R. Li, Efficient hydrogen evolution on Cu nanodots-decorated Ni_3S_2 nanotubes by optimizing atomic hydrogen adsorption and desorption, *J. Am. Chem. Soc.* 140 (2) (2018) 610-617.

137.   X. Meng, J. Han, L. Lu, G. Qiu, Z. Wang, C. Sun, Fe^{2+}-doped layered double (Ni, Fe) hydroxides as efficient electrocatalysts for water splitting and self-powered electrochemical systems." *Small*, 15 (41) (2019) 1902551.

138.   C. Sun, T. Wang, C. Sun, F. Li, Layered double (Ni, Fe) hydroxide grown on nickel foam and modified by nickel carbonyl powder and carbon black as an efficient electrode for water splitting, *Int. J. Hydrog. Energy*, (2021).

139.   X. Lu, K. Ye, S. Zhang, J. Zhang, J. Yang, Y. Huang, H. Ji. "Amorphous type FeOOH modified defective BiVO4 photoanodes for photoelectrochemical water oxidation." *Chem. Eng. J.* 428 (2022) 131027.

140. W.D. Chemelewski, H.-C. Lee, J.-F. Lin, A.J. Bard, C.B. Mullins, Amorphous FeOOH oxygen evolution reaction catalyst for photoelectrochemical water splitting, *J. Am. Chem. Soc.* 136 (7) (2014) 2843-2850.

141. C. Liu, Y. Han, L. Yao, L. Liang, J. He, Q. Hao, J. Zhang, Y. Li, H. Liu, Engineering Bimetallic NiFe-Based Hydroxides/Selenides Heterostructure Nanosheet Arrays for Highly-Efficient Oxygen Evolution Reaction, *Small* 17 (7) (2021) 2007334.

142. Q. Xu, H. Jiang, X. Duan, Z. Jiang, Y. Hu, S.W. Boettcher, W. Zhang, S. Guo, C. Li, Fluorination-enabled Reconstruction of NiFe Electrocatalysts for Efficient Water Oxidation, *Nano Lett.* 21(1) (2020) 492-499.

143. S. Huang, Y. Meng, Y. Cao, F. Yao, Z. He, X. Wang, H. Pan, M. Wu, Amorphous $NiWO_4$ nanoparticles boosting the alkaline hydrogen evolution performance of Ni_3S_2 electrocatalysts, *Appl. Catal. B* 274 (2020) 119120.

144. N. McIntyre, M. Cook, X-ray photoelectron studies on some oxides and hydroxides of cobalt, nickel, and copper, *Anal. Chem.* 47 (13) (1975) 2208-2213.

145. X. Feng, Q. Jiao, W. Chen, Y. Dang, Z. Dai, S.L. Suib, J. Zhang, Y. Zhao, H. Li, C. Feng, Cactus-like $NiCo_2S_4@$ NiFe LDH hollow spheres as an effective oxygen bifunctional electrocatalyst in alkaline solution, *Appl. Catal. B* 286 (2021) 119869.

146. J. Huang, J. Han, R. Wang, Y. Zhang, X. Wang, X. Zhang, Z. Zhang, Y. Zhang, B. Song, S. Jin, Improving Electrocatalysts for Oxygen Evolution Using $Ni_x Fe_{3-x} O_4$/Ni Hybrid Nanostructures Formed by Solvothermal Synthesis, *ACS Energy Lett.* 3(7) (2018) 1698-1707.

147. Z. Cai, D. Zhou, M. Wang, S.M. Bak, Y. Wu, Z. Wu, Y. Tian, X. Xiong, Y. Li, W. Liu, Introducing Fe^{2+} into nickel-iron layered double hydroxide: local structure modulated

water oxidation activity, *Angew. Chem., Int. Edit.* 130 (2018) 9536-9540.

148.	J. Zhou, L. Yu, Q. Zhu, C. Huang, Y. Yu, Defective and ultrathin NiFe LDH nanosheets decorated on V-doped Ni_3S_2 nanorod arrays: a 3D core-shell electrocatalyst for efficient water oxidation, *J. Mater. Chem.* 7 (2019) 18118-18125.

149.	C. Huang, L. Yu, W. Zhang, Q. Xiao, J. Zhou, Y. Zhang, P. An, J. Zhang, Y. Yu, "N-doped Ni-Mo based sulfides for high-efficiency and stable hydrogen evolution reaction." *Appl. Catal. B* 276 (2020): 119137.

150.	O. Qi, S. Cheng, C Yang, Z. Lei, Vertically grown pn heterojunction FeCoNi LDH/CuO arrays with modulated interfacial charges to facilitate electrocatalytic oxygen evolution reaction, *J. Mater. Chem. A* (2022).

151.	Y. Duan, Z.Y. Yu, S.J. Hu, X.S. Zheng, C.T. Zhang, H.H. Ding, B.C. Hu, Q.Q. Fu, Z.L. Yu, X. Zheng, Scaled-up synthesis of amorphous NiFeMo oxides and their rapid surface reconstruction for superior oxygen evolution catalysis, *Angew. Chem., Int. Edit.* 131 (2019) 15919-15924.

152.	Y. Tang, Q. Liu, L. Dong, H.B. Wu, X.-Y. Yu, Activating the hydrogen evolution and overall water splitting performance of NiFe LDH by cation doping and plasma reduction, *Appl. Catal. B* 266 (2020) 118627.

153.	C. Dong, T. Kou, H. Gao, Z. Peng, Z. Zhang, Eutectic-derived mesoporous Ni-Fe-O nanowire network catalyzing oxygen evolution and overall water splitting, *Adv. Energy Mater.* 8 (5) (2018) 1701347.

154.	N. Gultom, H. Abdullah, C. Hsu, D. -HKuo, Activating nickel iron layer double hydroxide for alkaline hydrogen evolution reaction and overall water splitting by electrodepositing nickel hydroxide, *Chem. Eng. J.* 419 (2021) 129608.

230

155.		Peng, Y., Y. Zhang, A. Guo, M. Mao, Y. Wang, Y. Long, G. Fan, Universal low-temperature oxidative thermal redispersion strategy for green and sustainable fabrication of oxygen-rich carbons anchored metal nanoparticles for hydrogen evolution reactions, *Chem. Eng. J.* (2021)133648.

156.		G. Zhang, Y.-S. Feng, W.-T. Lu, D. He, C.-Y. Wang, Y.-K. Li, X.-Y. Wang, F.-F. Cao, Enhanced catalysis of electrochemical overall water splitting in alkaline media by Fe doping in Ni_3S_2 nanosheet arrays, *ACS Catal.* 8 (6) (2018) 5431-5441.

157.		Q. Xu, M. Chu, M. Liu, J. Zhang, H. Jiang, C. Li, Fluorine-triggered surface reconstruction of Ni3S2 electrocatalysts towards enhanced water oxidation, *Chem. Eng. J.* 411 (2021) 128488.

158.		S. Liu, X.F. Lu, J. Xiao, X. Wang, X.W. Lou, Bi_2O_3 nanosheets grown on multi-channel carbon matrix to catalyze efficient CO_2 electroreduction to HCOOH, *Angew. Chem., Int. Edit.* 58 (2019) 13828-13833.

159.		Y. Guo, T. Wang, Q. Yang, X. Li, H. Li, Y. Wang, T. Jiao, Z. Huang, B. Dong, W. Zhang, Highly Efficient Electrochemical Reduction of Nitrogen to Ammonia on Surface Termination Modified Ti_3C_2T x MXene Nanosheets, *ACS nano*. 14 (7) (2020) 9089-9097.

160.		S.-Q Liu, M.-G Gao, R.-F Feng, L. Gong, H. Zeng, J.-L Luo. "Electronic delocalization of bismuth oxide induced by sulfur doping for efficient CO2 electroreduction to formate." *ACS Catal.* 11(12) (2021): 7604-7612.

161.		K. Dastafkan, Q. Meyer, X. Chen, C. Zhao, Efficient oxygen evolution and gas bubble release achieved by a low gas bubble adhesive iron-nickel vanadate electrocatalyst, *Small* 16 (32) (2020) 2002412.

162.		X. Shan, J. Liu, H. Mu, Y. Xiao, B. Mei, W. Liu, G. Lin, Z. Jiang, L. Wen, L. Jiang,

An engineered superhydrophilic/superaerophobic electrocatalyst composed of the supported $CoMoS_x$ chalcogel for overall water splitting, *Angew. Chem., Int. Edit.* 59 (4) (2020) 1659-1665.

163.   B.S. Yeo, A.T. Bell, In situ Raman study of nickel oxide and gold-supported nickel oxide catalysts for the electrochemical evolution of oxygen, *J. Phys. Chem. C.* 116 (15) (2012) 8394-8400.

164.   D. Friebel, M.W. Louie, M. Bajdich, K.E. Sanwald, Y. Cai, A.M. Wise, M.-J. Cheng, D. Sokaras, T.-C. Weng, R. Alonso-Mori, Identification of highly active Fe sites in (Ni, Fe) OOH for electrocatalytic water splitting, *J. Am. Chem. Soc.* 137 (3) (2015) 1305-1313.

165.   L. Trotochaud, S.L. Young, J.K. Ranney, S.W. Boettcher, Nickel–iron oxyhydroxide oxygen-evolution electrocatalysts: the role of intentional and incidental iron incorporation, *J. Am. Chem. Soc.* 136 (18) (2014) 6744-6753.

166.   J. H, C. Zhang, L. Jiang, H. Lin, Y. An, D. Zhou, M. Leung, and S. Yang. "Nanohybridization of MoS2 with layered double hydroxides efficiently synergizes the hydrogen evolution in alkaline media." *Joule* (2) (2017) 383-393.

167.   C. Liang, P. Zou, A. Nairan, Y. Zhang, J. Liu, K. Liu, S. Hu, F. Kang, H.J. Fan, C. Yang, Exceptional performance of hierarchical Ni–Fe oxyhydroxide@ NiFe alloy nanowire array electrocatalysts for large current density water splitting, *Energy Environ. Sci.* 13 (2020) 86-95.

168.   L. Yu, L. Wu, B. McElhenny, S. Song, D. Luo, F. Zhang, Y. Yu, S. Chen, Z. Ren, Ultrafast room-temperature synthesis of porous S-doped Ni/Fe (oxy) hydroxide electrodes for oxygen evolution catalysis in seawater splitting, *Energy Environ. Sci.* 13 (2020) 3439-

3446.

169.　　S. Niu, W.J. Jiang, T. Tang, L.P. Yuan, H. Luo, J.S. Hu, Autogenous growth of hierarchical NiFe(OH)$_x$/FeS nanosheet-on-microsheet arrays for synergistically enhanced high-output water oxidation, *Adv. Funct. Mater.* 29 (2019) 1902180.

170.　　J. Chen, H. Li, Z. Yu, C. Liu, Z. Yuan, C. Wang, S. Zhao, G. Henkelman, S. Li, L. Wei, Octahedral Coordinated Trivalent Cobalt Enriched Multimetal Oxygen-Evolution Catalysts, *Adv. Energy Mater.* 10 (2020) 2002593.

171.　　S. Niu, W.-J. Jiang, Z. Wei, T. Tang, J. Ma, J.-S. Hu, L.-J. Wan, Se-doping activates FeOOH for cost-effective and efficient electrochemical water oxidation, *J. Am. Chem. Soc.* 141 (2019) 7005-7013.

172.　　Q. Zhang, N.M. Bedford, J. Pan, X. Lu, R. Amal, A fully reversible water electrolyzer cell made up from FeCoNi (oxy) hydroxide atomic layers, *Adv. Energy Mater.* 9 (2019) 1901312.

173.　　Y. Wang, S. Tao, H. Lin, G. Wang, K. Zhao, R. Cai, K. Tao, C. Zhang, M. Sun, J. Hu, Atomically targeting NiFe LDH to create multivacancies for OER catalysis with a small organic anchor, *Nano Energy* 81 (2021) 105606.

174.　　J. Chen, H. Li, S. Chen, J. Fei, C. Liu, Z. Yu, K. Shin, Z. Liu, L. Song, G. Henkelman, Co–Fe–Cr (oxy) Hydroxides as Efficient Oxygen Evolution Reaction Catalysts, *Adv. Energy Mater.* 11 (2021) 2003412.

175.　　Y. Sun, R. Li, X. Chen, J. Wu, Y. Xie, X. Wang, K. Ma, L. Wang, Z. Zhang, Q. Liao, A-Site Management Prompts the Dynamic Reconstructed Active Phase of Perovskite Oxide OER Catalysts, *Adv. Energy Mater.* 11 (2021) 2003755.

176.　　H. Yan, Y. Xie, A. Wu, Z. Cai, L. Wang, C. Tian, X. Zhang, H. Fu, Anion-Modulated

HER and OER Activities of 3D Ni–V-Based Interstitial Compound Heterojunctions for High-Efficiency and Stable Overall Water Splitting, *Adv. Mater*. 31 (2019) 1901174.

177.   X. Li, Z. Kou, S. Xi, W. Zang, T. Yang, L. Zhang, J. Wang, Porous $NiCo_2S_4$/FeOOH nanowire arrays with rich sulfide/hydroxide interfaces enable high OER activity, *Nano Energy* 78 (2020) 105230.

178.   L. Bai, C.-S. Hsu, D.T. Alexander, H.M. Chen, X. Hu, A cobalt–iron double-atom catalyst for the oxygen evolution reaction, *J. Am. Chem. Soc.* 141 (2019) 14190-14199.

179.   R. Li, B. Hu, T. Yu, H. Chen, Y. Wang, S. Song, Insights into Correlation among Surface-Structure-Activity of Cobalt-Derived Pre-Catalyst for Oxygen Evolution Reaction, *Adv. Sci*. 7 (2020) 1902830.

180.   H. Zhang, Q. Jiang, J.H. Hadden, F. Xie, D.J. Riley, Pd Ion-Exchange and Ammonia Etching of a Prussian Blue Analogue to Produce a High-Performance Water-Splitting Catalyst, *Adv. Funct. Mater*. 31 (2021) 2008989.

181.   W. Ni, A. Krammer, C.S. Hsu, H.M. Chen, A. Schüler, X. Hu, Ni_3N as an active hydrogen oxidation reaction catalyst in alkaline medium, *Angew. Chem., Int. Edit*. 58 (2019) 7445-7449.

182.   Y. Li, X. Tan, R.K. Hocking, X. Bo, H. Ren, B. Johannessen, S.C. Smith, C. Zhao, Implanting Ni-O-VOx sites into Cu-doped Ni for low-overpotential alkaline hydrogen evolution, *Nat. Commun*. 11 (2020) 1-9.

183.   C. Liu, T. Gong, J. Zhang, X. Zheng, J. Mao, H. Liu, Y. Li, Q. Hao, Engineering Ni_2P-$NiSe_2$ heterostructure interface for highly efficient alkaline hydrogen evolution, *Appl. Catal. B*. 262 (2020) 118245.

184.   D. Zhao, K. Sun, W.C. Cheong, L. Zheng, C. Zhang, S. Liu, X. Cao, K. Wu, Y. Pan,

Z. Zhuang, Synergistically Interactive Pyridinic-N–MoP Sites: Identified Active Centers for Enhanced Hydrogen Evolution in Alkaline Solution, *Angew. Chem., Int. Edit.* 132 (2020) 9067-9075.

185.   Q. He, D. Tian, H. Jiang, D. Cao, S. Wei, D. Liu, P. Song, Y. Lin, L. Song, Achieving efficient alkaline hydrogen evolution reaction over a Ni_5P_4 catalyst incorporating single-atomic Ru sites, *Adv. Mater.* 32 (2020) 1906972.

186.   W. Chen, J. Gu, Y. Du, F. Song, F. Bu, J. Li, Y. Yuan, R. Luo, Q. Liu, D. Zhang, Achieving Rich and Active Alkaline Hydrogen Evolution Heterostructures via Interface Engineering on 2D 1T-MoS_2 Quantum Sheets, *Adv. Funct. Mater*. 30 (2020) 2000551.

187.   Y. Yang, K. Zhang, H. Lin, X. Li, H.C. Chan, L. Yang, Q. Gao, MoS_2–Ni_3S_2 heteronanorods as efficient and stable bifunctional electrocatalysts for overall water splitting, *Acs Catal*. 7 (2017) 2357-2366.

188.   X. Zheng, Y. Zhang, H. Liu, D. Fu, J. Chen, J. Wang, C. Zhong, Y. Deng, X. Han, W. Hu, In situ fabrication of heterostructure on nickel foam with tuned composition for enhancing water-splitting performance, *Small* 14 (2018) 1803666.

189.   H. Sun, Y. Lian, C. Yang, L. Xiong, P. Qi, Q. Mu, X. Zhao, J. Guo, Z. Deng, Y. Peng, A hierarchical nickel–carbon structure templated by metal–organic frameworks for efficient overall water splitting, *Energy Environ. Sci*. 11 (2018) 2363-2371.

190.   Z. Qiu, C.-W. Tai, G.A. Niklasson, T. Edvinsson, Direct observation of active catalyst surface phases and the effect of dynamic self-optimization in NiFe-layered double hydroxides for alkaline water splitting, *Energy Environ. Sci*. 12 (2019) 572-581.

191.   Y. Xiong, L. Xu, C. Jin, Q. Sun, Interface-engineered atomically thin Ni_3S_2/MnO_2 heterogeneous nanoarrays for efficient overall water splitting in alkaline media, *Appl. Catal.*

B 254 (2019) 329-338.

192.   H. Zhou, F. Yu, Q. Zhu, J. Sun, F. Qin, L. Yu, J. Bao, Y. Yu, S. Chen, Z. Ren, Water splitting by electrolysis at high current densities under 1.6 volts, *Energy Environ. Sci.* 11 (2018) 2858-2864.

193.   H. Li, S. Chen, Y. Zhang, Q. Zhang, X. Jia, Q. Zhang, L. Gu, X. Sun, L. Song, X. Wang, Systematic design of superaerophobic nanotube-array electrode comprised of transition-metal sulfides for overall water splitting, *Nat. Commun*. 9 (2018) 1-12.

194.   Z. Qiu, Y. Ma, T. Edvinsson, In operando Raman investigation of Fe doping influence on catalytic NiO intermediates for enhanced overall water splitting, *Nano Energy* 66 (2019) 104118.

195.   Y.K. Li, G. Zhang, W.T. Lu, F.F. Cao, Amorphous Ni–Fe–Mo suboxides coupled with Ni network as porous nanoplate array on nickel foam: a highly efficient and durable bifunctional electrode for overall water splitting, *Adv. Sci*. 7 (2020) 1902034

196.   A. Hayat, M. Sohail, H. Ali, T.A. Taha, H.I.A. Qazi, N. Ur Rahman, Z. Ajmal, A. Kalam, A.G. Al-Sehemi, S. Wageh, M.A. Amin, A. Palamanit, W.I. Nawawi, E.F. Newair, Y. Orooji, Recent Advances and Future Perspectives of Metal-Based Electrocatalysts for Overall Electrochemical Water Splitting, *Chem. Rec*. 23 (2023) e202200149.

197.   S.Y. Tee, K.Y. Win, W.S. Teo, L.D. Koh, S. Liu, C.P. Teng, M.Y. Han, Recent Progress in Energy-Driven Water Splitting, *Adv. Sci*. 4 (2017) 1600337.

198.   S.-Q. Liu, M.-R. Gao, S. Liu, J.-L. Luo, Hierarchically assembling cobalt/nickel carbonate hydroxide on copper nitride nanowires for highly efficient water splitting, *Appl. Catal. B* 292 (2021) 120148.

199.   Z. Wang, C. Li, K. Domen, Recent developments in heterogeneous photocatalysts

for solar-driven overall water splitting, *Chem. Soc. Rev*. 48 (2019) 2109-2125.

200.   C. Xing, Y. Xue, B. Huang, H. Yu, L. Hui, Y. Fang, Y. Liu, Y. Zhao, Z. Li, Y. Li, Fluorographdiyne: A Metal-Free Catalyst for Applications in Water Reduction and Oxidation, *Angew. Chem., Int. Ed*. 58 (2019) 13897-13903.

201.   Y. Zhang, X. Zheng, X. Guo, J. Zhang, A. Yuan, Y. Du, F. Gao, Design of modified MOFs electrocatalysts for water splitting: High current density operation and long-term stability, *Appl. Catal. B* 336 (2023) 122891.

202.   R. Frydendal, E.A. Paoli, B.P. Knudsen, B. Wickman, P. Malacrida, I.E.L. Stephens, I. Chorkendorff, Benchmarking the Stability of Oxygen Evolution Reaction Catalysts: The Importance of Monitoring Mass Losses, *Chem. Electro. Chem*. 1 (2014) 2075-2081.

203.   T. Reier, H.N. Nong, D. Teschner, R. Schlögl, P. Strasser, Electrocatalytic Oxygen Evolution Reaction in Acidic Environments - Reaction Mechanisms and Catalysts, *Adv. Energy Mater*. 7 (2017) 1601275.

204.   T. ul Haq, Y. Haik, A roadmap towards sustainable anode design for alkaline water electrolysis, *Appl. Catal. B* 334 (2023) 122853.

205.   R. Li, K. Xiang, Z. Liu, Z. Peng, Y. Zou, S. Wang, Recent Advances in Upgrading of Low-Cost Oxidants to Value-Added Products by Electrocatalytic Reduction Reaction, *Adv. Funct. Mater*. 32 (2022) 2208212.

206.   H.Y. Wang, M.L. Sun, J.T. Ren, Z.Y. Yuan, Circumventing Challenges: Design of Anodic Electrocatalysts for Hybrid Water Electrolysis Systems, *Adv. Energy Mater*. 13 (2022) 2203568.

207.   N. Zhang, Y. Zou, L. Tao, W. Chen, L. Zhou, Z. Liu, B. Zhou, G. Huang, H. Lin, S. Wang, Electrochemical Oxidation of 5-Hydroxymethylfurfural on Nickel Nitride/Carbon

Nanosheets: Reaction Pathway Determined by In Situ Sum Frequency Generation Vibrational Spectroscopy, *Angew. Chem., Int. Ed*. 58 (2019) 15895-15903.

208.   B. You, X. Liu, N. Jiang, Y. Sun, A General Strategy for Decoupled Hydrogen Production from Water Splitting by Integrating Oxidative Biomass Valorization, *J. Am. Chem. Soc.* 138 (2016) 13639-13646.

209.   Y. Lu, C.L. Dong, Y.C. Huang, Y. Zou, Z. Liu, Y. Liu, Y. Li, N. He, J. Shi, S. Wang, Identifying the Geometric Site Dependence of Spinel Oxides for the Electrooxidation of 5-Hydroxymethylfurfural, *Angew. Chem., Int. Ed*. 59 (2020) 19215-19221.

210.   S.H. Swan, Environmental phthalate exposure in relation to reproductive outcomes and other health endpoints in humans, *Environ. Res*. 108 (2008) 177-184.

211.   Y. Xie, L. Sun, X. Pan, Z. Zhou, G. Zhao, Selective two-electron electrocatalytic conversion of 5-Hydroxymethylfurfural boosting hydrogen production under neutral condition over Co(OH)$_2$-CeO$_2$ catalyst, *Appl. Catal. B* 338 (2023) 123068.

212.   T. Wang, X. Cao, L. Jiao, Progress in Hydrogen Production Coupled with Electrochemical Oxidation of Small Molecules, *Angew. Chem., Int. Ed*. 61 (2022) e202213328.

213.   B. You, N. Jiang, X. Liu, Y. Sun, Simultaneous H$_2$ Generation and Biomass Upgrading in Water by an Efficient Noble-Metal-Free Bifunctional Electrocatalyst, *Angew. Chem., Int. Ed.* 55 (2016) 9913-9917.

214.   Y. Wang, M. Zhang, Y. Liu, Z. Zheng, B. Liu, M. Chen, G. Guan, K. Yan, Recent Advances on Transition-Metal-Based Layered Double Hydroxides Nanosheets for Electrocatalytic Energy Conversion, *Adv. Sci*. 10 (2023) e2207519.

215.   X. Luo, P. Ji, P. Wang, R. Cheng, D. Chen, C. Lin, J. Zhang, J. He, Z. Shi, N. Li, S.

Xiao, S. Mu, Interface Engineering of Hierarchical Branched Mo-Doped Ni_3S_2/Ni_xP_y Hollow Heterostructure Nanorods for Efficient Overall Water Splitting, *Adv. Energy Mater.*, 10 (2020) 1903891.

216.   J. Shan, Y. Zheng, B. Shi, K. Davey, S.-Z. Qiao, Regulating Electrocatalysts via Surface and Interface Engineering for Acidic Water Electrooxidation, *ACS Energy Lett.* 4 (2019) 2719-2730.

217.   Y.J. Sa, C.W. Lee, S.Y. Lee, J. Na, U. Lee, Y.J. Hwang, Catalyst-electrolyte interface chemistry for electrochemical CO_2 reduction, *Chem. Soc. Rev.* 49 (2020) 6632-6665.

218.   G. Yang, Y. Jiao, H. Yan, Y. Xie, A. Wu, X. Dong, D. Guo, C. Tian, H. Fu, Interfacial Engineering of MoO_2 -FeP Heterojunction for Highly Efficient Hydrogen Evolution Coupled with Biomass Electrooxidation, *Adv. Mater.* 32 (2020) e2000455.

219.   Y. Zhang, Y. Lin, T. Duan, L. Song, Interfacial engineering of heterogeneous catalysts for electrocatalysis, *Mater. Today*, 48 (2021) 115-134.

220.   S.-Q. Liu, H.-R. Wen, G. Ying, Y.-W. Zhu, X.-Z. Fu, R. Sun, C.-P. Wong, Amorphous $Ni(OH)_2$ encounter with crystalline CuS in hollow spheres: A mesoporous nano-shelled heterostructure for hydrogen evolution electrocatalysis, *Nano Energy*, 44 (2018) 7-14.

221.   W. Yuan, T. Jiang, X. Fang, Y. Fan, S. Qian, Y. Gao, N. Cheng, H. Xue, J. Tian, Interface engineering of S-doped $Co_2P@Ni_2P$ core–shell heterostructures for efficient and energy-saving water splitting, *Chem. Eng. J.* 439 (2022) 135743.

222.   H. Wang, Y. Zhou, S. Tao, CoP-CoOOH heterojunction with modulating interfacial electronic structure: A robust biomass-upgrading electrocatalyst, *Appl. Catal. B* 315 (2022)

121588.

223. T. Liu, P. Li, N. Yao, G. Cheng, S. Chen, W. Luo, Y. Yin, CoP-Doped MOF-Based Electrocatalyst for pH-Universal Hydrogen Evolution Reaction, *Angew. Chem., Int. Ed*. 58 (2019) 4679-4684.

224. Z. Liang, W. Zhou, S. Gao, R. Zhao, H. Zhang, Y. Tang, J. Cheng, T. Qiu, B. Zhu, C. Qu, W. Guo, Q. Wang, R. Zou, Fabrication of Hollow CoP/TiO$_x$ Heterostructures for Enhanced Oxygen Evolution Reaction, *Small*, 16 (2020) e1905075.

225. J.X. Feng, S.Y. Tong, Y.X. Tong, G.R. Li, Pt-like Hydrogen Evolution Electrocatalysis on PANI/CoP Hybrid Nanowires by Weakening the Shackles of Hydrogen Ions on the Surfaces of Catalysts, *J. Am. Chem. Soc*. 140 (2018) 5118-5126.

226. A.D. Wilson, R.H. Newell, M.J. McNevin, J.T. Muckerman, M. Rakowski DuBois, D.L. DuBois, Hydrogen oxidation and production using nickel-based molecular catalysts with positioned proton relays, *J. Am. Chem. Soc*. 128 (2006) 358-366.

227. E.J. Popczun, J.R. McKone, C.G. Read, A.J. Biacchi, A.M. Wiltrout, N.S. Lewis, R.E. Schaak, Nanostructured nickel phosphide as an electrocatalyst for the hydrogen evolution reaction, *J. Am. Chem. Soc*. 135 (2013) 9267-9270.

228. Y. Lin, K. Sun, S. Liu, X. Chen, Y. Cheng, W.C. Cheong, Z. Chen, L. Zheng, J. Zhang, X. Li, Y. Pan, C. Chen, Construction of CoP/NiCoP Nanotadpoles Heterojunction Interface for Wide pH Hydrogen Evolution Electrocatalysis and Supercapacitor, *Adv. Energy Mater.* 9 (2019) 1901213.

229. P.A. O'Day, J.J. Rehr, S.I. Zabinsky, G.E. Brown, Jr., Extended X-ray Absorption Fine Structure (EXAFS) Analysis of Disorder and Multiple-Scattering in Complex Crystalline Solids, *J. Am. Chem. Soc*. 116 (2002) 2938-2949.

230.   K. Xu, H. Cheng, H. Lv, J. Wang, L. Liu, S. Liu, X. Wu, W. Chu, C. Wu, Y. Xie, Controllable Surface Reorganization Engineering on Cobalt Phosphide Nanowire Arrays for Efficient Alkaline Hydrogen Evolution Reaction, *Adv. Mater*. 30 (2018) 1703322.

231.   Z. Chen, C.X. Kronawitter, B.E. Koel, Facet-dependent activity and stability of Co_3O_4 nanocrystals towards the oxygen evolution reaction, *Phys. Chem. Chem. Phys*. 17 (2015) 29387-29393.

232.   G. Rajeshkhanna, E. Umeshbabu, G.R. Rao, In situ grown nano-architectures of Co_3O_4 on Ni-foam for charge storage application, *J. Chem. Sci*. 129 (2016) 157-166.

233.   T.I. Singh, G. Rajeshkhanna, U.N. Pan, T. Kshetri, H. Lin, N.H. Kim, J.H. Lee, Alkaline Water Splitting Enhancement by MOF-Derived Fe-Co-Oxide/Co@NC-mNS Heterostructure: Boosting OER and HER through Defect Engineering and In Situ Oxidation, *Small*, 17 (2021) e2101312.

234.   X. Wan, C. Zhou, J. Chen, W. Deng, Q. Zhang, Y. Yang, Y. Wang, Base-Free Aerobic Oxidation of 5-Hydroxymethyl-furfural to 2,5-Furandicarboxylic Acid in Water Catalyzed by Functionalized Carbon Nanotube-Supported Au–Pd Alloy Nanoparticles, *ACS Catal*. 4 (2014) 2175-2185.

235.   M.-M. Zhu, X.-L. Du, Y. Zhao, B.-B. Mei, Q. Zhang, F.-F. Sun, Z. Jiang, Y.-M. Liu, H.-Y. He, Y. Cao, Ring-Opening Transformation of 5-Hydroxymethylfurfural Using a Golden Single-Atomic-Site Palladium Catalyst, *ACS Catal*. 9 (2019) 6212-6222.

236.   J. Hu, C. Zhang, L. Jiang, H. Lin, Y. An, D. Zhou, M.K.H. Leung, S. Yang, Nanohybridization of MoS_2 with Layered Double Hydroxides Efficiently Synergizes the Hydrogen Evolution in Alkaline Media, *Joule*, 1 (2017) 383-393.

237.   S.-W. Wu, S.-Q. Liu, X.-H. Tan, W.-Y. Zhang, K. Cadien, Z. Li, Ni_3S_2-embedded

NiFe LDH porous nanosheets with abundant heterointerfaces for high-current water electrolysis, *Chem. Eng. J.* 442 (2022) 136105.

238.   Q. Dong, T. Su, W. Ge, Y. Ren, Y. Liu, W. Wang, Q. Wang, X. Dong, Atomic Doping and Anion Reconstructed CoF_2 Electrocatalyst for Oxygen Evolution Reaction, *Adv. Mater. Interfaces* 7 (2020) 1901939.

239.   P. Ji, R. Yu, P. Wang, X. Pan, H. Jin, D. Zheng, D. Chen, J. Zhu, Z. Pu, J. Wu, S. Mu, Ultra-Fast and In-Depth Reconstruction of Transition Metal Fluorides in Electrocatalytic Hydrogen Evolution Processes, *Adv. Sci.* 9 (2022) e2103567.

240.   X. Deng, G.Y. Xu, Y.J. Zhang, L. Wang, J. Zhang, J.F. Li, X.Z. Fu, J.L. Luo, Understanding the Roles of Electrogenerated Co^{3+} and Co^{4+} in Selectivity-Tuned 5-Hydroxymethylfurfural Oxidation, *Angew. Chem., Int. Ed.* 60 (2021) 20535-20542.

241.   Q. Fu, T. Wu, G. Fu, T. Gao, J. Han, T. Yao, Y. Zhang, W. Zhong, X. Wang, B. Song, Skutterudite-Type Ternary $Co_{1-x}Ni_xP_3$ Nanoneedle Array Electrocatalysts for Enhanced Hydrogen and Oxygen Evolution, *ACS Energy Lett.* 3 (2018) 1744-1752.

242.   J. Liu, Y. Gao, X. Tang, K. Zhan, B. Zhao, B.Y. Xia, Y. Yan, Metal–organic framework-derived hierarchical ultrathin CoP nanosheets for overall water splitting, *J. Mater. Chem A*, 8 (2020) 19254-19261.

243.   M. Lefèvre, E. Proietti, F. Jaouen and J.-P. Dodelet, *science*, 2009, 324, 71-74.

244.   S. Liu, C. Li, M. J. Zachman, Y. Zeng, H. Yu, B. Li, M. Wang, J. Braaten, J. Liu and H. M. Meyer, *Nat. Energy*, 2022, 7, 652-663.

245.   J. Li, M. Chen, D. A. Cullen, S. Hwang, M. Wang, B. Li, K. Liu, S. Karakalos, M. Lucero and H. Zhang, *Nat. Catal.*, 2018, 1, 935-945.

246.   W. Li, D. Wang, Y. Zhang, L. Tao, T. Wang, Y. Zou, Y. Wang, R. Chen and S. Wang, *Adv. Mater.*, 2020, 32, 1907879.

247.   M. Zhao, H. Liu, H. Zhang, W. Chen, H. Sun, Z. Wang, B. Zhang, L. Song, Y. Yang and C. Ma, *Energy Environ. Sci.*, 2021, 14, 6455-6463.

248.   F. Luo, A. Roy, L. Silvioli, D. A. Cullen, A. Zitolo, M. T. Sougrati, I. C. Oguz, T. Mineva, D. Teschner and S. Wagner, *Nat. Mater.*, 2020, 19, 1215-1223.

249.   J. Wang, Z. Huang, W. Liu, C. Chang, H. Tang, Z. Li, W. Chen, C. Jia, T. Yao and S. Wei, *J. Am. Chem. Soc.*, 2017, 139, 17281-17284.

250.   L. Xie, X. P. Zhang, B. Zhao, P. Li, J. Qi, X. Guo, B. Wang, H. Lei, W. Zhang and U. P. Apfel, *Angew. Chem. Int. Ed.*, 2021, 133, 7654-7659.

251.   X.-P. Zhang, A. Chandra, Y.-M. Lee, R. Cao, K. Ray and W. Nam, *Chem. Soc. Rev.*, 2021, 50, 4804-4811.

252.   V. R. Stamenkovic, B. Fowler, B. S. Mun, G. Wang, P. N. Ross, C. A. Lucas and N. M. Markovic, *science*, 2007, 315, 493-497.

253.   H. Ze, X. Chen, X.-T. Wang, Y.-H. Wang, Q.-Q. Chen, J.-S. Lin, Y.-J. Zhang, X.-G. Zhang, Z.-Q. Tian and J.-F. Li, *J. Am. Chem. Soc.*, 2021, 143, 1318-1322.

254.   Y. Guo, M. Wang, Q. Zhu, D. Xiao and D. Ma, *Nature Catal.*, 2022, 5, 766-776.

255.   S. Li, J. Liu, Z. Yin, P. Ren, L. Lin, Y. Gong, C. Yang, X. Zheng, R. Cao, S. Yao and Y. Deng, *ACS Catal.,* 2019, 10, 907-913.

256.   L. Yang, X. Zhang, L. Yu, J. Hou, Z. Zhou and R. Lv, *Adv. Mater.*, 2022, 34, 2105410.

257.   X. Xie, L. Peng, H. Yang, G. I. Waterhouse, L. Shang and T. Zhang, *Adv. Mater.*, 2021, 33, 2101038.

258.   Y. Chen, S. Ji, Y. Wang, J. Dong, W. Chen, Z. Li, R. Shen, L. Zheng, Z. Zhuang and D. Wang, *Angew. Chem. Int. Ed.*, 2017, 129, 7041-7045.

259.   A. Han, X. Wang, K. Tang, Z. Zhang, C. Ye, K. Kong, H. Hu, L. Zheng, P. Jiang and C. Zhao, *Angew. Chem. Int. Ed.,* 2021, 60, 19262-19271.

260.   A. Kulkarni, S. Siahrostami, A. Patel and J. K. Nørskov, *Chemical Reviews*, 2018, 118, 2302-2312.

261.   S. Kattel and G. Wang, *J. Phys. Chem. Lett.*, 2014, 5, 452-456.

262.   L. Huang, J. Chen, L. Gan, J. Wang and S. Dong, *Sci. Adv.*, 2019, 5, eaav5490.

263.   N. Zhang, T. Zhou, J. Ge, Y. Lin, Z. Du, W. Wang, Q. Jiao, R. Yuan, Y. Tian and W. J. M. Chu, *Matter*, 2020, 3, 509-521.

264.   W. Ye, S. Chen, Y. Lin, L. Yang, S. Chen, X. Zheng, Z. Qi, C. Wang, R. Long and M. J. C. Chen, *Chem*, 2019, 5, 2865-2878.

265.   Z. Zhu, H. Yin, Y. Wang, C. H. Chuang, L. Xing, M. Dong, Y. R. Lu, G. Casillas-Garcia, Y. Zheng and S. Chen, *Adv. Mater.*, 2020, 32, 2004670.

266.   G. Yang, J. Zhu, P. Yuan, Y. Hu, G. Qu, B.-A. Lu, X. Xue, H. Yin, W. Cheng and J. Cheng, *Nat. Commun.*, 2021, 12, 1-10.

267.   A. Han, X. Wang, K. Tang, Z. Zhang, C. Ye, K. Kong, H. Hu, L. Zheng, P. Jiang and C. Zhao, *Angew. Chem. Int. Ed.*, 2021, 60, 19262-19271.

268.   H. Li, Y. Wen, M. Jiang, Y. Yao, H. Zhou, Z. Huang, J. Li, S. Jiao, Y. Kuang and S. Luo, *Adv. Funct. Mater.*, 2021, 31, 2011289.

269.   T. He, Y. Chen, Q. Liu, B. Lu, X. Song, H. Liu, M. Liu, Y. N. Liu, Y. Zhang and X. Ouyang, *Angew. Chem. Int. Ed.*, 2022, 61, e202201007.

270.   S. H. Lee, J. Kim, D. Y. Chung, J. M. Yoo, H. S. Lee, M. J. Kim, B. S. Mun, S. G. Kwon, Y.-E. Sung and T. Hyeon, *J. Am. Chem. Soc.*, 2019, 141, 2035-2045.

271.   X. Wan, X. Liu, Y. Li, R. Yu, L. Zheng, W. Yan, H. Wang, M. Xu and J. Shui, *Nat. Catal.*, 2019, 2, 259-268.

272.   X. Fu, P. Zamani, J. Y. Choi, F. M. Hassan, G. Jiang, D. C. Higgins, Y. Zhang, M. A. Hoque and Z. Chen, *Adv. Mater.*, 2017, 29, 1604456.

273.   Y. Ye, F. Cai, H. Li, H. Wu, G. Wang, Y. Li, S. Miao, S. Xie, R. Si and J. Wang, *Nano Energy*, 2017, 38, 281-289.

274.   S. H. Lee, J. Kim, D. Y. Chung, J. M. Yoo, H. S. Lee, M. J. Kim, B. S. Mun, S. G. Kwon, Y.-E. Sung and T. Hyeon, *J. Am. Chem. Soc.*, 2019, 141, 2035-2045.

275.   H.-W. Liang, X. Zhuang, S. Brüller, X. Feng and K. J. N. c. Müllen, *Nat. Commun.*, 2014, 5, 1-7.

276.   Y. He, H. Guo, S. Hwang, X. Yang, Z. He, J. Braaten, S. Karakalos, W. Shan, M. Wang and H. Zhou, *Adv. Mater.*, 2020, 32, 2003577.

277.   X. Xie, L. Peng, H. Yang, G. I. Waterhouse, L. Shang and T. J. A. M. Zhang, *Adv. Mater.*, 2021, 33, 2101038.

278.   Y. He, H. Guo, S. Hwang, X. Yang, Z. He, J. Braaten, S. Karakalos, W. Shan, M. Wang and H. J. A. M. Zhou, *Adv. Mater.*, 2020, 32, 2003577.

279.   Z. Wang, X. Jin, C. Zhu, Y. Liu, H. Tan, R. Ku, Y. Zhang, L. Zhou, Z. Liu and S. J. Hwang, *Adv. Mater.*, 2021, 33, 2104718.

280.   M. Tong, F. Sun, Y. Xie, Y. Wang, Y. Yang, C. Tian, L. Wang and H. Fu, *Angew. Chem. Int. Ed.*, 2021, 60, 14005-14012.

281.   H. Yang, Y. Wu, G. Li, Q. Lin, Q. Hu, Q. Zhang, J. Liu and C. He, *J. Am. Chem. Soc.*, 2019, 141, 12717-12723.

282.   F. Huang, Y. Deng, Y. Chen, X. Cai, M. Peng, Z. Jia, J. Xie, D. Xiao, X. Wen, N. Wang and Z. Jiang, *Nat. commun.,* 2019, 10, 4431.

283.   T. He, Y. Chen, Q. Liu, B. Lu, X. Song, H. Liu, M. Liu, Y. N. Liu, Y. Zhang, X. Ouyang and S Chen, *Angew. Chem. Int. Ed.*, 2022, 61, e202201007.

284.   J. Zhou, P. N. Duchesne, Y. Hu, J. Wang, P. Zhang, Y. Li, T. Regier and H. Dai, *Phys. Chem. Chem. Phys*., 2014, 16, 15787-15791.

285.   W.-J. Jiang, L. Gu, L. Li, Y. Zhang, X. Zhang, L.-J. Zhang, J.-Q. Wang, J.-S. Hu, Z. Wei and L. Wan, *J. Am. Chem. Soc.*, 2016, 138, 3570-3578.

286.   X. Guo, H. Xu, W. Li, Y. Liu, Y. Shi, Q. Li and H. Pang, *Adv. Sci.,* 2023, 10, 2206084.

287.   L. Ouyang, E. S. Thrall, M. M. Deshmukh and H. Park, *Adv. Mater.,* 2006, 18, 1437-1440.

288.   F. A. Cotton, G. Wilkinson, C. A. Murillo and M. Bochmann, *Advanced inorganic chemistry*, John Wiley and Sons, Inc., 1999.

289.   S. A. Guda, A. A. Guda, M. A. Soldatov, K. A. Lomachenko, A. L. Bugaev, C. Lamberti, W. Gawelda, C. Bressler, G. Smolentsev, A. V. Soldatov, Y. Joly, *J. Chem. Theory Comput*., 2015, 11, 4512-4521.

290.   S. Xu, Y. Kim, D. Higgins, M. Yusuf, T. F. Jaramillo and F. B. Prinz, *Electrochim. Acta*, 2017, 255, 99-108.

291.   Y. Tian, X. Liu, L. Xu, D. Yuan, Y. Dou, J. Qiu, H. Li, J. Ma, Y. Wang, D. Su and S. Zhang, *Adv. Funct. Mater.*, 2021, 31, 2101239.

292.	W. Zhai, S. Huang, C. Lu, X. Tang, L. Li, B. Huang, T. Hu, K. Yuan, X. Zhuang and Y. Chen, *Small*, 2022, 18, 2107225.

293.	R. Cao, R. Thapa, H. Kim, X. Xu, M. Gyu Kim, Q. Li, N. Park, M. Liu and J. Cho, *Nat. Commun.*, 2013, 4, 1-7.

294.	R. Pal, L.-M. Wang, Y. Pei, L.-S. Wang and X. C. Zeng, *J. Am. Chem. Soc.*, 2012, 134, 9438-9445.

295.	Y. Sun, L. Silvioli, N. R. Sahraie, W. Ju, J. Li, A. Zitolo, S. Li, A. Bagger, L. Arnarson and X. Wang, *J. Am. Chem. Soc.*, 2019, 141, 12372-12381.

296.	X. Ao, W. Zhang, Z. Li, J.-G. Li, L. Soule, X. Huang, W.-H. Chiang, H. M. Chen, C. Wang, M. Liu and X.C. Zeng, *ACS nano*, 2019, 13, 11853-11862.

297.	T. Cui, Y. P. Wang, T. Ye, J. Wu, Z. Chen, J. Li, Y. Lei, D. Wang and Y. Li, *Angew. Chem. Int. Ed.*, 2022, 61, e202115219.

298.	J. K. Nørskov, J. Rossmeisl, A. Logadottir, L. Lindqvist, J. R. Kitchin, T. Bligaard and H. Jónsson, *J. Phys. Chem. B.*, 2004, 108, 17886-17892.

299.	H. Lee, O. Gwon, K. Choi, L. Zhang, J. Zhou, J. Park, J.-W. Yoo, J.-Q. Wang, J. H. Lee and G. Kim, *ACS Catal.*, 2020, 10, 4664-4670.

300.	K. Liu, J. Fu, Y. Lin, T. Luo, G. Ni, H. Li, Z. Lin and M. Liu, *Nat. Commun.*, 2022, 13, 1-8.

301.	D. C. Koningsberger and R. Prins, 1987.

302.	B. Ravel and M. Newville, *J. Synchrotron Radiat*, 2005, 12, 537-541.

303.	H. Funke, A. Scheinost and M. Chukalina, *Phys. Rev. B*, 2005, 71, 094110.

304.	H. Funke, M. Chukalina and A. Scheinost, *J. Synchrotron Radiat*, 2007, 14, 426-432.

305. O. Bunău, A. Y. Ramos and Y. Joly, *Wiley*, 2021.

306. Y. Joly, A. Y. Ramos and O. Bunău, *Wiley*, 2022.

307. S. Niu, S. Li, Y. Du, X. Han and P. Xu, *ACS Energy Lett*, 2020, 5, 1083-1087.

308. S. G. Ji, H. Kim, C. Park, W. Kim and C. Choi, *ACS Catal.*, 2020, 10, 10773-10783.

309. G. Yang, J. Zhu, P. Yuan, Y. Hu, G. Qu, B.-A. Lu, X. Xue, H. Yin, W. Cheng, J. Cheng and W. Xu, *Nat. Commun.*, 2021, 12, 1734.

310. G. Kresse and J. Furthmüller, *Comput. Mater. Sci.*, 1996, 6, 15-50.

311. G. Kresse and J. Furthmüller, *Phys. Rev. B*, 1996, 54, 11169-11186.

312. G. Kresse and J. Hafner, *J. Phys. Condens. Matter*, 1994, 6, 8245-8257.

313. G. Kresse and D. Joubert, *Phys. Rev. B*, 1999, 59, 1758-1775.

314. G. Kresse and J. Hafner, *Phys. Rev. B*, 1993, 47, 558-561.

315. P. E. Blöchl, *Phys. Rev. B,* 1994, 50, 17953-17979.

316. J. P. Perdew, K. Burke and M. Ernzerhof, *Phys. Rev. Lett.*, 1996, 77, 3865-3868.

317. J. Klimeš, A. Bowler Dr Fau - Michaelides and A. Michaelides, *Condens. Matter*, 2009, 22, 022201.

318. J. Klimeš, D. R. Bowler and A. Michaelides, *Phys. Rev. B*, 2011, 83, 195131.

319. Malcolm W. Chase, Jr., *NIST-JANAF thermochemical tables*, Fourth edition. Washington, DC : American Chemical Society ; New York : American Institute of Physics for the National Institute of Standards and Technology, 1998.

320. J. K. Nørskov, J. Rossmeisl, A. Logadottir, L. Lindqvist, J. R. Kitchin, T. Bligaard and H. Jónsson, *J. Phys. Chem. B*, 2004, 108, 17886-17892.

321. X. Wan, Q. Liu, J. Liu, S. Liu, X. Liu, L. Zheng, J. Shang, R. Yu and J. Shui, *Nat. commun.*, 2022, 13, 2963.

322.   S. An, G. Zhang, T. Wang, W. Zhang, K. Li, C. Song, J. T. Miller, S. Miao, J. Wang and X. Guo, *ACS nano*, 2018, 12, 9441-9450.

323.   T. He, Y. Chen, Q. Liu, B. Lu, X. Song, H. Liu, M. Liu, Y. N. Liu, Y. Zhang and X. Ouyang, *Angew. Chem. Int. Ed.,* 2022, 61, e202201007.

324.   H. Li, S. Di, P. Niu, S. Wang, J. Wang, L. Li, *Energy Environ. Sci.*, 2022, 15, 1601-1610.

325.   B. Ji, J. Gou, Y. Zheng, X. Zhou, P. Kidkhunthod, Y. Wang, Q. Tang and Y. Tang, *Adv. Mater.,* 2022, 34, 2202714.

326.   Z. Wang, X. Jin, C. Zhu, Y. Liu, H. Tan, R. Ku, Y. Zhang, L. Zhou, Z. Liu, S. J. Hwang and H.J. Fan, *Adv. Mater.*, 2021, 33, 2104718.

327.   G. Yang, J. Zhu, P. Yuan, Y. Hu, G. Qu, B.-A. Lu, X. Xue, H. Yin, W. Cheng, J. Cheng and W. Xu, *Nat. Commun.,* 2021, 12, 1-10.

328.   M. Tong, F. Sun, Y. Xie, Y. Wang, Y. Yang, C. Tian, L. Wang and H. Fu, *Angew. Chem. Int. Ed.,* 2021, 60, 14005-14012.

329.   J. Xue, Y. Li and J. Hu, *J. Mater. Chem. A*, 2020, 8, 7145-7157.

330.   A. Han, X. Wang, K. Tang, Z. Zhang, C. Ye, K. Kong, H. Hu, L. Zheng, P. Jiang, C. Zhao and Q. Zhang *Angew. Chem. Int. Ed.,* 2021, 60, 19262-19271.

331.   J. Chen, H. Li, C. Fan, Q. Meng, Y. Tang, X. Qiu, G. Fu, T. Ma., *Adv. Mater.,* 2020, **32**, 2003134.

332.   Z. Zhu, H. Yin, Y. Wang, C. H. Chuang, L. Xing, M. Dong, Y. R. Lu, G. Casillas-Garcia, Y. Zheng, S. Chen and Y. Dou, *Adv. Mater.,* 2020, 32, 2004670.

333.   Rao, P., Deng, Y., Fan, W. *et al.* Movable type printing method to synthesize high-entropy single-atom catalysts. *Nat Commun.,* 2022, **13**, 5071.

334.   X. Li, C.-S. Cao, S.-F. Hung, Y.-R. Lu, W. Cai, A. I. Rykov, S. Miao, S. Xi, H. Yang, Z. Hu, J. Wang, *Chem* 2020, 6, 3440-3454.

335.   K. Yuan, D. Lützenkirchen-Hecht, L. Li, L. Shuai, Y. Li, R. Cao, M. Qiu, X. Zhuang, M. K. Leung, Y. Chen, U. Scherf, *J. Am. Chem. Soc.* 2020, 142, 2404-2412.

336.   L. Yang, X. Zhang, L. Yu, J. Hou, Z. Zhou and R. Lv, *Adv. Mater.,* 2022, **34**, 2105410.

337.   X. Tan, H. Li, W. Zhang, K. Jiang, S. Zhai, W. Zhang, N. Chen, H. Li and Z. Li, *Chem Catal.,* 2022, **2**, 816-835.

338.   C. Zhu, Q. Shi, B. Z. Xu, S. Fu, G. Wan, C. Yang, S. Yao, J. Song, H. Zhou, D. Du and S.P. Beckman, *Adv. Energy Mater.,* 2018, **8**, 1801956.

339.   S. N. Zhao, J. K. Li, R. Wang, J. Cai and S. Q. Zang, *Adv. Mater*., 2022, **34**, 2107291.

340.   X. Ao, W. Zhang, Z. Li, J.-G. Li, L. Soule, X. Huang, W.-H. Chiang, H. M. Chen, C. Wang, M. Liu and X.C. Zeng, *ACS nano,* 2019, **13**, 11853-11862.

341.   H. Huang, D. Yu, F. Hu, S. C. Huang, J. Song, H. Y. Chen, L. L. Li and S. J. A. C. Peng, *Angew. Chem. Int. Ed.,* 2022, **134**, e202116068.

342.   Y. Zhou, R. Lu, X. Tao, Z. Qiu, G. Chen, J. Yang, Y. Zhao, X. Feng, K. J. J. o. t. A. C. S. Müllen, *J. Am. Chem. Soc.*, 2023, **145**, 3647-3655.

343.   Q. Feng, X. Wang, M. Klingenhof, M. Heggen and P. Strasser, *Angew. Chem. Int. Ed.,* 2022, 61, e202203728.

344.   W. He, X. Li, Z. Qian, Z. Liu and Z. Tang, *Int. J. Electrochem. Sci*, 2019, 14, 8781-8792.